Use of Dynamic Test Methods to Reveal Mechanical Properties of Nanomaterials

by

H. S. Tanvir Ahmed, B.S.M.E, M.S.M.E

A Dissertation

In

MECHANICAL ENGINEERING

Submitted to the Graduate Faculty
of Texas Tech University in
Partial Fulfillment of
the Requirements for
the Degree of

DOCTOR OF PHILOSOPHY

Approved

Alan F. Jankowski, Ph.D.
(Chairperson of the Committee)

Jharna Chaudhuri, Ph.D.

Alexander Idesman, Ph.D.

Michelle Pantoya, Ph.D.

Shameem Siddiqui, Ph.D.

Fred Hartmeister
Dean of the Graduate School

December, 2010

Dedicated to my parents, my family and friends.

ACKNOWLEDGMENTS

"…Then which of the favors of your Lord will you deny" (Al-Quran: 55)

Praise be to the most merciful, the most gracious, who created heavens and earth and everything in-between. It is the almighty God who taught human beings how to read and write. Without His will, kindness and mercy, the completion of this work would have never been possible.

I would like to express my sincere gratitude and appreciation to my thesis advisor, Dr. Alan F. Jankowski, not only for his keen supervision and valuable suggestions, but also for teaching me how to work on solving the riddles of everyday life. I enjoyed talking with him not only about research, but also exchanging views about socio-cultural events, politics and history of human evolution. His continuous support made my stay at the mechanical engineering department full of joy and excitement and guided me to achieve my career goals. I am also thankful to my doctoral committee Dr. Jharna Chaudhuri, Dr. Alexander Idesman, Dr. Michelle Pantoya and Dr. Shameem Siddiqui for their continual support and inspiration.

None of this would have possible without the love and encouragement of my parents, my brother and sister, and my friends. Their constant back-ups from a land half around the world has always been like a beacon to me. I thank my uncle, Engr. Nazmul Hasan, who inspired me to pursue this higher study, when I was about to let the opportunity go away in order to take care of a difficult situation. Thanks to my wife for her patience and support.

PREFACE

This dissertation is based upon the research conducted in the Nanomaterials Lab of Mechanical Engineering Department at Texas Tech University. The purpose of this dissertation is to find suitable test methods to measure the mechanical properties of nanomaterials. Different chapters in this dissertation describe different techniques for testing nanomaterials. In general, the mechanical characterization of nanomaterials has been limited to small range of strain rates with available static techniques. Even though some of the dynamic techniques have originated a long time ago (for example, the scratch technique was developed by German mineralogist Friedrich Mohs during the early 1800s), not many improvements have been made towards developing the details of the techniques as well as analyzing the outcome results.

Nanomaterials show a great promise as future materials to be used in various industrial applications like MEMS, NEMS, band-gap engineering etc. In such prospective applications, these materials may go through different strain rates as induced by either mechanical or thermal load. For this reason, it is very important to find out their elastic and plastic properties over a wide range of strain rates. The methodologies developed in this dissertation will enable us to measure the elastic properties of thin films as well as the plastic properties in terms of the strain rate sensitivity of strength as described by the Dorn equation.

Chapter 1 introduces how a tensile testing machine can be used in a dynamic manner and thereby, measure strain rate sensitivity exponents for micro-to-nano porous silver, dense silver, bulk Au-Cu metallic alloy and bulk nanocrystalline nickel. These tensile test results establish the baseline for comparison with other test results

such as micro and nano-scratch. Different modeling equations are proposed in this section to predict the experimental data from tensile tests. This chapter also describes potential change of elastic properties of porous materials, as can be seen with intermittent tensile test experiments.

The micro-scratch techniques are described in Chapter 2, where epoxy mounted porous and dense silver as well as nanocrystalline Nickel foils are scratched on cross-sections at different strain rates. The hardness properties of the foils are measured from the dimensions of the produced scratches. An optical microscope is used to scan the surface to measure the necessary scratch dimension. As it is seen in this section, there is good agreement between the tensile data and the micro-scratch data.

Nano-scratch technique is quite like the micro-scratch, however, done on a much smaller scale and requires more precise control of the equipment. Artificial ceramic bone and a Au-Ni nanocrystalline nanolaminate (ncnl) are tested with this technique as documented in Chapter 3. This chapter introduces how the grain boundary and layer pair area of a ncnl can be included in the analysis for hardness measurement.

Chapter 4 describes how the elastic properties of thin films can be measured using a probe with a vibrating cantilever. This technique is fairly new and is widely known as the tapping mode frequency shift. Yet, the method is based on Hertzian contact mechanics developed over a century ago. This technique measures the modulus in the normal to plane direction of the thin films.

The first three chapters are to show that scratch test can measure the hardness in a wide range of strain rates and can be correlated with the more common tensile test. Of course, scratch test is less prone to brittle fracture and stress concentration because of its shear type of deformation. With scratch technique, it is possible to measure hardness of a specific area, for example, the hardness of either the fiber or the matrix or both in a fiber-matrix composite. Tensile, micro and nano scratch can be used in conjunction to describe mechanical behavior of a material for a significant loading rate range. The fourth chapter is to provide the details of the underlying formulations of the tapping mode technique, which essentially has the ability to measure elastic anisotropy of the material.

With the increase of use of nanomaterials foreseen for this century, the author believes that this research will enable to correctly characterize the mechanical properties of such materials in a wider range of applications.

TABLE OF CONTENTS

ABSTRACT

Dynamic indentation techniques like micro and nanoscratch compared to static nanoindentation offer more robust extraction of mechanical properties of thin films, with higher level of control during experimentations. The velocity of the scratch indenter can be changed for probing the material properties at a wide range of strain rate. Considering the potential of this technique, detailed knowledge about the applicability of scratch method to different material systems is essential to create strategies for controlling appropriate physical feature for better mechanical properties at nanoscale.

Micro-scratch testing of free-standing micro-to-nano porous and dense metal foils shows a different rate sensitivity exponent at higher strain rate, suggesting a different mode of deformation. Continuous and interrupted tensile testing have been done on foils to provide a base line for comparison of strain rate sensitivity as well as possible stiffening effect under progressive load. Tensile testing of nanocrystalline metal alloys has been conducted to do the comparison with prior micro-scratch results. Nano-scratch testing on nanocrystalline nanolaminates and artificial ceramic bone (coatings of hydroxyapatite) are tested to reveal strength and strain rate sensitivity. In addition, a new technique known as the tapping mode measurement is investigated to determine the elastic-plastic transition and measure the elastic modulus of metallic nanolaminates and hydroxyapatite thin films for comparison to static nanoindentation.

LIST OF TABLES

LIST OF FIGURES

CHAPTER 1

TENSILE TESTING OF NANOMATERIALS

1.1 Introduction

Porous materials have a combination of mechanical properties that make them attractive for many engineering applications. They are lightweight, have a capacity to undergo large deformation without generation of localized damaging peak stresses, and possess high surface area per unit volume [1]. Porous metal membranes may be considered as ideal candidates [2] for lightweight-structural sandwich panels, energy absorption devices, and heat sinks. The use of porous metal coatings is ever increasing in renewable-energy system applications [3] as solar cells and hydrogen fuel cells. Recent researches on nanoporous materials are suggestive of their future uses as electrochemical [4] or chemical [5] actuation, tunable conductors [6, 7] and magnets [8, 9]. In particular, the scale of porosity in metal coatings is particularly important to their catalytic performance [10]. Potentially just as important is the mechanical stability of the porous coating in these devices. Thus, understanding the mechanical behavior of these foams in a wide range of strain rates is important for such potential applications, where the rate of deformation may originate as rapid thermal stress-strain cycles.

Use of compression testing and nanoindentation to reveal mechanical properties of porous materials is been reported by many researchers [2, 11, 12, 13, 14, 15, 16, 17, 18]. In this study, a series of rate-dependent tensile tests are conducted to better understand the operative deformation mechanisms in the evaluation of strength as the scale of the porous structure changes from the micro-to-nano regime.

1

Commercially available, free-standing silver (Ag) membranes with constituent micron-to-submicron porosity and fully dense foils are evaluated here for their rate dependency of strength. Preliminary findings [19] indicate that the strain-rate sensitivity of tensile tested specimens is found to increase as length scale decreases. The trends are similar to those experimental results reported for bulk nanocrystalline metals. Underlying structural features that can contribute to this mechanical behavior include pore size, filament or strut size, and the grain size within. These features of length scale are evaluated through monotonic and interrupted tensile testing.

In this study, the effect of pore size, filament size and grain size on yield strength of commercially available porous Ag subjected to different strain rate are investigated. Different pore sizes of the porous Ag, i.e. 0.2 μm, 0.45 μm, 0.8 μm and 3 μm, are studied. For testing the specimens, we have applied tensile testing which is free from the bending and buckling problems associated with compression testing.

The strain rate sensitivity behavior of nanocrystalline nickel (Ni) is also being researched here. The nickel foils are obtained from the electro-deposition process and are available in fully dense condition. Many researchers [20, 21, 22, 23, 24, 25] are studying for the room temperature strain rate sensitivity of fine grained submicron Ni because of its high strain rate sensitivity exponent (*m*) and its excellent prospect in terms of functionality in the MEMS/NEMS area [26].

In addition, the rate sensitivity behavior of nanocrystalline gold-copper (Au-Cu) is being investigated here. The free standing Au-Cu foils are obtained from pulsed electro-deposition process [27, 28, 29] and are available in fully dense condition.

Micron thick film of Au-Cu alloy is considered to be an attractive option for use as a

high pressure vessel [30] for laser fusion experiments, where high strain rates occur

with a low rise time. As such, the strain rate sensitivity of these alloys is important to

be examined. Previously, tensile testing [31] was conducted on Au-Cu alloys, but the

rate sensitivity behavior is yet to be investigated.

1.2 Materials

Porous silver membranes of 25 mm diameter of varying nominal pore sizes,

i.e. 0.22 µm, 0.45 µm, 0.8 µm and 3.0 µm are procured from General Electric

Osmonics[TM]. The purity of the silver membranes is stated to be 99.97% [32]. The

average thickness of the foils ranges from 57 to 79 µm as measured from a stack of ten

foils with a micrometer. Average cross-section of the membranes is measured using a

micrometer from a stack of 10 foils. SEM images on cross-section of the foils validate

this measurement. The weight of the sample is measured using a microbalance and

sample density ρ is calculated using the formulation:

$$\rho = \frac{w}{\pi r^2 h} \tag{1.1}$$

where, h is the average thickness of the foil and w is the weight of the foil. Porosity p

is given by

$$p = 1 - \frac{\rho}{\rho_{Ag}} \tag{1.2}$$

where, ρ_{Ag} is the density of fully dense silver and is 10.5 gm/cc. A die is designed

(Figure 1.1) following ASTM standards (length is equal to or greater than three times

the width.) to produce two test specimens from a single disc and was made through

NC milling. Tensile test specimens are cut from the foils using this die, resulting in a

gage length of 10 mm and width of 3 mm.
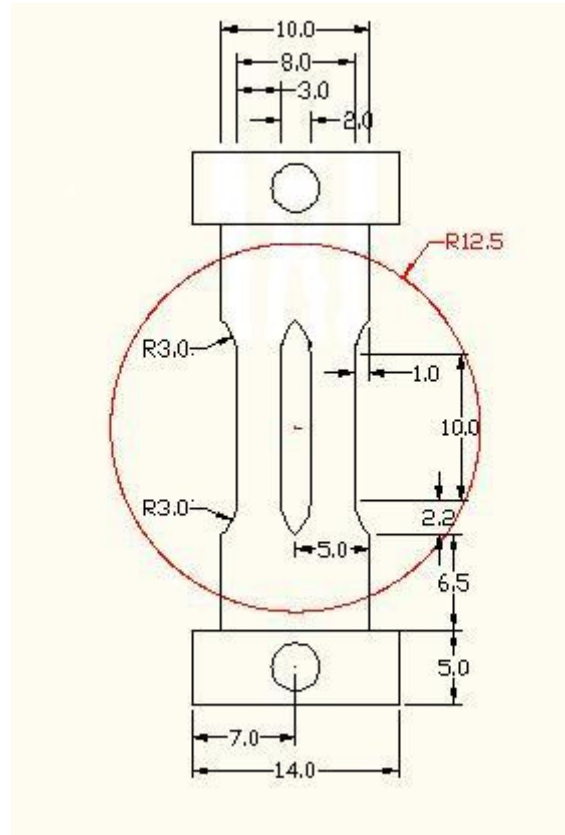
Figure 1.1: Design of die (dimensions in mm)

SEM images are taken in plan view and in cross-section of the samples to

provide surface morphology and structural features. Some definition of grain sizes

within each filament is also available from these images. Lineal intercept method is

used to measure the filament sizes of the different foils, wherein six different straight

lines are drawn at equal angular spacing on the plan view SEM image of the foils. The

measurements of the filaments are taken between the intercept points along the lines.

The grain sizes are estimated to be the average of the shortest distances, i.e. the

widths, of the filaments, assuming that the filaments have a bamboo-type structure wherein grains are adjacent to one another to form the structure. The average grain size, irrespective of the pore sizes of the samples, is measured to be 2.47±0.19 μm. Table 1.1 summarizes the measurements of the foils of each nominal pore size:

Table 1.1: Measurements on the foils according to their nominal pore sizes

Pore size (μm)	Average thickness (μm)	Ave. filament size (μm)	Average Porosity	Ave. grain size (μm)
0.22	57 ± 1	6.08 ± 2.50	0.258 ± 0.008	2.77 ± 0.62
0.45	60 ± 3	8.12 ± 5.62	0.341 ± 0.017	2.33 ± 0.41
0.80	79 ± 2	3.81 ± 1.54	0.482 ± 0.019	2.27 ± 0.43
3.00	79 ± 2	5.87 ± 3.60	0.502 ± 0.045	2.50 ± 0.52

Both in-plane and cross-sectional SEM images reveal that the pores transit through the thickness as well through the cross-section, which denotes the pore structure to be three dimensional. For a porous material, it is necessary to use corrected cross-sectional area instead of the geometrical cross-sectional area in the measurement of stress and elasticity. The corrected cross-sectional area A_c is given by:

$$A_c = A(1-p)^n \tag{1.3}$$

where, A is the geometric cross-sectional area, p is the porosity and $n= 1$ (for 2-D pore morphology, wherein the pores run through the thickness only), 1.5 (for 3-D pore morphology) [1]. A representative plan view and cross-section SEM image on a 0.8 μm membrane is given in Figure 1.2, which shows that the pores on plan view and on thickness are of nearly equivalent structure, hence implying that the value of n to be

1.5. The plan view is taken prior to deformation and the cross-sectional image is taken after the sample was tested to failure. As it is seen from this figure, the pre versus post deformation images are quite similar and do not show significant difference in pore size or filament width, except for some locations where cup and cone formations may have generated.
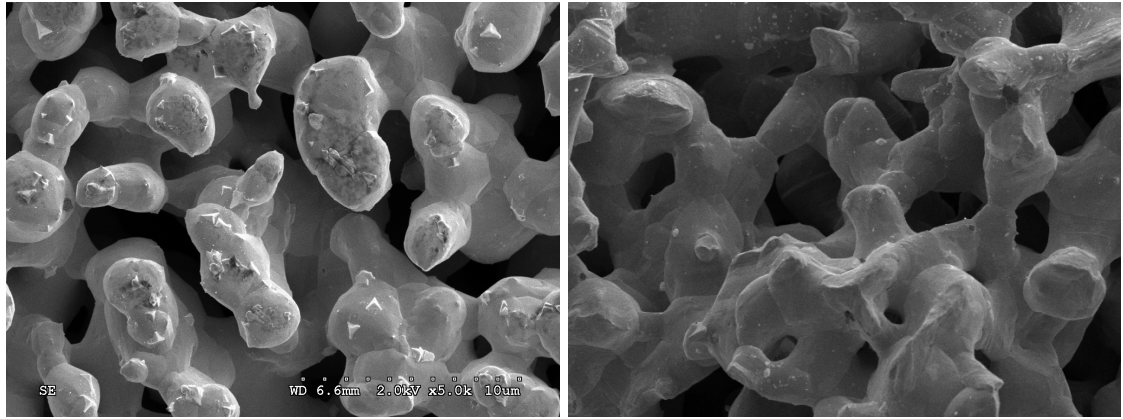
Figure 1.2: SEM images of plan view on left (pre-deformation) and of cross-section on right (post-deformation) of a 0.8 µm foil

For comparison of the mechanical properties of these porous structures, fully dense silver foils with 99.95% reported purity are procured from 'SurePure Chemetals' [33]. Tensile test specimens are die cut from this foils using the same die (as shown in Figure 1.1) to produce test pieces of 10 mm gage length and 3 mm width. The thickness of these dense foils is 50±3 µm as measured with a micrometer and verified with an optical microscope. Figure 1.3 shows a representative cross-section of the dense silver.

In addition to the Ag foils, electrodeposited nanocrystalline Au-Cu thin film foils [27, 28, 29] are available for study. Segments from these as-deposited thin films

are used to serve as tensile test specimens. Because of the deposition condition, the test pieces are thinner at the middle while thicker at the ends. This as-deposition condition is utilized to make the dog-bone shaped test pieces from the thin films. Tensile testing is conducted at different rates on these specimens to provide the strain rate sensitivity.
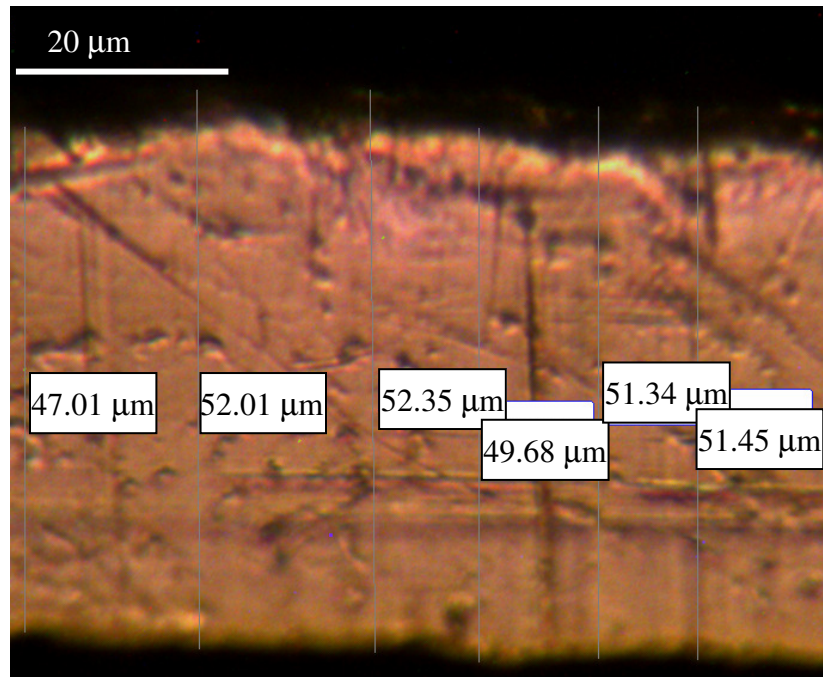
Figure 1.3: Cross-section of a dense silver foil measured with an optical microscope
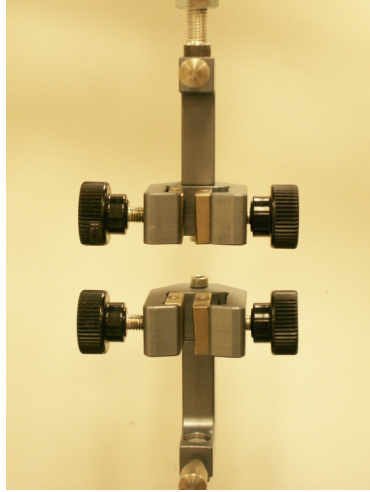
Figure 1.4: Detachable serrated grips used for tensile tests

1.3 Experimental methods and Analysis

1.3.1 Tensile test of Ag foils

The tensile test specimens are mounted on a TestResources^{TM} universal testing machine using detachable clamps with serrated grip surfaces (Figure 1.4). Rate sensitive testing is done on the specimens by moving the linear actuator of the machine over the displacement of 10 mm while varying the displacement time from 10^{+1} sec to 10^{+4} sec. The strain rate ($\dot{\varepsilon}$) is given by:

$$\dot{\varepsilon} = \frac{(\Delta l / l)}{\Delta t} \tag{1.4}$$

where, Δl is the displacement of the actuator (up to 10 mm), l is the initial length of the specimen = 10 mm and Δt is the associated displacement time. Thus, the associated strain rates will range from 10^{-1}/sec to 10^{-4}/sec. The data acquisition system logs the normal load from a load sensor as the displacement sensor (Linearly Variable Differential Transducer, LVDT) records the crosshead position as a function of time at a user specified frequency. The displacement-measured load curves are fit with a

twenty point moving average. Engineering stresses for the specimens are calculated using corrected cross-sectional area A_c.
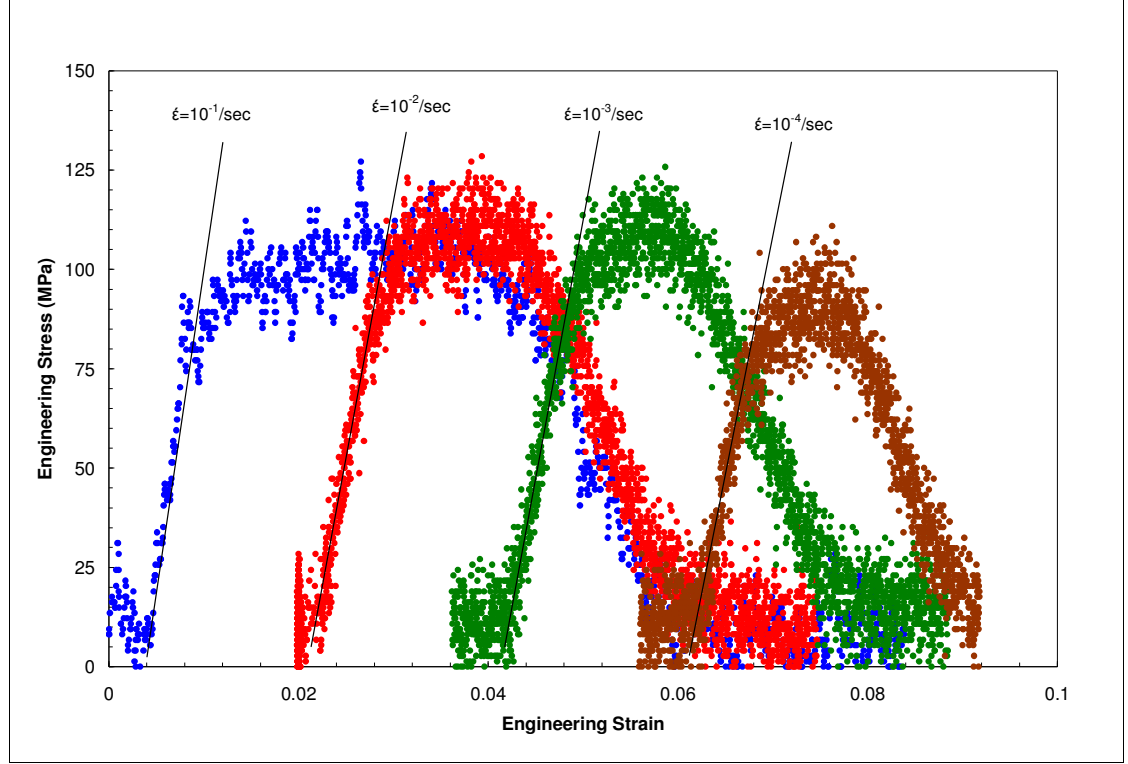
Figure 1.5: Engineering stress versus engineering strain curves for a 0.2 μm sample for different strain rates

A sample engineering stress versus engineering strain curve is shown on Figure 1.5 for 0.2 μm foil for different strain rates. The yield stress (σ_y) is determined at a point on the loading curve beyond which the linearity of the elastic regime is lost (correlation coefficient at least 95%). The linear elastic part of the loading curve is determined using best available linear fit as indicated by the corresponding correlation coefficient (R^2). The elastic modulus (E) is determined from the slope of the linear fit with an error bar calculated from the corresponding R^2 value as:

% of error = E $(1-R^2) \times 100\%$ (1.5)

From Figure 1.5, it appears that the elastic modulus, measured at the onset of yield point of the engineering stress versus engineering strain curve of the Ag foils (for a particular pore size), is constant for the entire range of the strain rate. This observation is taken into consideration that the average elastic modulus for a particular pore size sample does not depend on the rate of loading and should remain constant. Figure 1.6 shows the average elastic modulus as a function of porosity for different pore size samples. Using linear fit, the porosity at which the elasticity would go to zero (i.e., the elastic modulus at critical porosity P_c) is calculated to be 65.5% and the elastic modulus for fully dense Ag (i.e. at porosity P=0) is estimated to be 25.07 GPa.
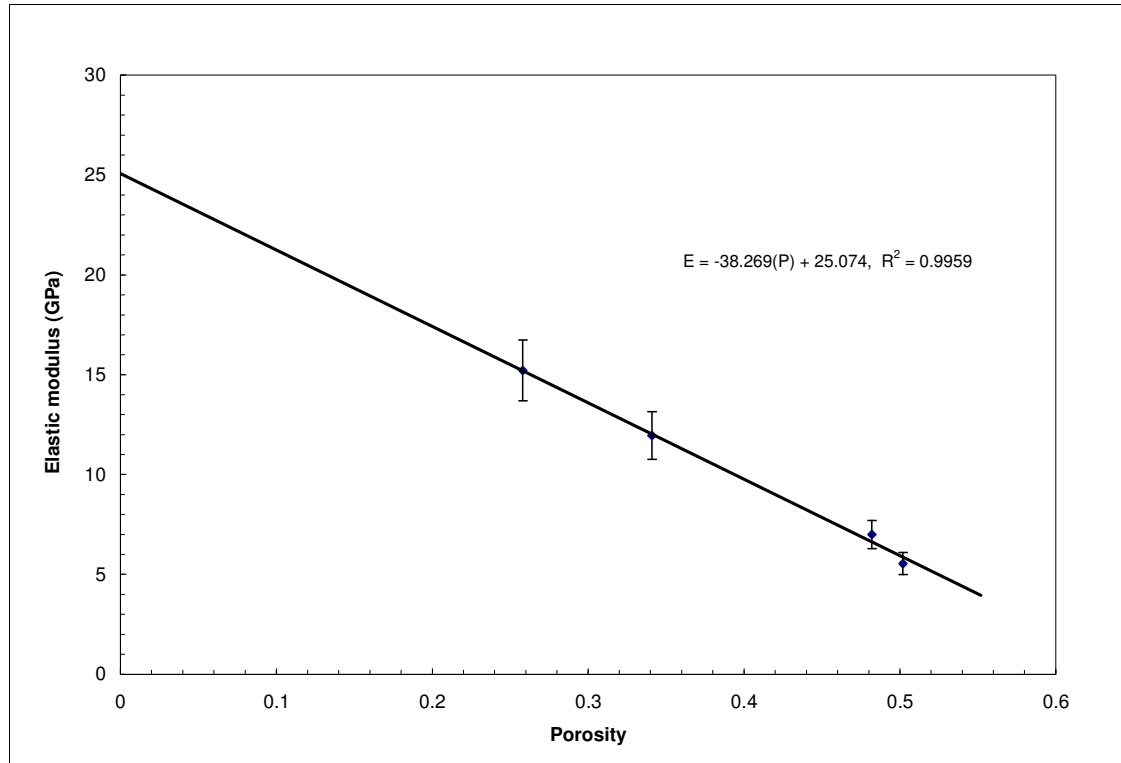
Figure 1.6: Average elasticity plot for different porosity samples

Elastic constant of fully dense Ag in pure tension is reported to be $c_{11}=124.0$ GPa [34]. Other elastic constants are reported as: $c_{12}=93.4$ GPa, $c'=\frac{1}{2}(c_{11}-c_{12}) =15.3$ GPa and $c_{44}=46.1$ GPa [34]. These values are in well agreement with the reported values for silver at room temperature by Neighbours and Alers [35] and by Overton and Gaffney [36], i.e., $c_{11}=123.99$ GPa, $c_{12}=93.67$ GPa, $c'=15.16$ GPa and $c_{44}=46.12$ GPa. Similar values are obtained by Hiki and Granato [37], Chang and Himmel [38] and Wolfenden and Harmouche [39]. The stiffness constants for cubic structure of Ag are calculated as follows ($c_{11}=123.99$ GPa, $c_{12}=93.67$ GPa and $c_{44}=46.12$ GPa):

$$s_{11} = \frac{c_{11}+c_{12}}{(c_{11}-c_{12})(c_{11}+2c_{12})} = 0.023058 \ (GPa)^{-1} \tag{1.6}$$

$$s_{12} = \frac{-c_{12}}{(c_{11}-c_{12})(c_{11}+2c_{12})} = -0.009923 \ (GPa)^{-1} \tag{1.7}$$

$$s_{44} = \frac{1}{c_{44}} = 0.02168 \ (GPa)^{-1} \tag{1.8}$$

With the stiffness constants, the directional (surface) elastic modulus E for the cubic system is given as [40]:

$$\frac{1}{E} = s_{11} - 2(s_{11} - s_{12} - \frac{1}{2}s_{44})(l^2m^2 + m^2n^2 + n^2l^2) \tag{1.9}$$

where, l, m and n are the direction cosines. For (100), (110) and (111) directions, the direction cosines are (1,0,0), $(\frac{1}{\sqrt{2}}, \frac{1}{\sqrt{2}}, 0)$ and $(\frac{1}{\sqrt{3}}, \frac{1}{\sqrt{3}}, \frac{1}{\sqrt{3}})$ respectively. Thus, the surface moduli $E(100)$, $E(110)$ and $E(111)$ are calculated to be 43.37 GPa, 83.42 GPa and 120.51 GPa respectively. The Ag samples used in this experiment do not have any

specific orientation of grains and are polycrystalline in nature. So, the elastic modulus of these foils does not necessarily have any preferential direction and is obtained by experiment. The multiple monotonic tensile tests conducted over a strain rate range of 10^{-4}/sec to 10^{-1}/sec yield an average Young's modulus E of dense silver to be around 36 GPa. The shear modulus G and bulk modulus K are calculated here for reference, using the following equations:

$$G = \frac{1}{2(s_{11} - s_{12})} = 15.16 \text{ GPa} \tag{1.10}$$

$$K = \frac{EG}{3(3G - E)} = 103.87 \text{ GPa} \tag{1.11}$$
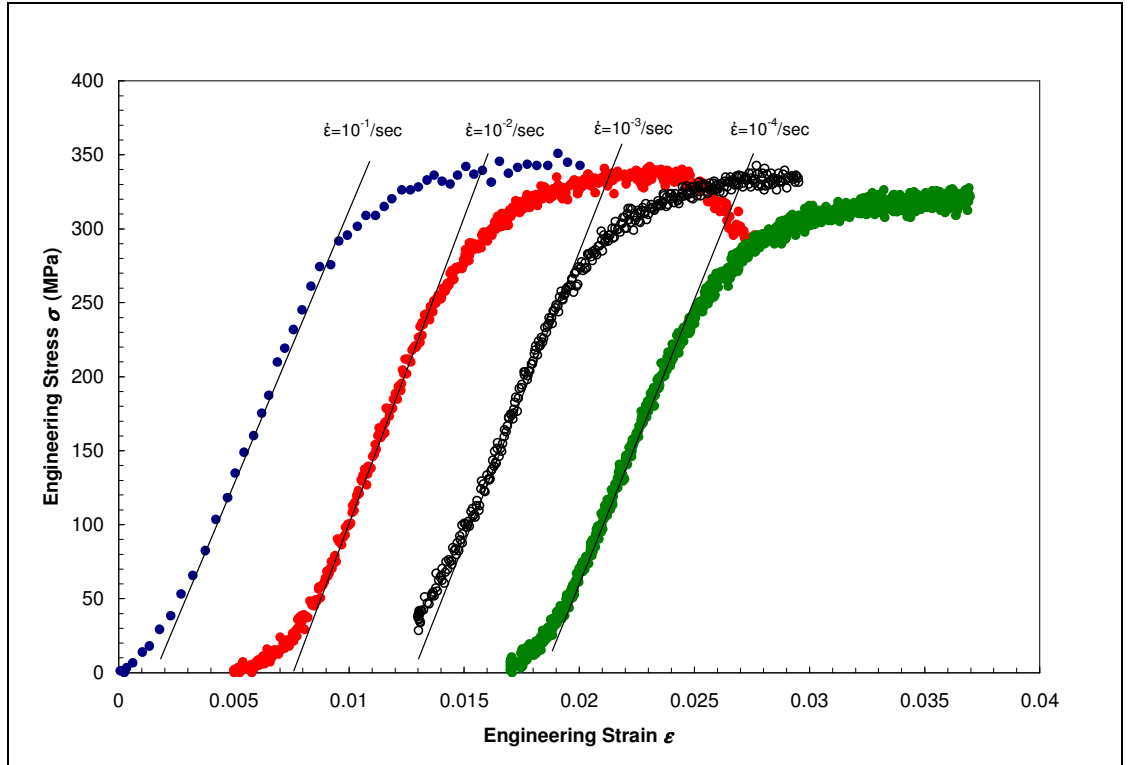
Figure 1.7: Engineering stress-strain plot of fully dense silver at different strain rates
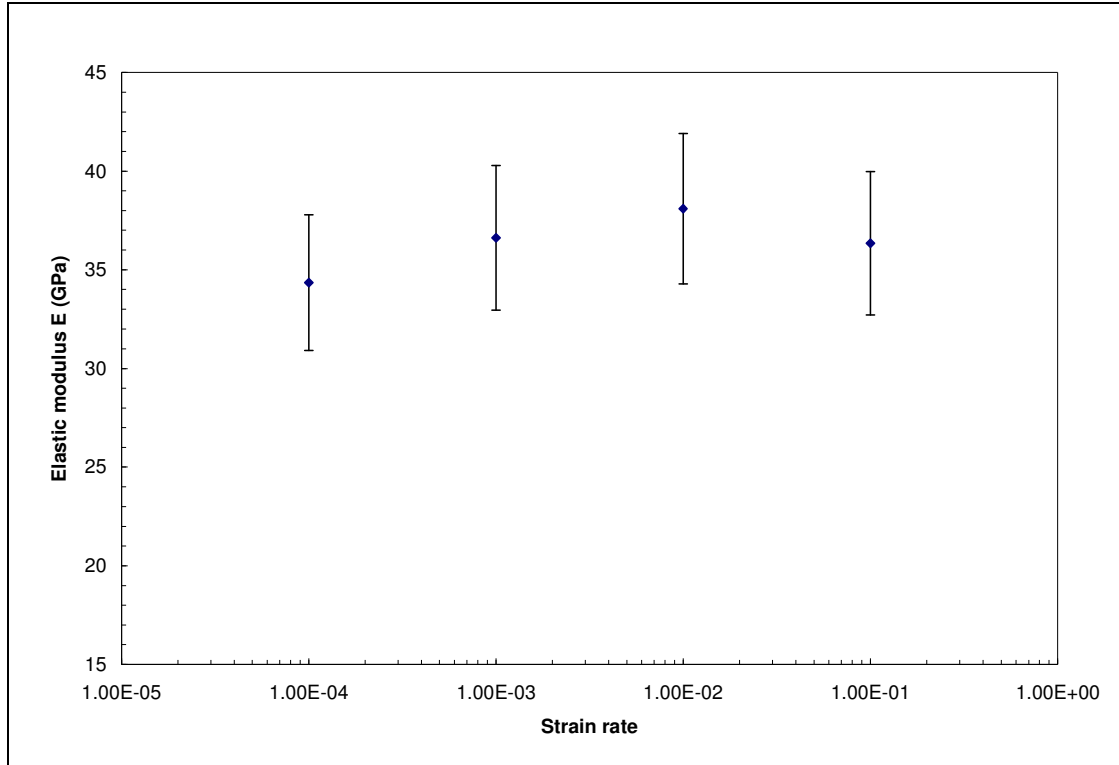
Figure 1.8: Elastic modulus of fully dense silver measured at different strain rates

The elastic modulus of fully dense silver from the plot of Figure 1.6 is

estimated towards a value in between the *G* and E value by the linear trend line, as

porosity goes to zero. For comparison, similar rate dependent tensile tests are done on

fully dense silver (99.95% pure) specimens and the measured elastic moduli are

plotted on Figure 1.7 and Figure 1.8. The average elastic modulus of dense silver is

calculated to be 36.35±1.54 GPa from these experiments. However, lack of surface

finish of the specimens may undermine the value by a bit. The author believes the

major discrepancy to be resulting from the surface irregularities and micro-cracks

present in the sample, as evidenced from the cross-section image on Figure 1.3. Some

level of stress-concentration factors are also introduced during the making of the

13

specimens using the die. These affect the yield strength and the elastic modulus of the samples. Error in strain measurement, cross-section measurement and alloy impurity plays a significant role in mechanical properties of the material. Also, for polycrystalline samples, there is a possibility of mixed mode deformation (comprising of shear, bending and tension) between the grains, which may lead to lower elastic modulus.

The linear extrapolated value of elastic modulus of dense silver from Figure 1.6 and the actual value obtained through experiments are close (25.07 GPa as opposed to 36.35 GPa), but not in good agreement with each other. There can be several underlying reasons for this. In open cell foams, the initial deformation occurs through bending [2], which may lower the elastic moduli of the porous samples as well as the extrapolated value. The validity of the linearity of the elastic regime of the stress-strain curve of porous samples is limited due to the early plastic deformations [41], as random pores essentially work as micro-cracks in the sample. These reasons suggest that a linear extrapolation may not be ideal for estimating elastic modulus at varying porosity.

For estimation of the fully dense elastic modulus and critical elasticity, several researchers proposed specific equations other than using a linear curve fit. Yeheskel, et al. [42] used two different equations to predict the elastic modulus of fully dense solids which are:

$$E_s = \frac{E}{(1 - k_1 P)} \tag{1.12}$$

$$E_s = Ee^{k_2 P} \qquad (1.13)$$

where, E_s is the elastic modulus of the fully dense solid, E is the elastic modulus of porous material, P is the porosity and k_1 and k_2 are fitting coefficients. As discussed earlier, the E value of fully dense silver is measured to be 36.35 GPa. Taking this value as E_s and taking k_1 and k_2 to be 1.25 and 3.45, respectively, equation (1.12) and (1.13) are plotted on Figure 1.10. In these cases, the critical porosity P_c (porosity at which the strength becomes zero) is derived from the prediction of the linear fit of the strength plot and is approximated to be 80%. The assumption of zero strength at 80% porosity originates from the strength plot and is discussed later in this section.

Gibson [2] proposed a relative approach for the estimation of the Young's modulus of the open-cell porous membranes:

$$\frac{E}{E_s} = C\left(\frac{\rho}{\rho_s}\right)^2 \qquad (1.14)$$

where, E and ρ are the elastic modulus and density of the membrane, respectively. The relative modulus $\left(\dfrac{E}{E_s}\right)$ is plotted as a function of the relative density $\left(\dfrac{\rho}{\rho_s}\right)$ in Figure 1.9 and the data are fitted with a power law. As a crosscheck to the reported value of the coefficient C (which is a constant related to the cell geometry) to be 0.98 [43, 44] and the exponent to be 2 [2], the values found here are 0.9946 and 2.6714, respectively.

The plotted trendline is labeled: $E/Es = 0.9946(\rho/\rho_s)^{2.6714}$, $R^2 = 0.9765$
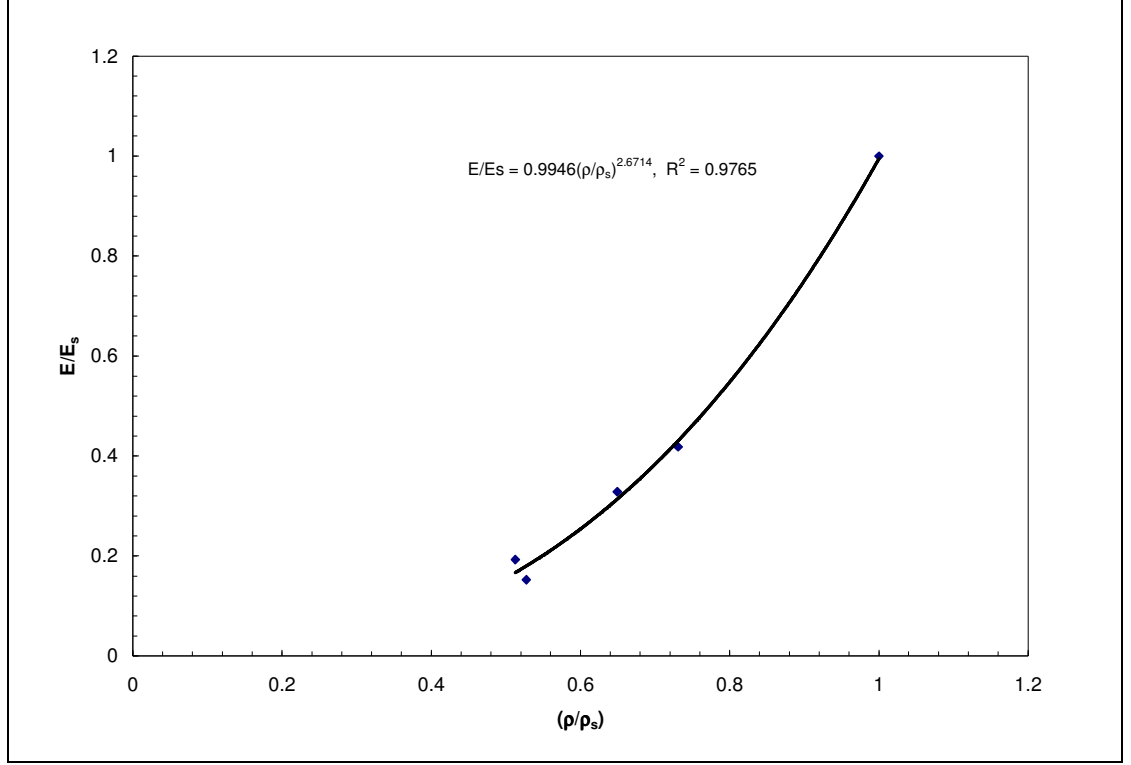
Figure 1.9: Relative elastic modulus as a function of relative density

Li and Aubertin [45] proposed a general equation for the prediction of uni-axial strength based on actual porosity P and critical porosity P_c as follows:

$$\sigma_P = \left\{ \sigma_s \left[1 - \sin^{x_1} \left(\frac{\pi}{2} \frac{P}{P_c} \right) \right] + \langle \sigma_s \rangle \cos^{x_2} \left(\frac{\pi}{2} \frac{P}{P_c} \right) \right\} \times \left\{ 1 - \frac{\langle \sigma_s \rangle}{2\sigma_s} \right\}$$

(1.15)

where, σ_P is the strength at a particular porosity P, σ_s is the strength of the fully dense solid (corresponding to $P=0$), x_1 and x_2 are material parameters and $\langle \ \rangle$ are the MacCauley brackets ($\langle z \rangle = 0.5(z + |z|)$). This equation can be used for both tension and compression. Hence, the MacCauley brackets are used to take care of the sign of

the stress. Under tensile conditions, the author [45] reported a reduction of equation (1.14) which is given by:

$$\sigma_P = \sigma_s \left[1 - \sin^{x_1}\left(\frac{\pi}{2} \frac{P}{P_c} \right) \right] \tag{1.16}$$

A similar approach is taken to generate functions for trendlines for the elastic modulus, with one inflection point near the critical porosity and another inflection point near the fully dense modulus value:

$$E = 0.5E_s \left(1 - \sin^a\left(\frac{\pi}{2} \frac{P}{P_c} \right) + \cos^b\left(\frac{\pi}{2} \frac{P}{P_c} \right) \right) \tag{1.17}$$

$$E = E_s \left(1 - \sin^c\left(\frac{\pi}{2} \frac{P}{P_c} \right) \right) \tag{1.18}$$

where E, E_s, P and P_s hold same notions as described earlier. Approximating a, b and c to be 0.25, 2.2 and 0.83, respectively, equation (1.17) and (1.18) are plotted in Figure 1.10, along with other trendlines for prediction of elastic modulus.

The approximations of a, b and c are generated from the interest of making the trendlines go through the experimental data set as closely as possible. Using different critical porosity values (P_c) may result in a better fit. However, in this case, the intention is to compare different equations with the same base parameters. As it can be seen from Figure 1.6 and Figure 1.10, both equation (1.13) and equation (1.18) are good approximations for elastic modulus at different measured porosity.
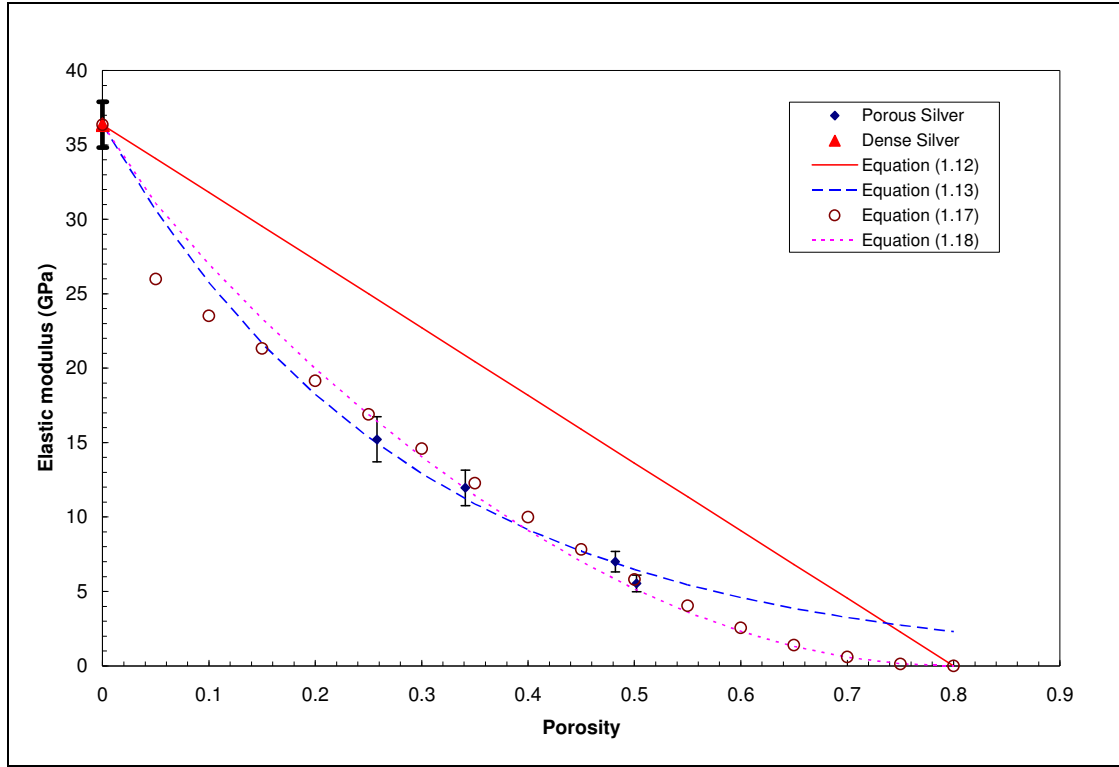
Figure 1.10: Trend lines for prediction of elastic modulus of Ag at different porosity

In addition to the role of porosity on elastic modulus, the dependency of mechanical yield strength on structural features of the porous membranes is investigated here. A Hall-Petch formulation [46, 47, 48, 49, 50, 51, 52] is indicative of dislocation based plasticity and relates the dependency of strength to the square root of structural size:

$$\sigma = \sigma_0 + \frac{k_\sigma}{\sqrt{h_g}} \tag{1.19}$$

where, σ is the yield strength, σ_0 is the intrinsic strength, k_σ is the strengthening coefficient and h_g is the measure of dimensional size. Since, the grain size of the porous sample sets does not vary beyond the statistical standard deviation, a Hall-

Petch evaluation of yield strength depending on structural dimensional feature (for example grain size) is not possible. Even though a similar statistical trend exists with the pore size of the samples, structural features like grain size or filament size does not provide such a correlation. To estimate the yield strength at the fully dense condition, the yield strength versus porosity plot of Figure 1.11 at every strain rate is extrapolated to *P*=0 to provide an intercept value with a linear fit.
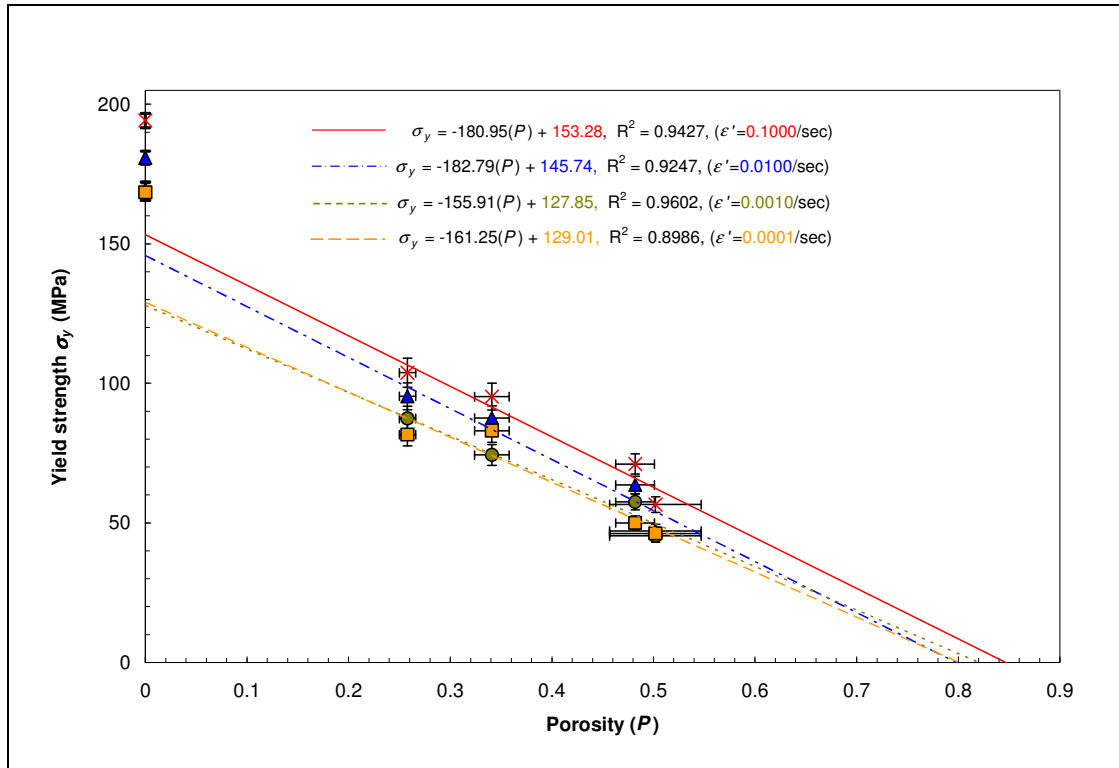
Figure 1.11: The yield stress versus porosity plot of different membranes at different strain rates

The intercept values at *P*=0 range from 127 to 153 MPa as the strain rate increases from 10^{-4} per second to 10^{-1} per second. The average tensile strength of annealed silver wire is reported to be 125 MPa [53]. The strength values at each strain

rate at zero porosity may be representative of shortest structural dimension, i.e. the in-filament grain size which is the average of the grain size values listed in Table 1.1 and is calculated to be 2.47±0.19 μm. The grain size information of the annealed silver wire is not available and hence, the strength of 125 MPa may not be an appropriate value to do the comparison with. Moreover, the associated purity of silver plays a big role on its strength [54]. For another comparison, the fully dense Ag samples are tested in the same strain rate range, i.e., 10^{-4} to 10^{-1} per second and is plotted in Figure 1.11 at *P*=0, representing the fully dense state. In this case, the yield strength at fully dense condition is higher compared to the extrapolated values. The fully dense samples are assumed to be cold rolled during their production as 50 μm foils and hence could have higher strength compared to annealed samples. Since the yield strength of samples depends on the grain size, the information of that structural feature on the fully dense samples is yet to be investigated which would enable their characterization in a better way. Nevertheless, the overall trend of the increase of strength estimation at *P*=0 seems reasonably satisfactory.

From Figure 1.11, a 'zero' intercept yield strength is estimated at an average porosity of 81.8±1.8% which appears to be invariant with the change in strain rate. The general trend of the yield strength appears to decrease in a linear fashion with increasing porosity, though it seems that at higher porosity values, the strength may decrease more rapidly. In accordance with equation (1.15), the effect of porosity on strength of porous materials has been studied by Aubertin and Li [55] and has been shown that the plastic deformation in porous materials occur in more than one way (tension, shear, bending, etc.). The non-linear relationship of multi-axial inelastic

deformation leading to the strength of the porous material as a function of porosity is proposed [45] as shown in equation (1.15). As stated earlier, this equation reduces to equation (1.16) under uniaxial tensile condition. Figure 1.12 shows the trend lines based on equation (1.15) and Figure 1.13 shows the trend lines based on equation (1.16) as a function of porosity for different strain rates. In these figures, the experimental value from fully dense silver is not plotted, as these values are not appropriate for comparison, most likely, because of different grain size. In Figure 1.12, x_1 and x_2 are fit as 6 and 2 respectively, critical porosity P_c=80%. The critical porosity and the intercept strength values at P=0 are determined using curve fitting with the experimental data. In linear fit, the critical porosity value comes to be about 81% (Figure 1.11). Hence these two P_c values are in good agreement with each other. However, the intercept values of yield strength come out to be lower than that predicted by the linear fit. The experimental values of yield strength of fully dense foils are not presented here and will be ignored in further plots, because there is an apparent distinction of grain sizes between the fully dense and porous samples.

In Figure 1.13, on the other hand, the cosine term of equation (1.15) is neglected. In fact, for pure tension, the terms in the MacCauley brackets of equation (1.15) become zero and hence the cosine term disappears [45]. In the resulting equation (equation (1.16)) x_1 is assumed to be 4.5 with the critical porosity at 80% and the trend lines are fitted to the existing experimental data. Even though the overall fit for the experimental data seems to be very good, the prediction for intercept values at P=0 are lower with these trend lines compared to those with linear fit (Figure 1.11) or with equation (1.15) (Figure 1.12).
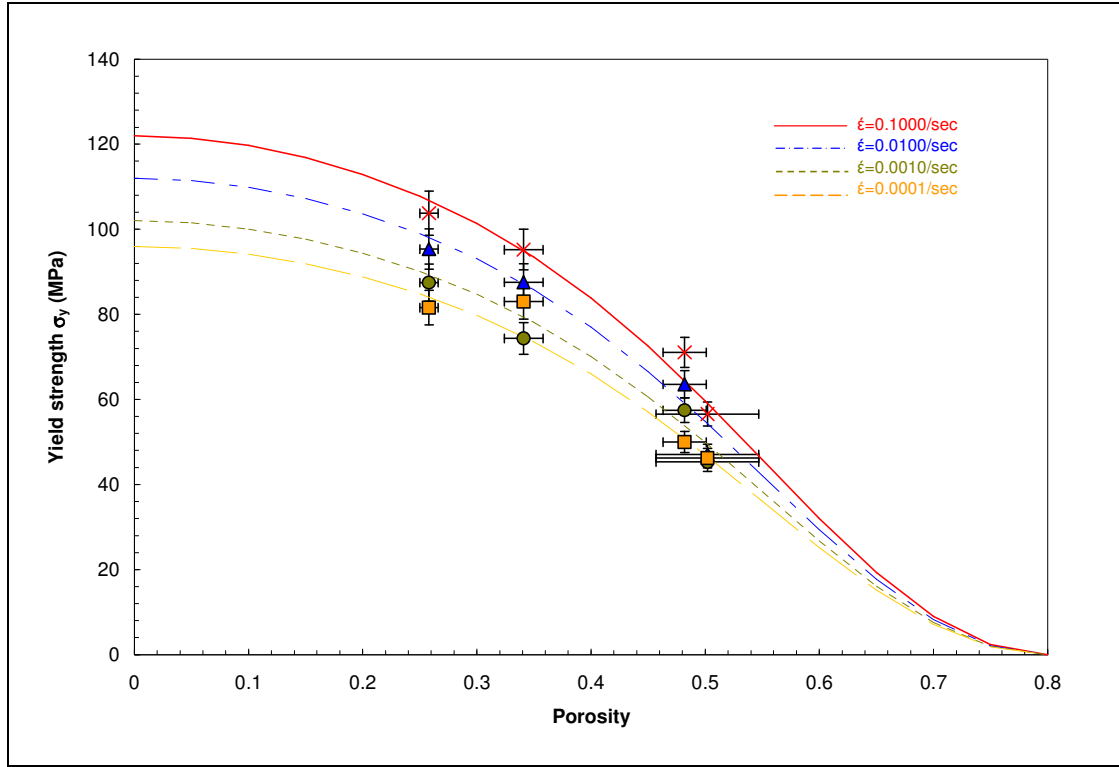
Figure 1.12: Strength as a function of porosity (equation (1.15))

Strain rate sensitivity is the ability of the material to uniformly plastically deform under load, without the localized concentration of stress and originates in the formula given by Dorn:

$$\sigma = c(\dot{\varepsilon}^{m}) \qquad (1.20)$$

where, σ is the stress, c is a constant, $\dot{\varepsilon}$ is the strain rate (i.e., ε/t) and m is the strain rate sensitivity exponent. Thus, from the power law fit, the strain rate sensitivity is obtained as the slope of the fit and is given by:

$$m = \partial(\ln \sigma) / \partial \ln(\dot{\varepsilon}) \qquad (1.21)$$

The measured yield strength from the engineering stress versus engineering strain curves of different porosity samples are plotted in Figure 1.14 as a function of strain rate in a logarithmic scale. The overall strain rate dependent behavior of the porous membranes having similar grain size (h_g) is also plotted in this figure (i.e., the intercept values of linear fit on Figure 1.11). And finally, the experimental data set of the dense silver is plotted for comparison. The data points are fitted with power law relationship from which the strain rate sensitivity is obtained for each sample set.
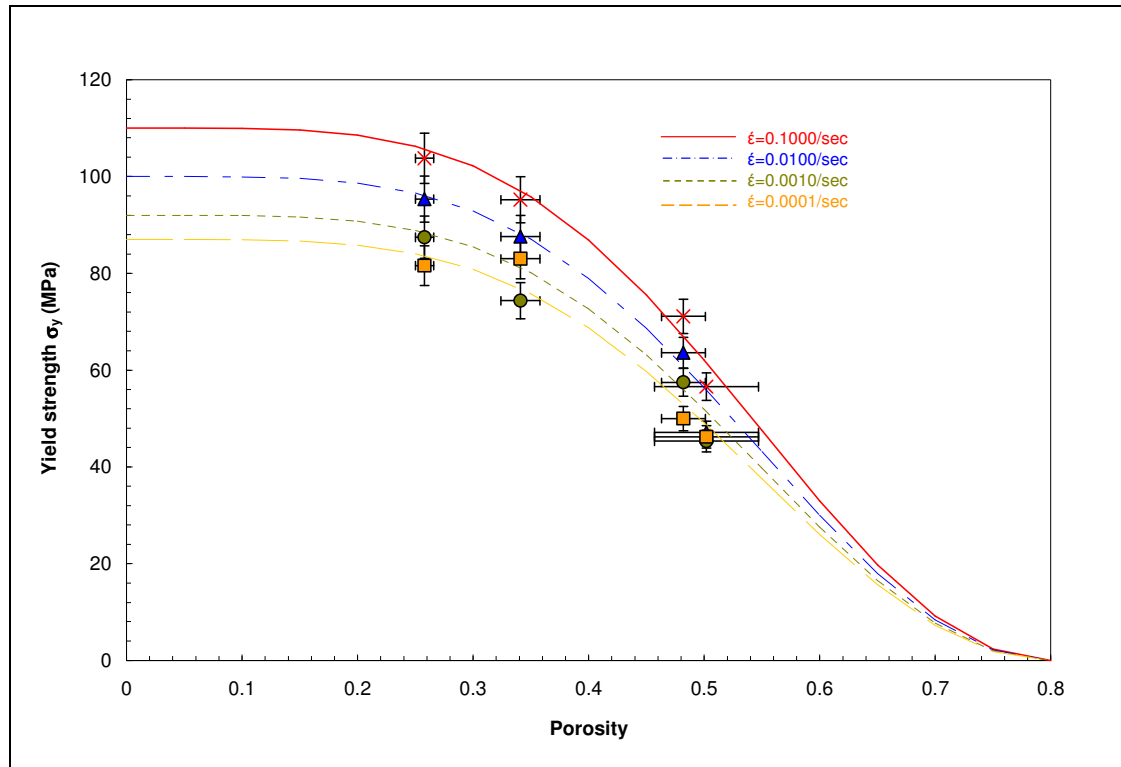
Figure 1.13: Strength as a function of porosity (equation (1.16))

The analysis for variation of yield strength of the porous samples with strain rate for the grain size case (h_g) yields a strain rate exponent of 0.0281±0.00383 and that for the fully dense samples yields 0.0215±0.00219. Even though these two rate

sensitivity exponent values are close to each other, the trend line for dense silver is positioned above in Figure 1.14 compared to that of the h_g line of the porous silver, which means, the dense silver has higher strength compared to porous silver at a particular strain rate. This means that the particular dense silver foils used in these experiments have smaller grain size compared to the rest of the porous membranes. This difference in the strength plot may originate from work hardening of the samples as well, perhaps during their production as films. So, the rate sensitivity exponent (*m*) may follow the grain size trend (higher *m* with decreasing *hg*) but the yield strength may not.
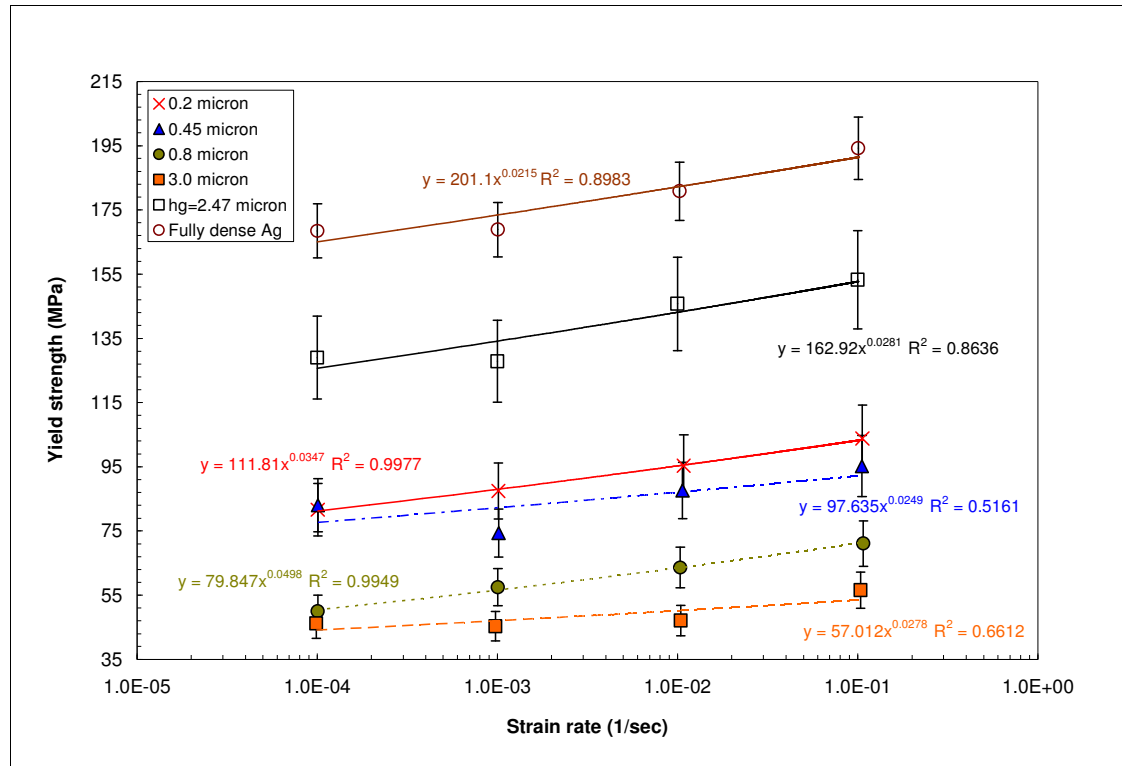
Figure 1.14: The log-log plot of yield strength versus strain rate. The values are fit with a power-law relationship to produce the strain rate exponent for each sample set.

The variation of rate sensitivity exponent *m* generally depends on some measure of structural feature size and generally increases with decreasing dimension [19, 26, 56]. Most reports present the variation of '*m*' with the change in grain size (h_g). The rate sensitivity of the porous membranes as a function of the grain size (h_g) is plotted on Figure 1.15. In addition, strain-rate exponents of nanocrystalline submicron gold computed from the tensile tests [57] are plotted in this figure for comparative reference of *m* to the dependency on grain size dimension of the porous membranes.
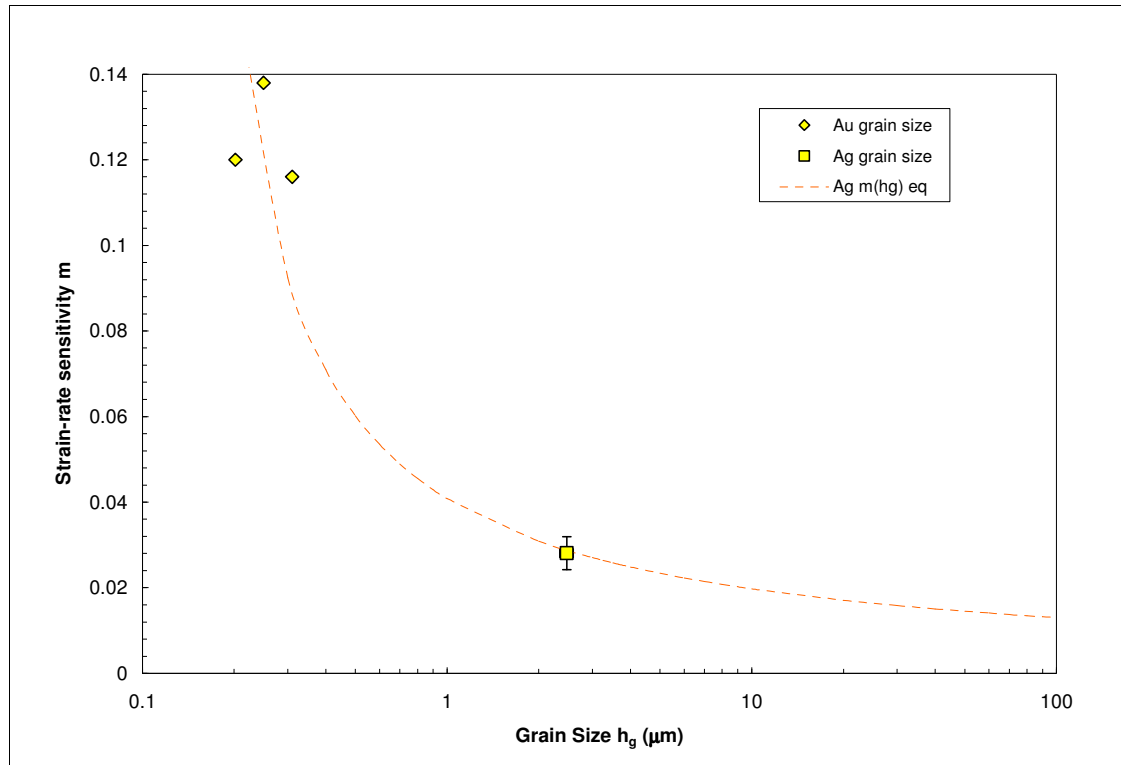
Figure 1.15: Strain rate sensitivity as a function of grain size

For nanocrystalline materials, an expression of rate sensitivity *m* with respect to activation volume *V* for plastic deformation with a characteristic activation length (or dislocation line length) *L* is found in the references [26, 58; 59]. Firstly, the critical

stress σ for bow-out of an edge dislocation from Frank-Read source in the slip planes is expressed as [59]:

$$\sigma = \frac{0.36Gb}{L}\left(\ln\left(\frac{L}{b}\right) - 1.653\right) \tag{1.22a}$$

$$\sigma = \frac{0.36Gb}{L}\ln\left(\frac{L}{b}\right) - \frac{0.59508Gb}{L} \tag{1.22b}$$

where, G is the shear modulus of rigidity and b is the Burger's vector. The constant 1.653 at the end of expression arose following the assumptions of edge dislocation and a Poisson ratio of 0.33. Activation volume V equals Lb^2 for dislocation based deformation [26]. Relationship between activation volume and strain rate sensitivity is originally proposed by Cahn and Nabarro [60] and is given by:

$$m = \frac{\sqrt{3}kT}{V \cdot \sigma_f} \tag{1.23}$$

where, k is Boltzman constant (8.62×10^{-5} eV/K), T is temperature (K) and σ_f is the flow stress. The constant of $\sqrt{3}$ originates from assuming Von Mises criterion for yielding and hence, converting the original expression of shear mode of deformation to tensile mode of deformation. Using equation (1.22) and (1.23), the final relationship between m and V is given as below:

$$m = \frac{\sqrt{3}kT}{0.36G}\left(\frac{L}{V}\right)^{1.5}\left[\ln\left(\frac{L^3}{V}\right)^{0.5} - 1.653\right]^{-1} \tag{1.24}$$

The general relationship can be given as:

$$m = c_1 \left(\frac{L}{V}\right)^{1.5} \left[\ln\left(\frac{L^3}{V}\right)^{0.5} - c_2 \right]^{-1} \tag{1.25}$$

where, c_1 and c_2 are constants depending on shear modulus G, Burger's vector b and temperature T. For experiments at the same room temperature, c_1 and c_2 will only depend upon G and b. It is not possible to have dislocations extending beyond the grain boundary limit. Hence, the upper limit of the length of dislocation line L should depend on the grain size h_g. Conceptually, L/h_g approaches unity for very small h_g and asymptotically approaches very small values (or zero) for very large h_g [59]. Based on these physical boundary conditions, it can be reasonably assumed that for a single grain larger than the theoretical limit of the grain size (where, the line length for a single dislocation is basically the physical dimension of the grain):

$$\frac{L}{h_g} \sim h_g^{-n} \tag{1.26a}$$

$$L = c \cdot h_g^{1-n} \tag{1.26b}$$

where, c is a constant with the unit of $(nm)^n$, n is an exponent that is less than unity. The actual value of this power factor depends on the mechanism of deformation [26]. Assuming Hall-Petch relationship for large grain size, i.e., comparing the second term of equation (1.22b) with that of equation (1.19), it is reasonable to assume:

$$L = c \cdot h_g^{\frac{1}{2}} \tag{1.27}$$

Hence, the value of the power factor n in equation (1.26b) is assumed to be ½. Thus, assuming Hall-Petch, the functional relationship between grain size h_g and strain rate sensitivity m can be derived from equation (1.25) and (1.27):

$$m = c_1 \left(\frac{L}{Lb^2} \right)^{1.5} \left[\ln\left(\frac{L^3}{Lb^2} \right)^{0.5} - c_2 \right]^{-1} \tag{1.28a}$$

$$m = c_1 b^{-3} \left[\ln\left(\frac{c^2 h_g}{b^2} \right)^{0.5} - c_2 \right]^{-1} \tag{1.28b}$$

$$m = c_3 \left[\ln\left(c_4 \cdot h_g^{0.5} \right) - c_5 \right]^{-1} \tag{1.28c}$$

where, c_3, c_4 and c_5 are constants. Equation (1.28c) is used to curve fit (represented by the dashed line on Figure 1.15) the h_g value of m for silver taking c_3, c_4 and c_5 to be 0.044, 15.3 and 1.65 respectively and assuming that for grain sizes above several microns, typical m values are equal to 0.01−0.02. This corroborates with the findings by Dao, et al. [19] for many fully-dense metals like nickel and copper. For porous materials, it is proposed [1] that the filament size (i.e., the width of the filament) can be considered as a measure of characteristic length instead. The reason proposed is that the filament size is the medium for deformation and porosity is the free space. With similar grain sizes, different membranes may possess different porosity with different filament sizes and hence, should have different plasticity characteristics. Whereas, the grain size based deformation will only be able to explain the overall general trend, the filament size based deformation should allow for more detailed characterization of the behavior. To evaluate this, the strain rate sensitivity data of the

membranes as a function of the filament size are plotted in Figure 1.16. Furthermore, the final form of equation (1.28c) is used with filament size h_f as the variable to simulate a trend line for the *m* values:

$$m = c_6 \left[\ln\left(c_7 \cdot h_f^{\,0.5} \right) - c_8 \right]^{-1} \tag{1.29}$$

The constants c_6, c_7 and c_8 are taken to be 0.03, 8.4 and 2.1, respectively. The trend line is plotted as a dashed-dot line on Figure 1.16. It becomes very apparent from this figure that the filament size based trend line better predicts the rate sensitivity behavior of the membranes. Based on this trend line, it is also apparent that the rate sensitivity value rises more rapidly as filament size gets smaller, as compared to the grain size based trend line.
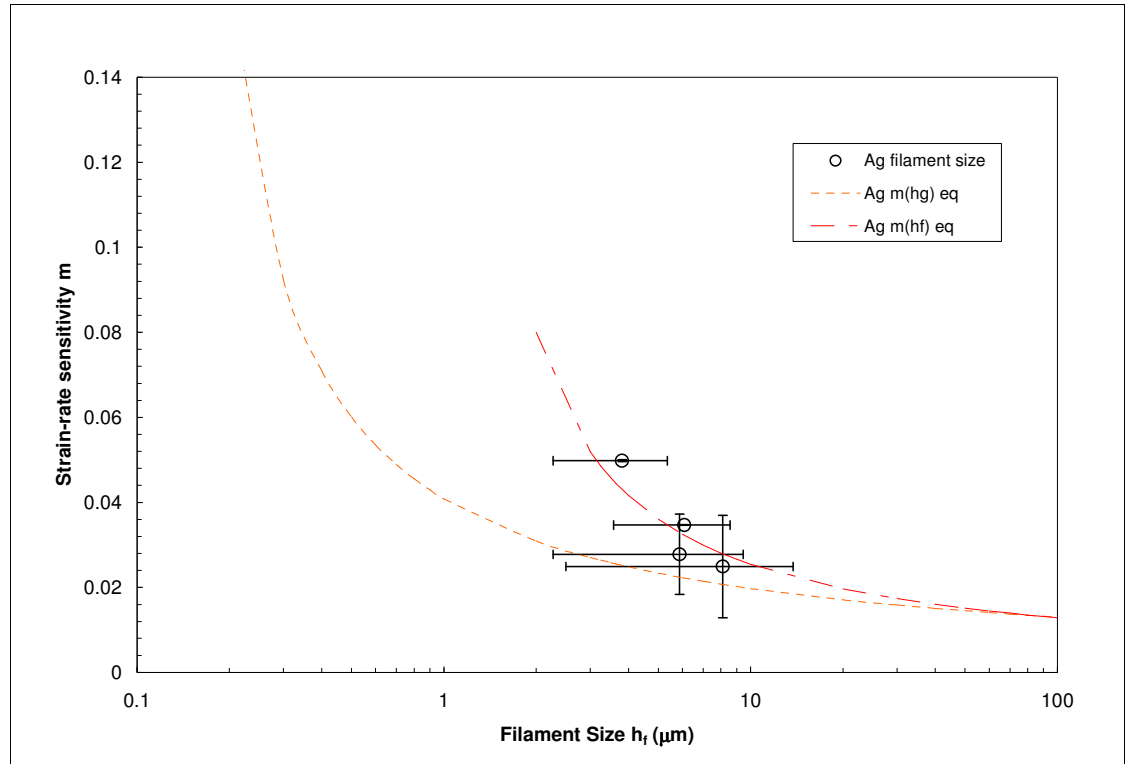
Figure 1.16: Strain rate sensitivity as a function of filament size

As stated earlier, porosity may have an additional effect on deformation. Porosity is a portrayal of the void space contained in the structure and also, is the available space for the filaments or struts for deformation. Thus, it is proposed that porosity is a measure of the activation volume. Porosity may couple with the filament size and may consequence different rate sensitivity for membranes having same filament size but different amount of available void space or porosity. Equation (1.25) is adopted to use filament size as activation length and porosity as activation volume and is given by:

$$m = c_9 \left(\frac{h_f}{P} \right)^{1.5} \left[\ln\left(\frac{h_f^{\,3}}{P} \right)^{0.5} - c_{10} \right]^{-1} \tag{1.30}$$
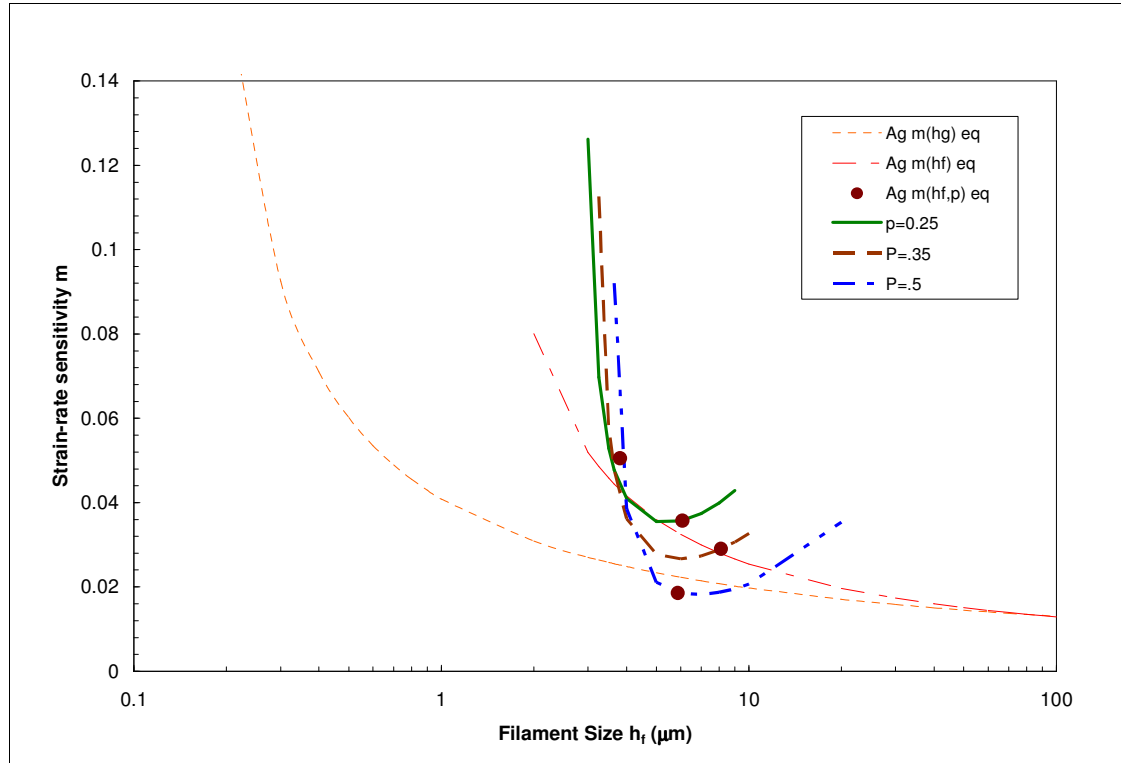
Figure 1.17: Porosity effect in strain rate sensitivity

Equation (1.30) is plotted as filled circle markers in Figure 1.17 for the specific cases of the four different membranes used in this experiment, taking c_9 and c_{10} to be 0.000367 and 2.21, respectively. Furthermore, trend lines for three different porosity $P=0.25$, $P=0.35$ and $P=0.5$ (average porosity of 0.8 micron and 3.0 micron membranes are quite close to 0.5) are also plotted in Figure 1.17 to show the general effect of porosity on rate sensitivity. These trend lines are completely different from those general trends plotted for grain size and filament size being the only variable. As seen from this figure, the prediction of rate sensitivity governed by the solid trend lines (using filament size and porosity as inputs) seems to be more accurate and representative of the experimental data. It is also suggested that, higher rate sensitivity exponent may be achievable for porous materials with larger filament sizes (larger than ~5 μm where the local minima takes place), if the porosity is kept at a constant value. At constant filament size, membranes with lower porosity will have higher rate sensitivity.

1.3.2 Intermittent test of Ag foils

The continuous loading of the porous membranes in tension produces typical engineering stress-strain curves, as shown in Figure 1.5. The linear elastic regime of the loading curves is linearly fitted with highest correlation coefficient to obtain the elastic modulus. It is seen from these tension tests that the elastic modulus of the membranes does not change with the strain rate and remains fairly constant for each porosity samples. However, for deformation of the membrane, it is postulated that the porous membrane will first plastically deform as an open cell structure, and then continue to deform wherein the open cell structure collapses through shear

deformation under tensile loading as the filaments (or struts) realign with the load direction through a bending-shearing mode, primarily at the junctions between the filaments [61]. Generally speaking, the junctions between filaments can be visualized as ball joints with three degree of rotational freedom and the filaments align themselves with the direction of the tension as loading starts and become parallel to each other as the test specimen is loaded to its ultimate strength. Once the filaments are aligned with the direction of the load, the structure will stiffen and the deformation mechanism will change from shear towards uniaxial. For the deformation mode to change, the elastic modulus measured from the tensile loading should also change as the open filament structure condenses under tensile elongation. One way of assessing this postulate is to do the intermittent tensile test wherein, the loading curve will be interrupted after initial yielding, by complete unloading and reloading [57, 62]. The reloading should go up to a load level beyond the yield load of the previous cycle. Figure 1.18 shows a typical stress-strain curve for a 0.2 micron nominal pore size membrane at 10^{-3}/sec strain rate wherein the loading curve will be interrupted at positions marked by horizontal dashed lines beyond the initial yield point and up to the ultimate stress. It is suggested that an increase in the elastic modulus will progress with the amount of plastic deformation until the ultimate strength level is reached. Thereafter, localized necking will reduce the cross-section so that further deformation will provide a decrease in the engineering stress and computed elastic modulus.
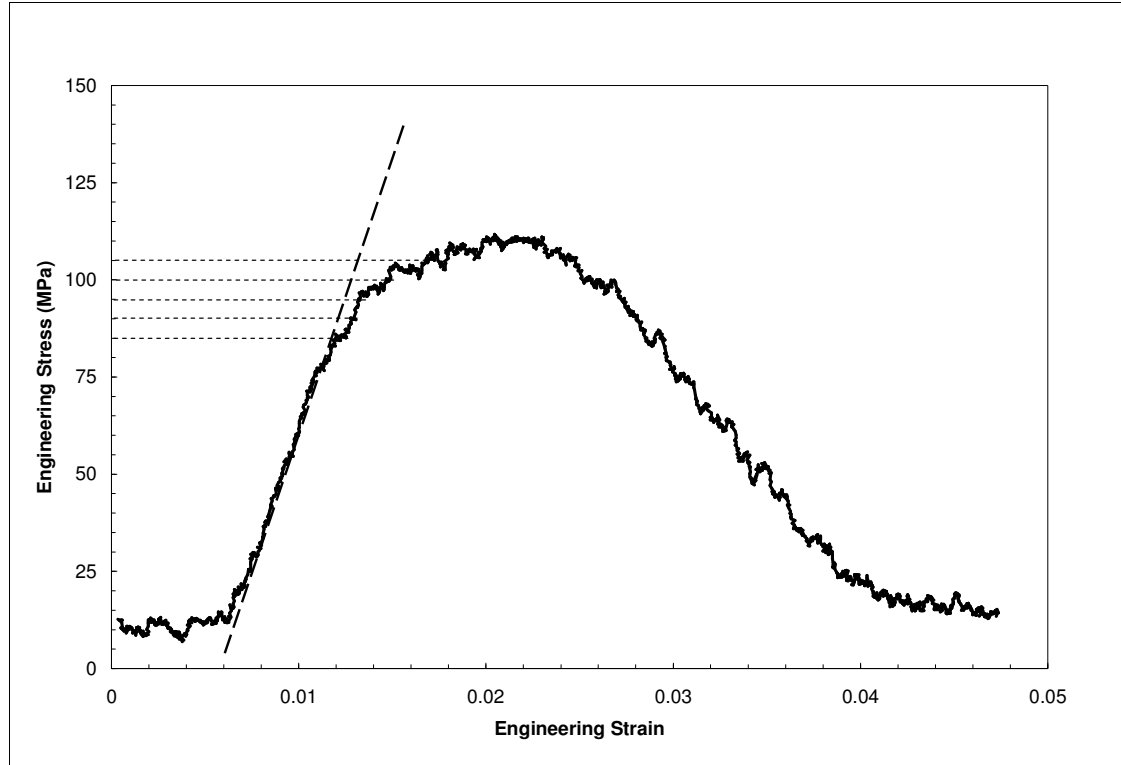
Figure 1.18: Typical stress strain curve (20 point average of the original curve for 0.2 micron membrane at 10^{-3}/sec strain rate) and positions of interruptions

As it is seen from Figure 1.18, for incremented tensile load tests beyond the initial yield point, there are approximately five additional modulus measurements as this porous sample is subjected to further plastic deformation at 10^{-3}/ sec strain rate. However, such number of additional measurements is not always possible. For slower strain rates, there is enough time to manipulate the loading system. For increasing strain rates, the number of measurements decreases as loading goes up very quickly and interruption at an estimated load level (which has to be higher than the preceded load) becomes difficult. For membranes with higher porosity, the interruption is difficult even for lower strain rates, mostly because of their unpredictable strength

after the yielding and/or because of quick necking and fracturing. For this reason, more than one test is done at each strain rate to achieve sufficient confidence level. The incremental load curve for a 0.2 micron nominal pore size membrane tested at 10^{-3} per second strain rate is shown in Figure 1.19. With each successive interval of time, the load is seen to increase.
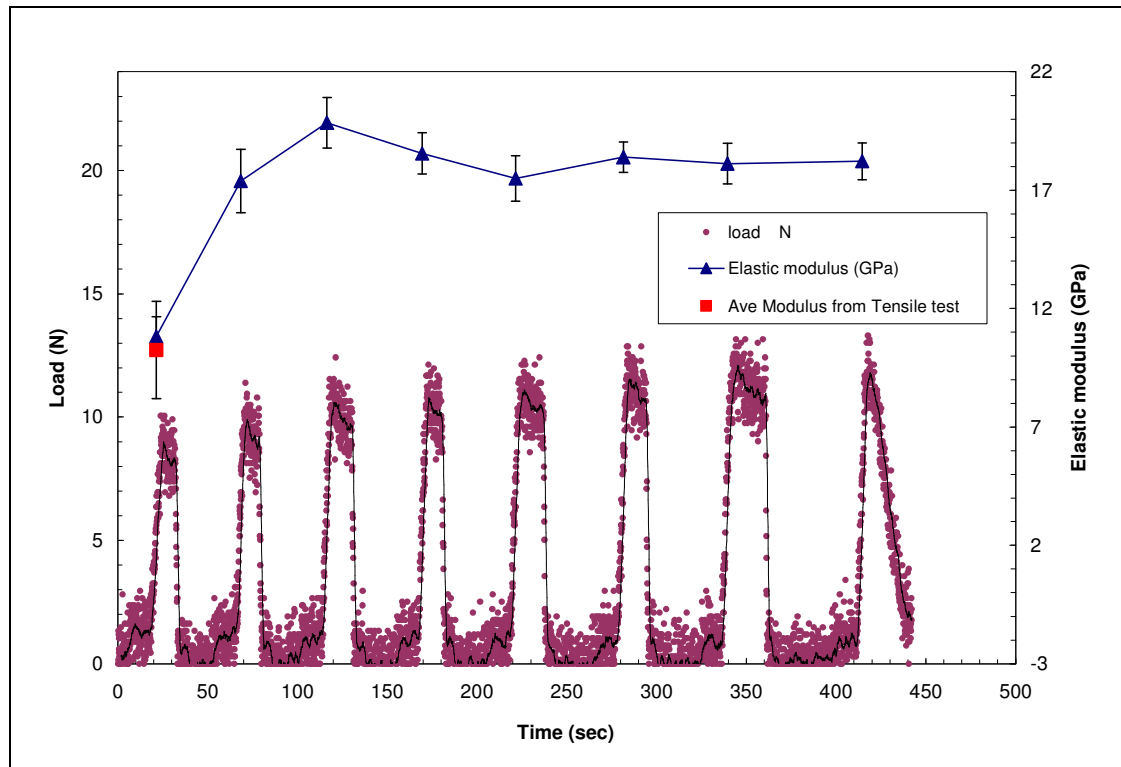
Figure 1.19: Interrupted tensile test of 0.2 micron nominal pore size membrane at 10^{-3}/sec strain rate to show the change in elastic modulus with progression of load

The modulus is measured (using corrected cross-sectional area) as the slope of the linear portion to the loading curve for each increment. The elastic regime is identified using a linear fit and a 20 point average trend line. The abscissa in Figure 1.19 is

shown in time (sec) to clearly demonstrate the succession of loading-unloading cycles with increased load.
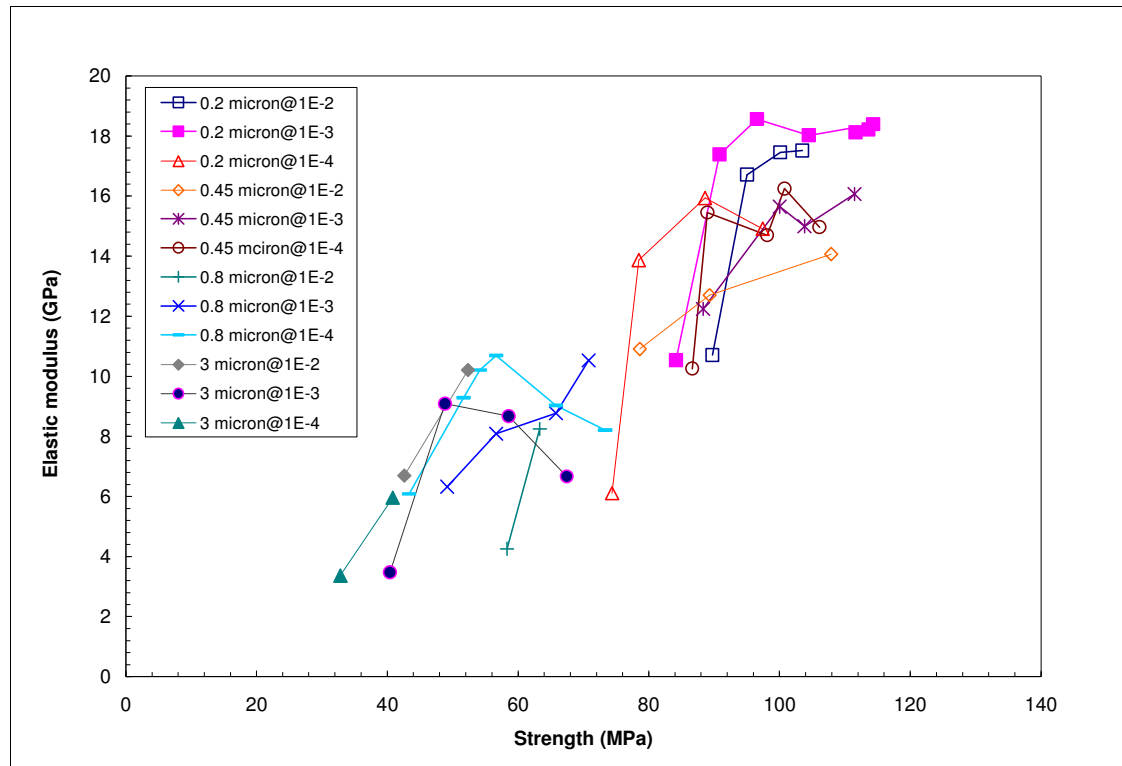
Figure 1.20: The elastic modulus of porous silver membranes as measured through incremented tensile loading are plotted as a function of the applied engineering stress

The variation in the elastic modulus with the measured engineering stress (assuming the cross-sectional area being constant) is plotted in Figure 1.20. This figure includes all of the modulus values from the onset of initial yielding through the final yield point (i.e. the ultimate stress) as measured from each interrupted loading interval. It can be seen from this figure that some modulus values decrease at a stress level beyond the ultimate strength, indicating the loading regime wherein the specimens undergo localized necking. Average modulus values are plotted for all the

tests conducted at each strain rate. It can be seen that the modulus values increase with a decrease in porosity. Also, the modulus is found to increase with increasing plastic deformation up to a certain limit wherein the stress level starts to drop because of localized necking. The maximum modulus value is found in Figure 1.20 in the upper plateau regions for each level of membrane porosity, irrespective of the associated strain rates.

In a similar fashion, intermittent tests have been conducted on dense silver specimens over 10^{-4}, 10^{-3} and 10^{-2} per second strain rates. Figure 1.21 shows an example of the resulting elastic modulus after each successive plastic deformation that the sample goes through. Like the porous samples, the dense silver specimens also show an increase in modulus at higher amount of plastic deformation. This increment in modulus, too, plateaus out after certain amount of work hardening. Figure 1.22 plots all the data on elastic modulus of dense silver as a function of the applied engineering stress over all the strain rates. The average of the maximum modulus values (i.e. the plateau region) is shown with a horizontal line. These maximum elastic modulus values (independent of strain rate) determined from the incremented tensile tests are plotted as a linear function of membrane porosity in Figure 1.23.
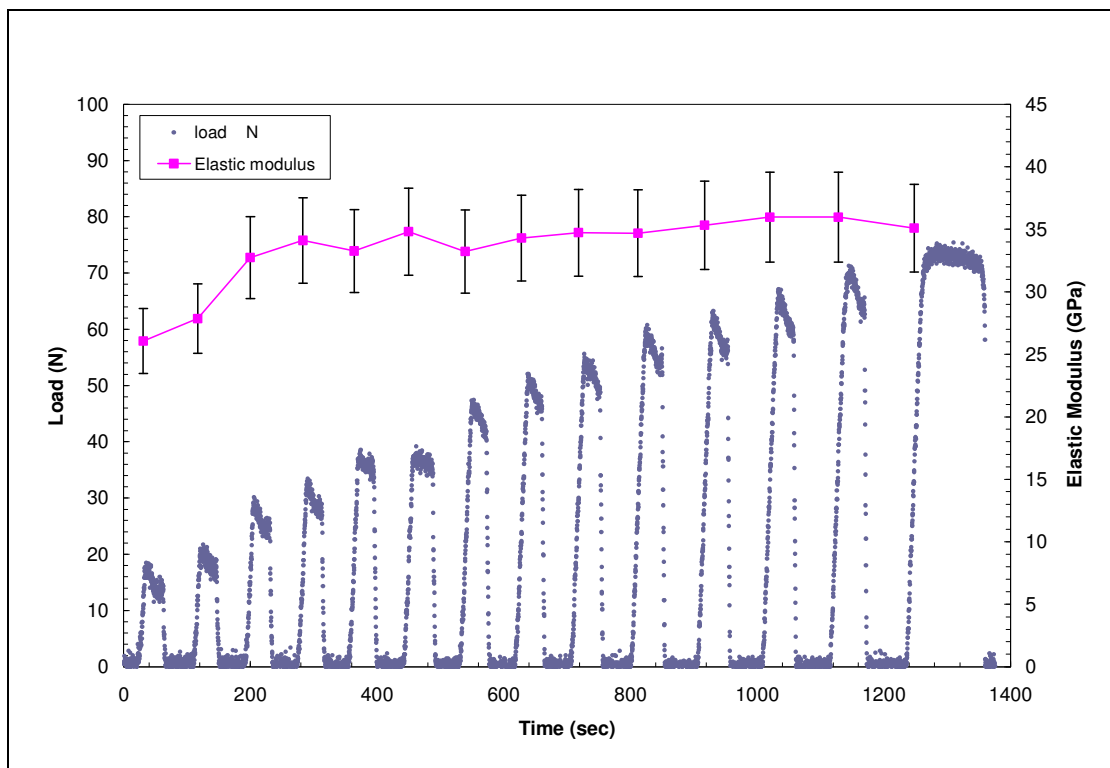
Figure 1.21: Change in elastic modulus of dense silver with progression of load at a

strain rate of 10^{-3} per second
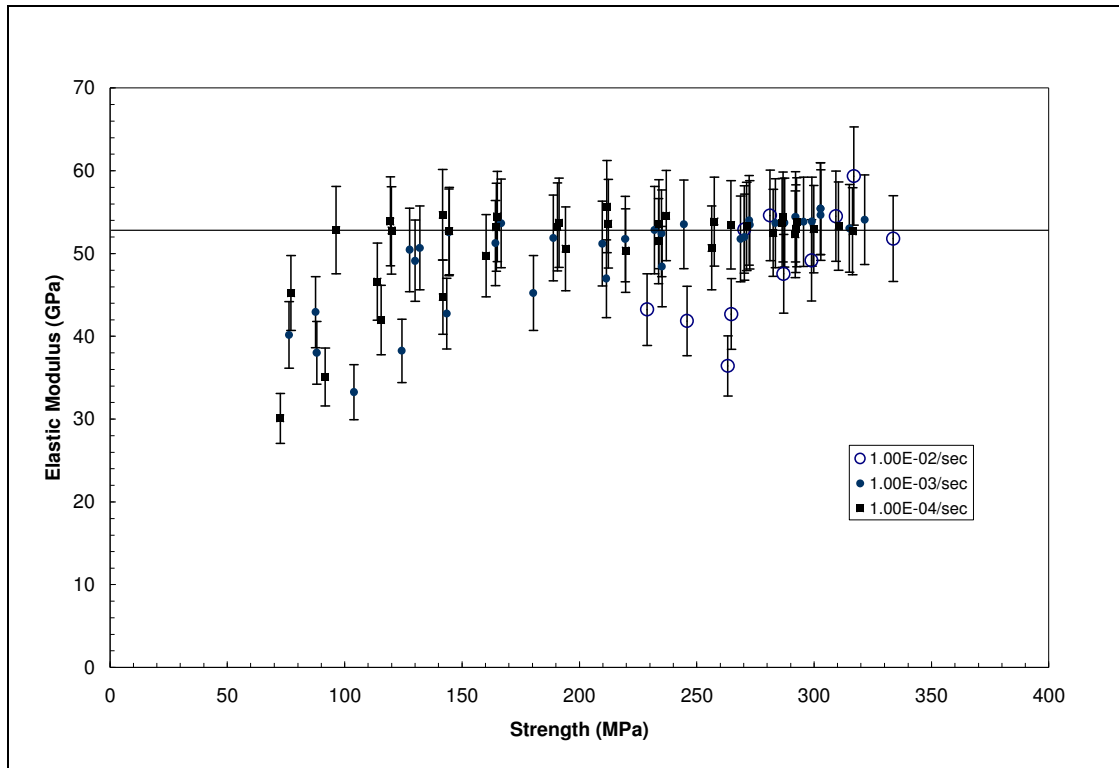
Figure 1.22: Elastic modulus from interrupted test of dense silver as a function of

applied engineering stress over different strain rates
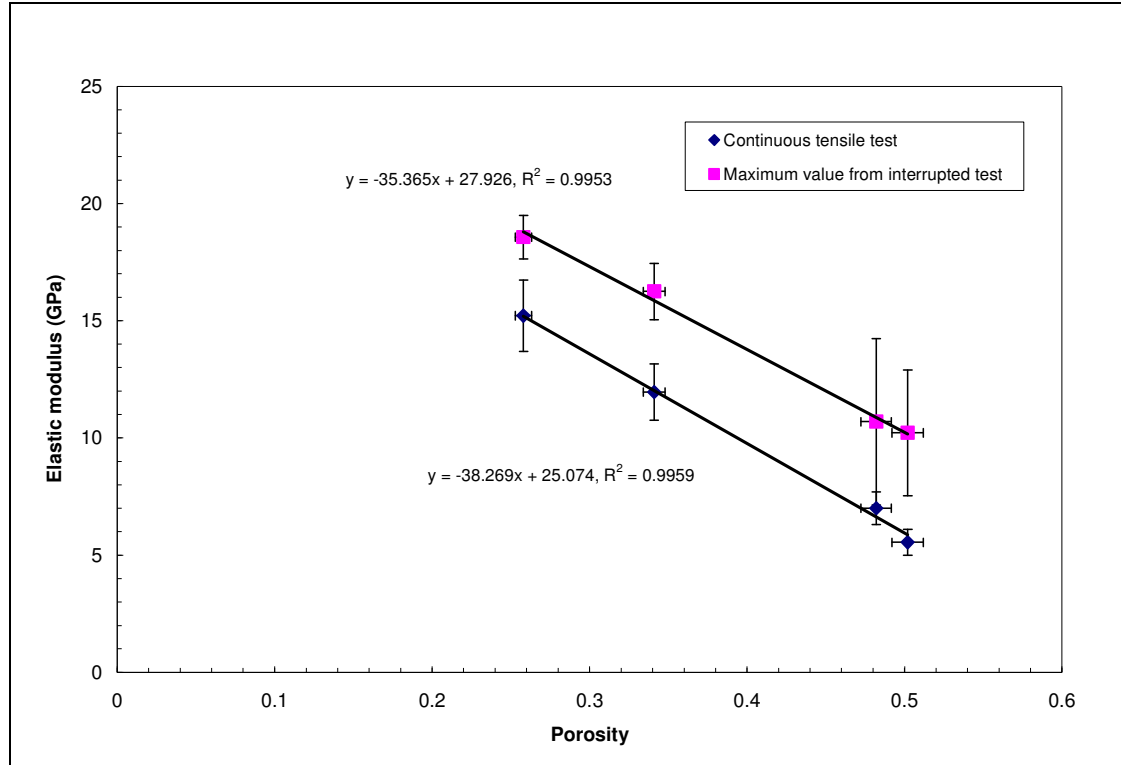
Figure 1.23: Variation of elastic modulus with porosity for silver membranes as

measured using tensile test (initial onset of yielding) and interrupted test (at ultimate

strength)

From Figure 1.23, it is clearly evident that the porous membranes

progressively stiffen when subjected to increasing plastic deformation. The intercept

value found using a linear fit for the stiffened modulus suggests a small increment

from 25.07 GPa at the initial yield condition to 27.93 GPa at the maximum stiffened

condition (i.e. at ultimate stress). This suggests that higher porosity membranes stiffen

more under progressive loading compared to lower porosity membranes. Both

monotonic loading and interrupted loading predicts similar elastic modulus values at

fully dense condition. The linear extrapolation of the curve for maximum modulus

value in Figure 1.23 also suggests the critical porosity P_c (porosity at which strength

goes to zero) to be 0.79, which is in very well agreement with modeling data found

from tensile testing.

1.3.3 Tensile test of electrodeposited nanocrystalline Ni

The tensile test specimens on nanocrystalline Nickel are obtained as pulsed

electrodeposited thin films [63] on stainless steel surface. Copper is used as a buffer

layer on the stainless steel to provide the ease of removing the deposited nickel. Free

standing test pieces are laser cut to have a nominal width of about 1.4mm, while the

thickness of the specimens is determined by the as-deposited condition, being

nominally about 50 microns. The test specimens are mounted on the tensile tester

using heavy-duty serrated grips (Figure 1.24).
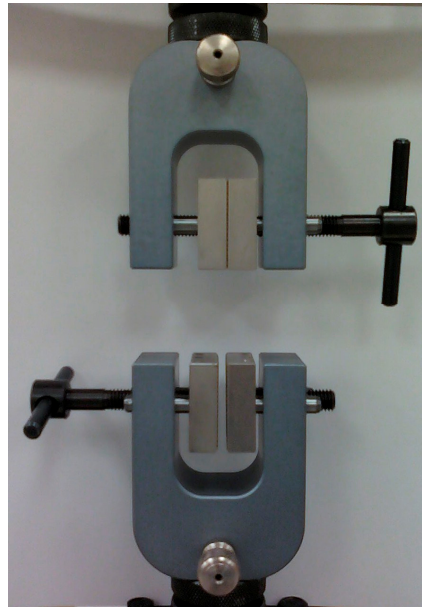
Figure 1.24: Serrated grips for mounting the nanocrystalline Ni foils

Rate sensitive tensile testing is done on the samples using the same technique as described in section 1.3.1 Tensile test of Ag foils. The tests are carried out at strain rates of 10^{-5} to 10^{-1}. For each strain rate, at least two or three samples are tested to failure and the data is recorded as a function of time. Optical microscopy of the cross-sections of the samples after failure is done at various magnifications to provide more accurate measurements of the thickness and width and also, to provide some identification of ductile or brittle failure. A typical optical image of the thickness of such a foil at about 600X magnification is shown on Figure 1.25. The yield strength is measured from the engineering stress versus engineering strain curve at a point where the linearity of loading starts to deviate. The linear loading regime is defined using a 20-point moving average and a linear fit. The highest correlation coefficient of the linear fit provides the limits of the linear part while the 20-point average shows an overall behavior. Figure 1.26 shows a comparative plot of the engineering stress versus engineering strain curves at different strain rates measured at room temperature. The measured yield strengths of the samples are plotted on Figure 1.27 as a function of the applied strain rate on a logarithmic scale. The exponent of the power law fit of the data points provides the strain rate sensitivity of the nickel specimens.

A linear relationship is fitted on plot of ln(strain rate) versus yield stress (in units of MPa) to reveal the activation volume (Figure 1.28). The activation volume V is given by [60]:

$$V = k_B T \frac{\partial \ln \dot{\varepsilon}}{\partial \sigma} \qquad \text{(1.31a)}$$

$$\frac{\partial \ln \dot{\varepsilon}}{\partial \sigma} = \frac{V}{k_B T} \tag{1.31b}$$

where, k_B is the Boltzman constant (1.381×10^{-23} J/K) and T is the temperature. The

slope of ln(strain rate) versus yield stress would give a value equal to $\dfrac{V}{k_B T}$. At room

temperature (T=300K) the value of $k_B T$ equals to 4.142×10^{-21} J. Thus the activation

volume in nm^3 is given by 4.142 times the slope of the linear fit of the above

mentioned plot, if yield stress is plotted in the units of MPa. Higher activation volume

means larger grain size and vice versa. The activation volume for this case becomes

0.0733nm^3 which implies that the grain size of the nanocrystalline nickel is about 10

nm [26], assuming Burger's vector for perfect dislocation. The atomic radius of nickel

is 124pm [64] and hence, the Burger's vectors are given by [65]:

$$b_{perfect} = \frac{a}{\sqrt{2}} = \frac{0.124 \times 2}{\sqrt{2}} = 0.175 \text{nm} \tag{1.32 a}$$

$$b_{partial} = \frac{1}{\sqrt{3}} b_{perfect} = 0.1012 \text{nm} \tag{1.32b}$$

$$b_{mixture} = \frac{1}{2} (b_{perfect} + b_{partial}) = 0.1381 \text{nm} \tag{1.32c}$$

Thus, assuming perfect, partial and mixture type of dislocations, the activation volume

becomes 13.677b^3, 70.72b^3 and 27.83b^3 respectively.

Figure 1.29 shows the strain rate sensitivity of nanocrystalline copper [19] and

nanocrystalline nickel [26] as a function of grain size. A general trend of increasing

rate sensitivity is observed with a decrease in grain size. This behavior is predicted by using the formulation proposed by Gu, et al. [26] in the following form:

$$m = c_1[\ln(c_2\sqrt{d}) - c_3]^{-1} \qquad (1.33)$$

where, c_1, c_2 and c_3 are constants depending on the shear modulus of rigidity (G) and burger's vector (b). This equation is based on the assumption of valid Hall-Petch strengthening mechanism. A more detailed study on this derivation is documented in the earlier section (1.3.1 Tensile test of Ag foils). The behavior of strain rate sensitivity as a function of grain size is predicted using equation (1.33) and is plotted on Figure 1.29. Here, c_1, c_2 and c_3 are taken to be 0.018, 3.0 and 1.65 respectively [66]. The value of strain rate sensitivity of the current study is also plotted in the same figure and is in well accordance with both the previous experimental data found in literature [26] and prediction by the model equation (1.33). The strain rate sensitivity of these nanocrystalline nickel samples is found to be higher than the conventional coarse-grained samples.
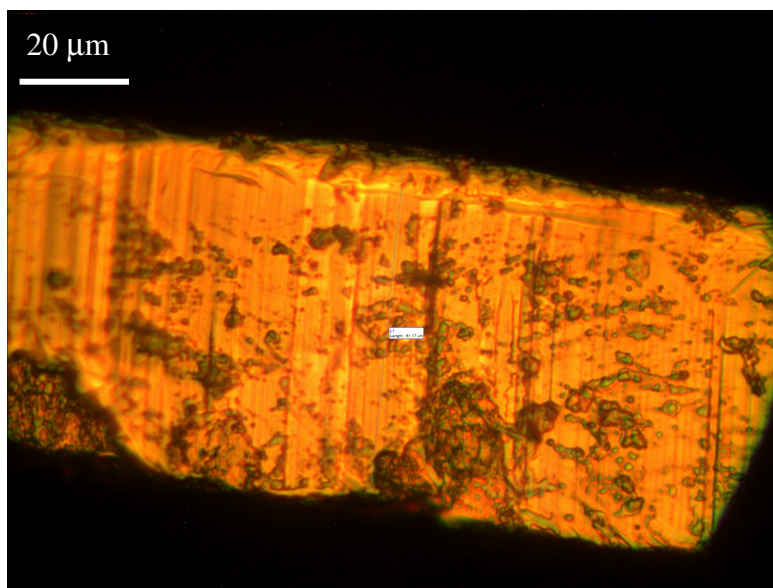
Figure 1.25: A typical thickness of the nanocrystalline nickel as viewed under the

optical microscope at 600X magnification.
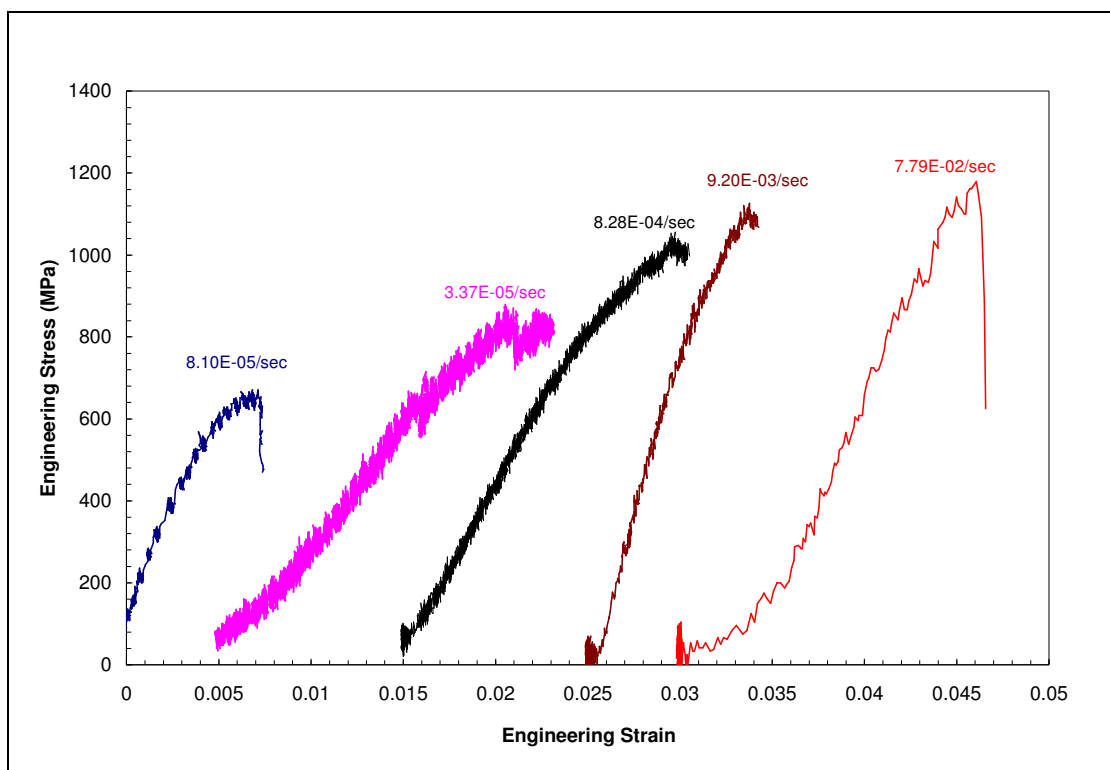
Figure 1.26: Engineering Stress-strain curves of NC nickel at different strain rates
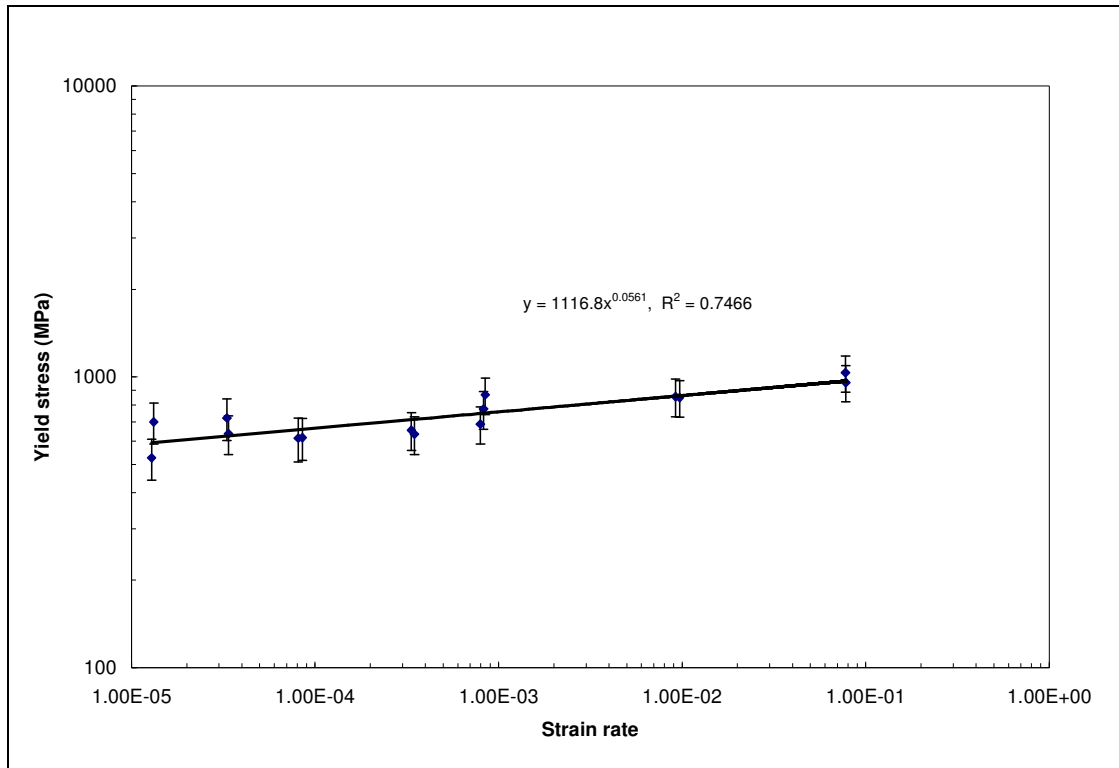
Figure 1.27: Power law fit of the stress versus strain rate to provide the strain rate

sensitivity of nanocrystalline nickel
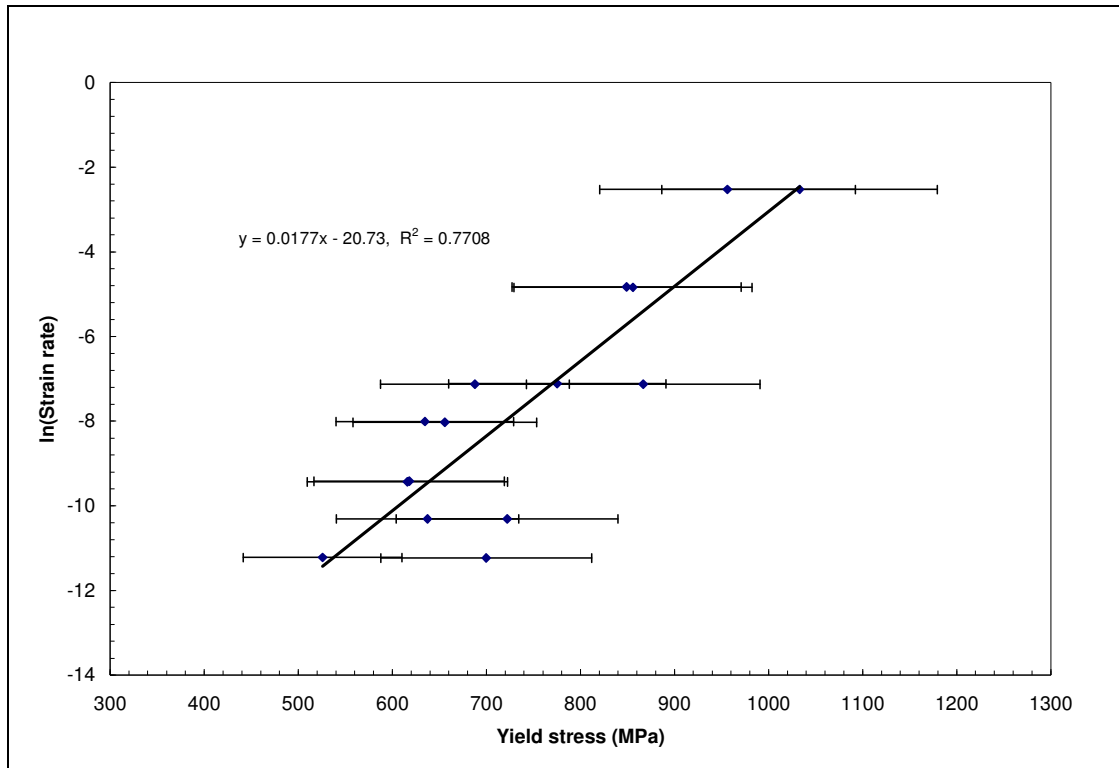
Figure 1.28: Activation volume is calculated from the slope of linear fit of ln(strain

rate) versus yield stress
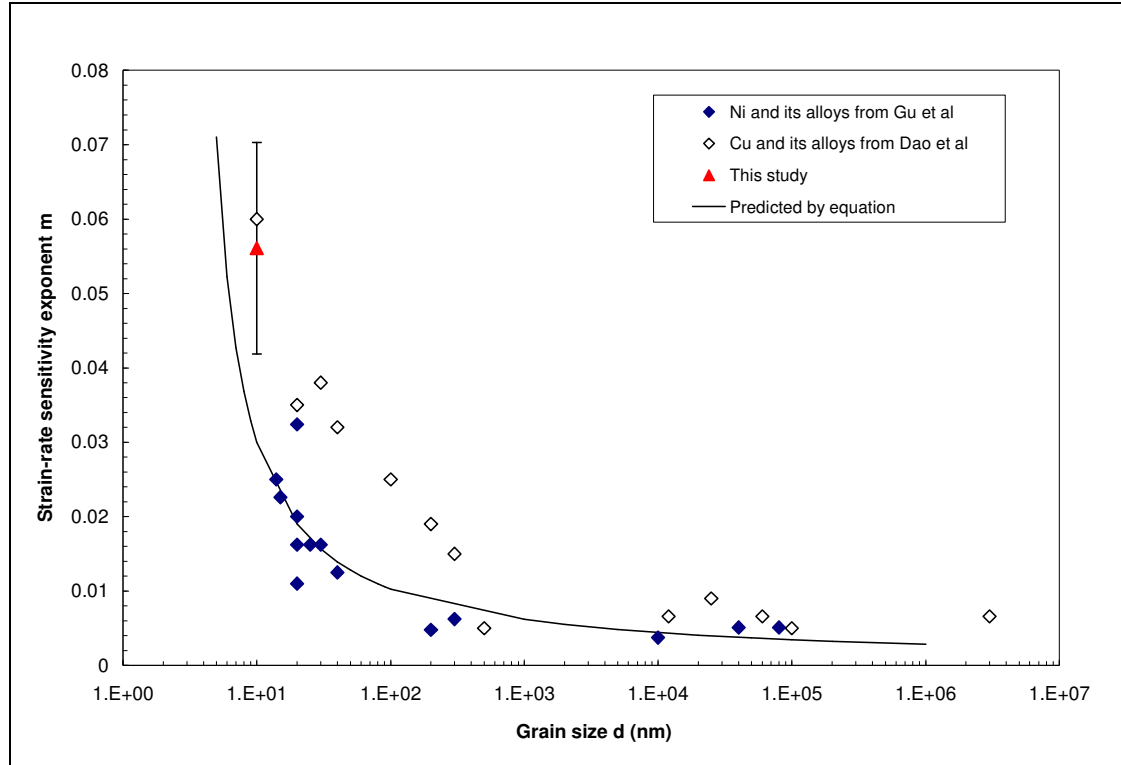
Figure 1.29: Strain rate sensitivity of Cu [19] and Ni [26] as a function of grain size

1.3.4 Tensile test of nanocrystalline Au-Cu foils

The nanocrystalline Au-Cu alloys have a composition of $Au_{(100-x)}$-$Cu_{(x)}$ where

x< 20 weight percent and are about 20 μm in thickness. The free-standing foils are

synthesized [27, 28, 29] using electrodeposition through pulsed current. The laser-cut

foils are tested to failure in tension using the TestResources tensile testing machine

and are mounted using wire grippers. Rate sensitivity experiments are performed by

moving the linear actuator over a constant distance while varying the test time. Figure

1.30 shows a representing load-time plot for a Au-Cu sample. SEM images are taken

of the failed cross-section to determine the width. Figure 1.31 shows such an image

from which the width of the corresponding sample was determined. Highest load

value from the load-time plot is taken to obtain the ultimate strength of the sample.
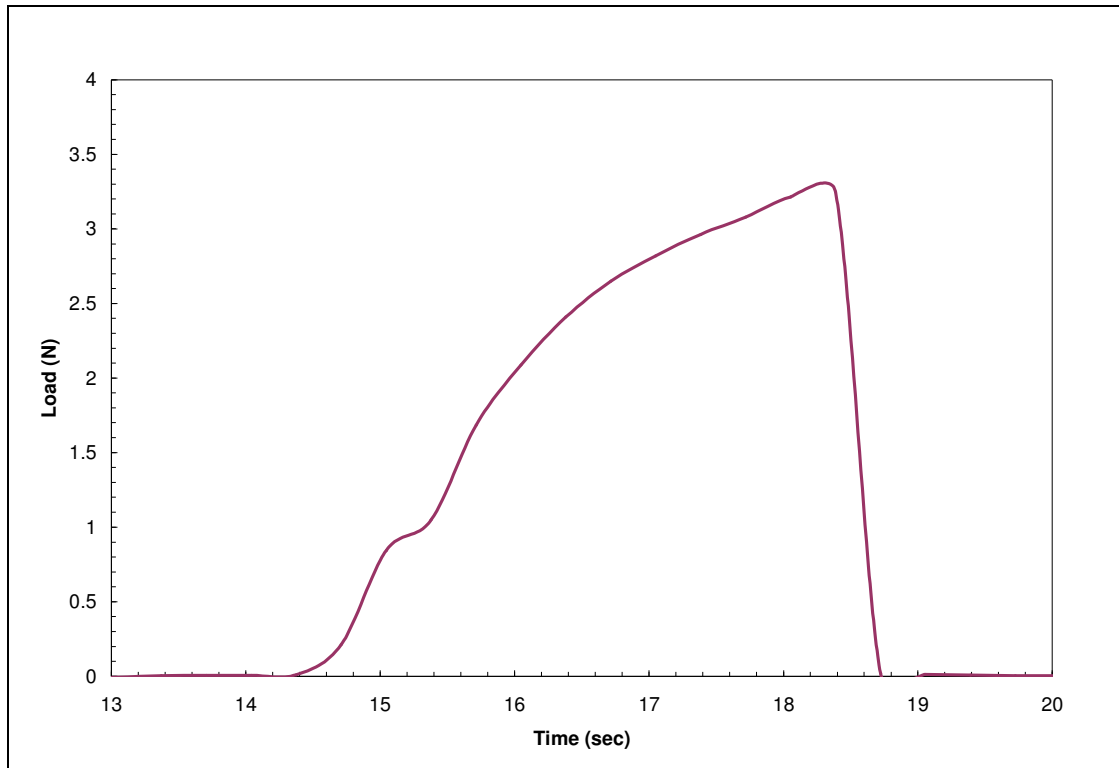
Figure 1.30: Load-time plot for a Au-Cu sample
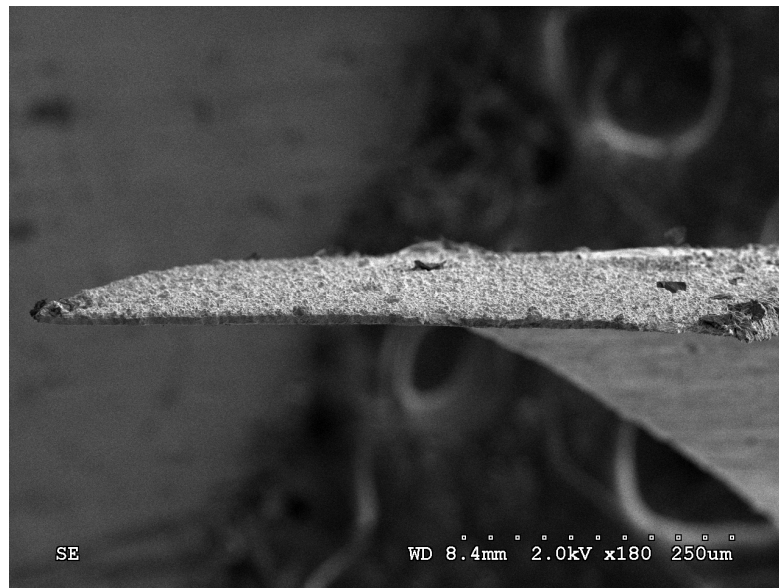
Figure 1.31: SEM image is used on failed cross-section of a Au-Cu sample for

measuring the width.

48

The chart shows: y-axis "Tensile strength (MPa)" ranging from 100 to 500, x-axis "Strain rate (1/sec)" ranging from 0.0001 to 0.0100. Annotation: $y = 810.14x^{0.1393}$, $R^2 = 0.8514$
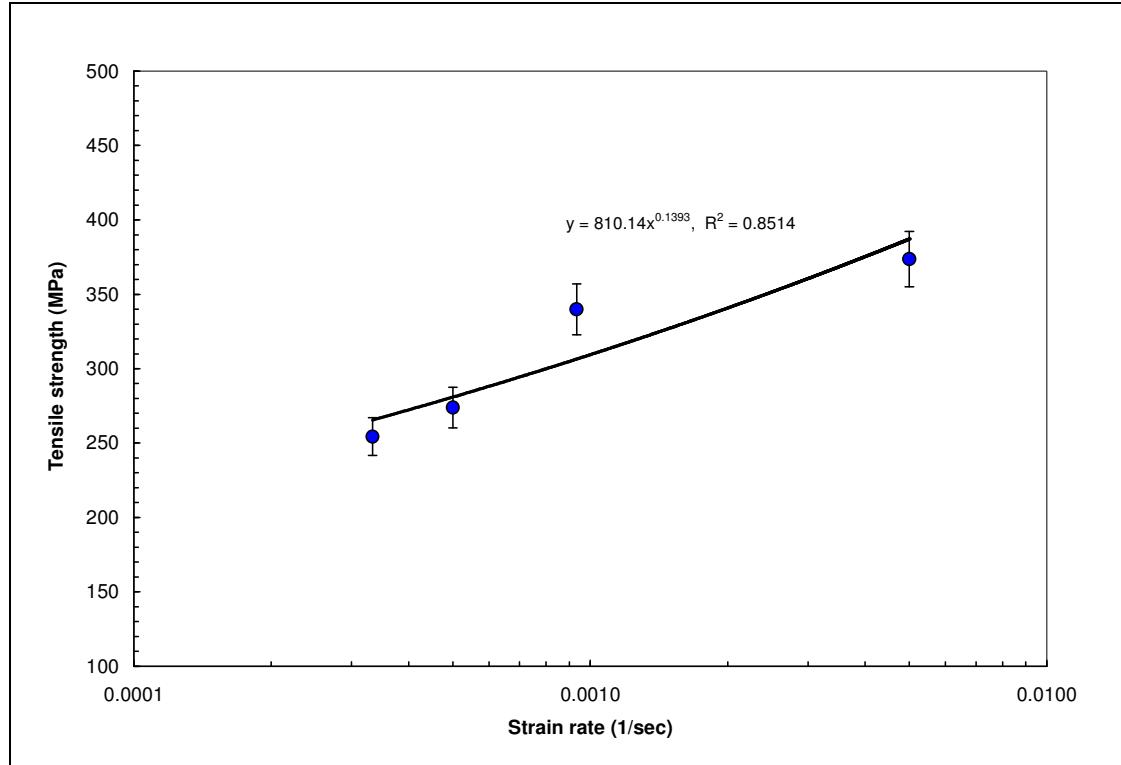
Figure 1.32: Strain rate sensitivity plot for the Au-Cu samples

Figure 1.32 shows the log-log plot of tensile strength versus strain rate. The data points are fitted with a power law relationship to determine the strain rate sensitivity exponent. The grain size of the samples used in this experiment is calculated [27, 28, 29] to be 10.33 nm. The strain rate sensitivity exponent value (i.e., $m = 0.1393$) from this experiment is in a very well agreement with the micro-scratch results obtained by Nyakiti and Jankowski [66] and is shown in Figure 1.33 as a function of log-scale grain size (d_g). Equation (1.33) has been used to predict the behavior of these nanocrystalline Au-Cu samples. The constants c_1, c_2 and c_3 are taken to be 0.080, 3.0 and 1.65 respectively [66].
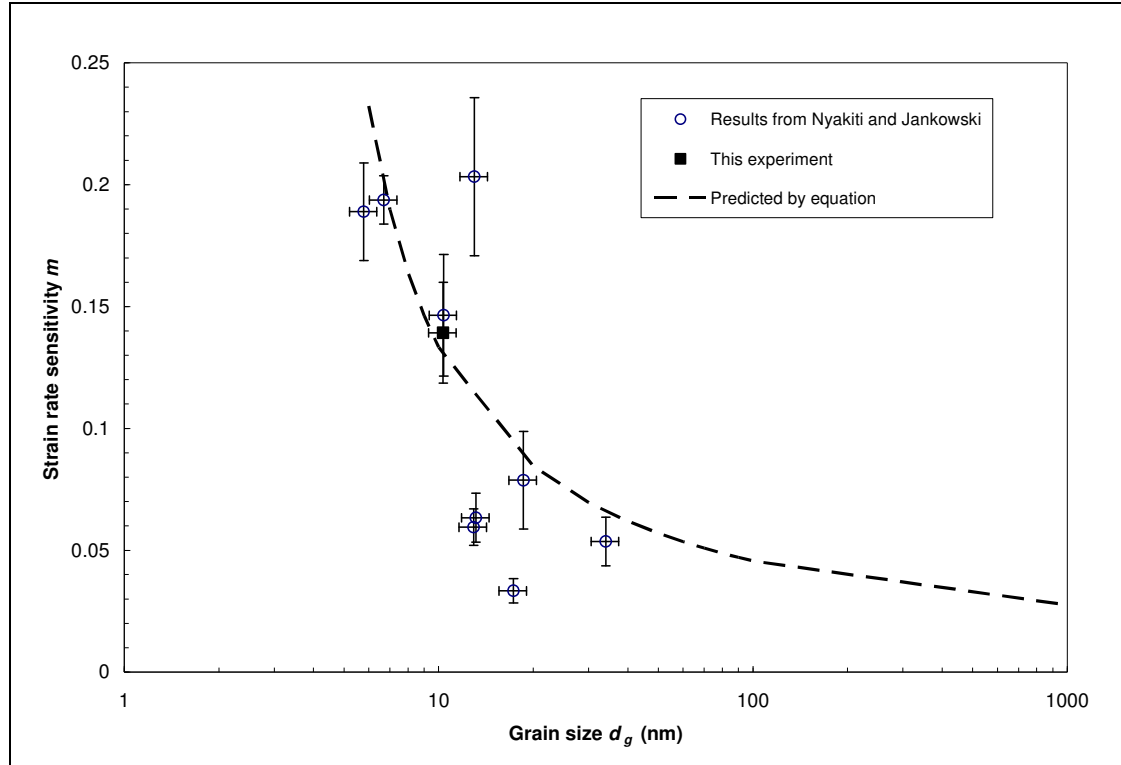
Figure 1.33: Strain rate sensitivity as a function of grain size for nanocrystalline

Au-Cu samples.

1.4 Summary

1. Tensile testing of porous silver membranes and fully dense foils are done at

various strain rates. The measured elastic modulus for the porous membranes appear

to be indicative of the *G* modulus and follows a trend line as the porosity goes from

~80% to fully dense condition. The change of yield strength with porosity has been

modeled with the theory of Li and Aubertin [45] and is found to have good correlation

with the experimental data. A 2.47 μm average grain size of the membranes is

measured from SEM images of the porous membranes and is somewhat invariant with

porosity. Strain rate sensitivity found from the rate dependent tensile testing has been

plotted as a function of the grain size and is in well accordance with the analytical

model provided by Gu, et al. [26]. Alternately, it is proposed [1] that strain rate sensitivity exponent can be modeled if the filament size and porosity are substituted in the analytical equations. Models for these expressions in equations (1.29) and (1.30) are plotted in Figure 1.16 and Figure 1.17 against the experimental data and are found to be in good agreement. The implication is that strain rate sensitivity exponent will increase as the filament size decreases, and will increase more rapidly as porosity increases.

2. Interrupted tensile tests are done on porous silver membranes at different strain rates to show the stiffening behavior of porous materials under tensile loading. It is observed that the membranes show an elastic modulus close to the *G* value. However, as deformation progresses, an upper plateau in the elastic modulus is approached that is different than modulus found in monotonic loading conditions. This upper plateau in the modulus measurement is more indicative of a value close to that measured for fully dense silver foils. It is anticipated that elastic modulus can increase for materials that strain harden by as much as 10-15%, i.e., Figure 1.22 data. Thus, it is postulated that the filaments (or struts) are linked with each other with "ball joints" that would, in essence, realign to each other in the direction of applied load. This realignment of the load bearing filaments gives the membrane more elasticity provided that necking is not yet formed.

3. Rate dependent tensile testing has been conducted on nanocrystalline electro-deposited nickel to provide the strain rate sensitivity. The as-deposited condition provides the necessary shape for the test specimens. The thickness and width of the samples are better estimated using optical microscopy. The activation

volume is found to be about 0.07 nm^3 which is suggestive of a grain size below 10 nm. The rate sensitivity is plotted as function of the grain size and is found to follow the similar trend from literature data for Hall-Petch strengthening mechanism. The experimental data is modeled based on an analytical model of bow-out of an edge dislocation [26, 59] and has good correlation with the plotted trend line.

4. Nanocrystalline Au-Cu samples are tested in tension at different strain rates. Strain rate sensitivity exponent of the samples has been obtained through a log-log plot of the strength versus strain rate. The 10.33 nm grain size samples show a strain rate exponent of 0.1393. This value is very close to projected value by the trend line obtained by Nyakiti and Jankowski [66] through micro-scratch testing of Au-Cu samples with different weight percent of Cu.

CHAPTER 2

MICRO-SCRATCH TESTING OF POROUS MEMBRANES

2.1 Introduction

Mechanical behavior of materials on a wide range of strain rates has been of interest to many researchers [e.g.: 19, 20, 57, 62, 67, 68, 69, 70]. Most materials are known to have different strength at different rate of loading, hence, exhibits at least some level of strain rate sensitivity. Many testing methods, for example, tension, compression, torsion, etc. can be applied to reveal the rate sensitive nature of materials. Among those, tensile [1, 27, 31, 57, 62, 71] and compression tests [11, 12, 13] are probably the most common method of testing specimens for about 10^{-4} to 10^{-1} per second strain rates [1, 20, 27, 69]. At the slower end of strain rate experiments with tensile tester has a difficulty of not being able to deform the sample in a highly continuous (or monotonic) fashion. In most cases, the linear actuator of the instrument for tensile deformation moves in a discrete manner in slower rates, which become evident from the plot of load versus time recording. Clusters of data points can be seen in the load-time curve as the actuator moves and tries to keep up with the input signal at such slower speeds. At faster rates, the major problem lies with the speed of data acquisition. In spite of these practical issues associated with the hardware of the experimental setup, tensile test provides highly accurate estimates of the stress-strain plots of the materials.

Faster rate tests, for example, 10^{0} to 10^{+4} per second strain rates are mostly reported to be conducted by Split Hopkinson Pressure Bar (SPHB) technique [72, 73, 74, 75, 76]. In this setup, a gas driven projectile hits an incident bar while the

specimen is situated between the incident bar and a transmitter bar. Both these

incident and transmitter bars have significantly large dimensions compared to the

specimen size and are equipped with strain gauges. Data are recorded from these strain

gauges from these bars as the specimen is compressed in the in-between position.

Despite its popularity, there are some reports that indicate that SHPB results may

sometimes be misleading [75, 76]. The major postulations behind SHPB experiments

rises from assuming uniform deformation of the sample (i.e. stress equilibrium) and no

frictional response of the system, which, sometimes are not the actual case.

As an alternative, scratch hardness measurements, originally introduced by

Mohs in 1824 [77], have evolved as a method for measuring mechanical properties of

bulk materials and thin films. Rate sensitive scratch tests can be done to reveal the

strain rate sensitivity of a material. Inherent rise time for scratch velocity prohibits the

sample from being shock loaded. Also, the scratch test method is not as sensitive to

the internal flaws and defects present the material as it is for tensile experiments at

high rates. In tensile tests, the internal defects present in the test material often lead to

premature failure through the stress concentration effect. Significant variation [31, 60

71] can result in the measurement of strength from such high rate tensile tests. As

such, scratch testing can be utilized as a better option for testing materials at high

strain rates. The aim of this research is to conduct micro-scratch experiments on

porous silver foils to high strain rates and compare the results with tensile tests, to

generate a longer range strain rate sensitivity plot for the porous silver membranes.

2.2 Background

Several researchers documented a change in the sensitivity exponent for various material systems as they compared uniaxial compression test with Split Hopkinson Pressure Bar (SHPB) test for a wide range of strain rates. Freund and Hutchinson [78]studied the problem of crack growth in plastics in high strain rate and reported the existence of a transition shear stress at a transition plastic strain. Below that transition stress, the dislocation motion is controlled by lattice resistance or discrete obstacles and above that transition stress the regime is controlled by phonon drag. Armstrong and Zerilli [79] reported similar transitioning behavior towards high rate sensitivity for copper and α-iron. Follansbee [80] speculated that limited dislocation mobility by phonon drag could lead to higher rate sensitivity.

A general description of the mechanical response associated with rate sensitivity is given by Harding [72]. He summarized the strain-rate response of materials into three major categories, with corresponding rate controlling mechanisms. These three regions are shown in the following schematic (Figure 2.1) labeled as I, II and III.
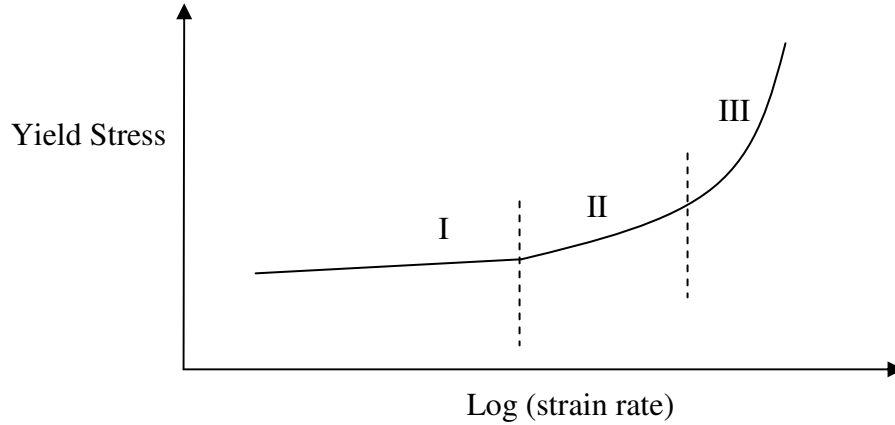
Figure 2.1: Schematic of different regions of rate sensitivity

The first segment, denoted as I, is referred to the region where low strain rates and high temperatures are active and has almost a constant, rate independent flow stress. The major underlying rate controlling mechanism in this region in stated to be athermal flow, where presence of precipitates puts forward long-range friction stress. Thermal vibrations in the lattice are insufficient in providing energy to overcome this long-range barrier. Even though crystal structure of the material has some influences on this athermal friction stress, the major positive contributions come from the presence of alloy content in the material. Materials with higher alloy content will show lower strain rate sensitivity [20, 72].

The second segment (II) is the region where higher strain rates are active at lower temperatures [72] and a linear dependence of flow stress on the logarithmic strain rate in observed. The transition from region I to region II is reported to be around 10^{-1} strain rate for annealed mild steel at room temperature [72]. At this section of the rate sensitivity, short range barriers such as dislocations and their interactions become relatively more important compared to the long range barriers (i.e., alloy

content). The flow stress is thermally activated which means the lattice vibrations can assist by supplying enough energy to overcome these barriers and flow stress becomes dependent on temperature and strain rate.

At higher rates of strain, a significant increase in the rate sensitivity exponent is observable, as shown in segment III (and as will be seen in the micro-scratch experiments of the porous foils). Harding [72] reported this transition from segment II to segment III at about $5 \times 10^{+3}$ strain rate for annealed mild steel at room temperature. Freund and Hutchinson [78] reported a similar transitioning strain rate (between 10^{+3} and 10^{+4} strain rate), however did not show the intermediate zone (region II) as a separate section. Armstrong and Walley [74] collected a numerous results of research conducted in this area in the review paper and stated that additional deformation features such as deformation twinning, adiabatic shear banding and dislocation or twin generations play very important roles in very high strain rate regime for shock loading. They also reported that behavior of shock loading (as obtained from SHPB) and shockless loading (with a continuous increase in load in a very small rise time) may differ significantly and may be more governed by drag resisting velocities of dislocations for shockless loading. This phenomenon is widely known as "phonon drag", whereas the original dislocation density is required to move at the upper limiting speed, i.e. the speed of sound and rate exponent increases most likely because of the "saturation of the mobile dislocations average velocity" [20].

Dioh, et al. [75, 76] studied the high strain rate properties of materials using SHPB and demonstrated that in some case, the higher rate sensitivity above certain strain rates is the outcome of generalization of the impact problem by assuming

equality of stress all over the deforming specimen. In reality, he showed that the stress wave form generated by high impact velocity of the pressure bar induces stress and strain gradients and thus, is different from uniform stress assumption that neglects the dynamic effect.

Today, many researchers can now use scratch technique as a comparable method for investigating mechanical properties of materials. Nyakiti and Jankowski [66] studied rate sensitivity behavior of gold-copper alloys using micro-scratch experiments. The range of micro-scratch strain rates was comparable with the limits of tensile testing and thus, reported values of sensitivity exponents were consistent with values as obtained by tensile tests.

2.3 Experimental methods and analysis

2.3.1 Micro-scratch experiment of porous silver foils

Membranes of varying nominal pore sizes (0.2, 0.45, 0.8 and 3.0 micron) are procured from General Electric Osmonics^{TM}. The porosity of the membranes is characterized using the same procedure as stated in Chapter 1. The estimation of grain size is obtained with lineal intercept method (also explained in Chapter 1) on the plan view images of the samples using a Hitachi S-4300 SE/N SEM. The samples are cut in rectangular sizeable dimensions using an X-acto knife and are mounted on plan view on a steel stub using epoxy glue on all four corners of the samples.

The micro-scratch experiments are conducted using a Universal Micro Tribometer^{TM} (UMT), mounted on a mechanical vibration isolation table. A spheroconical diamond Rockwell tip of 12.5 μm radius having 60-deg angle is used to produce the scratches on the mounted samples. Figure 2.2 shows a typical set up for

conducting the micro-scratch test. A nominal load of 10 gm (98 mN) normal to the

sample surface is used to make the constant load scratches. During a scratch test, the

Y-stage of the UMT that contains the sample on it moves in the direction of the

scratch and the tip remains constant at its position, applying the load on the surface. A

force feedback system that records the applied force as a function of time is used to

measure the actual force and scratch velocity. To induce different velocities of

scratches, associated time is varied while the lengths of scratches remain same. Seven

different scratch velocities i.e. 0.3 mm/sec, 0.5 mm/sec, 1 mm/sec, 2 mm/sec, 3

mm/sec, 5 mm/sec and 10 mm/sec are used to produce all the scratches on the foils. At

least three scratches are produced at every scratch speed to obtain a good statistical

average. Figure 2.3 shows an optical microscope image of a sample containing all the

scratches at different velocities.
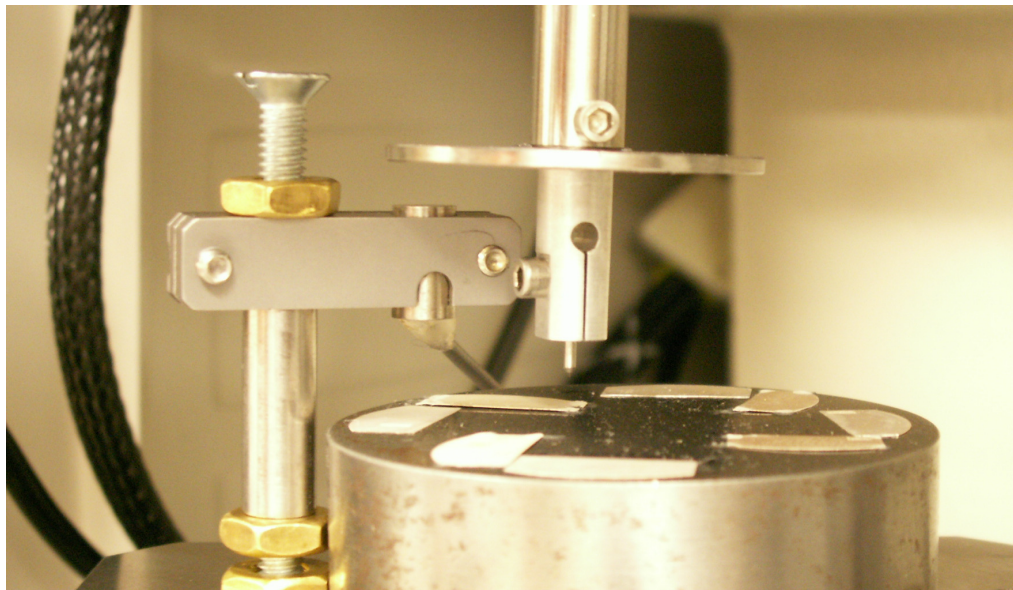
Figure 2.2: Micro scratch test rig
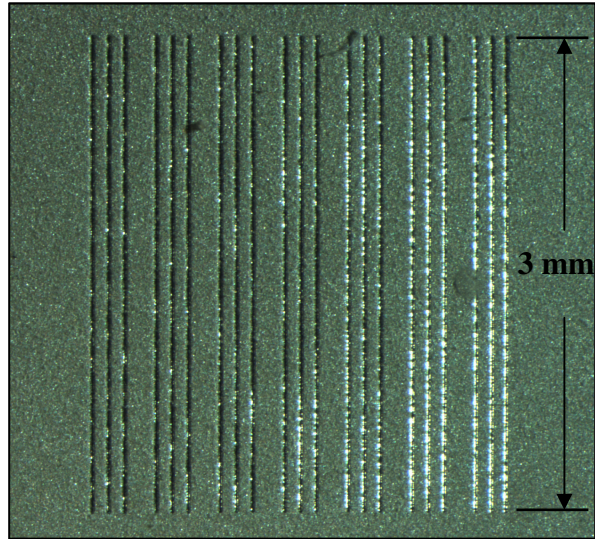
Figure 2.3: Scratches at different velocities on a single membrane mounted on plan

view
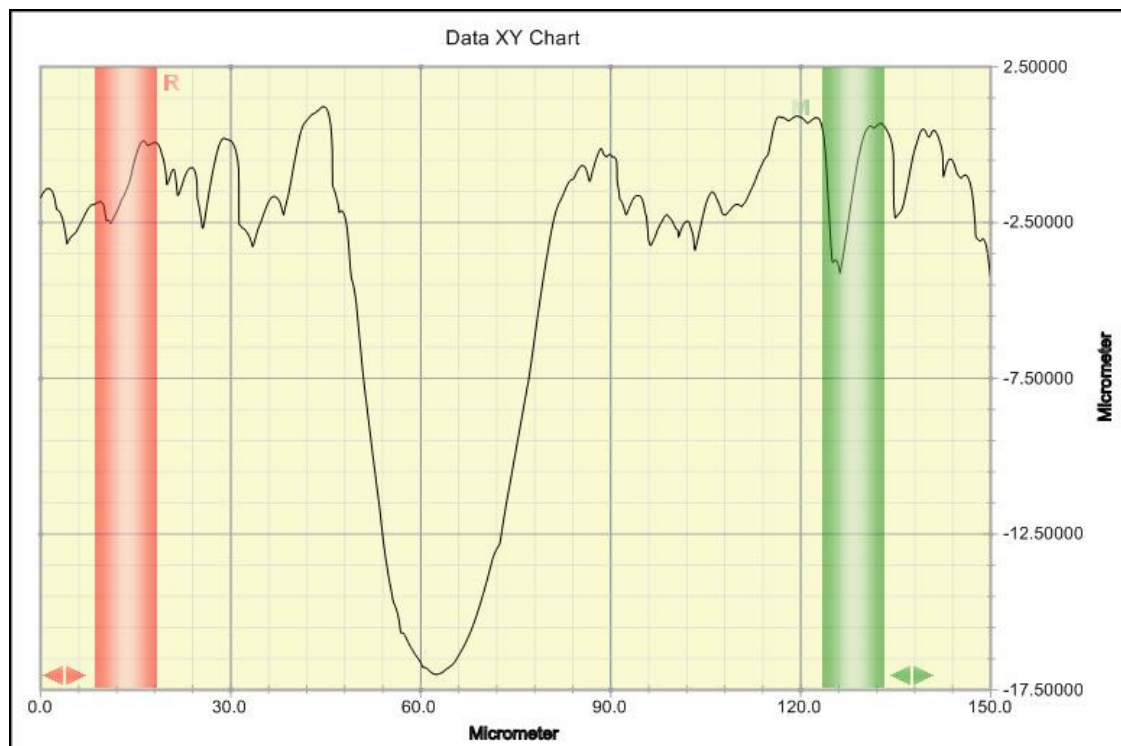
Figure 2.4: A sample scan on one of the scratches using the profiler using a 0.7 μm

tip

The width of the micro-scratch profiles are scanned using a Veeco Dektak 150 surface profiler mounted on an air suspended table. The scan of the scratch width is done using a spheroconical tip of radius 0.7 µm that has a 45 deg angle of inclination, with a stylus tracking force of 8 mg (78.4 µN). Figure 2.4 shows a typical output from the profiler which shows the scan of the width of a scratch and also shows the background surface profile.

Since the material is porous, scan on an apparently 'flat' surface provides lots of ups and downs. Thus, defining a horizontal background from which the scratch width would be measured becomes difficult. Defining the marker positions to evaluate the width is a challenge for the porous materials because of the associated high 'surface roughness'. For measuring the width using the contact profilometer, the tilt of the scan is adjusted first using wide left and right markers, to sample a considerable segment of the background (as shown in Figure 2.4 using red and green marker colors). Then, a horizontal line is drawn at the average step height of the membrane, accompanied by two other horizontal lines which define at least 90% confidence level of covering the roughness. Figure 2.5 illustrates the methodology. The width of the scratch is measured at these three horizontal lines and an average of those widths is taken to be representative of the particular scratch, i.e.

$$w = \frac{w_1 + w_2 + w_3}{3} \tag{2.1}$$

The scratch hardness (H_s) is computed by dividing the scratch load by the projection of half of the area of the tip leading in the direction of the scratch. The empirical expression is given by:

$$H_s = c \frac{F}{w^2} \tag{2.2}$$

where, H_s is the hardness, F is the scratch load and w is the associated width of the scratch. The constant c is a geometric function related to the indenter tip shape. Assuming that the scratch does not go beyond the initial hemispherical region of the tip, c equals $8/\pi$ for the projection of the leading half area of the indenter. The deformation path of the scratch is represented by the measured scratch width (w). And usually, the depth of scratch is much less compared to the width of the scratch. Even though the depth and width of the scratch are geometrically related to each other for a well-defined tip, the depth of the scratch involves some level of elastic rebound of the material. Scratch test involves primarily a shear type of deformation because the material is sheared along the direction of the scratch. During this shear type of deformation, the scratch width remains unchanged. Hence, the width of the scratch offers a better measurement of the actual volume of the material that undergoes the deformation. For this reason, the width of the scratch is used to determine the scratch hardness in equation (2.2). The strain rate ($\dot{\varepsilon}$) for micro-scratch experiments are empirically derived [66] to be:

$$\dot{\varepsilon} = \frac{v}{w} \tag{2.3}$$

where, v is the velocity of the stylus producing the scratch and w is the resultant scratch width. Strain rate sensitivity of strength (σ) for a material is given by famous Dorn equation:

$$\sigma = c\dot{\varepsilon}^m \tag{2.4}$$

where, *m* is the strain rate sensitivity exponent and c is a constant. Thus *m* is derived

from this equation by taking logarithm on both sides of equation (2.4) as:

$$m = \frac{\delta \ln \sigma}{\delta \ln \dot{\varepsilon}} \qquad (2.5)$$
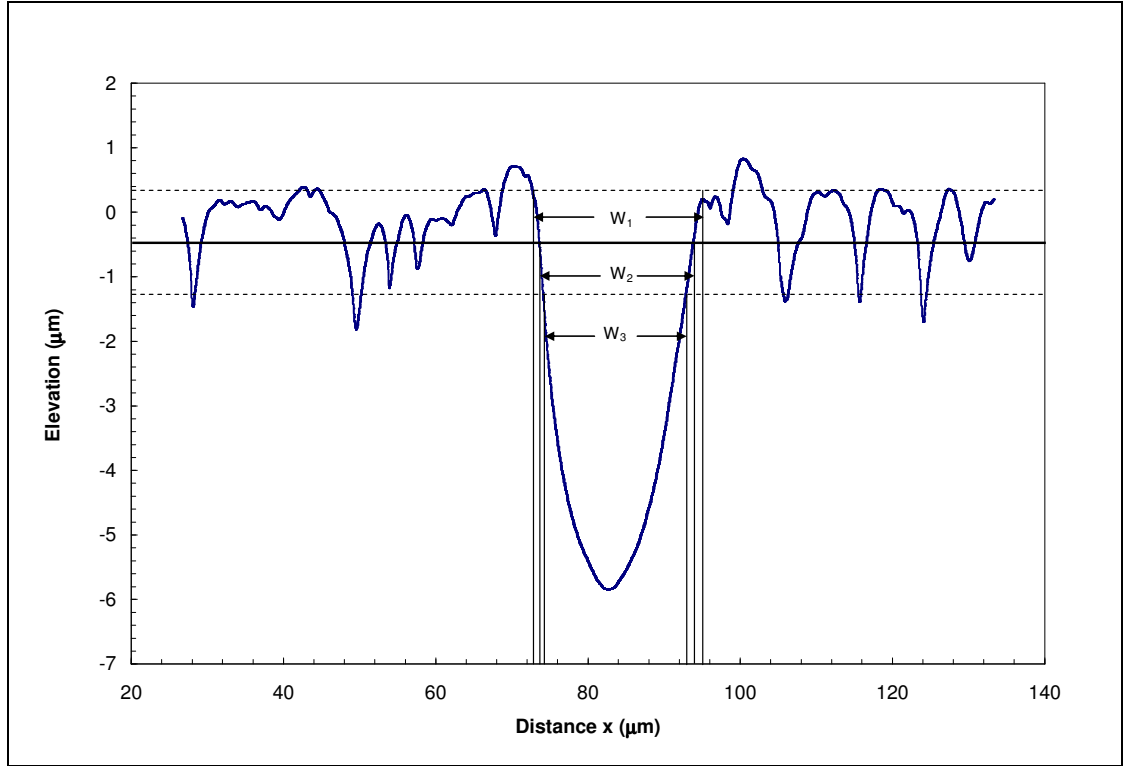
Figure 2.5: Illustrating the measurement of the scratch width for porous materials
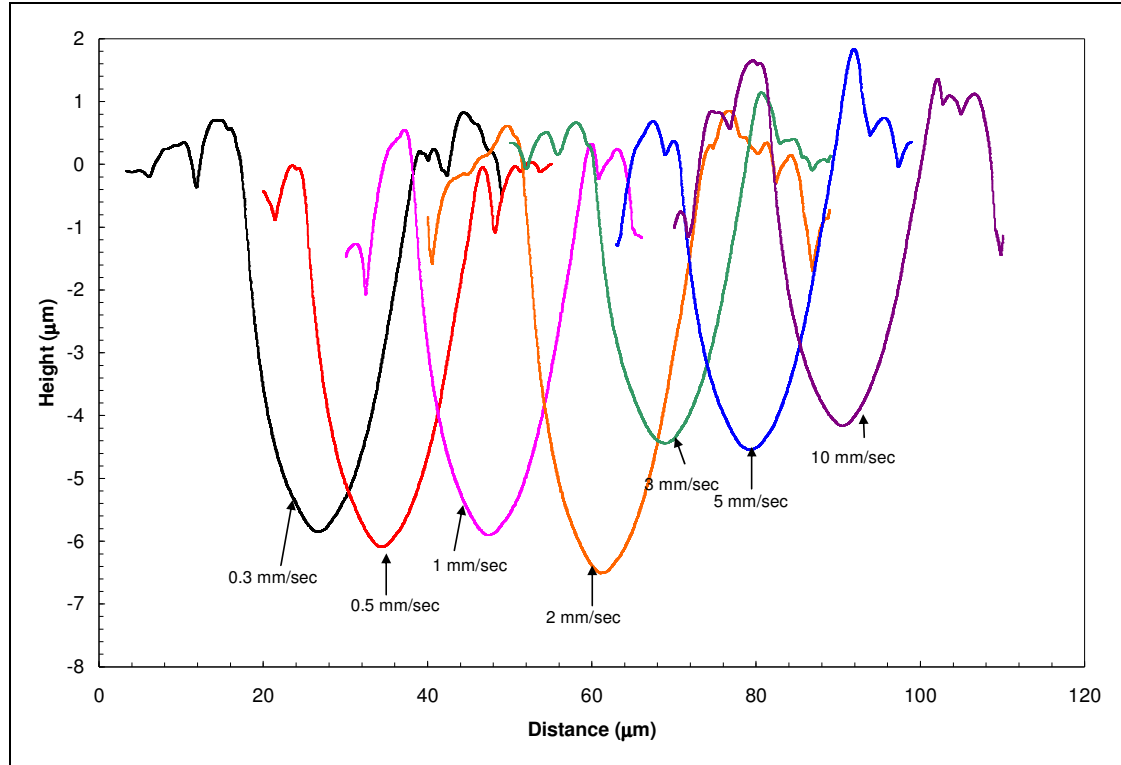
Figure 2.6: A comparative study of the width of scratches at different velocities on

0.45 micron foil

A plot of $\ln \dot{\varepsilon}$ versus $\ln \sigma$ will yield a linear curve with a slope (*m*) equal to the strain

rate sensitivity. For the scratch test data, the hardness (H_s) is plotted rather than the

strength (σ), since hardness and strength are related according to $\sigma \sim cH_s$, where *c* is

a constant having a typical value of 1/3 [81, 82].

The rate sensitivity plots of 0.2, 0.45, 0.8 and 3.0 micron pore size membranes

are shown in Figures 2.7-2.10, respectively. For reference, the yield strengths obtained

from the tensile tests as a function of strain rate are plotted as well. Material

deformation under scratch is mostly of shear type and hence, to compare the scratch

hardness with the tensile hardness (1/3 times the tensile strength), the scratch hardness

values are multiplied by $\sqrt{3}$. These hardness values (which are uniaxial in essence) are plotted in the aforementioned figures. Figure 2.11 shows the rate sensitivity plot for fully dense silver. From these figures, it can be seen that the slope of the data points from different regions lie at different elevations. These discontinuities originate from assuming a constant *c* value of 1/3 in strength-hardness relationship. These discontinuities are more evident in higher porosity membranes (i.e. the slope of data points from region II moves higher in elevation). At different level of indentations, different tip geometry is active and hence, it is necessary to consider different corresponding *c* values. However, for calculating strain rate sensitivity, only the slope of the power law fit is important and the elevation of the plot (corresponding to different *c* values) can be neglected without any significant error. From these figures, it is also evident that for some specimens there may be little or no transitional zone between low (region I) and intermediate (region II) strain rate sensitivity. These phenomena can be observed for high porosity membranes (0.8 and 3.0 micron nominal pore size) as well as for fully dense foil. To investigate any possible difference, similar rate dependent micro-scratches are done on the cross-section of the dense samples. The samples were prepared using epoxy mount in cross-section and involved grinding and polishing at different smoothness levels to remove surface roughness and other possible artifacts from the vacuum casting process. The data from scratch on plan view and on cross-section overlaps, as it can be seen from Figure 2.11. It is also found that at intermediate regime (region II) the rate sensitivity exponents of all porosity membranes are somewhat comparable. Similar trend lines were reported by Harding [72] in a study on commercial-purity aluminum (i.e. the higher strain rate exponents

are alike). Table 2.1 lists the strain rate sensitivity exponents obtained for different

regimes of all the specimens.
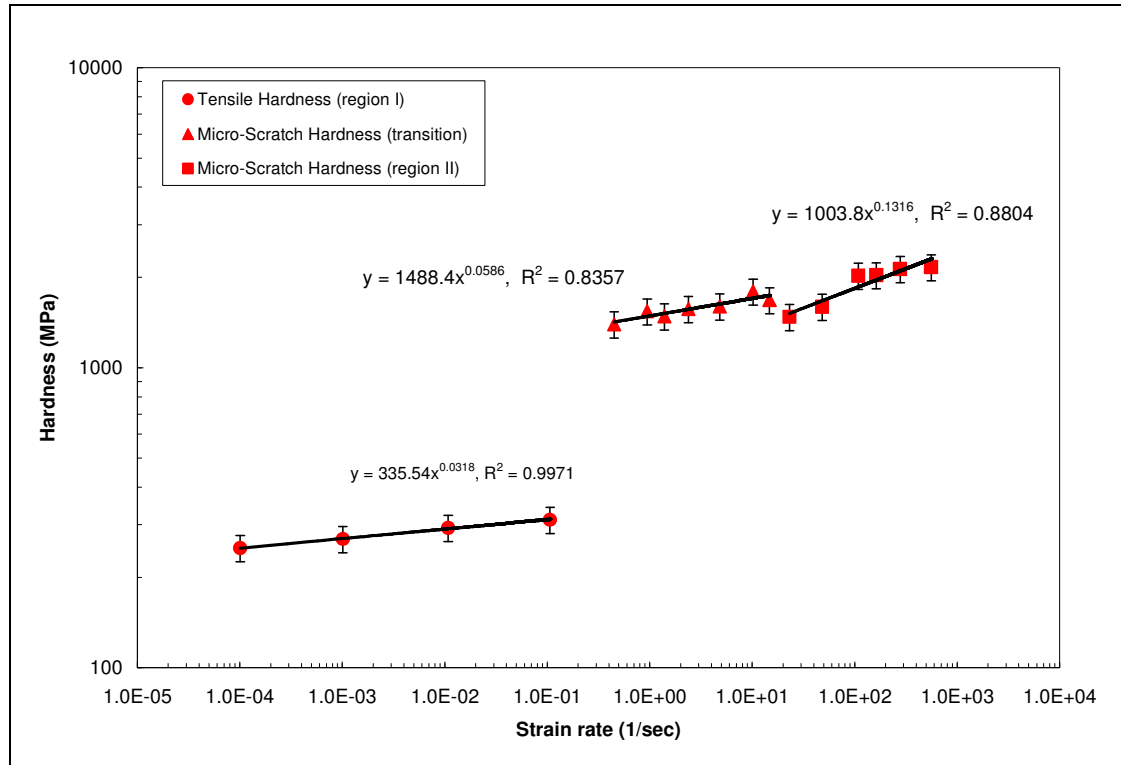
Figure 2.7: Rate sensitivity plot of 0.2 micron pore size membrane
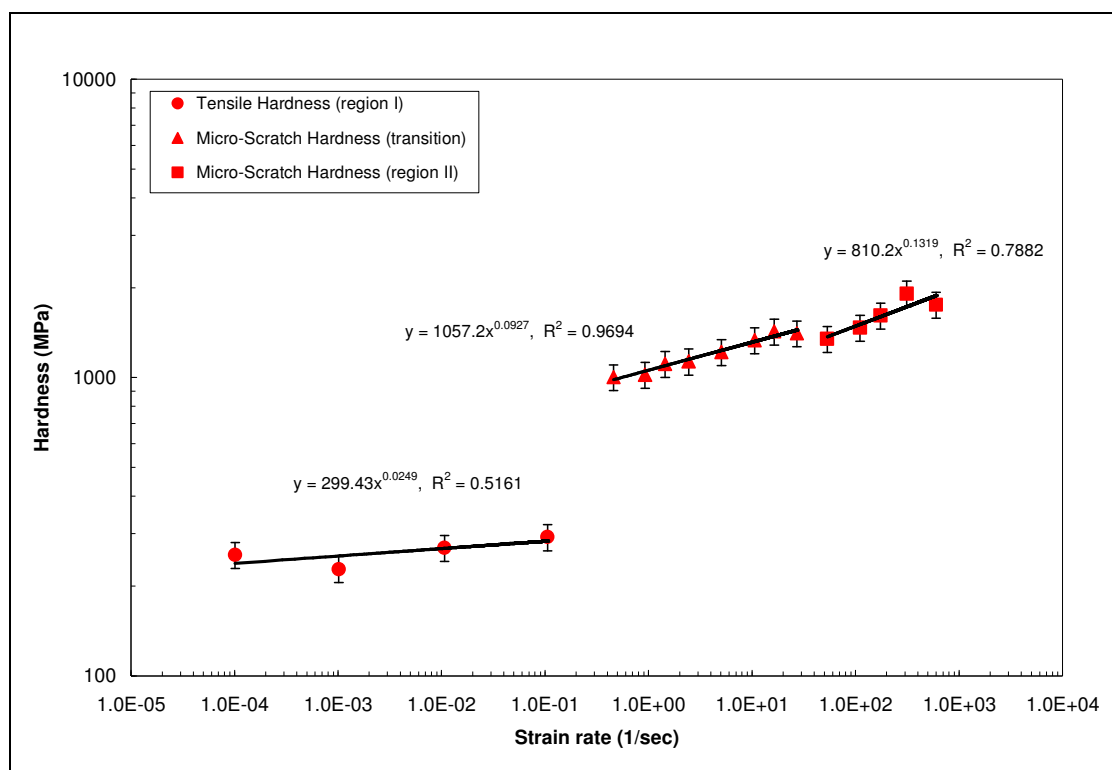
Figure 2.8: Rate sensitivity plot of 0.45 micron pore size membrane
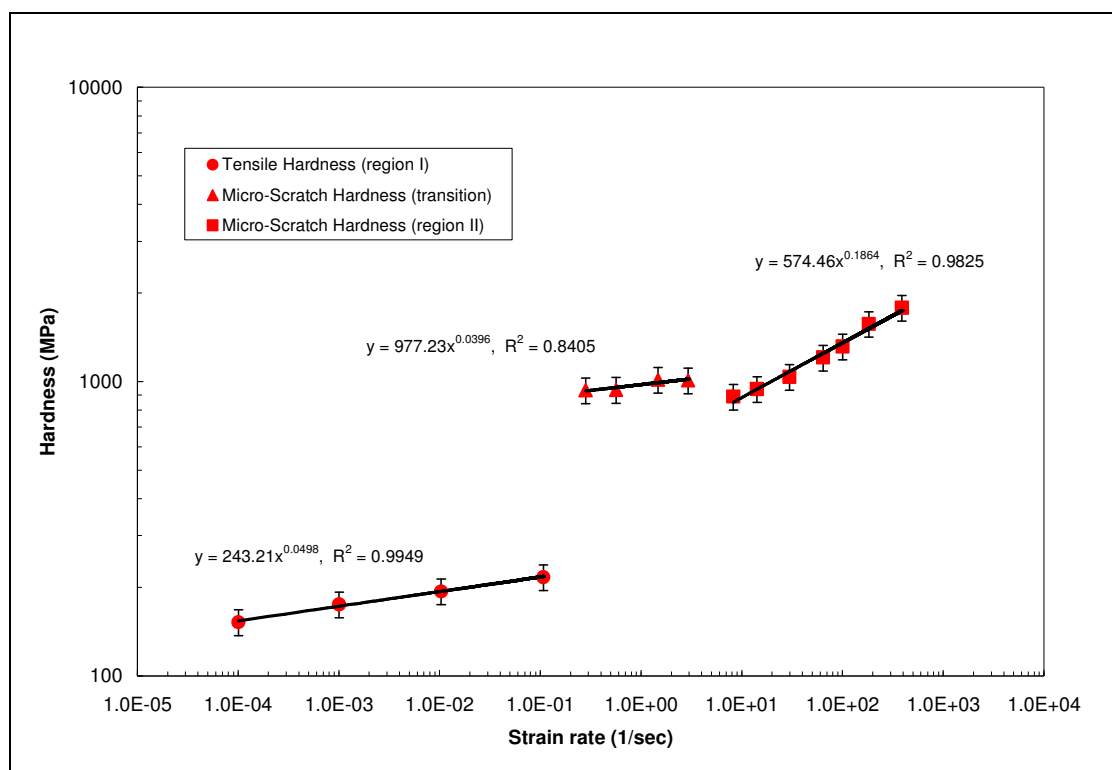
Figure 2.9: Rate sensitivity plot of 0.8 micron pore size membrane
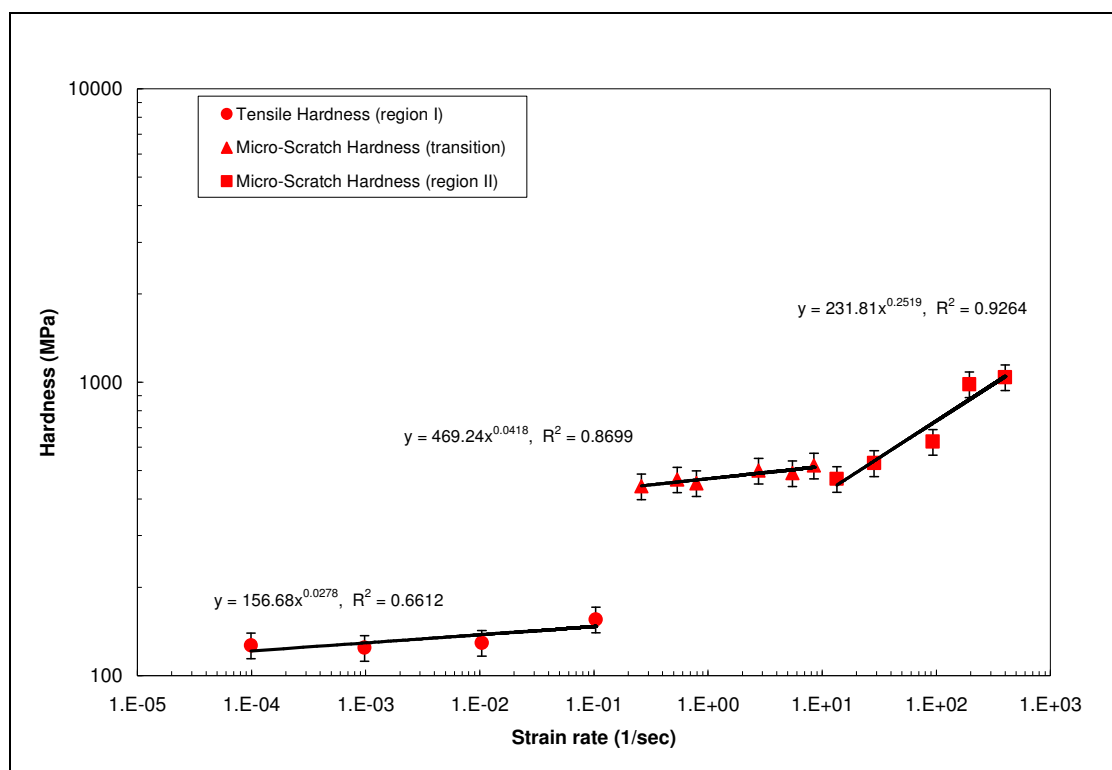
Figure 2.10: Rate sensitivity plot of 3.0 micron pore size membrane
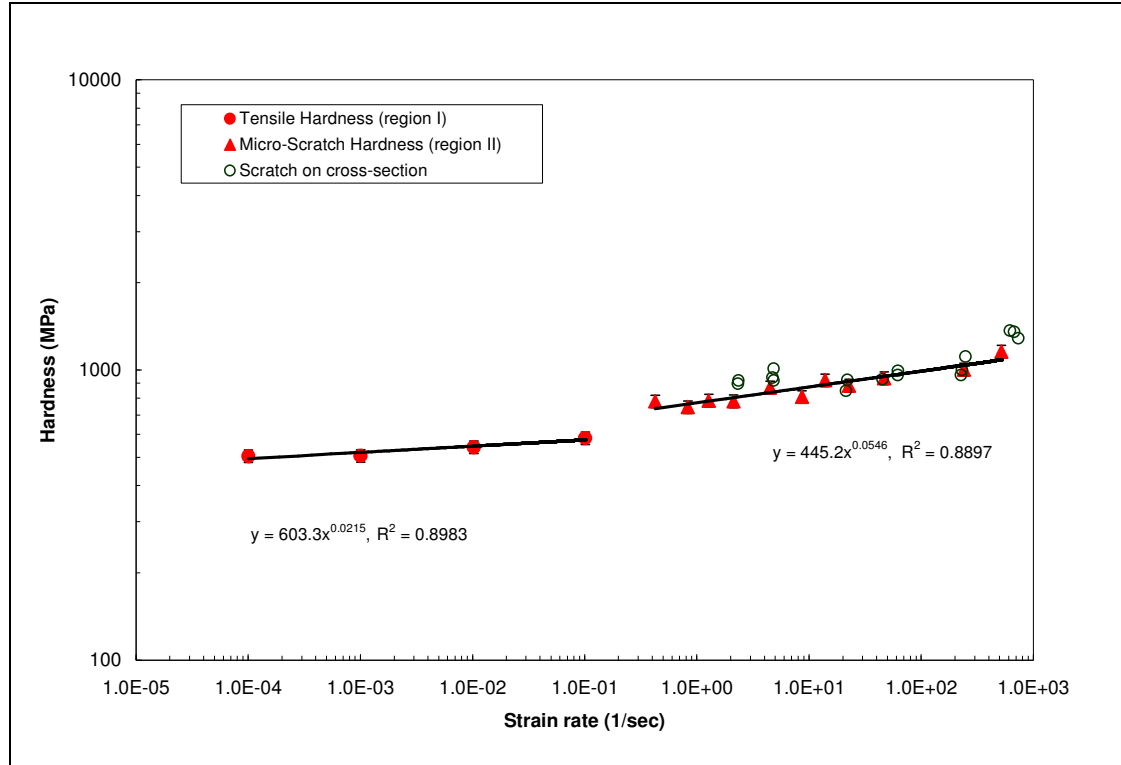
Figure 2.11: Rate sensitivity plot of fully dense silver foil

Table 2.1: Strain rate sensitivity exponents for different regimes of all specimens

Specimen	Porosity	Strain rate sensitivity exponent		
		Region I	Transition	Region II
0.2 micron	0.258±0.008	0.0318±0.002	0.0586±0.009	0.1316±0.016
0.45 micron	0.341±0.017	0.0249±0.012	0.0927±0.005	0.1319±0.028
0.8 micron	0.482±0.019	0.0498±0.003	0.0396±0.006	0.1864±0.003
3.0 micron	0.502±0.045	0.0278±0.009	0.0418±0.005	0.2519±0.019
Fully Dense		0.0215±0.002	0.0546±0.006	

To investigate any possible higher accuracy in the strain rate sensitivity, an attempt has been taken to calculate the hardness using actual area under the tip during scratch as opposed to using the projected area (i.e. $\pi w^2/8$). Assuming the side wall of

the conical tip is tangent to the hemispherical region, the actual area of deformation during the scratch with the tip is given by:

(a) For scratch within the spherical region:

$$A = \pi r^2 \sin^{-1}\left(\frac{w}{2r}\right)\left[\frac{1-\cos\left\{\sin^{-1}\left(\frac{w}{2r}\right)\right\}}{\sin^{-1}\left(\frac{w}{2r}\right)}\right]$$
(2.6)

(b) For scratch beyond the spherical region ($\alpha=30^\circ$):

$$A = \frac{\pi w}{4}\left(\frac{w}{2\cos\alpha} - r\tan\alpha\right) + \frac{\pi r^2}{2}$$
(2.7)
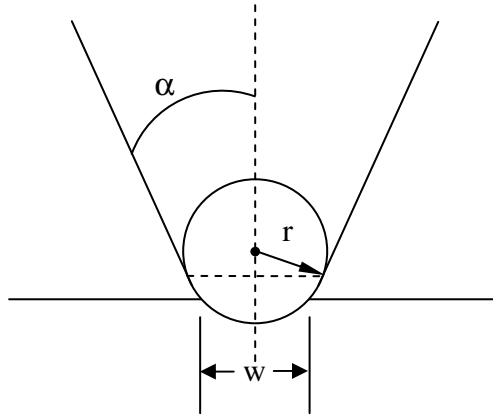
Figure 2.12: Schematic of the Rockwell tip used for micro-scratch experiment

Figure 2.12 shows a schematic from which the geometrical area is formulated to these expressions. In Figure 2.13, the hardness values calculated using projected area and actual area are shown for 0.2 micron pore size membrane. It is noticeable that no significant accuracies are achieved in the strain rate sensitivity by using actual area under the tip. The slope of the power law fit remains fairly constant for both data sets.
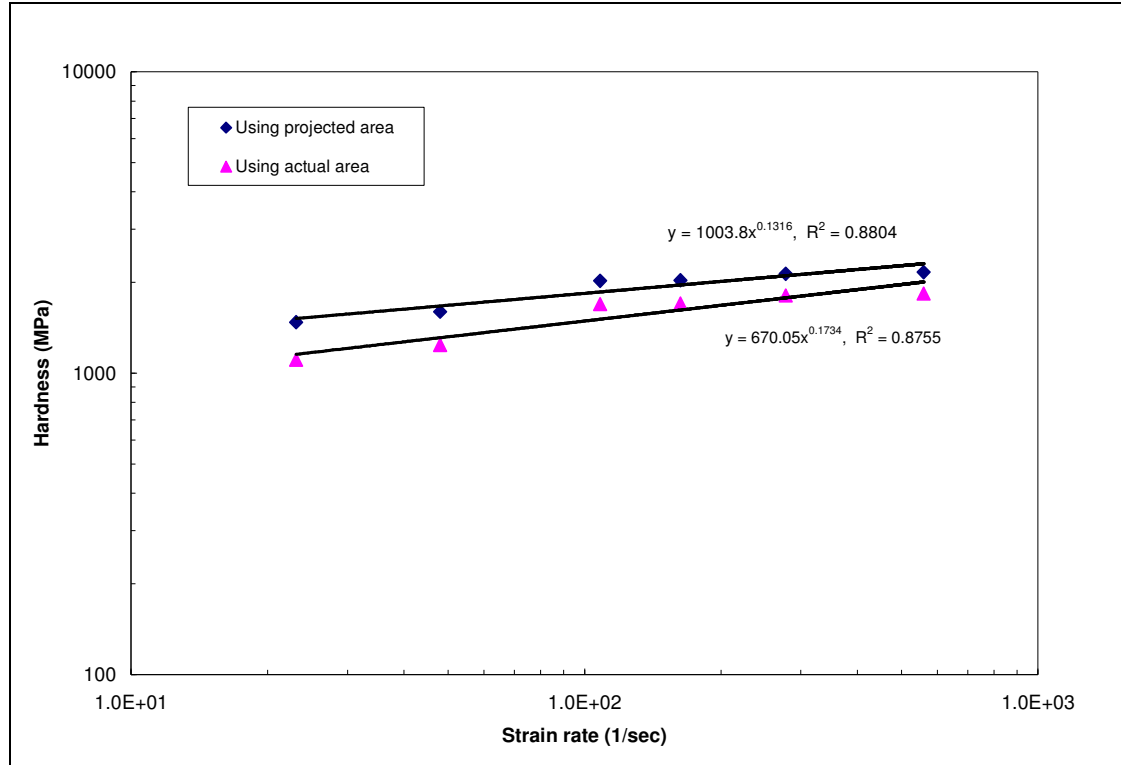
Figure 2.13: Comparison between hardness values using projected indentation area

and actual indentation area

And, the changes in the slope values are well within the error limits as calculated from

the associated correlation coefficients. However, there are significant difference in the

rate sensitivity values as found from tensile test and scratch test (Figure 2.7-2.11). At

strain rates higher than certain critical value, there is a discretely observable upturn in

the yield stress dependence on strain rate. This change in strain rate sensitivity at high

strain rates is seen for all porosity membranes. Gu, et al. showed that the strain rate

sensitivity value found using different test techniques may vary significantly [26].

However, he used nanoindentation and tensile test to compare his results; and for

nanoindentation experiments, a significant source of error may originate from the

potential for work hardening of the face-centered-cubic material samples, which, Gu, et al. did not take into consideration during explaining his results. For the scratch and tensile tests of porous silver membranes, this author believes that the test method is not the underlying reason for the observed change in the strain rate sensitivity. Rather, the change of deformation mechanism from alloy and dislocation based strengthening (region I in Figure 2.1) to higher dislocation based strengthening (region II in Figure 2.1) is the fundamental cause of the observed higher rate sensitivity exponent, as obtained by the micro-scratch experiments in these cases. Similar behavior is observed by many researchers for other materials at high strain rates [20, 72, 74, 79]. The region of 'phonon drag' (region III in Figure 2.1) is observed at even higher strain rates and generally occurs at strain rates higher than 10^3/sec. To access this 'phonon drag' regime, higher strain rate experiments are necessary, as may be obtainable by other techniques, for example, nano-scratch testing.

2.3.2 Micro-scratch experiment of nanocrystalline Ni

Electro-deposited nanocrystalline Ni foils are mounted in cross-section using epoxy. Prior to the scratch test, the preparation of the samples involved grinding and polishing at different smoothness levels to remove surface roughness and other possible artifacts from the vacuum casting process. Rate dependent micro-scratches are done on the cross-section of these polished samples. The widths of the scratches are measured with an optical microscope. Figure 2.14 shows an optical image of a scratch done at 5 mm/sec. The data from scratch on cross-section is shown in Figure 2.15. For reference, the tensile test data of the nc Ni foils from section 1.3.3 is plotted with the micro-scratch data. It is observed that the strain rate sensitivity exponent of

nanocrystalline Ni increases from 0.0561±0.01 to 0.085±0.01 as the strain rate

increases.
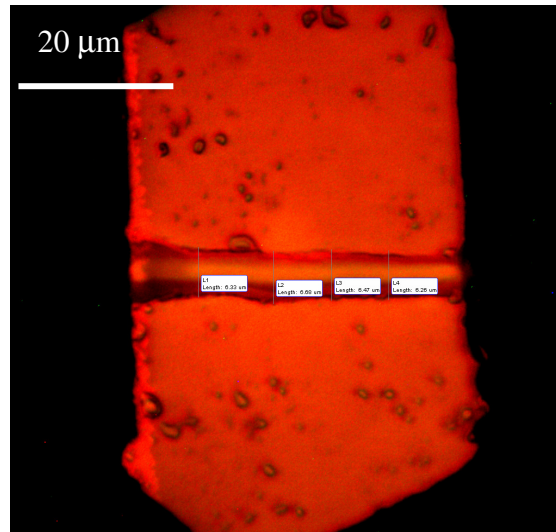
Figure 2.14: Measurement of a scratch at 5mm/sec on the nc Ni with an optical

microscope
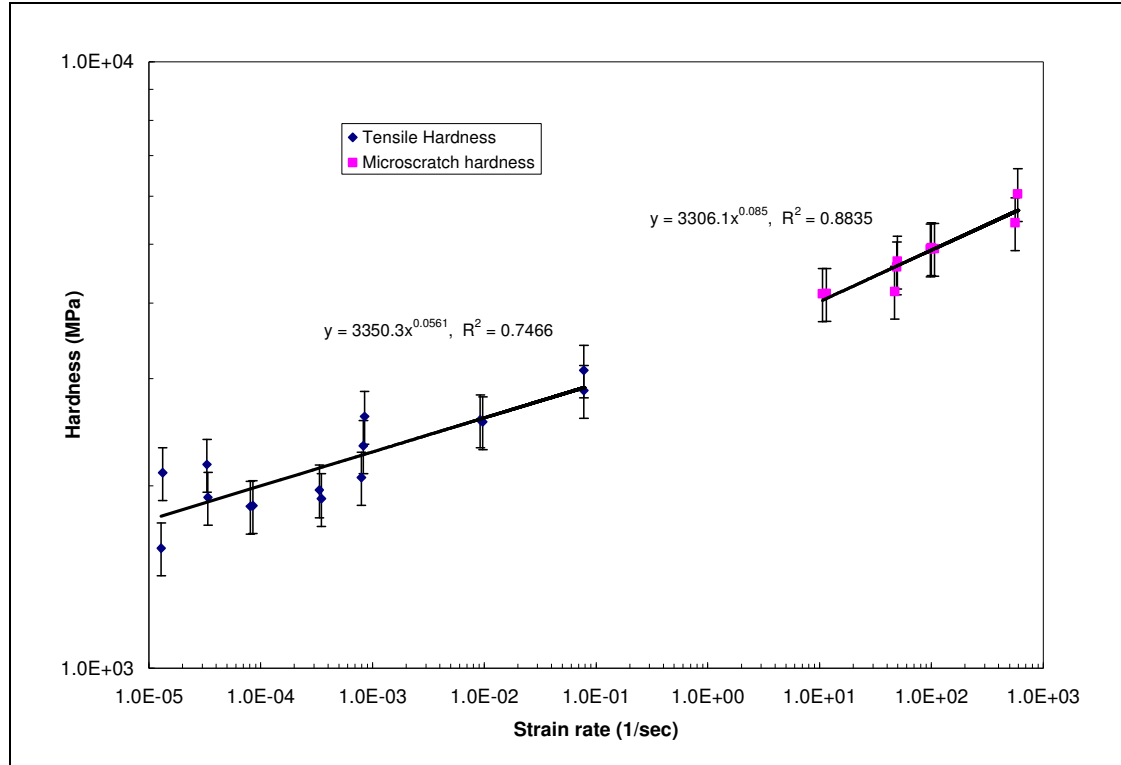
Figure 2.15: Comparison of tensile hardness with micro-scratch hardness and

associated strain rate sensitivity of nanocrystalline Ni

2.4 Summary

Strain rate above 10^{-1}/sec, in general, are not achievable with tensile testing

because of the limitations to conducting tensile test method. In addition, a ductile-

brittle transition in tensile behavior can occur at higher strain rates due to the inherent

flaws, such as defects, stress concentrations, surface roughness, etc., present in the test

specimen, which can then undermine the genuine strain rate sensitivity. Measurements

at even higher strain rates can be done with SHPB. However, in SHPB, there is a

shock front and in shock loading, there is possibility of phase change during the

experiment because of sudden spike in the temperature wiping out the necessary

thermal equilibrium condition, though not likely for Ag. A method to investigate the

strain rate sensitivity of materials at higher strain rates is micro-scratch testing. Experimental data on rate sensitivity of various porosity silver membranes are obtained using scratch testing at different velocities. Shockless continuous loading makes it possible to explore the rate sensitivity without the effect from phase changing. Use of actual area as opposed to projected area of scratch front does not improve the rate sensitivity value by much. An increase of rate sensitivity value occurs at a typical value of about 10^{+1} per second strain rate. This higher rate sensitivity exponent occurs mostly from the higher interaction between dislocations and grain boundaries. Experimental results show that shockless micro-scratch experiments can well-simulate the mechanical behavior at higher strain rates, making it a suitable method compared to SHPB where a shock front exists during high rate loading.

CHAPTER 3

NANOSCRATCH TESTING OF Au/Ni THIN FILMS AND HYDROXYAPATITE CERAMICS

3.1 Introduction

Strain rate sensitivity of the flow stress is one of the key parameters to understand the deformation kinetics in nanocrystalline materials. Literature studies show that the strengthening of nanocrystalline materials with increasing strain rate as the grain size decreases to about 10 nm [70].The dependence of material plasticity on grain size has been of interest to many researchers. The nanometer grain-size structures, compared with conventional coarse grained materials, offer high strengths and better wear resistances [19, 26, 83]. High strain-rate sensitivities appear [19, 84] to be governed by grain boundary deformation processes as grain boundary sliding and grain boundary rotation. The strategy to make materials with ultra-high strength is to limit the dislocation movements required for plastic deformations [85, 86]. However, the ability to change shape without failure (ductility) is often reduced as a compromise to the high strength nc materials. In addition to grain size, laminating or layering is a method of reducing size to the nanoscale in order to change the mechanical properties of the materials [87]. Therefore, nanocrystalline nanolaminates (ncnl) may come with the high strength and the potential for flexibility and ductility at the same time. Relevant industrial applications of nanocrystalline nanolaminates include optical band-pass filters for x-rays and neutrons [88, 89, 90, 91], giant magneto-resistance [92, 93] for high-density recording media, in low temperature stability analysis [94, 95, 96], for bonding through high energetic reactivity and ultra-high wear resistant coatings [97, 98, 99, 100]. In spite of their advantages, the strengthening behavior for

nanocrystalline nanolaminates has not been fully explained, whether it is due to grain size or the layer pair spacing. In addition, experimental observation of the potential softening behavior in the Hall-Petch effect at grain size less than 10 nm is not sufficiently documented in the literature.

With scratch testing on the surfaces of the ncnl, the hardness of the material can be calculated as shown by many researchers [83, 101, 102, 103], which can then be correlated with the strength of the material [81, 82]. The hardness and strength of a hydroxyapatite ceramic coating, and metallic nanocrystalline nanolaminates is now measured using a NanoAnalyzer[TM] capable of micro and nano-scale scratches. By varying the time of scratches, i.e. the scratch velocity, the material surfaces are subjected to different strain rates. The results are used to determine the strain rate sensitivity of these metal-metal composites. The implications of grain size and laminate spacing on the strength, i.e. hardness, of the ncnl(s) are revealed.

3.2 Experimental Approach

Nanocrystalline nanolaminates are described by to primary structural features which are the characteristic layer pair spacing and the grain size. The layer pair spacing is also known as the composition wavelength for the alternating sequence of the laminas. A schematic for a typical nanocrystalline nanolaminate structure is shown in Figure 3.1(a). The two types of interfaces that originate from such structuring are: from the grain boundaries and from the layering of the laminates (Figure 3.1). The grain boundary interfaces impede dislocation motions for strengthening the solid and possibly, the interfaces formed between the layers do the same. During the hardness measurements using nanoscale probing techniques, it is postulated that the mechanical

response of the sample comes from both these interfaces. The contribution from these interfaces can vary significantly depending on the size of the indentation. That is, at a certain depth, the grain boundary effect may contribute more or less than the layering effect. Thus, it is important to quantify the contribution from both these two effects on the measurement. From this quantification, a particular depth or width of indentation (Figure 3.1) can be chosen to obtain responses from both layer pair and grain boundary interfaces.

(a)   (b)
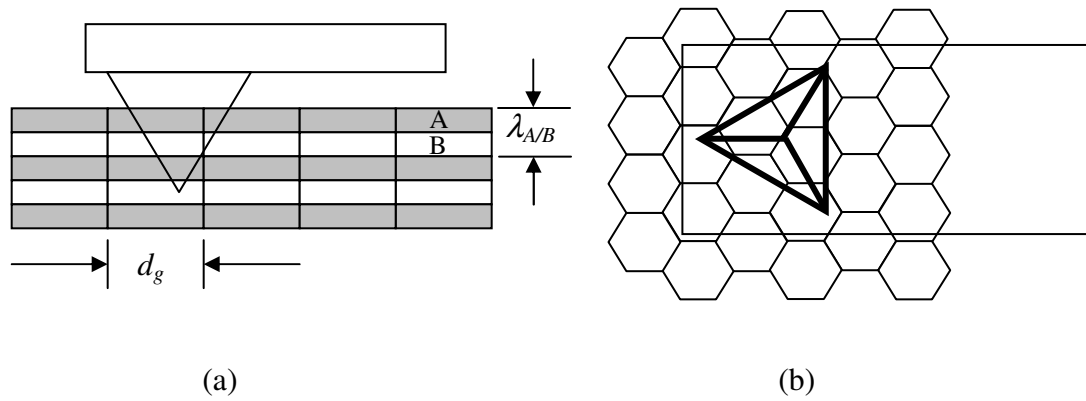
Figure 3.1: (a) Side view and (b) top view of the schematics of indentation (with a pyramidal Berkovich tip) on a nanocrystalline nanolaminate (the columnar grain size d_g is the diameter of the circular equivalent of the hexagonal grain and $\lambda_{A/B}$ is the layer pair size)

For modeling the grain boundary interface, it is necessary to compute the number of the grains that are being intercepted by the indentation, because the grain boundary effect is a direct function of the number of the grains. Densely packed hexagonal grains of columnar type are incrementally placed against each other to find out the maximum number of coincident boundaries (Figure 3.2). The number of

common interfaces is being recorded as the number of cells increases. This data is

fitted as an excel plot with x-axis being number of cells and y-axis being number of

common boundaries, as shown on Figure 3.3. Different order polynomials are used to

fit the data to provide a suitable equation for predicting the number of grain boundary

interfaces. In the case of a lower order polynomial, the lower limit of the number of

grains at which there exists a practical intercept area is high. For example, a fourth

order polynomial can predict the number of interfaces (within 10% of the actual

number of interfaces) only at a minimum of 13 grains. A sixth order polynomial, on

the other hand, can predict the values with significant accuracy at a minimum of 3

grains. However, this accuracy of prediction remains valid for only up to several

thousand grains. At high number of grains, the calculation by higher order

polynomials deviates highly from the actual number of interfaces.
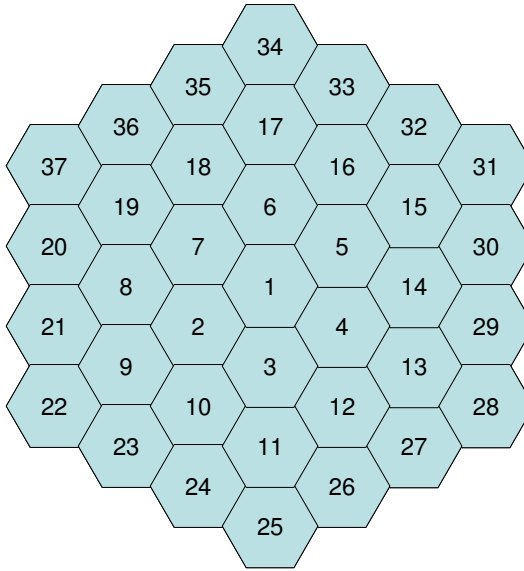
Figure 3.2: Densely packed hexagonal grains are incrementally placed according to

the numbers to find out the number of interfaces

The plot shows a graph with "Maximum coincident boundary" on the y-axis (ranging from 0 to 800) and "No. of hexagonal cells" on the x-axis (ranging from 0 to 300). The fitted equation displayed is:

$$y = 2E\text{-}12x^6 - 1E\text{-}09x^5 + 5E\text{-}07x^4 - 1E\text{-}04x^3 + 0.01x^2 + 2.2725x - 4.3681$$
$$R^2 = 1$$
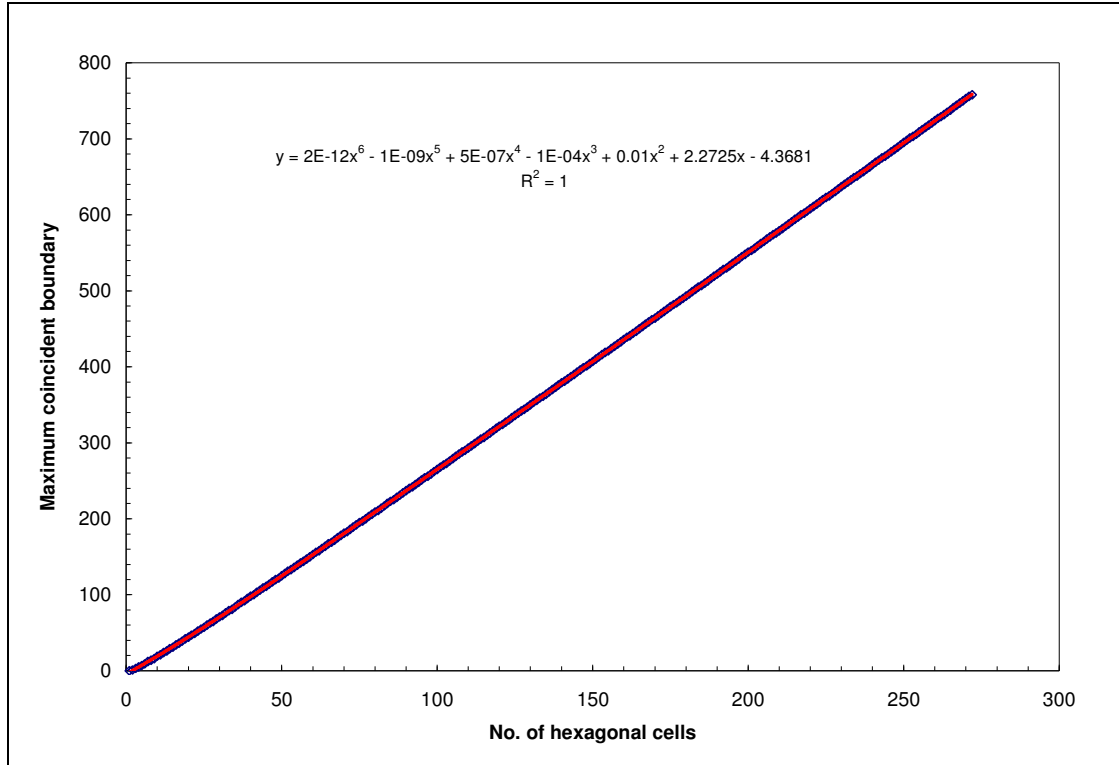
Figure 3.3: Relationship of number of coincident boundaries with number of

hexagonal grains in a densely packed condition

Figure 3.4 shows a plot where number of interfaces per cell is plotted with

increasing number of cells on the x-axis. As the number of cells increases, the

intercept boundary per cell decreases and plateaus out about a value of 2.8.

Theoretically, the maximum number of intercept boundary per cell that is possible is

less than 3.0 (Figure 3.2 and 3.4). The polynomials and other logarithmic fits that were

used to fit the data could not simulate this asymptotic behavior of the intercept

boundary per cell. All the equations apparently overestimate this asymptotic value by

a factor of at least 2, for high number of grains. Because of this reason, a general value

of 3.0 is used to model the behavior of the intercept boundary per cell. This value of

3.0 is very close to the actual number (Figure 3.4) as well as to the theoretical approximation. However, this simplification overestimates the number of coincident boundaries for up to first 150 grains. The volume of indentation that is necessary for quantifying the boundary effects of nanocrystalline nanolaminates involves much higher number of grains and hence, this error up to 150 grains is insignificant.
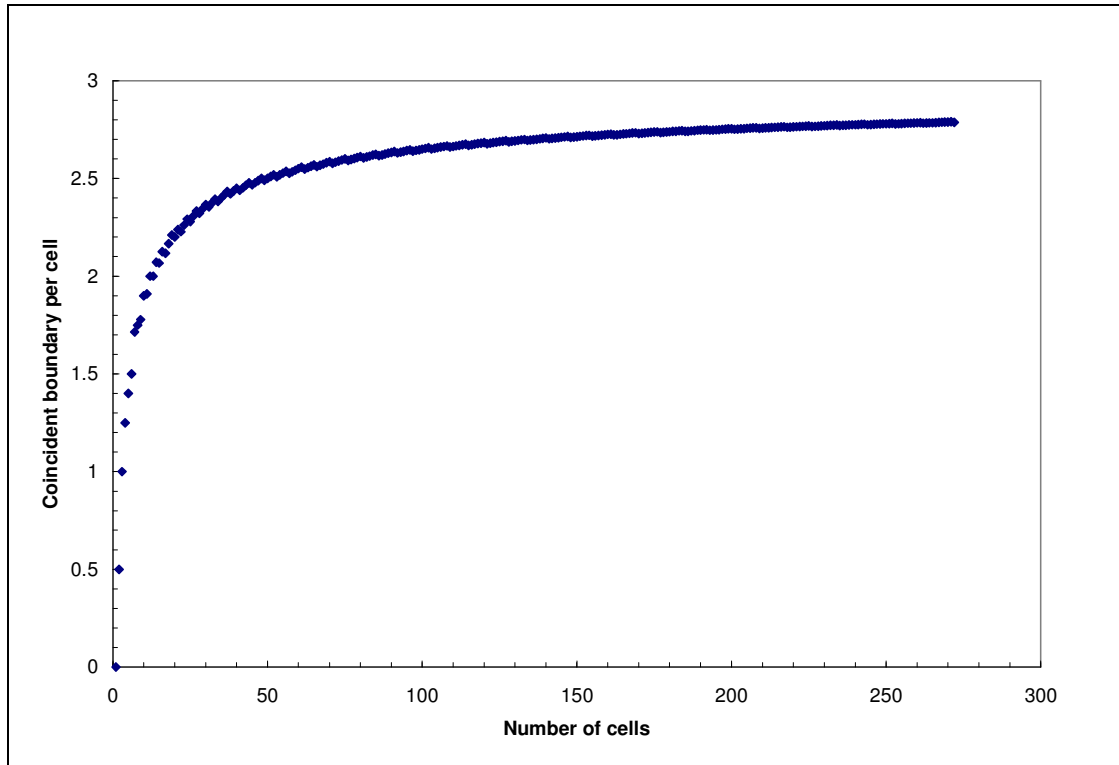
Figure 3.4: Plot of coincident boundary per cell versus number of cells shows a plateau value around 2.8 boundaries per cell

A MATLAB program (Appendix III) is written to simulate the intercept area of the indenter for layer pair and grain boundary contributions. In the program, the geometry of Berkovich tip is considered to have a triangular base and a spherical tip with a transition in between. In the transition part, the sphere is considered to be

tangent on the three common side lines of the faces of the tip. The orientation of the tip with respect to the cantilever, hence with respect to the direction of the scratch, is not considered in the model. Tip radiuses of 50 nm and 500 nm are used for simulation to find out possible affect of change in the intercept area on tip shape. Based on the radius of the hemisphere, the overall size (i.e. volume) of the indenter can either increase or decrease. For example, with a sharper tip radius, the overall volume will be less compared to a dull tip (larger tip radius) indenter. As the schematic of Figure 3.1 suggests, the amount of intercept area for both grain boundary and layer pair would increase as the indenter goes deeper into the system. Figure 3.5 shows the relationship between actual grain size d_g and the structural dimension h_g of the hexagonal grain that is used in the simulation. Figure 3.6 shows the geometry and SEM image of a Berkovich tip. Figure 3.7 shows an exaggerated geometry that is used for modeling.
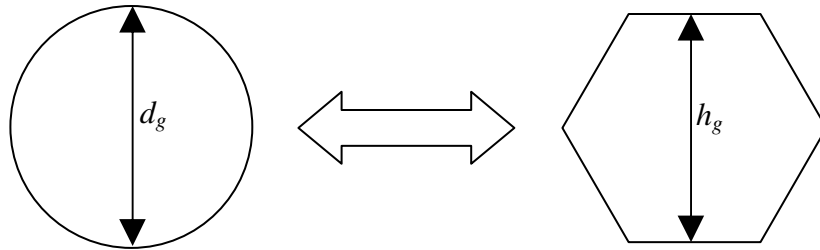
Figure 3.5: The relationship between columnar grain size d_g and hexagonal grain size h_g used in the model
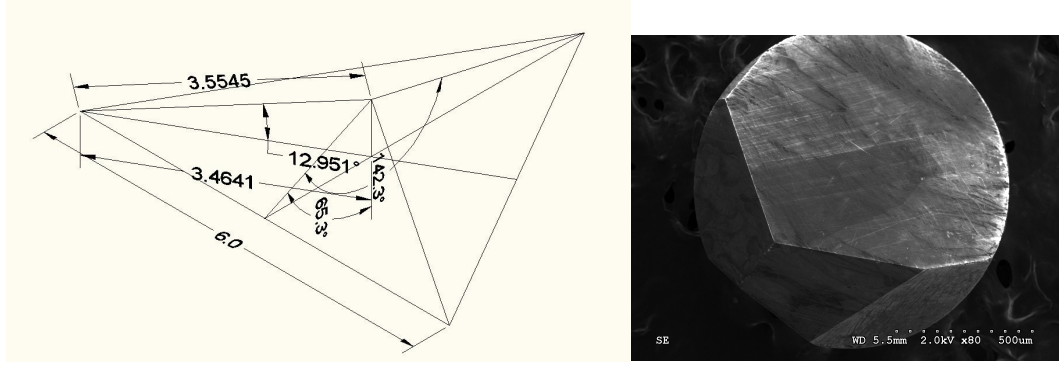
Figure 3.6: Geometry (left) and SEM image (right) of a diamond Berkovich tip. The

length of the marker is 500 μm on the SEM image
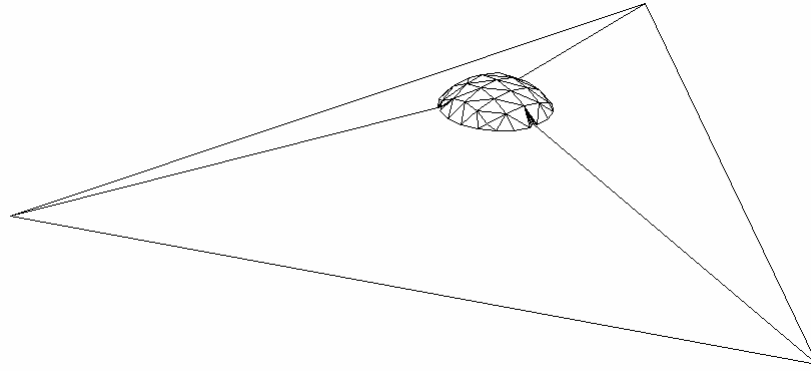
Figure 3.7: Exaggerated model geometry (the hemisphere is not tangent to the

sidelines in this picture)

With simple geometrical calculation from Figure 3.5, it can be shown that:

$$h_g = \sqrt{\frac{\pi}{2\sqrt{3}} d_g^2}$$

(3.1)

The expression from equation (3.1) is used in the MATLAB model to calculate the

intercept area, with d_g being a structural input parameter for a particular ncnl. Figure

3.8 shows a plot of grain boundary and layer pair intercept area on a laminated film as

the width of indentation increases. In this case, the modeling has been done for a structure that has densely packed hexagonal columnar shaped grains with grain size (d_g) being 16 nm and layer pair spacing ($\lambda_{A/B}$) being 0.8 nm. The characteristic dimension (i.e., volume of the indent divided by the intercept area) is plotted as the indent goes deeper into the system. A Berkovich tip (as shown in Figure 3.6 and 3.7) with a 50 nm tip radius is used in this model. As mentioned earlier, the shape of the tip does not have continuity in all directions as the geometry goes from the hemispherical section to the triangular section. This discontinuity is observable in the computation of the interface area as it can be seen in Figure 3.8 at about 20 nm of indentation width. The depth of indentation also goes through a fluctuation due to the change of shape of the indenter. Other than this discontinuity, the penetration depth can be assumed to be linear until the spherical penetration as well as for the pyramidal penetration, with different slopes. The asymptotic characteristic length computed for the layer pair intercept area is half of the layer pair size, as each interface of the layer pair contributes to the calculation. However, for the grain size, all sides of the hexagonal grain does not contribute to the intercept area and thus, the asymptotic characteristic dimension computed for the grain boundary intercept area is little less than 50% of the grain size. This factor of ~50% is associated with the coefficients of the predictive equation modeled from Figure 3.2 and 3.4.
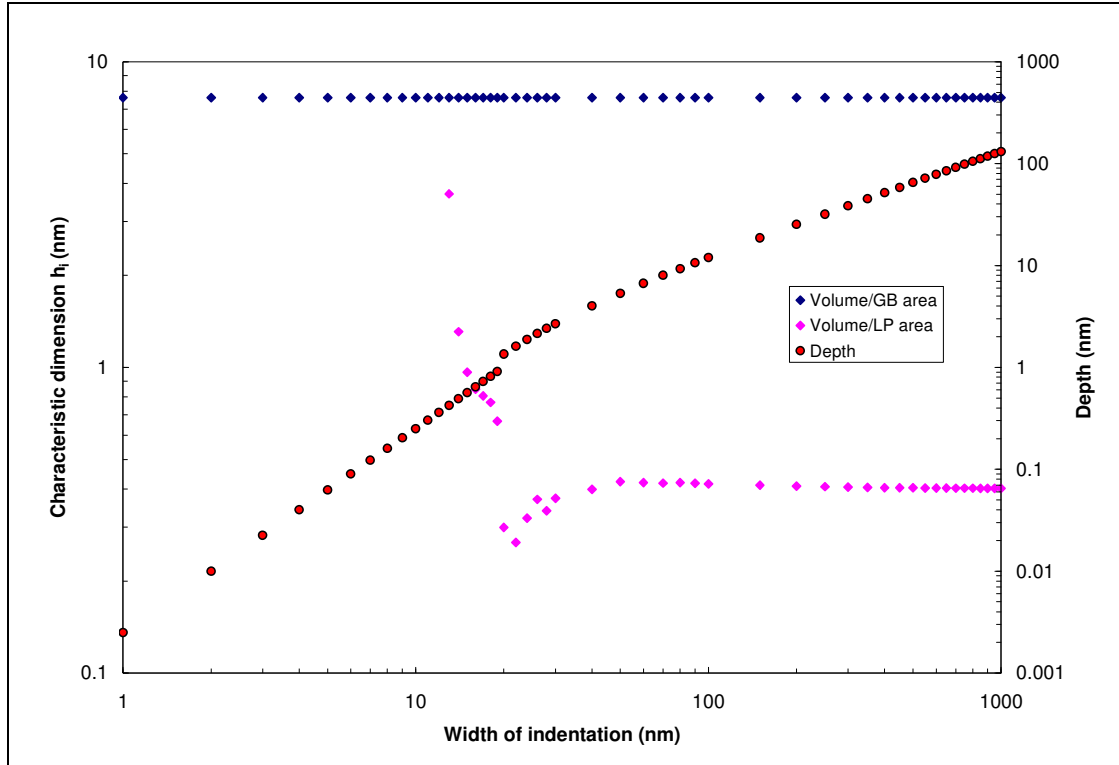
Figure 3.8: Characteristic dimension for grain boundary and layer pair intercept area, as computed for a 16 nm grain size (d_g) and 0.8 nm layer pair size laminate

At a very small indentation depth (or width), the indenter tip does not reach the first layer interface and hence contribution of intercepted area only comes from the grain boundaries, provided the grains are small enough. As the indentation increases, this layer interface contribution increases, almost at a continuous fashion (except where the shape of the indenter changes from hemispherical to pyramidal). However, since the indenter meets with layer pair interfaces intermittently, the initial part of the curve fluctuates before the die-out of fluctuations occurs. This fluctuation is dominantly observable if the layer pair size is considerably higher compared to the grain size. Figure 3.9 shows such a case where the grain size is 15.2 nm and the layer

pair size is 4.5 nm. Figure 3.10 shows the dependency of the depth with the width of

indentation as the radius of the tip increases from 50 nm to 500 nm for a Berkovich

tip.
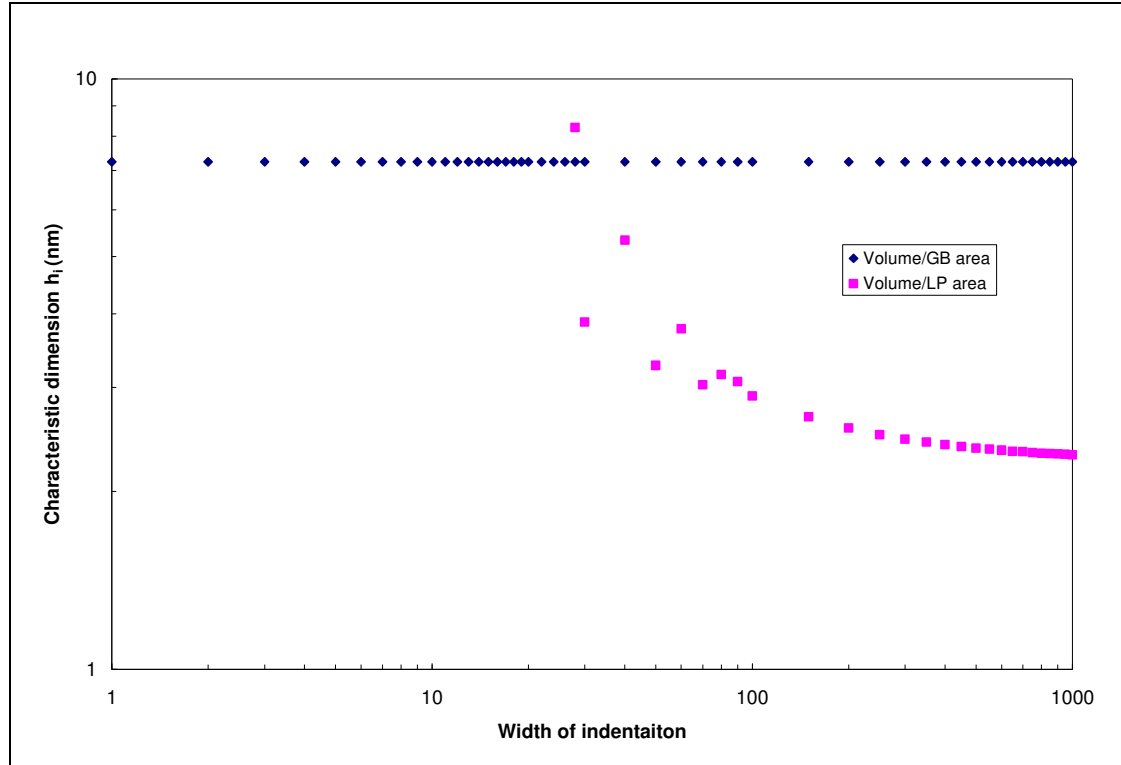
Figure 3.9: Characteristic dimension for grain boundary and layer pair intercept area,

as computed for a 15.2 nm grain size and 4.5 nm layer pair size laminate
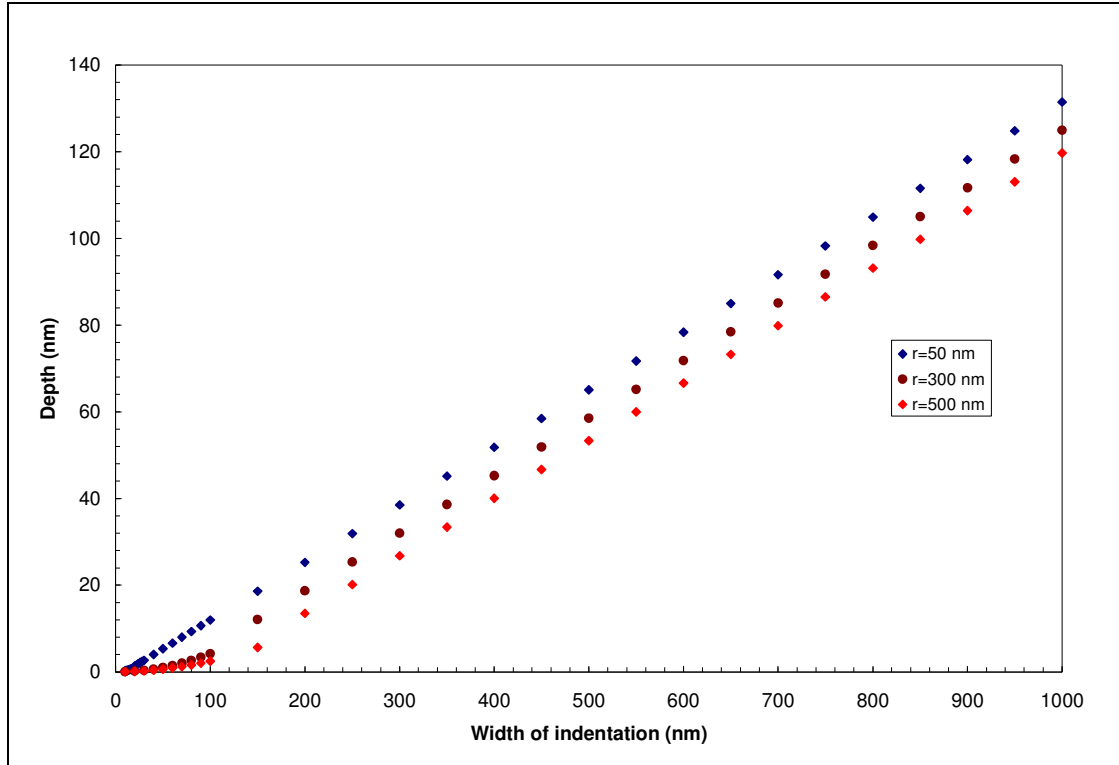
Figure 3.10: Depth of indentation as a function of width for different tip radius for a

Berkovich type tip

3.3 Experimental method

The use of nanoscale probing techniques makes the mechanical property

measurement of ultra thin films accessible, which is otherwise not quite possible with

macroscopic techniques such as tensile or compression tests. Static nanoindentation

analysis generally assumes a homogeneity and isotropy of the test material which is

seldom the case. Moreover, nanoindentation is limited to 10% depth of film thickness

as the technique is highly prone to sensing substrate effect [104], as the pressure

volume during loading lies directly beneath the indenter tip. In nanoscratch technique,

the pressure volume lies in front of the scratch and hence, much thinner films can be

tested with scratch technique which otherwise are not possible with nanoindentation

[103]. For these reasons, nanoscratch technique has evolved as an advantageous

measurement procedure for testing thin films deposited on substrates [102]. A

NanoAnalyzer[TM] (trade mark of Center for Tribology, CETR Inc.) is capable of

making micro-length nano-width scratches. A number of scratches are produced on

the coated surface of the optically flat samples. These scratches are made with a

diamond Berkovich tip (conical and cube corner tips are also available for producing

scratches) mounted on a ceramic cantilever (some tips are mounted on metal

cantilevers). A typical probe-cantilever arrangement is shown on Figure 3.11. A

normal load ranging from 100 μN to 2 mN is applied to produce the scratches. The

velocity of scratches is changed from set to set to induce a strain rate effect [66].

Generally, at least three scratches are done at each combination of load and velocity to

obtain a sound statistical correlation. After each set of scratches, the coating surface is

scanned perpendicular to the scratch in order to measure the width without any effect

from thermal drift. Each scratch is measured at several positions (typically at 5

positions or more) to provide a statistical average of the scratch width.
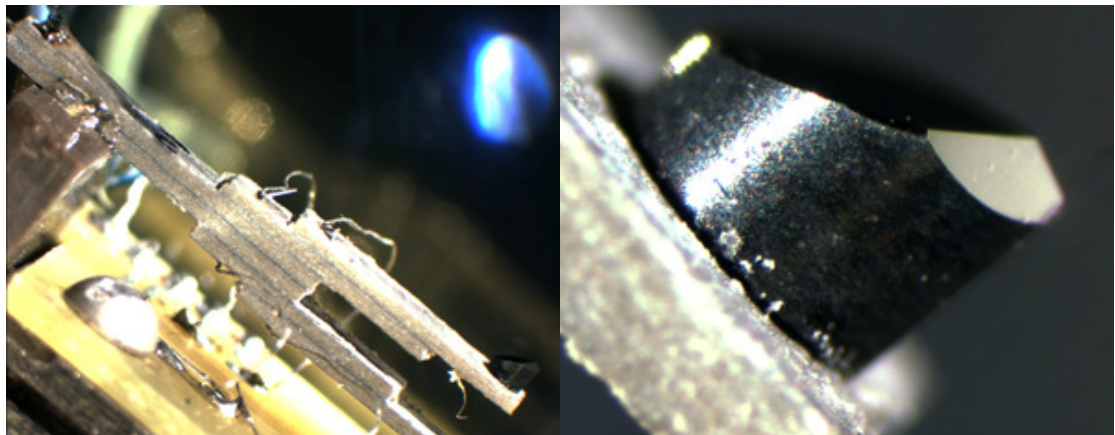
Figure 3.11: A typical probe-cantilever arrangement is shown on left figure while a

Berkovich tip is shown on the right

The strain-rate $\dot{\varepsilon}$ is calculated using the following formula [66]:

$$\dot{\varepsilon} = \frac{V}{w} \tag{3.2}$$

where, V is the velocity of the scratch (nm/sec) and w is the width of the scratch (nm).

The relationship between Strength (σ) and Strain-rate ($\dot{\varepsilon}$) can be found using the

Dorn relationship as:

$$\sigma = \dot{\varepsilon}^m \tag{3.3}$$

where, m is the strain-rate sensitivity exponent. Rewriting equation (3.2) after taking

the natural logarithm, we find that,

$$m = \frac{\partial \ln \sigma}{\partial \ln \dot{\varepsilon}} \tag{3.4}$$

From equation (3.4), a plot of "$\partial \ln \dot{\varepsilon}$ versus $\partial \ln \sigma$" will yield a linear curve with a

slope equal to the strain rate sensitivity. In our case, the hardness (H) is plotted rather

than the strength (σ), since hardness and strength are related according to $\sigma \sim cH$,

where c is a constant having a typical value of 1/3 [81, 82].

The scratch hardness can be computed in two methods: calibration method and

direct method. In calibration method, several different scratches at the same loading

rate (typically at a median velocity of the entire scratch speed range) is conducted on

surfaces with know hardness values, for example, fused silica (9.5±0.5 GPa). A

particular width of scratches is targeted for this purpose. In this instance, let us take an

example for the case of the nanolaminate modeled in Figure 3.8. From Figure 3.8,

both the grain boundary and layer pair interfaces will contribute to interfaces that

affect the hardness of the sample if the scratch width is at least 40 nm. So, similarly wide scratches are to be produced on the known surface for comparison. This scratch hardness data on the calibration surface would provide the basis of comparison at all velocity scratches on the unknown material. According to sclerometry technique [105], hardness value (*H*) of a surface is calculated as:

$$H = k \frac{F}{w^2} \tag{3.5}$$

where, *k* is a coefficient of the tip shape, *F* is the constant indenter load and *w* is the resulting scratch width. For the material under study, the comparative hardness equation can be written as [106]:

$$\frac{H_S}{H_R} = \frac{k_S}{k_R} \left(\frac{F_S}{F_R} \right) \left(\frac{w_R}{w_S} \right)^2 \tag{3.6}$$

where, the subscripts *S* and *R* denote sample and reference materials, respectively. If, similar width scratches are conducted on both the reference material and the sample, the tip shape coefficient essentially remains the same and thus, equation (3.6) can be written for this case as:

$$H_S = H_R \left(\frac{F_S}{F_R} \right) \tag{3.7}$$

This is the governing equation for measuring hardness of a sample using calibration method. In the direct method, the scratch hardness is measured independently based on the physical parameters [83, 101, 102, 103] used during the

scratch experiment. The equation for hardness of the sample in this method is given as:

$$F = \frac{\pi}{2} H r^2 \sin^2 \alpha - s r^2 \left\{ \sin \alpha - (\cos^2 \alpha) \ln(\sec \alpha + \tan \alpha) \right\} \quad (3.8)$$

where, F is the normal load of scratch, H is the hardness, r is the radius of the tip, α is the contact angle of the indenter tip with the sample surface and s is the shear stress or surface traction [83]. If the scratch is within the upper hemispherical region of the tip (see Figure 3.6 and 3.7), contact angle α can be found from simple geometrical relationship:

$$\alpha = \sin^{-1}\left(\frac{w}{2r}\right) \quad (3.9)$$

However, it must be noted here that, Tayebi, et al. [101, 102, 103] tried to make the indentation hardness and scratch hardness same in terms of magnitude. Hence, he incorporated the second term in equation (3.8), in addition to the projected area of the leading half of the indenter tip during scratch. However, these two types of hardness values are not really the same because of their associated type of deformations. In the indentation hardness, the volume of deformation is located beneath the tip whereas during scratch, the deformation volume remains in front of the tip along the scratch direction. Mostly because of this reason, a simpler equation is used in the direct method of hardness measurement, by omitting the second term:

$$F = \frac{\pi}{2} H r^2 \sin^2 \alpha \quad (3.10)$$

Substituting equation (3.9) into equation (3.10), scratch hardness H_s is given by:

$$H_s = \frac{8F}{\pi w^2} \tag{3.11}$$

The coefficient $8/\pi$ in front of equation (3.11) is an approximation for the projection of the leading half of the spherical region of the tip. A more exact equation can be developed by using the actual area (instead of the projected area) under the tip based on the scratch width and tip geometry. If the scratch is within the spherical part, then the actual area of the leading half is given by:

$$A = \pi r^2 \sin^{-1}\left(\frac{w}{2r}\right) \left[\frac{1 - \cos\left\{\sin^{-1}\left(\frac{w}{2r}\right)\right\}}{\sin^{-1}\left(\frac{w}{2r}\right)} \right] \tag{3.12}$$

If the scratch is beyond the spherical regime, then the coefficient (which is $8/\pi$ for this instance) will be different and will depend on the tip geometry (as for example, pyramidal for Berkovich, Cube corner tip, and conical for Rockwell conical tip). This is why, it is better to use a generalized expression for equation (3.11) as:

$$H_s = C \frac{F}{w^2} \tag{3.13}$$

where, C is a coefficient that may be calibrated depending on the overall geometry of the tip.

The major controversy in using the direct method of hardness measurement lies within the tip itself. The actual shape of the tip varies from manufacturer to manufacturer and may not have a perfect geometrical shape with a well-defined tip radius or symmetry of revolution [105]. Even the blunt conical tips are found to be

93

parabolic in the axis of revolution. This uncertainty mainly lies with the synthetic

diamond used in the tip and the associated machining technique. For example [107],

the high resolution SEM image of a Berkovich tip reveals lack of smoothness on the

indenter tip (Figure 1 in the reference). Manufacturers' data on the radius of the tip is

not sufficient and is found be quite blunt compared to their advertised values. Also,

the sharp radius of the tip becomes dull very quickly as subsequent experiments are

done with the same tip. In such nano-regime hardness tests, the tip geometry is

extremely important to be accounted for [108] and hence, researchers using

nanoscratch technique mostly use the calibration method [105, 106]. However, in the

present study, strain rate sensitivity of the material is looked for and using exact

coefficient (C in equation (3.13)) would move the fitted curve up or down, without

any change in the slope. Thus, direct measurement method is employed here to find

out rate sensitivity exponents.

3.4 Experimental results

For producing a nano-scratch, the surface of the sample is first cleaned with

alcohol and then a small area is scanned with the cantilever tip to find out possible

surface defects which need to be avoided during the experiment. To reduce the

possible effect of thermal drift due to air currents, the NanoAnalyzer^{TM} machine is

operated with an environmental cover. A number of constant-load scratches are made

with the tip on the test surface using different nominal load values (N_o) of 100μN to 2

mN. The actual normal load (N) is measured for each scratch using a load cell. The

length (h) of the scratches can be made arbitrary. In this study, h is limited to 5

microns for all the scratches. After the scratches are produced, the surface is scanned

for scratch width in the direction perpendicular to the scratches. Only the widths that correspond to both grain boundary and layer pair interface contribution (see Figures 3.8 and 3.9) of that particular sample are taken into account for calculation. The scratches are measured at seven different sections and an average width is computed to provide a statistical standard. Velocity dependent scratches are conducted to induce strain rate effects on hardness and then, the scratch hardness (H_s) of the test material for that particular strain rate is computed using equation (3.13). Figure 3.12 shows scratches with 1 mN indenter force and at 50 nm/sec scratch velocity on Hydroxyapatite ceramic coating on silicon substrate [109], with Ti as buffer layer.
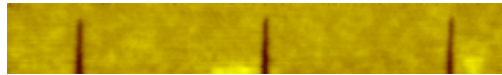
Figure 3.12: Scratches on Hydroxyapatite (4991012 Ti) at 50 nm/sec with 1 mN force
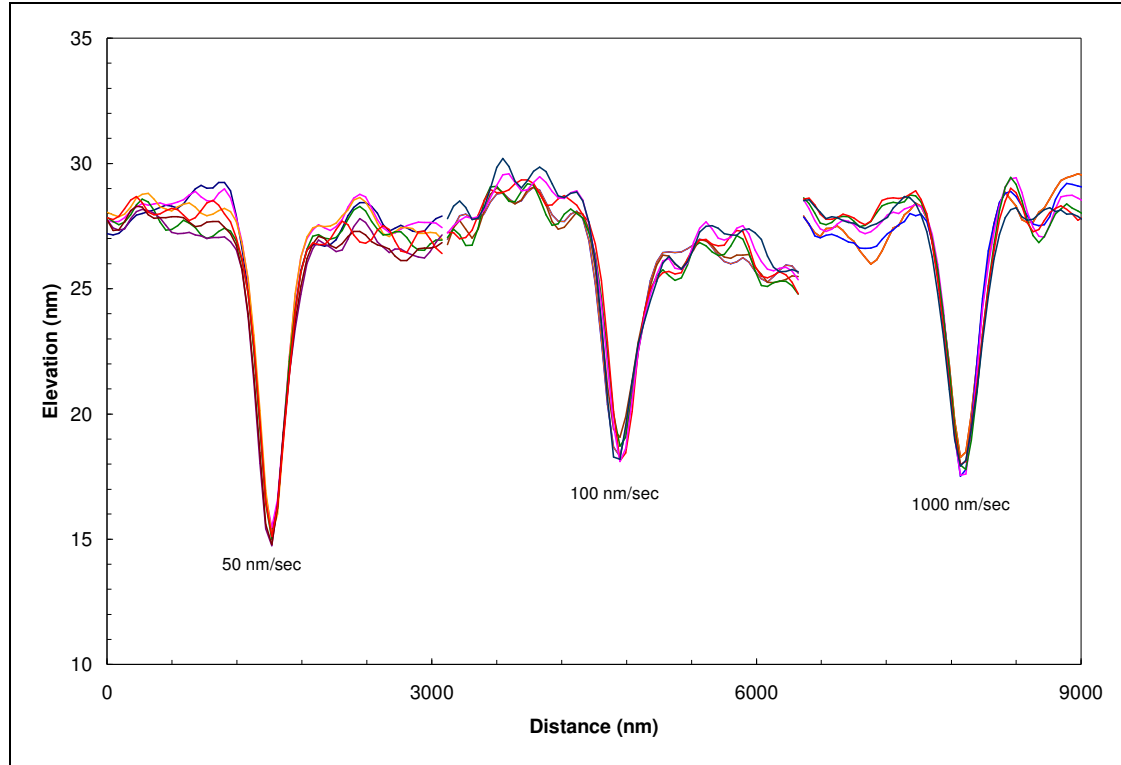
Figure 3.13: Scratch profiles with 1 mN force at different scratch velocities on

Hydroxyapatite (4991012 Ti)

The scratch profiles at three different scratch velocities on the hydroxyapatite

[110] ceramic film are seen in Figure 3.13. As this plot suggests, the width as well as

the height of scratches tends to be larger as the scratch speed decreases. Figure 3.14

plots the hardness value computed for this film at scratch velocities ranging from 10

nm/sec to 5 μm/sec on a log-log plot. Hence, the strain rate sensitivity is obtained as

the slope of the power law fit of the data. The hardness of the film is calculated using

equation 3.13 and for simplicity, C is taken to be 8/π. Prior ramp load testing by Nieh,

et al. [109] at constant scratch speed shows a linear variation of the scratch width with

respect to increasing scratch load. This result suggests that the hydroxyapatite coating

does not strain harden. The strain rate sensitivity exponent found from this experiment is found to be 0.0159 which also shows almost no strain hardening behavior of the coating. Table 3.1 presents the data from this scratch experiment on this artificial bone.

<figure>
y = 2.9855x^{0.0159}

Y-axis: Hardness H$_s$ (GPa), ranging from 1 to 10

X-axis: Strain rate έ (1/sec), ranging from 1.0E-02 to 1.0E+01
</figure>
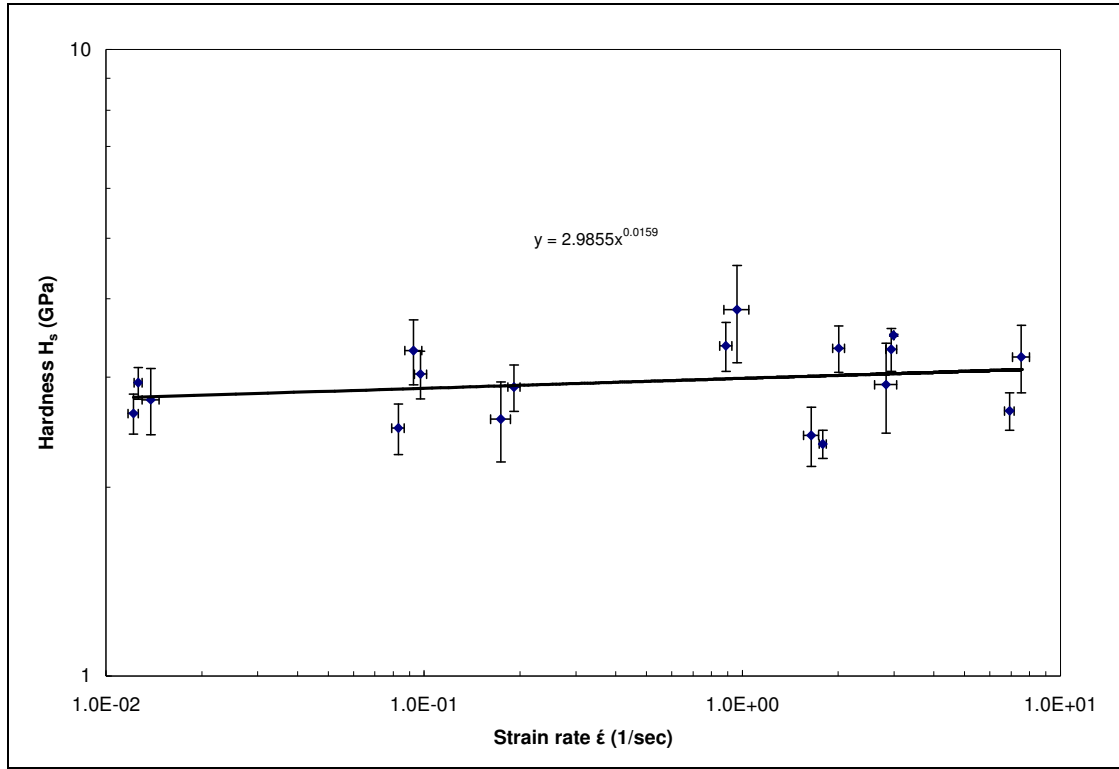
Figure 3.14: Strain rate sensitivity of the Hydroxyapatite coating (4991012 Ti)

Table 3.1: Hardness values calculated for the Hydroxyapatite film (4991012 Ti) as per strain-rates

Nominal Scratch velocity (nm/sec)	Actual Scratch Velocity (nm/sec)	Nominal Load N_o (µN)	Actual Load N (µN)	Width w (nm)	Strain-rate $\dot{\varepsilon}$ (1/sec)	Hardness H_s (GPa)
5000	5000	1000	556.815	665.8±39.36	7.53±0.46	3.23±0.4
			542.21	723.08±24.41	6.92±0.24	2.65±0.18
2000	2000	1000	569.082	710.03±54.75	2.83±0.23	2.92±0.48
			613.6	668.34±1.31	2.99±0.006	3.5±0.01
			603.266	681.11±26.27	2.94±0.11	3.32±0.26
1000	1250	1000	506	623±26.39	2.01±0.085	3.34±0.28
			546	760.7±42.6	1.65±0.09	2.42±0.26
			448	697.92±18.09	1.79±0.05	2.35±0.12
500	625	1000	632.17	654±59.49	0.96±0.086	3.84±0.68
			652.28	704.43±31.45	0.89±0.04	3.36±0.3
100	111.11	1000	381	580.57±24.95	0.19±0.008	2.89±0.25
			408	639.71±42.67	0.17±0.012	2.57±0.38
50	56.82	1000	488	616±39.88	0.092±0.0057	3.31±0.39
			458	686.86±31.63	0.083±0.0038	2.49±0.23
			405	584.57±26.22	0.097±0.0043	3.03±0.26
10	10.10	1000	707	829.71±30.92	0.012±0.0004	2.62±0.19
			576	732.43±45.13	0.014±0.0008	2.76±0.33
			739	801.29±24.36	0.013±0.0004	2.94±0.17

In a similar fashion, scratches are conducted on a Au-Ni nanolaminate sample [87] with a grain size of 6.9 nm and a layer pair spacing of 1.8 nm. Figure 3.15 shows scratches at 100 µm/sec. This experiment was done using the CETR NA-1 whereas the CETR NA-2 was used for testing the hydroxyapatite coating. Figure 3.16 shows the profiles of the scratches at different scratch velocities and Table 3.2 lists scratch parameters at this particular scratch speed. Table 3.3 lists the measured values of strain rates and hardness. Figure 3.17 shows the log-log plot of hardness versus strain rate for 1.5 mN loading [111].
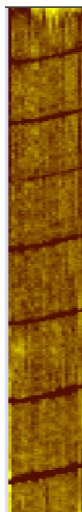
Figure 3.15: Scratches at 100 µm/sec on Au-Ni nanolaminate surface

Table 3.2: Scratch parameters at 100 µm/sec for the sample shown in Figure 3.15

Nominal Load N_o (µN)	Actual Load N (µN)	Width w (nm)
100	534.80	318.60±25.81
200	771.25	459.45±49.52
800	889.46	529.87±58.11
1000	899.95	536.12±53.16
1500	981.16	584.50±91.67
2000	1017.42	606.10±87.40
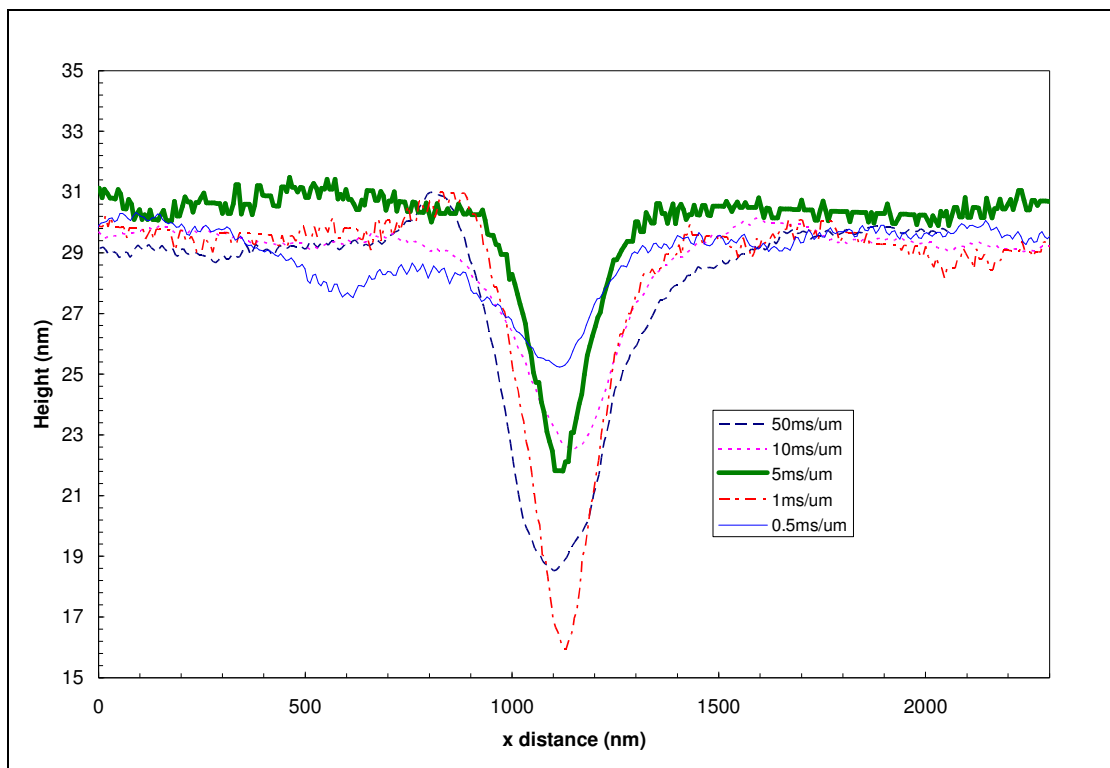
Figure 3.16: Scratch profiles with 1.5 mN force at different scratch velocities on the

Au-Ni sample surface

Table 3.3: Hardness values calculated as per strain-rates for the Au-Ni sample

Scratch Velocity (μm/sec)	Nominal load N_o (μN)	Actual Load N (μN)	Strain-rate $\dot{\varepsilon}$ (1/sec)	Hardness H_s (GPa)
20	1000	923.73	36.34	3.5±0.26
	1500	977.59	34.34	
	2000	1089.57	30.81	
100	1000	899.95	186.53	3.95±0.97
	1500	981.16	171.09	
	2000	1017.42	164.99	
200	800	682.43	491.96	8.97±1.42
	1000	742.87	451.94	
	1500	774.04	433.74	
	2000	901.21	372.53	
1000	800	615.51	2727.25	14.89±3.02
	1000	663.29	2530.69	
	1500	740.70	2266.29	
	2000	771.86	2174.81	
5000	1500	646.26	5194.94	23.33±5.02
	2000	872.78	3846.6	
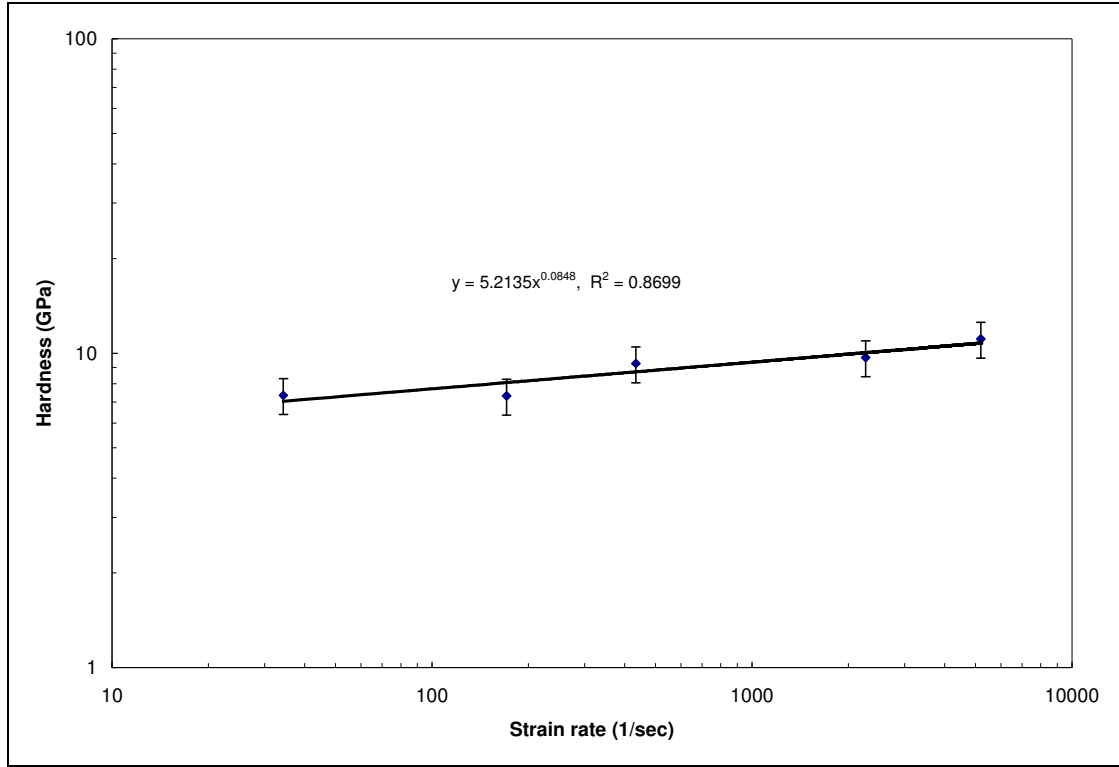
Figure 3.17: Strain rate sensitivity plot of Au-Ni nanolaminate for 1.5 mN load

The strain-rate sensitivity value computed from Figure 3.17 yields a value of *m* equal to 0.0848 [111, 112]. This value is plotted in Figure 3.18 as a function of the grain size, along with the rate sensitivity values for nanocrystalline Cu and Ni found in Gu, et al. [26] and Dao, et al. [19] respectively. The plot of Figure 3.18 indicates that the 6.9 nm grain size measured for the Au-Ni nanocrystalline nanolaminate is consistent with the trend with the results obtained for nanocrystalline face-centered-cubic metals as Ni and Cu. In addition, the predictive equation suggested by Gu, et al. [26] is also plotted here for simulating the trend. The equation given in [26] can be represented by:

$$m = c_1[\ln(c_2\sqrt{d}) - c_3]^{-1} \tag{3.14}$$

where, c_1, c_2 and c_3 are constants depending on the shear modulus of rigidity (G) and burger's vector (b). Here, c_1, c_2 and c_3 are taken to be 0.018, 3.0 and 1.65 respectively [66]. It must be noted here that the range of strain rates covered by nanoscratch experiments are, in general, within region II and may not be comparable with tensile test results obtained from the mentioned references.
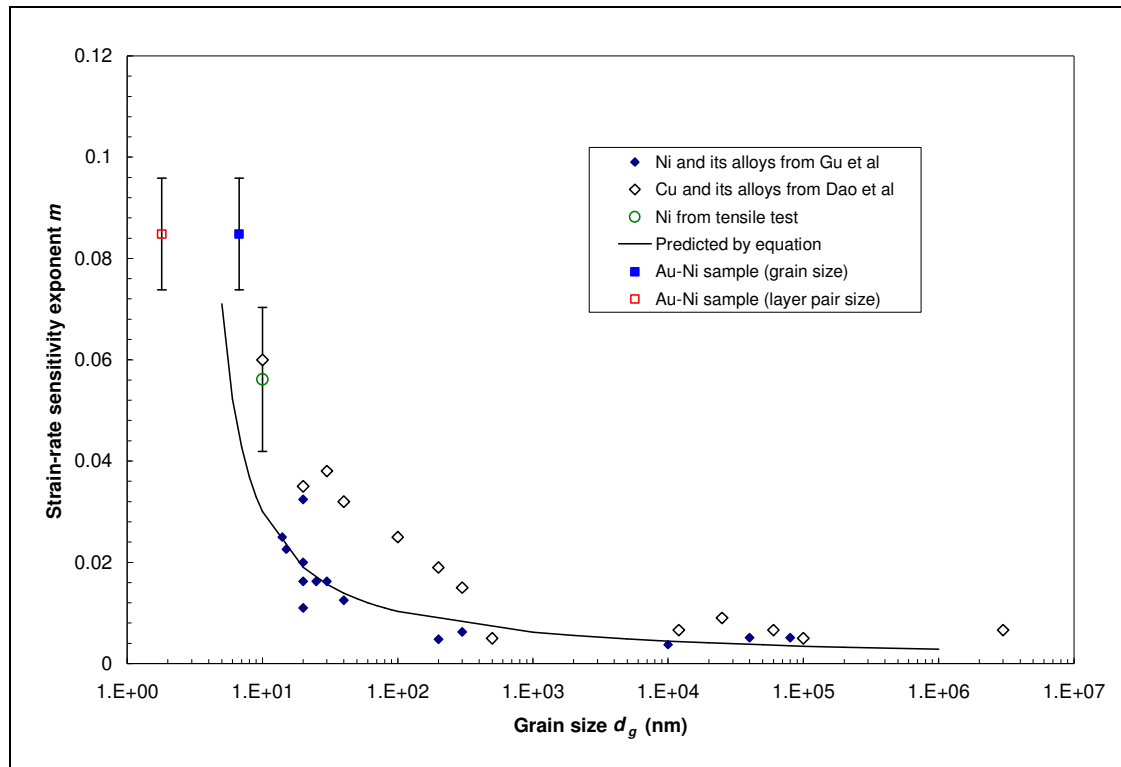
Figure 3.18: Strain rate sensitivity of the Au-Ni sample as a function of grain size and layer pair size

It has already been noted earlier that the characteristic dimension of nanocrystalline nanolaminates can be a sum of the contributions from layer pair interfaces and grain boundary interfaces. An average separation of the interfaces can

be computed as a diameter of a sphere where the spherical volume is equal to the hexagonal volume created by the grain size (d_g) and layer pair interfaces (λ) [113].
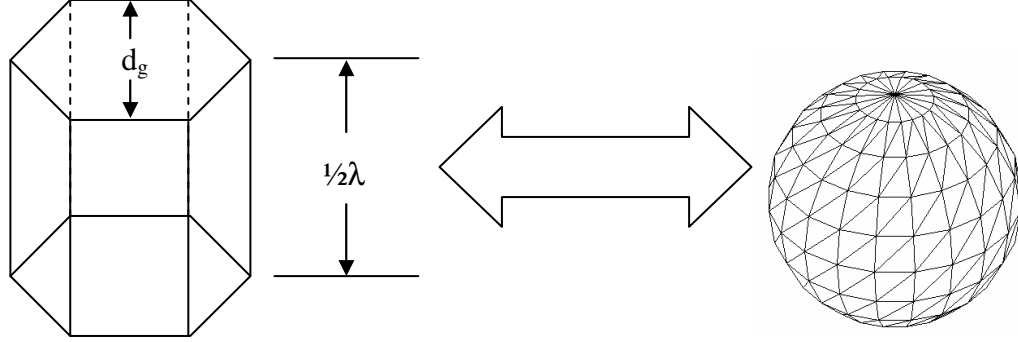
Figure 3.19: Schematic of equating the hexagonal grain volume with a spherical volume to find out the average separation of interfaces

The volume of the hexagonal grain (V_g) with ½λ height as shown in Figure 3.19 is given by:

$$V_g = \frac{\sqrt{3}}{2} d_g{}^2 \times \frac{1}{2} \lambda \qquad (3.15)$$

Equating equation (3.15) with the volume of a sphere with arbitrary diameter d_a yields:

$$\frac{\sqrt{3}}{2} d_g{}^2 \times \frac{1}{2} \lambda = \frac{4}{3} \pi \left(\frac{d_a}{2} \right)^3 \qquad (3.16a)$$

$$\left(\frac{d_a}{2} \right)^3 = \frac{3\sqrt{3}}{16\pi} d_g{}^2 \lambda \qquad (3.16b)$$

$$d_a = \left(\frac{3\sqrt{3}}{2\pi} d_g{}^2 \lambda \right)^{\frac{1}{3}} \qquad (3.16c)$$

Using this expression (equation (3.16c)), the average interfacial separation for the stated Au-Ni sample becomes 4.138 nm. Thus, the hardness value of this sample should be corresponding to this average separation dimension of 4.138 nm, instead of the gain size (6.9 nm) or the layer pair size (1.8 nm). Figure 3.20 is the plot of the rate sensitivity exponent where this consideration has been taken into account.
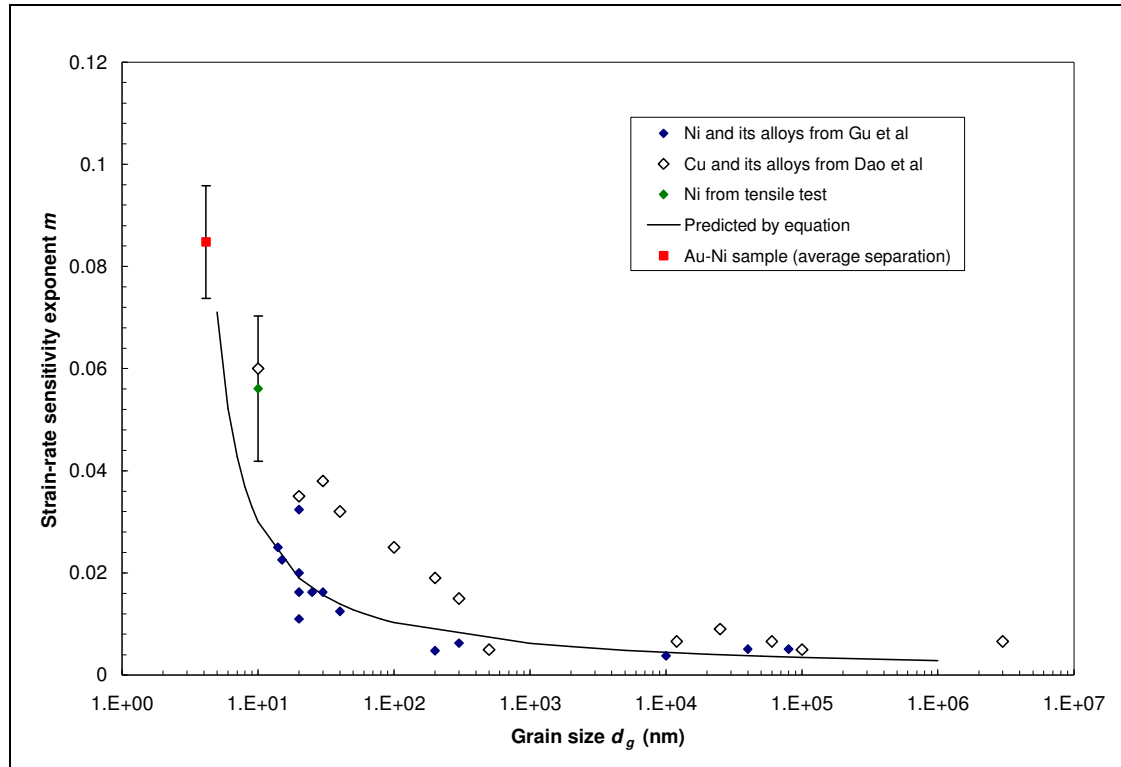
Figure 3.20: Strain rate sensitivity of Au-Ni as a function of average separation length

However, this model is subject to the consideration whether or not the dislocations actually move towards the interfaces between layers. It has been observed [114, 115] that edge dislocations in Au-Ni ncnl move in the direction parallel to the layer interfaces. Also, if the layer interfaces are not coherent, the resultant stress-strain

fields produced by the lattice misfit may not be sufficient to resist dislocation motion [113].

3.5 Summary

Micro-length scratches have been made on the surface of a Au-Ni ncnl and on Hydroxyapatite coating with constant loads at different scratch velocities. The scratches have been measured with the Nanoanalyzer^{TM} tool and software. The hardness of the materials is calculated by measuring the scratch width and the actual load. The strain rates have been measured as the ratio of the scratching velocity to the width of the scratch. The strain rate sensitivity exponent m has been plotted as a function of the grain size and compared with the data available from literature for nc Cu and Ni. It is found that m increases with decreasing value of grain size. A model has been established to predict the rate sensitivity as a function of grain size assuming that Hall-Petch is still valid. Another model has been suggested to find out the average distance of dislocation travel which could be more appropriate in correlation with the rate sensitivity. It must be noted here that strain hardening effects were not considered in this analysis. More points, however, are needed under 10 nm dimension to understand the complete trend of the behavior of strain-rate sensitivity exponent m.

CHAPTER 4

TAPPING MODE ELASTICITY OF NANOCRYSTALLINE THIN FILMS

4.1 Introduction

Structural features, for example grain size and layer pair spacing, can affect the mechanical properties of materials, e.g. strength, amount of plastic deformation, strain rate sensitivity, elasticity, etc. in diverse ways [116, 117]. As grain sizes get smaller and smaller, the dislocation motions get confined before pile-up occurs at the grain boundary, thereby increasing the strength as governed by Hall-Petch relationship dislocation based strengthening. Thus nanocrystalline materials, in general, show higher strength up to a certain limit after which dislocation based strengthening breaks down and softening occurs. For nanocrystalline nanolaminates, competing effects of grain size and laminate size can limit dislocation movement. Furthermore, because the layers of different materials having different lattice parameters try to match up, the resulting phenomenon can be a 'strained layer effect' or 'superlattice' effect [116, 117]. In such a laminate, the lamina having smaller lattice parameter matches up with the lamina having larger lattice parameter. Thereby residual tension is induced on the lamina having smaller lattice parameter and residual compression is induced on the alternate layers having larger lattice parameter. The resulting elastic modulus of the laminate is likely to be different from each of the individual laminas. There can be a significant effect to the presence of a buffer layer and its lattice parameter on the super-lattice effect of the laminated structure.

Au-Ni, Ta-V, Au-Nb and Cu-NiFe nanocrystalline nanolaminates [87, 100, 118] of different grain sizes and layer pair spacing are coated on Silicon 200 wafers,

with a Au or Ti buffer (epitaxial) layer for the Au-Ni nanolaminates and Ta buffer layer for the Ta-V nanolaminates. Elastic modulus of these nanolaminates is measured using Hertzian contact mechanics. The optically flat surfaces of the nanolaminates are point loaded with a highly stiff material (as e.g. Diamond) where surface adhesion effects are neglected.

4.2 Background

Many investigations on methods of non-destructive, elastic modulus measurement methods for thin films are reported now-a-days. Arnold, et al. [119] and Reinstädtler, et al. [120] studied the torsional resonance mode (TRmode) of Atomic Force Acoustic Microscopy (AFAM) method to measure elastic constants of anisotropic materials. In this method, a piezoelectric device is excited using an AC voltage to induce vibrations in the AFM cantilever, while the tip is in contact with the sample surface. Indentation elastic modulus is extracted from the tip-surface interaction assuming Hertzian contact mechanics. DeVecchio et al [121] used a similar technique wherein the deflection of the AFM cantilever was used to determine the localized modulus.

Etienne, et al. [122] studied the elastic modulus of thin films as a function of concentration depth. Vibrating reed measurements, proposed by Whiting, et al. [123], has similarities with the AFM technique. The major difference is in the vibrating reed method, the sample along with the substrate is exposed to piezoelectric vibrations whereas in AFM technique, the probe cantilever is vibrated. Oscillating bubble method [124] is another technique or measuring surface elasticity, however, is only limited to the measurements of liquids.

Perhaps, the most popular technique for measuring modulus is depth sensing

Nanoindentation as represented by the Oliver-Pharr method [125]. In this technique,

the indentation elastic modulus is calculated from the unloading part of the load

penetration-depth curve. Often, loading is done using a three-sided Berkovich tip and

the area function is achieved using indentations on calibration materials with known

hardness and modulus. The major underlying assumption of this technique is to treat

the sample material as homogeneous and isotropic which, in reality, is seldom the

case. Behaviors like material pile-up and sink-in from deformation are not well

understood. Moreover, the directionality of the extracted modulus is not well defined,

since the elastic response of the material comes from three directions of the

indentation displacement (using the Berkovich tip) and from the deformed structure

which lost its original configuration because of the indentation. Linear fitting of the

initial unloading curve [125] using a power-law function is a challenge, since fitting of

different percentage of the unloading curve may produce different results. Very little

indentation depth can be obtained on ceramic materials which have limited ductility

prior to fracture.

4.3 Experimental Technique

UMT NanoAnalyzer^{TM} tool, manufactured by CETR, is equipped with a

ceramic cantilever which has a diamond Berkovich tip mounted on it. As the freely

oscillating tip is brought closer to the material to be examined, the amplitude of

vibration decreases while the frequency of vibration of the tip rises. A frequency

feedback system moves the probe further into the material until a predefined

'frequency shift', i.e. change of the recorded frequency from its free-standing natural

frequency, is achieved [106]. A number of frequency shift curves are produced on the surface to achieve higher repeatability and accuracy. Elastic modulus is measured from these frequency shift curves, with some approximations, usually within 5% of the actual modulus value. Elastic modulus ranging from 50 GPa to about 1000 GPa are reported to be measured using this technique.

The frequency shift curve, as shown in Figure 4.1, has four major parts [126]:

> 1: The tip oscillates freely, without contact with the surface

> 2: The tip oscillates in contact with the viscous top layer present on the surface. This viscous layer is mainly present due to the existence of moisture from the air.
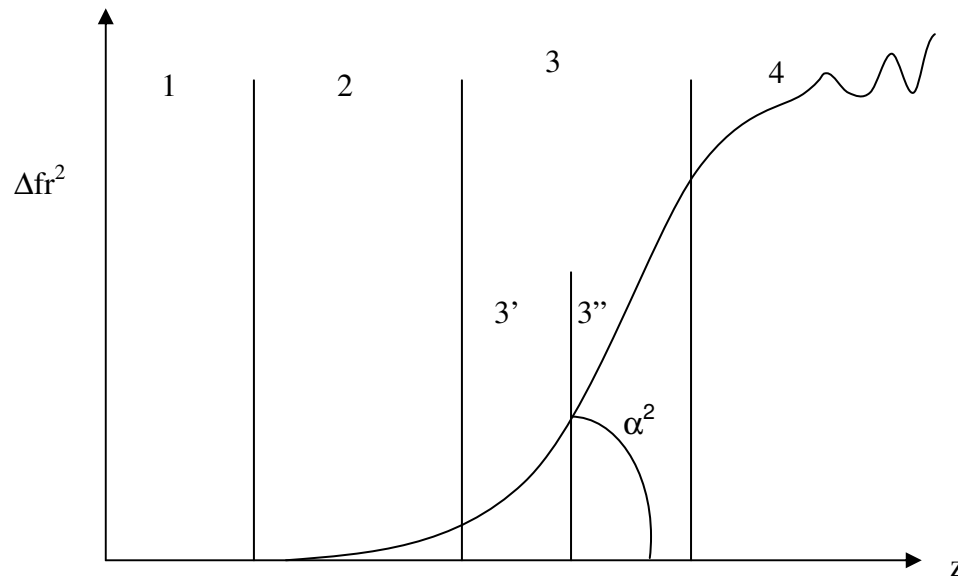
Figure 4.1: A typical frequency shift curve

> 3: This part represents direct interaction with the sample surface. This segment in the frequency shift curve has two sections, namely 3' and 3". Even though the probe tip is fully in contact with the sample surface at 3' section, the

probe base is still far from the surface and hence, there might be some point

during the oscillation while the tip is not in full contact with the surface. This

part occurs immediately after the tip starts to contact the surface passed the

viscous top layer. The tapping mode contact between sample and probe starts

from this section. In 3" part, the amplitude deceases as the probe is further

pushed against the surface, i.e. loading increases. At this point, the surface

atoms and probe tip begin to oscillate without separation. This part is well

recognized in the square of frequency shift curve as a linear regime and

hence, represents the working part of the curve and serves for the

measurement of the elastic properties of the material under study.

4: This segment represents the damping of probe frequency of oscillation,

primarily due to the plastic deformation of the material. Some other

associated effects of damping are surface adhesion due to stiction. In any

case, this portion represents initiation of material failure and is evidenced by

a deviation of frequency shift from the linear regime, usually with a short

horizontal jump in the Figure 4.1 plot. This horizontal feature in the curve

represents that no further frequency shift is achievable with an increase in

loading. This part may be an indication of the cyclic fatigue of the material

under study, and is yet to be developed for research purposes, which could

contribute to the formation of S-N curve in a very short time at frequency

loading of about 10^3 Hz. However, extraction of the S-N curve from this '4'

part of the frequency shift curve is complicated by the fact that the force is

continually increased (as the probe moves into the sample) on the surface

instead of keeping it at a constant value. Being able to record the frequency

shift value at a constant load (thereby, at a constant z height) and use of an

acoustic sensor (to record the sound when the material plastically deforms)

would be helpful in this regard. Nevertheless, use of an acoustic sensor can

be highly demanding in terms of the surrounding environmental condition.

Determining the linear regime of the frequency shift plot in regime 3' of Figure

4.1 can be very demanding analytically as is, especially so for highly compliant and

highly stiff materials. For the case of highly compliant materials, the plot in Figure 4.1

will be almost continuous without the presence of a distinct linear regime. The reason

is the elastic portion is so short that the plastic regime ensues at almost no extra load,

and without a horizontal damping section. Hence the plot from regime 1 to 4 looks

like a polynomial curve without clear-cut segments. Therefore, this tapping mode

technique gives good results for materials having elastic modulus greater than

approximately 50 GPa. On the other hand, the problem associated with highly stiff

materials is that the linear regime is so steep, and has such high slopes, that very few

data points are readily achievable. This is not a technique limitation but rather a

machine resolution limitation, and the real-time performance of the data acquisition. In

almost all cases, the amplitude curve plays a significant role in determining the linear

part, provided that the amplitude to tip radius ratio is of the order or 5% or less.

Typically, an amplitude value of 5 nm works very well for a wide range of materials,

using a diamond Berkovich indenter of about 100 nm radius. Note must be taken that,

this value is not the set amplitude value (which is generally of the order of 100 nm).

Rather, this is the value to which the probe is tuned to before measuring approach

curves. Sharper tips as achieved through the use of cube-corner indenters should better ensure conditions of point contact with flat surfaces.

Since the material starts to deform plastically as the probe is pressed further into the surface, the associated deformation imparts a damping action on the vibration of the probe, which results in a linear (horizontal) decrease in the frequency on the frequency shift plot and the amplitude becomes close to zero. On the other hand, it can be said that plastic deformation in the material starts when amplitude becomes zero. This phenomenon is observed for a wide range of materials and can be used to determine the upper part of the linear regime of the frequency shift. However, in analysis before positioning the right marker, all the produced frequency shift curves should be aligned on the same plot and for that also, the 'zero amplitude' can provide guidance for alignment. Another strategy to position the right marker that bounds the onset of plasticity is to conduct a range of frequency shift experiments from lower frequency to upper frequency and image the area. If, for a particular frequency, an indentation can be observed on the imaged surface, the right marker position should not go beyond the square of that frequency shift input value (See Figure 4.2). For positioning the left marker that bounds the onset of the elastic response, care must be taken to avoid the preceding non-linear section of the curve. One potential way of determining the linear section could be the use of correlation coefficient for a linear fit for a particular position of the left and right markers. Then, the maximum correlation coefficient for the maximum part of the curve would best determine the linear regime. This option, however, is yet to be implemented in the commercially available software.
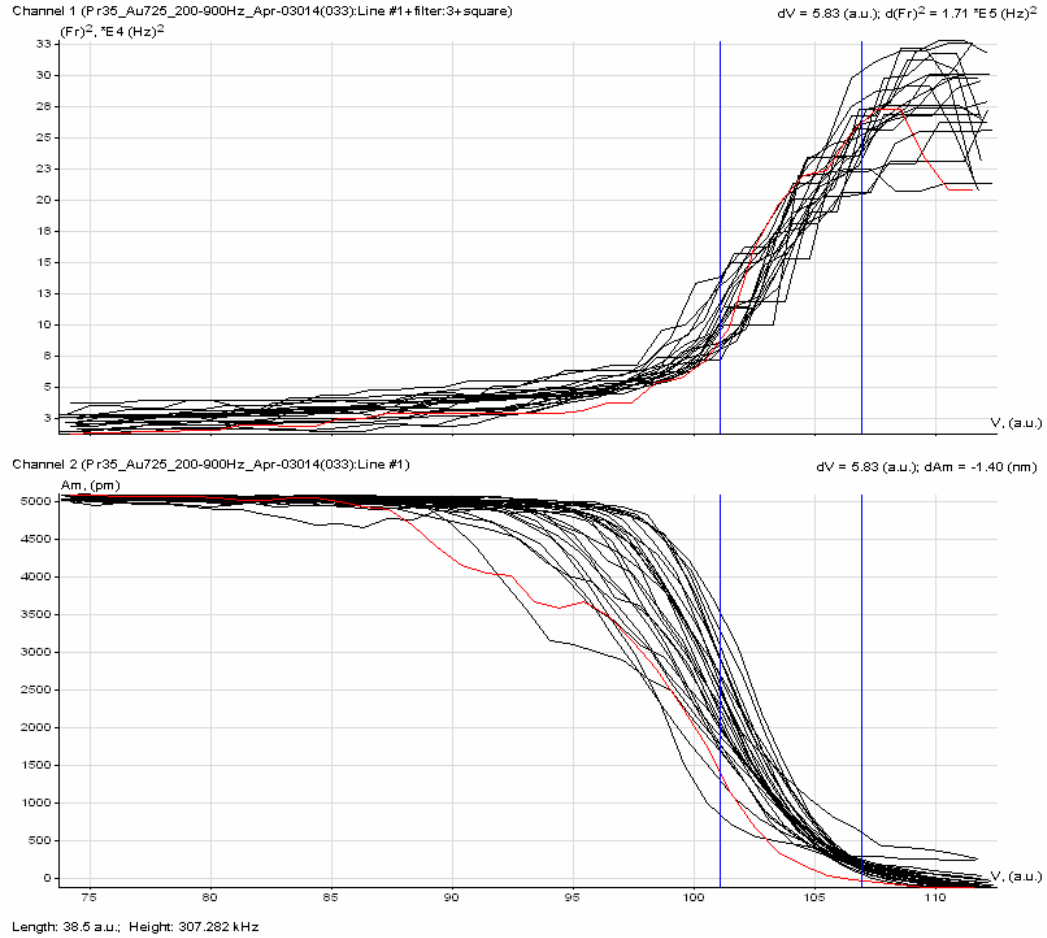
Figure 4.2: Approach curve (on top) and corresponding amplitude (on bottom) are shown for a nanocrystalline Au coating on silicon substrate

Once the linear regime is defined, the slope of the curve can be determined, which can be used to measure the localized elastic modulus. The measurement of elastic modulus can be done in two ways: using calibration method and using analytical method. The following derivation arrives at the final form of the elasticity equation from basic dynamics and Hertz's [127] equation of contact mechanics.

114

The radius 'a' of surface of contact between two spheres of radius R_1 and R_2, when pressed against each other by a constant force (P) was first studied by Hertz [127] and is given by [127]

$$a = \sqrt[3]{\left[\frac{3\pi}{4}\frac{P(K_1+K_2)}{\frac{1}{R_1}+\frac{1}{R_2}}\right]} \tag{4.1}$$

where, K_1 and K_2 are related to the elastic properties (Young's modulus E_1 and E_2) and Poisson ration (v) of the spheres as given by

$$K_1 = \frac{1-v_1^2}{\pi E_1^2} \quad \text{and} \quad K_2 = \frac{1-v_2^2}{\pi E_2^2}$$

For contact between a sphere ($R_1=R$) and a flat surface ($R_2 \approx \infty$), the equation (4.1) reduces to

$$a = \sqrt[3]{\frac{3\pi}{4}P\left(\frac{1-v_1^2}{\pi E_1}+\frac{1-v_2^2}{\pi E_2}\right)R} \tag{4.2}$$

The reduced elastic modulus (E^*) is given by

$$\frac{1}{E^*} = \frac{1-v_1^2}{E_1}+\frac{1-v_2^2}{E_2} \tag{4.3}$$

By substituting equation (4.3) into equation (4.2)

$$a = \sqrt[3]{\frac{3P}{4E^*}R} \tag{4.4}$$

(a)　　　　　　　　　　　　　　　　　(b)
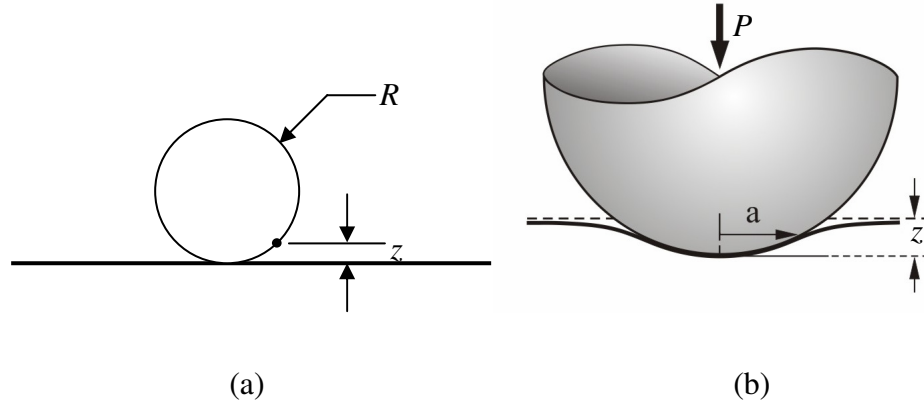
Figure 4.3: Contact between a sphere and a flat surface on the application of load P

For a point at a distance (z) from the plane of the surface of contact (Figure 4.3a) that is now within the surface of contact (after application of normal load P), z is given by

$$z = \frac{a^2}{R} \tag{4.5a}$$

$$a = \sqrt{Rz} \tag{4.5b}$$

By substituting equation (4.4) into equation (5b), we get

$$\sqrt{Rz} = \sqrt[3]{\frac{3P}{4E^*}} R \tag{4.6a}$$

$$z = \left(\frac{3P}{4E^*}\right)^{2/3} \left(\frac{1}{R}\right)^{1/3} \tag{4.6b}$$

The dynamic equivalent of the probe cantilever with a tip can be represented with a spring-mass system [128], as shown in Figure 4.4. For a displacement x, the equation of motion of this system is given by:

$$m\ddot{x} + k_c x = 0 \tag{4.7a}$$

116

$$\ddot{x} + \frac{k_c}{m} x = 0 \tag{4.7b}$$

where, the spring constant of the cantilever k_c is given by:

$$k_c = \frac{3EI}{L^3} \tag{4.7c}$$
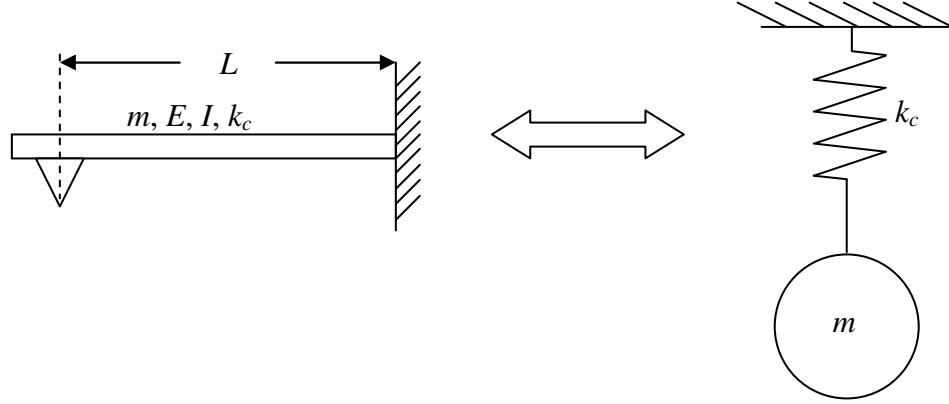
Figure 4.4: Cantilever with bending stiffness k_c and mass m is represented with a

spring-mass system

So the natural oscillation frequency of the system is given by:

$$\omega_n = \sqrt{\frac{k_c}{m}} = 2\pi f_0 \tag{4.8a}$$

$$m = \frac{k_c}{(2\pi f_0)^2} \tag{4.8b}$$
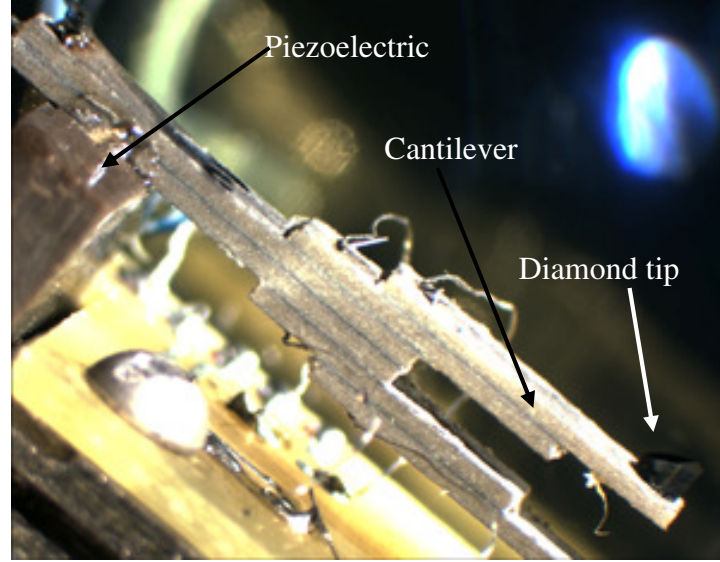
Figure 4.5: Actual probe as imaged by an optical microscope

An actual probe-cantilever system with diamond Berkovich tip is shown in Figure 4.5. When the probe is in contact with the surface, the dynamic system can be modeled [128] as shown in Figure 4.6. For a displacement x, the equation of motion of the system is given by:

$$m\ddot{x} + (k_c + k_s)x = 0 \tag{4.9a}$$

$$\ddot{x} + \left(\frac{k_c + k_s}{m}\right)x = 0 \tag{4.9b}$$
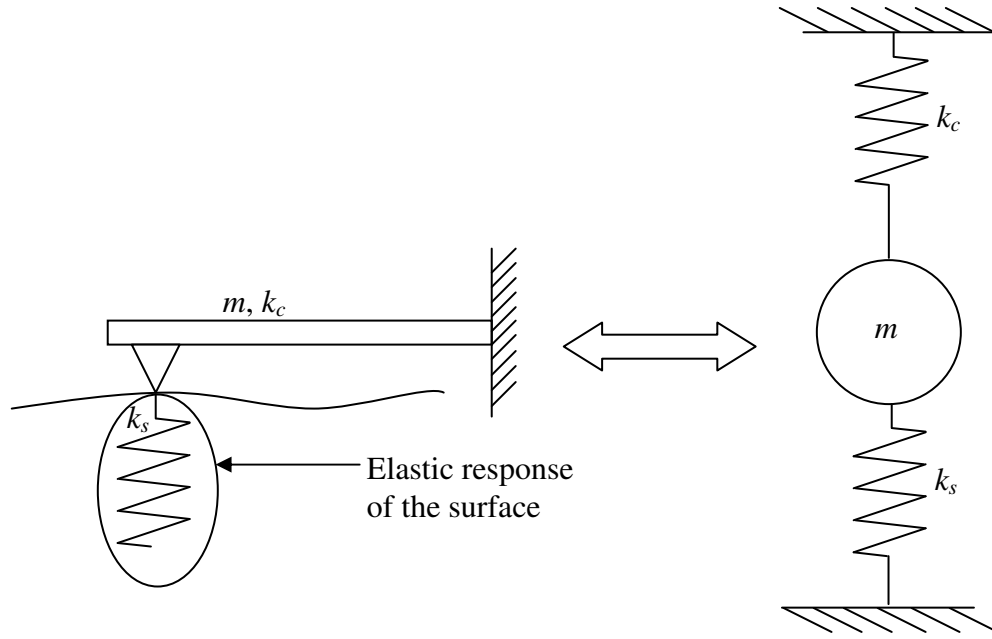
Figure 4.6: Probe in contact with a surface having a stiffness of k_s

Thus, the frequency of oscillation of the system described by equation (4.9b) is given by:

$$2\pi f = \sqrt{\frac{k_c + k_s}{m}} \tag{4.10a}$$

$$(2\pi f)^2 = \frac{k_c + k_s}{m} \tag{4.10b}$$

Replacing m by substituting equation (4.8b) into equation (4.10b) yields:

$$(2\pi f)^2 = \frac{k_c + k_s}{k_c}(2\pi f_0)^2 \tag{4.11}$$

Solving for f yields:

$$f = f_0\left(\sqrt{1 + \frac{k_s}{k_c}}\right) \tag{4.12}$$

The change of frequency (or, frequency shift) from natural oscillation (f_0) to that after in contact with the surface (f) is given by:

$$\Delta f = f - f_0 \tag{4.13}$$

Substituting equation (4.12) into equation (4.13) yields:

$$\Delta f = f_0 \left(\sqrt{1 + \frac{k_s}{k_c}} - 1 \right) \tag{4.14}$$

Using Taylor's expansion (with first two terms only) on equation (4.14) gives:

$$\Delta f = f_0 \left(\frac{k_s}{2k_c} \right) \tag{4.15}$$

Now, the stiffness of the surface k_s can be modeled as:

$$k_s = \frac{\partial P}{\partial z} \tag{4.16}$$

From equation (4.6b) we find that the load P equals:

$$P = \frac{4}{3} \sqrt{R} E^* z^{\frac{3}{2}} \tag{4.17}$$

Substituting equation (4.17) into equation (4.16):

$$k_s = \frac{\partial P}{\partial z} = 2\sqrt{R} E^* \sqrt{z} \tag{4.18}$$

Putting the expression of k_s from equation (4.18) into equation (4.15) yields an expression of the frequency shift:

$$\Delta f = \frac{f_0 \sqrt{R}}{k_c} E^* \sqrt{z} \qquad (4.19)$$

Taking squares on both sides of equation (4.19) gives:

$$\left(\Delta f\right)^2 = \alpha^2 z \qquad (4.20a)$$

$$\alpha^2 = \frac{\left(\Delta f\right)^2}{z} \qquad (4.20b)$$

where, α^2 is the slope of the square of frequency shift versus probe displacement plot and is given by:

$$\alpha = \frac{f_0 \sqrt{R}}{k_c} E^* \qquad (4.21)$$

Equation (4.21) is a simplified formula derived using only first two terms of the Taylor's expression in equation (4.14). This simplified formula is usually not used because of the error associated with it. A third term in the Taylor's expression gives better accuracy and the formula for α is given by:

$$\alpha = \frac{f_0 \sqrt{R}}{k_c} E^* \left[1 - \frac{1}{2} \left(\sqrt{R} E^* \right) \frac{\sqrt{z}}{k_c} \right] \qquad (4.22a)$$

$$\alpha = \frac{f_0 \sqrt{R}}{k_c} E^* \frac{1}{\sqrt{1 + \left(\sqrt{R} E^* \right) \frac{\sqrt{z}}{k_c}}} \qquad (4.22b)$$

The formula provided by the manufacturer (CETR) simplifies equation (4.22b) by introducing a constant *C* given by:

$$C = \frac{\sqrt{z}}{k_c} \tag{4.22c}$$

Hence, equation (4.22b) is simplified to:

$$\alpha = \frac{f_0\sqrt{R}}{k_c} E^* \frac{1}{\sqrt{1+C\sqrt{R}E^*}} \tag{4.23}$$

Solving for the reduced modulus (E^*) yields (only positive sign is taken into consideration):

$$E^* = \frac{C\sqrt{R} + \sqrt{(C\sqrt{R})^2 + 4\left(\dfrac{f_0\sqrt{R}}{\alpha k_c}\right)^2}}{2\left(\dfrac{f_0\sqrt{R}}{\alpha k_c}\right)^2} \tag{4.24}$$

Using this formula of equation (4.24), the reduced elastic modulus (E^*) of sample can be derived from the slope of frequency shift versus probe displacement plot, provided that the values of free standing frequency of oscillation of the cantilever f_0, cantilever bending stiffness k_c and tip radius R is exactly known. However, in reality, these values can only be determined with limited accuracy. Hence, calibration method for measurement of elastic modulus is more frequently put into use. In the calibration method, α values are measured for a number of materials with known elastic modulus, for example, materials with standard values are used such as fused silica, gold, nickel, sapphire and tungsten. Those α values from the standards are plotted as a function of the corresponding modulus values which can then be fitted with a power law relationship, as shown in Figure 4.7.
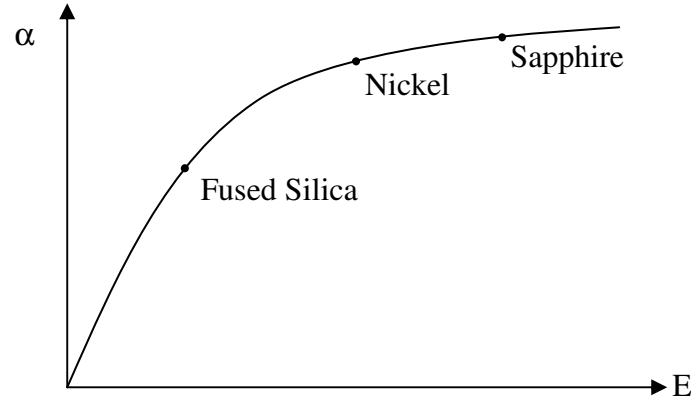
Figure 4.7: General trend of α to elastic modulus

The greater the number of calibration materials, the better the trend line fit will be, and the better the accurate calculation of the modulus of unknown sample will be. Once the trend line in Figure 4.7 is fully established, the modulus of unknown sample is calculated using the power law fit:

$$\alpha = a(E^*)^n \tag{4.25}$$

where, a is a constant. From equation (4.22), it is clearly observed that this is a quadratic equation of the reduced modulus (E^*) and hence, a power law fit of α versus E^* would yield a value of 0.5 for the exponent n for the ideal case. Equation (4.25) is derived from equation (4.22) as the f_0, k_c and R values remain same for measurements with the same probe for the analytic derivation.

The Hertz equation (equation 4.4) is reported [129, 130, 131] to hold true for large loads and sometimes overestimates the elastic modulus of the sample for low loads because the effect of surface energy at such small loads is neglected, assuming no contact surface at zero load. In the small load regime, Johnson-Kendall-Roberts

(JKR) model is reported [130] to be a better estimation of the contact radius, which is given by:

$$a^3 = \frac{3R}{4E^*}\left(P + 3\gamma\pi R + \sqrt{6\gamma\pi RP + (3\gamma\pi R)^2}\right) \tag{4.26}$$

where, γ is the surface energy term of the sample. Assuming $a = \sqrt{Rz}$ (from equation (4.5b)) and solving for $\dfrac{\partial P}{\partial z}$ (from equation (4.18)) yields the sample surface stiffness k_s:

$$k_s = \frac{\partial P}{\partial z} = \frac{2E^*\sqrt{Rz}\left(\sqrt{6\gamma\pi RP + (3\gamma\pi R)^2}\right)}{3\gamma\pi R + \sqrt{6\gamma\pi RP + (3\gamma\pi R)^2}} \tag{4.27}$$

The frequency shift is then given by:

$$\Delta f = \frac{f_0}{2k_c}k_s = \frac{f_0}{k_c}\frac{E^*\sqrt{Rz}\left(\sqrt{6\gamma\pi RP + (3\gamma\pi R)^2}\right)}{3\gamma\pi R + \sqrt{6\gamma\pi RP + (3\gamma\pi R)^2}} \tag{4.28}$$

This equation can be used to determine the elastic modulus of soft materials and even conceivably liquids, with the tapping mode frequency shift in which materials surface energy plays a significant role resulting in the change of contact area from the Hertz model. A similar model can be determined [132] from the Derjaguin-Muller-Toporov (DMT) equation:

$$a^3 = \frac{3R}{4E^*}(P + 2\gamma\pi R) \tag{4.29}$$

It must be noted here that these equations (equation (4.28) and (4.29)) are derived based on only the first two terms of the Taylors expression of equation (4.14). For a higher accuracy model, more terms need to be included in the derivation.

4.4 Results

A calibration curve was established for α versus E^* with several known materials including polycarbonate, fused silica, Au, Ni and sapphire [34, 40, 133, 134, 135, 136]. Table 4.1 represents the elastic modulus and corresponding reduced elastic modulus for all the calibration samples. In these calculations, the reduced elastic modulus of diamond tip is back calculated from Ta and V data and is taken to be 0.00075. Even though there are reports of Diamond modulus being 1140 GPa and corresponding Poisson ratio being 0.07 [126], these values are not consistent and hence, back calculation was necessary to find the appropriate value. Figure 4.8 shows the plot for the experimental calibration curve and the analytic equations (4.21) and (4.24). Once the calibration curve was formed, reduced elastic modulus of the unknown samples were calculated from the curve. It is worth noting that, all the calculations were done assuming Hertzian contact mechanics wherein the effect of adhesion was neglected. Even though the work of adhesion can play a significant role in low load contacts, we see from the calibration plot that this error may not be too high, i.e., the correlation coefficient for the power law fit is above 95%. Using this calibration curve, the modulus of sputter deposited nanocrystalline nanolaminate Au-Ni and Ta-V [87, 100, 118] samples were determined from corresponding frequency shift experiments.

Instead of using calibration, the reduced elastic modulus can also be calculated analytically from α values using equation 4.24, with values of k_c and R. There is no need to assume natural oscillation frequency f_0, since it is available from the tuning of the probe at the beginning of a tapping test and is fairly constant. The modulus values of calibration materials can help in assuming k_c and R. Figure 4.8 plots the experimental calibration curve along with the fits using different analytic equations (i.e. equation (4.21) and (4.4)). The reduced elastic modulus of the samples are plotted in Figure 4.9 with the experimental calibration curve. Table 4.2 represents the frequency shift data of the calibration materials and Table 4.3 represents all the data of the samples from the experimental calibration curve.

Table 4.1: Elastic modulus of calibration materials

Sample	Elastic modulus E (GPa)	Poisson ratio ν	Reference	Reduced elastic modulus E^* (GPa)
Polycarbonate	3±0.1	0.37		3.47
Sapphire	495±10	0.27	[40, 135]	381.25
Silicon(100)	130.13±5	0.27	[34, 40]	126.99
Fused Silica	72±1	0.17		70.24
Fused Quartz	72±1	0.17		70.24
Ta(110)	192.3±5	0.34	[40,134]	186.95
V(110)	124.7±5	0.37	[40,133]	130.35
Ag(111)	120.51±5	0.37	[35, 40]	126.39
Ni(111)	305±10	0.31	[40]	269.28
Hydroxyapatite	100±5	0.27	[109]	93.02

Determining the actual elastic modulus may vary a bit depending on the assumption of the Poisson ratio, especially for materials having Poisson ratio from 0.3 to 0.5. Figure 4.10 shows a generic relationship between actual elastic modulus and reduced elastic modulus depending on various Poisson ratios.

In determining the Poisson ratio of the sample (nanolaminates), a rule of mixture formula is used:

$$\upsilon = V_1\upsilon_1 + V_2\upsilon_2 \qquad (4.30)$$

where, V_1 and V_2 are the volume fractions (generally 0.5 each) and ν_1 and ν_2 are the Poisson ratios of the constituents of the sample.
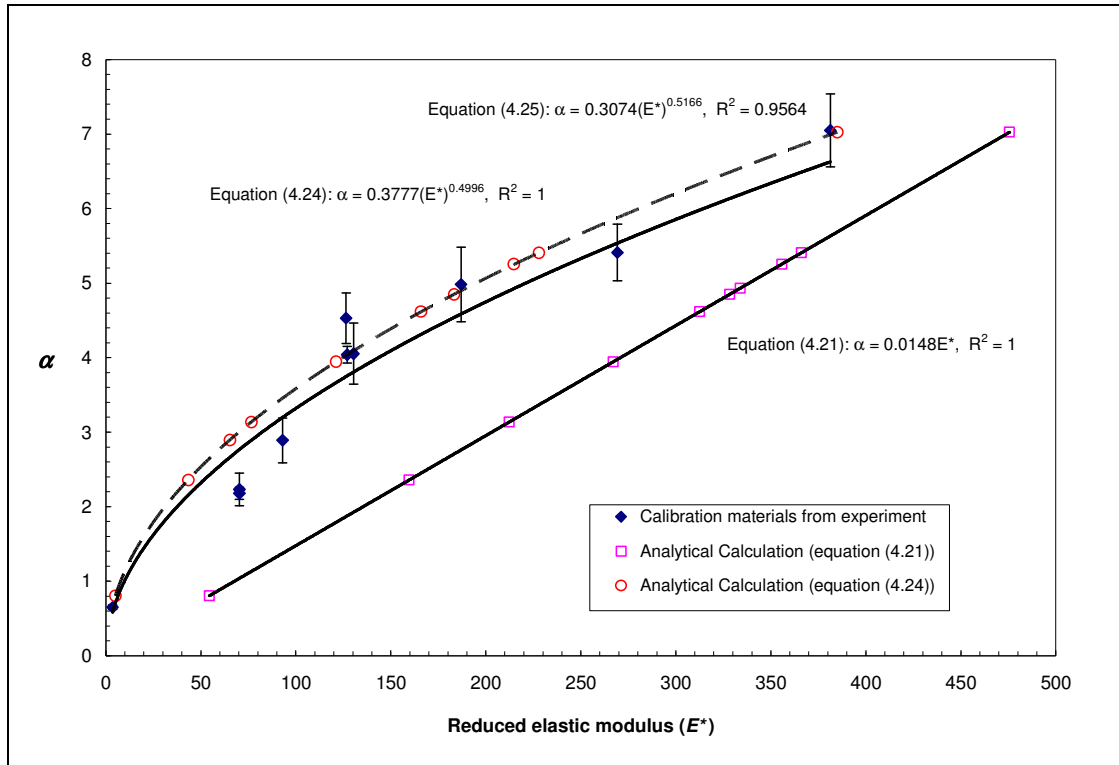
Figure 4.8: Power law fit for the known samples, to obtain the calibration curve
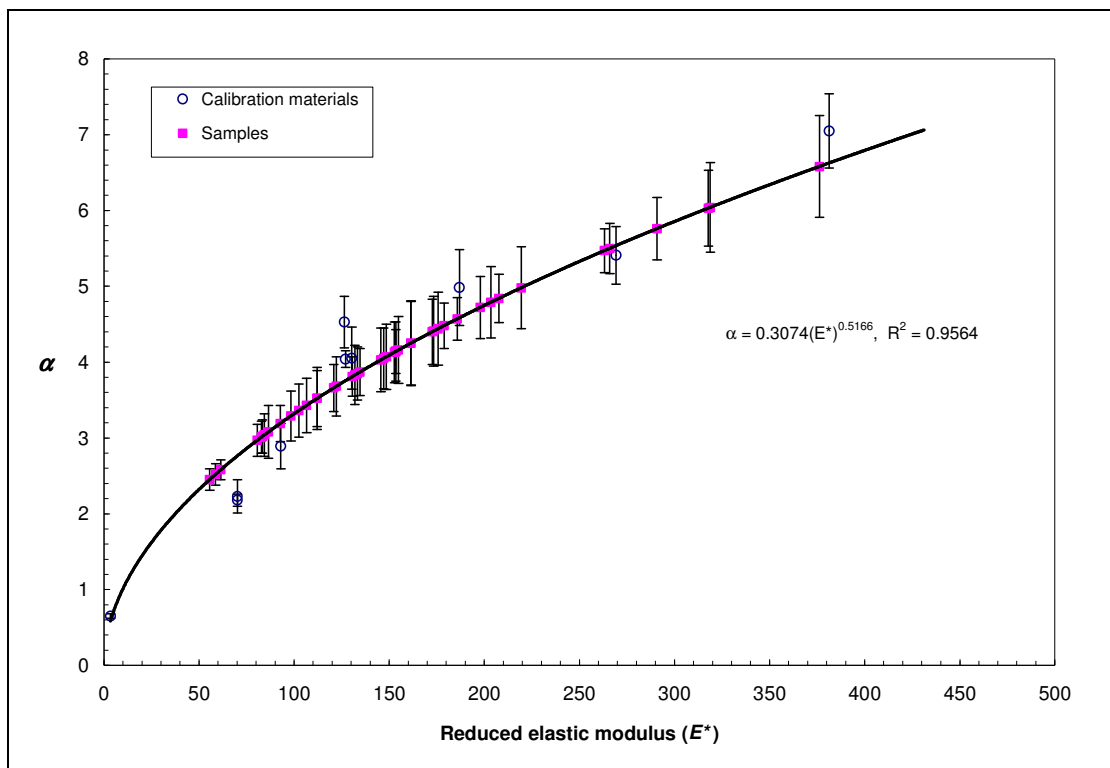
Figure 4.9: Reduced elastic modulus of samples determined from calibration curve
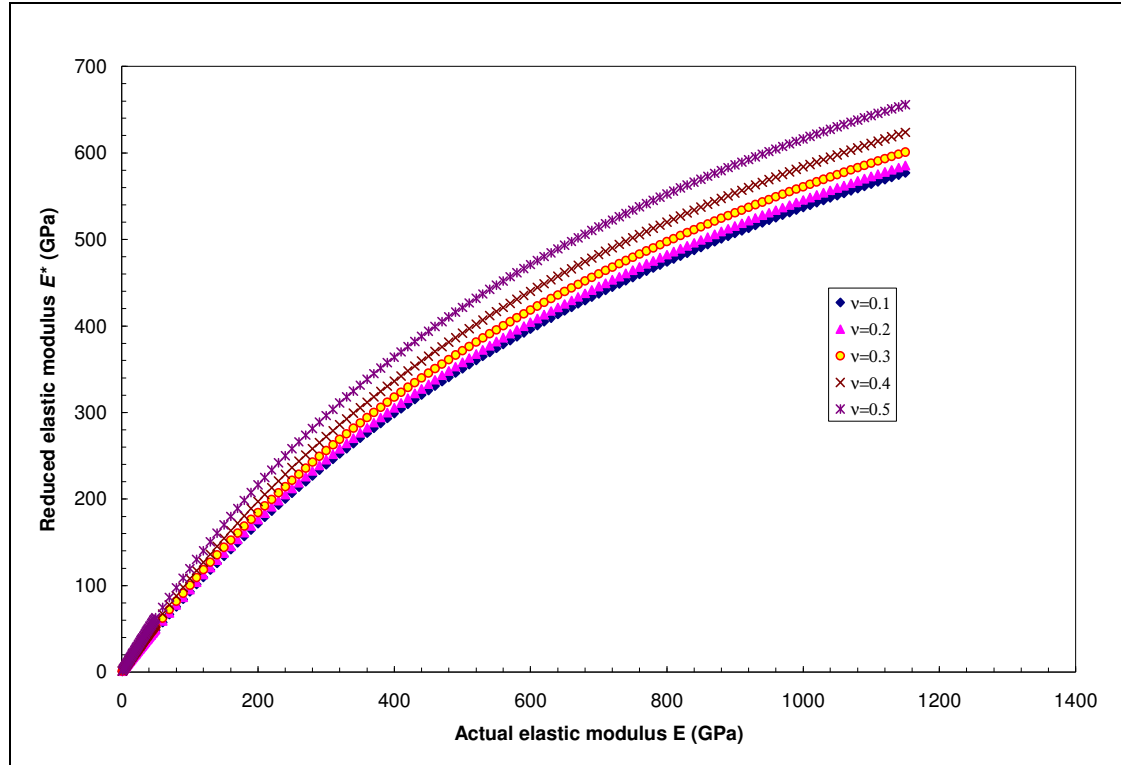
Figure 4.10: Variation of reduced elastic modulus with respect to actual elastic

modulus, as a function of Poisson ratio

Table 4.2: Frequency shift data of calibration materials with corresponding elastic

modulus

Sample	Poisson ratio ν	Actual modulus E (GPa)	Reduced modulus E^* (GPa)	Slope α
Polycarbonate	0.37	3.0	3.47	0.65±0.03
Sapphire	0.3	495	381.25	7.05±0.49
Silicon(100)	0.27	130.13	126.99	4.04±0.11
Fused Silica	0.17	72	70.24	2.18±0.08
Fused Quartz	0.17	72	70.24	2.23±0.22
Ta(110)	0.34	192.3	186.95	4.98±0.5
V(110)	0.37	124.7	130.35	4.05±0.41
Ag(111)	0.37	120.51	126.39	4.53±0.34
Ni(111)	0.31	305	269.28	5.41±0.38
Hydroxyapatite	0.27	100	93.02	2.89±0.3

Table 4.3: Calculation of sample modulus from calibration curve

Sample	Layer pair spacing λ (nm)	Poisson ratio ν	Slope α	Calculation from calibration curve	
				Reduced modulus E^* (GPa)	Actual modulus E (GPa)
Au-Ni	0.8	0.365	4.4±0.43	172.67	171.93
Au-Ni	4.5	0.365	3.68±0.39	122.18	116.59
Au-Ni	1.8	0.365	4.03±0.42	145.67	141.75
Au-Ni	2.5	0.365	4.16±0.44	154.91	151.92
Au-Ni	1.2	0.365	4.07±0.43	148.48	144.83
Au-Ni	2.6	0.365	4.13±0.40	152.75	149.53
Au-Ni	1.6	0.365	4.14±0.39	153.47	150.32
Au-Ni	0.9	0.365	4.05±0.40	147.08	143.29
Au-Ni	3.4	0.365	3.36±0.35	102.45	96.19
Au-Ni	1.2	0.365	4.44±0.48	175.72	175.43
Au-Ni	1.9	0.365	4.25±0.55	161.46	159.23
Au-Ni	1.6	0.365	4.57±0.28	185.82	187.14
Au-Ni	8.9	0.365	4.79±0.47	203.52	208.19
Au-Ni	2.0	0.365	3.19±0.24	92.66	86.31
Au-Ni	0.8	0.365	3.02±0.22	83.34	77.05
Au-Ni	2.9	0.365	3.52±0.41	112.11	106.09
Au-Nb	1.6	0.42	2.97±0.21	80.69	70.73
Au-Nb	3.2	0.42	4.48±0.30	178.80	170.07
Cu-NiFe	6.7	0.32	5.76±0.41	290.83	333.88
Cu-NiFe	4	0.32	4.84±0.32	207.66	220.78
Nb		0.4	4.14±0.29	153.47	145.68
Au-Nb	0.46	0.42	3.66±0.31	120.90	109.50
Ta-V	8.07	0.355	6.04±0.59	318.82	366.21
Ta-V	3.14	0.355	4.41±0.46	173.43	174.24
Ta-V	8.07	0.355	5.47±0.29	263.16	286.55
Ta-V	3.14	0.355	3.85±0.35	133.34	129.49

Figure 4.11 and 4.12 show the plots of the relationship between elastic modulus and layer pair spacing. Even though the modulus is plotted against the layer pair spacing, it is better to correlate the change of elastic modulus with the amount of elastic strain energy in the ncnl thin film during their deposition process [87]. Different amount of strain energy put into the system could result is different amount

of twinning or different type of grain boundary structure within the same grain and/or layer pair size. Probably that is why, materials with same layer structure show different elastic properties. From these Figures 4.11 and 4.12, it is apparent that there exists a general trend that with decreasing layer pair spacing, the elastic modulus decreases. In comparison for in-plane elastic moduli measurments [100] an increase is found as the layer pair spacing decreases. The decrease in elastic modulus correlates with an increase in the interface spacing for Au-Ni when tension is present [116]. This is seen for inter-planer spacings normal to the film surface [114, 115] for layer pairs between 1 to 4 nm. Thus the film modulus normal to its surface should decrease between 1 to 3 nm.
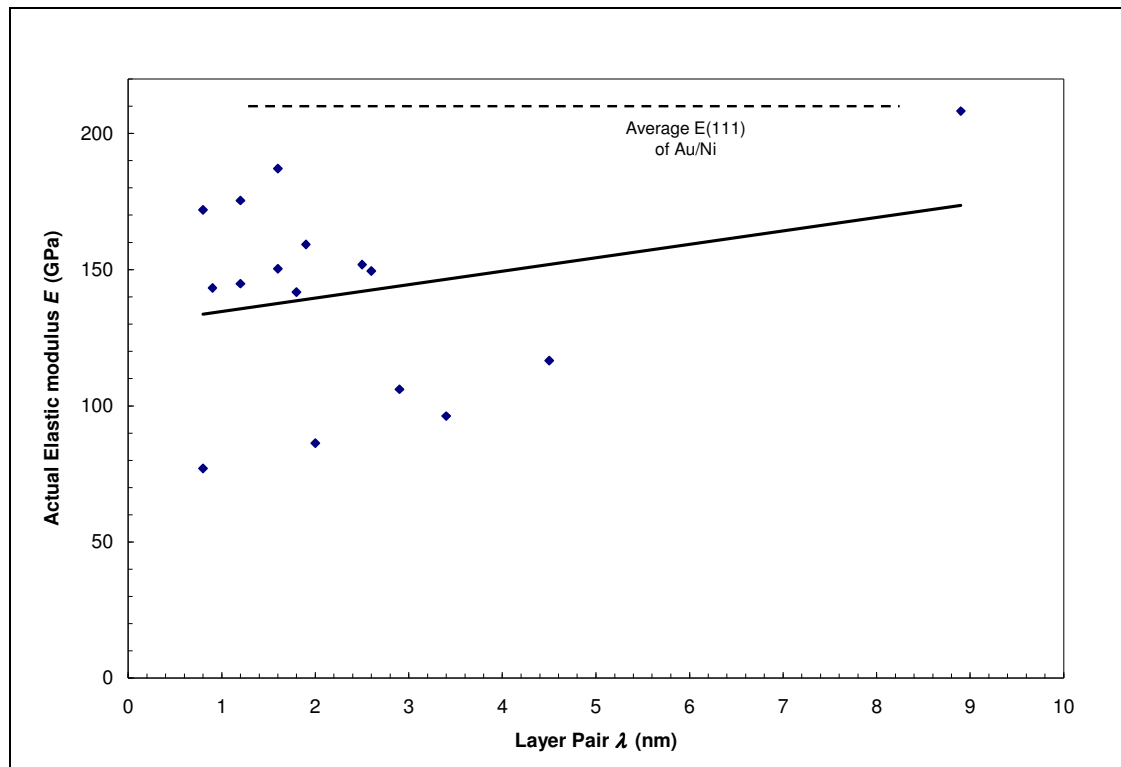
Figure 4.11: Elastic modulus of Au-Ni nanolaminates
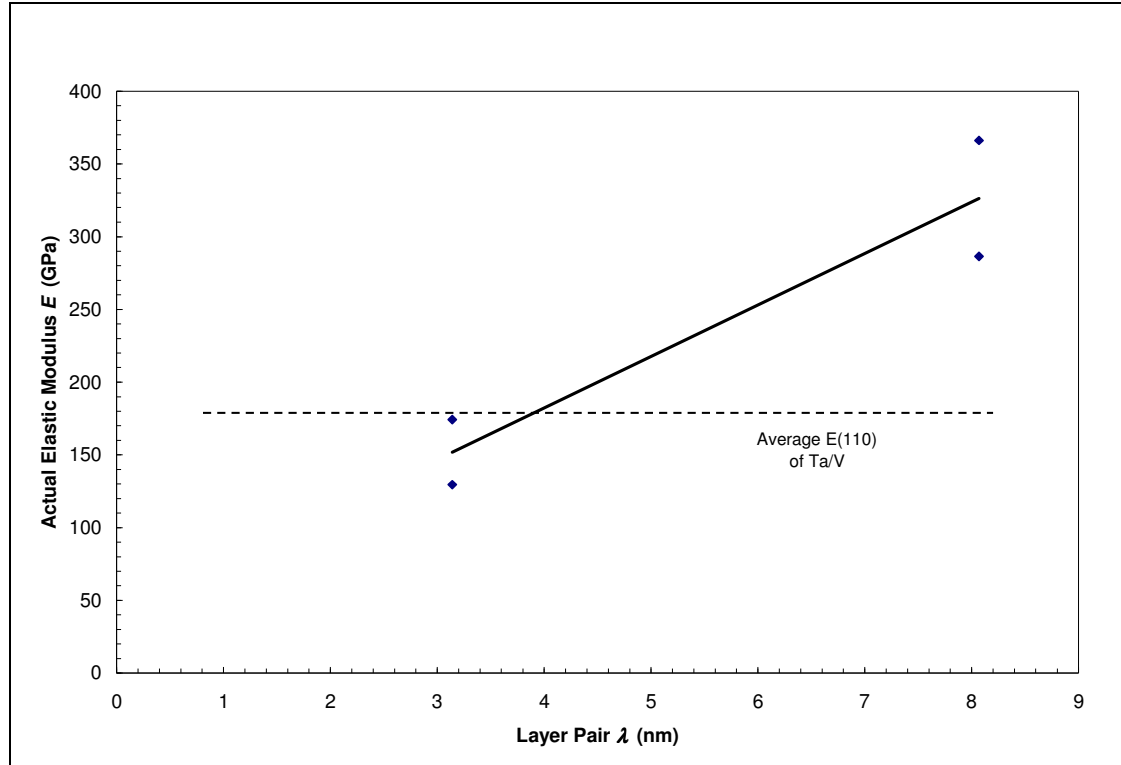
Figure 4.12: Elastic modulus of Ta-V nanolaminates

4.5 Discussion

Nanolaminate materials are reported [87, 137] to have super-lattice effects, where layers have an alternate distribution of residual tension and compression. The materials tested here are nanocrystalline nanolaminates and are highly non-homogeneous and anisotropic, because of the structure they have. Conventional analysis of nano-indentation experiments assumes the material to be homogenous and isotropic to compute the elastic modulus. Thus, such techniques have limitations to assess this kind of nanolaminate materials. Tapping mode frequency shift measurement of thin films is a technique that has been useful for several decades and the basics of that technique have been discussed here. However, this technique

assumes Hertzian contact and thereby neglects the effects of pull force or surface

adhesion in forming the analytical model. This results in some error in calculation of

the elastic modulus of the materials. To eliminate that, both JKR and DMT contact

mechanics have been used to develop a similar model, to determine the modulus from

frequency shift experiments. To have a measure of the surface adhesion, nano-

indentation can be done on the sample to make a complete load-displacement curve,

from which the amount of pull-off force can be determined (see Figure 4.13 below)

[138, 139]. From the pull-off force, surface adhesion γ can be determined which can

be used in the JKR or DMT model.
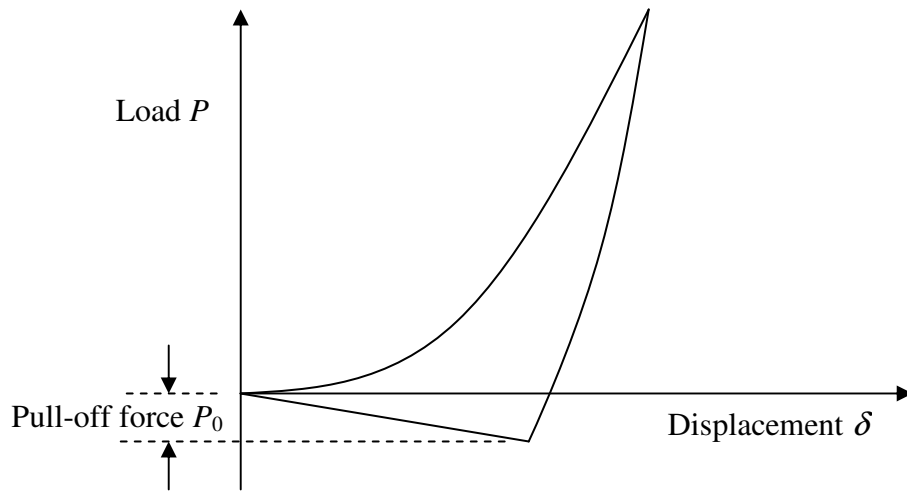
Figure 4.13: Schematic of a complete cycle of nano-indentation

For using analytic form, it is necessary to have the cantilever bending stiffness

(k_c), tip radius (R) and frequency of natural oscillation (f_0), which are usually only

approximately known. To have an estimate for these values, the analytic curve was

plotted with the calibration curve and was tried to match up the slope of the calibration

curve (see Figure 4.8). The significant difference between the experimental and

analytic equation (4.21) is attributable to the inherent error of the Taylor series expansion. If the k_c, R and f_0 values can be determined with significant accuracy, it will probably give better results if the equation is used with more terms from the expansion, as shown with equation (4.24).

Another significant source of error can generate from the estimation of Poisson ratio. As seen in Figure 4.10, higher Poisson ratios have bigger impact on estimation of the actual modulus of the sample. For determining the exact Poisson ratio, the same sample can be tested with for elastic modulus with frequency shift technique both in plane and in cross-section. The frequency slopes of these results need to be numerically solved for Poisson ratio and has to be validated using equation:

$$G = \frac{E}{2(1+v)} \tag{4.31}$$

Even though there exists a general trend for the elastic modulus with layer pair spacing of the nanolaminates, the total crystal energy of the synthesized laminated structure has [87, 117] a higher correlation with the elastic constants and film modulus. More experiments are necessary on almost continuously varying layer spacing samples, to obtain a better curve. Also, the roughness factors of both the sample and the tip [140] need to be considered for higher accuracy.

REFERENCE

[1] H.S.T. Ahmed, A.F. Jankowski, 'The mechanical strength of submicron porous silver foils', Surface and Coatings Technology 204, 2009, 1026-1029.

[2] L.J. Gibson, 'Mechanical behavior of metallic foams', Annual Review of Material Science 30, 2000, 191-227.

[3] A.F. Jankowski, J.P. Hayes, 'Sputter deposition of a spongelike morphology in metal coatings', Journal of Vacuum Science and Technology A 21, 2003, 422-425.

[4] J. Weissmüller, R.N. Viswanath, D. Kramer, P. Zimmer, R. Würschum, H. Gleiter, 'Charge-induced reversible strain in a metal', Science 300, 2003, 312-315.

[5] J. Biener, A. Wittstock, L. Zepeda-Ruiz, M.M. Biener, D. Kramer, R.N. Viswanath, J. Weissmüller, M. Bäumer, A.V. Hamza, 'Surface-chemistry-driven actuation in nanoporous gold', Nature Materials 8, 2009, 47-51.

[6] M. Sagmeister, U. Brossmann, S. Landgraf, R. Würschum, 'Electrically tunable resistance of a metal', Physical Review Letters 96, 2006, 156601-4.

[7] S. Dasgupta, S. Gottschalk, R. Kruk, H. Hahn, 'A nanoparticulate indium tin oxide field-effect transistor with solid electrolyte gating', Nanotechnology 19, 2008, 435203-8.

[8] H. Drings, R.N. Viswanath, D. Kramer, C. Lemier, J. Weissmüller, R. Würschum, 'Tuneable magnetic susceptibility of nanocrystalline palladium', Applied Physics Letters 88, 2006, 253103-5.

[9] S. Ghosh, C. Lemier, J. Weissmüller, 'Charge-dependent magnetization in nanoporous Pd-Co Alloys' IEEE Transactions on Magnetics 42, 2006, 3617-3619.

[10] J.D. Morse, A.F. Jankowski, R.T. Graff, J.P. Hayes, 'Novel proton exchange membrane thin-film fuel cell for microscale energy conversion', Journal of Vacuum Science and Technology A 18, 2000, 2003-2005.

[11] M. Hakamada, M. Mabuchi, 'Mechanical strength of nanoporous gold fabricated by dealloying', Scripta Materialia 56, 2007, 1003-1006.

[12] M.H. Lee, K.B. Kim, J.H. Han, J. Eckert, D.J. Sordelet, 'High strength porous Ti–6Al–4V foams synthesized by solid state powder processing', Journal of Physics D: Applied Physics 41, 2008, 105404-8.

[13] C.A. Volkert, E.T. Lilleodden, D. Kramer, J. Weissmuller, 'Approaching the theoretical strength in nanoporous Au', Applied Physics Letters 89, 2006, 061920-2.

[14] E.W. Andrews, G. Gioux, P. Onck, L.J. Gibson, 'Size effects in ductile cellular solids. Part II: experimental results', International Journal of Mechanical Sciences 43, 2001, 701-713.

[15] Z. Liu, C.S.L. Chuah, M.G. Scanlon, 'Compressive elastic modulus and its relationship to the structure of a hydrated starch foam', Acta Materialia 51, 2003, 365-371.

[16] U. Ramamurty, M.C. Kumaran, 'Mechanical property extraction through conical indentation of a closed-cell aluminum foam', Acta Materialia 52, 2004, 181-189.

[17] Y. Toivola, A. Stein, R.F. Cook, 'Depth-sensing indentation response of ordered silica foam', Journal of Materials Research 19, 2004, 260-271.

[18] M. Wilsea, K.L. Johnson, M.F. Ashby, 'Indentation of foamed plastics', International Journal of Mechanical Sciences 17, 1975, 457-460.

[19] M. Dao, L. Lu, R.J. Asaro, J.T.M. De Hosson, E. Ma, 'Toward a quantitative understanding of mechanical behavior of nanocrystalline metals', Acta Materialia 55, 2007, 4041–4065.

[20] R. Schwaiger, B. Moser, M. Dao, N. Chollacoop, S. Suresh, 'Some critical experiments on the strain-rate sensitivity of nanocrystalline nickel', Acta Materialia 51, 2003, 5159–5172.

[21] F.D. Torrea, H.V. Swygenhoven, M. Victoria, 'Nanocrystalline electrodeposited Ni: microstructure and tensile properties', Acta Materialia 50, 2002, 3957-3970.

[22] Y.M. Wang, E. Ma, 'On the origin of ultrahigh cryogenic strength of nanocrystalline metals', Applied Physics Letters 85, 2004, 2750-2752.

[23] C.D. Gu, J. Lian, Z. Jiang, Q. Jiang, 'Enhanced tensile ductility in an electrodeposited nanocrystalline Ni', Scripta Materialia 54, 2006, 579-584.

[24] X.Z. Liao, A.R. Kilmametov, R.Z. Valiev, H. Gao, X. Li, A.K. Mukherjee, J.F. Bingert, Y.T. Zhu, 'High-pressure torsion-induced grain growth in electrodeposited nanocrystalline Ni', Applied Physics Letters 88, 2006, 021909-021911.

[25] K.S. Kumar, S. Suresh, M.F. Chisholm, J.A. Horton, P. Wang, 'Deformation of electrodeposited nanocrystalline nickel', Acta Materialia 51, 2003, 387-405.

[26] C.D. Gu, J.S. Lian, Q. Jiang, W.T. Zheng, 'Experimental and modelling investigations on strain rate sensitivity of an electrodeposited 20 nm grain sized Ni', Journal of Physics D: Applied Physics 40, 2007, 7440–7446.

[27] A.F. Jankowski, C.K. Saw, J.P. Hayes, 'The thermal stability of nanocrystalline Au–Cu alloys', Thin Solid Films 515, 2006, 1152–1156.

[28] A.F. Jankowski, 'Modeling nanocrystalline grain growth during the pulsed electrodeposition of gold-copper', Electrochemical Society Transactions 1, 2006, 1-9.

[29] A.F. Jankowski, C.K. Saw, J.F. Harper, R.F. Vallier, J.L. Ferreira, J.P. Hayes, 'Nanocrystalline growth and grain-size effects in Au–Cu electrodeposits', Thin Solid Films 494, 2006, 268–273.

[30] J.D. Illige, C.M. Yu, S.A. Letts, 'Metal coatings for laser fusion targets by electroplating', Journal of Vacuum Science and Technology 18, 1981, 1209-12013.

[31] Y.M. Wang, A.F. Jankowski, A.V. Hamza, 'Strength and thermal stability of nanocrystalline gold alloys', Scripta Materialia 57, 2007, 301–304.

[32] GE Silver Membranes, GE Osmonics^{TM} Labstore, 5951 Clearwater Dr, Minnetonka, MN 55343

(http://www.osmolabstore.com/OsmoLabPage.dll?BuildPage&1&1&326)

[33] Surepure Chemetals, 5-W Nottingham Drive, Florham Park, New Jersey.

[34] H.B. Huntington, The Elastic Constants of Crystals, Chapter in Solid State Physics, 1958

[35] J.R. Neighbours, G.A. Alers, 'Elastic constants of silver and gold', Physical Review 111, 1958, 707-712.

[36] W.C. Overton, Jr., J. Gaffney, 'Temperature variation of elastic constants of cubic elements. I. Copper', Physical Review 98, 1955, 969-977.

[37] Y. Hiki, A.V. Granato, 'Anharmonicity in noble metals; Higher order elastic constants', Physical Review 144, 1966, 411-419.

[38] Y.A. Chang, L. Himmel, 'Temperature dependence of the elastic constants of Cu, Ag, and Au above room temperature', Journal of Applied Physics 37, 1966, 3567-3572.

[39] A. Wolfenden, M.R. Harmouche, 'Elastic constants of silver as a function of temperature', Journal of Materials Science 28, 1993, 1015-1018.

[40] J.F. Nye, Physical Properties of Crystals, 1960, Oxford.

[41] J. Kovacik, 'The tensile behaviour of porous metals made by GASAR process', Acta Materialia 46, 1998, 5413-5422.

[42] O. Yeheskel, M. Shokhat, M. Ratzker, M.P. Dariel, 'Elastic constants of porous silver compacts after acid assisted consolidation at room temperature', Journal of Materials Science 36, 2001, 1219 – 1225.

[43] H.X. Zhu, J.F. Knott, N.J. Mills, 'Analysis of the elastic properties of open-cell foams with tetrakaidecahedral cells', Journal of the Mechanics and Physics of Solids 45, 1997, 319-343.

[44] W.E. Warren, A.M. Kraynik, 'Linear elastic behavior of a low-density kelvin foam with open cells', Journal of Applied Mechanics 64, 1997, 787-794.

[45] L. Li, M. Aubertin, 'A general relationship between porosity and uniaxial strength of engineering materials', Canadian Journal of Civil Engineering 30, 2003, 644-658.

[46] E.O. Hall, 'The deformation and ageing of mild steel: III Discussion of results', Proceedings of the Physical Society. B64, 1951, 747-753.

[47] E.O. Hall, 'The brittle fracture of metals', Journal of Mechanics and Physics of Solids 1, 1953, 227-233.

[48] N.J. Petch, 'The cleavage strength of polycrystals', Journal of the Iron and Steel Institute, 174, 1953, 25-28.

[49] N.J. Petch, 'The fracture of metals', Progress in Metal Physics 5, 1954, 1-52.

[50] N.J. Petch, 'The upper yield stress of polycrystalline iron', Acta Metallurgica 12, 1964, 59-65.

[51] R.M. Douthwaite, N.J. Petch, 'A microhardness study relating to the flow stress of polycrystalline mild steel', Acta Metallurgica 18, 1970, 211-216.

[52] N.J. Petch, R.W. Armstrong, 'The tensile test', Acta Metallurgica 38, 1990, 2695-2700.

[53] F. Saeffel, G. Sachs, Zeitschrift Fur Metallkunde., 17, 1925, 33.

[54] K.C. Goretta, W.E. Delaney, J.L. Routbort, J. Wolfenstine, W. Zhang, E.E. Hellstrom, 'Creep of silver at 900 ºC', Superconductor Science and Technology 9, 1996, 422-426.

[55] M. Aubertin, L. Li, 'A porosity-dependent inelastic criterion for engineering materials', International Journal of Plasticity 20, 2004, 2179–2208.

[56] Y.M. Wang, A.V. Hamza, E. Ma, 'Temperature-dependent strain rate sensitivity and activation volume of nanocrystalline Ni', Acta Materialia 54, 2006, 2715-2726.

[57] R.D. Emery, G.L. Povirk, 'Tensile behavior of free standing gold films. Part II. Fine grained films', Acta Materialia 51, 2003, 2079-2087.

[58] J. Lian, C.D. Gu, Q. Jiang, Z. Jiang, 'Strain rate sensitivity of face-centered-cubic nanocrystalline materials based on dislocation deformation', Journal of Physics 99, 2006, 076103 (1-3).

[59] J. Lian, B. Baudelet, 'A modified Hall-Petch relationship for nanocrystalline materials', Nanostructured Materials 2, 1993, 415-419.

[60] J.W. Cahn, F.R.N. Nabarro, 'Thermal activation under shear', Philosophical Magazine A 81, 2001, 1409-1426.

[61] H.S.T. Ahmed, A.F. Jankwoski, 'Tensile deformation of micro-to-nanoporous metal membranes', 16th International Symposium on Plasticity, ed. Akhtar S. Khan, Proceedings Plasticity 10 (NEAT Press, 2010) 118-120.

[62] R.D. Emery, G.L. Povirk, 'Tensile behavior of free-standing gold films. Part I. Coarse grained films', Acta Materialia 51, 2003, 2067-2078.

[63] G.D. Hughes, S.D. Smith, C.S. Pande, H.R. Johnson, R.W. Armstrong, 'Hall-Petch strengthening for the microhardness of twelve nanometer grain diameter electrodeposited nickel', Scripta Metallurgica 20, 1986, 93-97.

[64] http://en.wikipedia.org/wiki/Nickel

[65] D. Hull, D.J. Bacon, 'Introduction to dislocations', 4th Edition, ISBN: 0750646810.

[66] L.O. Nyakiti, A.F. Jankowski, 'Characterization of strain-rate sensitivity and grain boundary structure in nanocrystalline Gold-Copper alloys', Metallurgical and Materials Transactions A 41, 2010, 838-847.

[67] Y.M. Wang, E. Ma, 'Three strategies to achieve uniform tensile deformation in a nanostructured metal', Acta Materialia 52, 2004, 1699–1709.

[68] R.J. Asaro, S. Suresh, 'Mechanistic models for the activation volume and rate sensitivity in metals with nanocrystalline grains and nano-scale twins', Acta Materialia 53, 2005, 3369–3382.

[69] L. Lu, R. Schwaiger, Z.W. Shan, M. Dao, K. Lu, S. Suresh, 'Nano-sized twins induce high rate sensitivity of flow stress in pure copper', Acta Materialia 53, 2005, 2169–2179.

[70] Q. Wei, S. Cheng, K.T. Ramesh, E. Ma, 'Effect of nanocrystalline and ultrafine grain sizes on the strain rate sensitivity and activation volume: fcc versus bcc metals', Materials Science and Engineering A 381, 2004, 71–79.

[71] A. F. Jankowski, Mechanics and Mechanisms of Finite Plastic Deformation – 14th Int. Symp. on Plasticity Proc., A.S. Khan and B. Farrokh, eds., NEAT Press, Fulton, MD, 2008, 187-189.

[72] J. Harding, 'The effect of high strain rate on material properties', in: TZ Blazynsky (Ed.), Materials at High Strain Rates, Elsevier Applied Science, 1987.

[73] L.D. Oosterkamp, A. Ivankovic, G. Venizelos, 'High strain rate properties of selected aluminium alloys', Material Science and Engineering A 278, 2000, 225-235.

[74] R.W. Armstrong, S.M. Walley, 'High strain rate properties of metals and alloys', International Materials Reviews 53, 2008, 105-128.

[75] N.N. Dioh, A. Ivankovic, P.S. Leevers, J.G. Williams, 'The high strain rate behavior of polymers', Journal De Physique, Colloque C8, 4, 1994, 119-124.

[76] N.N. Dioh, A. Ivankovic, P.S. Leevers, J.G. Williams, 'Stress wave propagation effects in split Hopkinson pressure bar test', Porc. R. Soc. Lond. A. 449, 1995, 187-204.

[77] F. Mohs, Grundriss der Mineralogie, 1824, English Translation by W. Haidinger, Treatise of Mineralogy (Constable, Edinburgh, Scotland, 1825).

[78] L.B. Freund, J.W. Hutchinson, 'High strain-rate crack growth in rate-dependent plastic solids', J. Mech. Phys. Solids 33, 1985, 169-191.

[79] R.W. Armstrong, F.J. Zerilli, 'Dislocation mechanics based analysis of material dynamics behavior', Journal De Physique, Colloque C3, 1988, 529-534.

[80] P.S. Follansbee, 'High-strain-rate deformation mechanisms in copper and implications for behavior during shock-wave deformation', APS topic of Shockwaves in Condensed Matter, 1987, edited by S.C. Schmidt and N.C. Holmes (Elsevier Science, Amsterdam, 1988), 249.

[81] J.T. Burwell, C.D. Strang, 'Metallic wear', Proceedings of the Royal Society of London. Series A, Mathematical and Physical Sciences 212, 1952, 470-477.

[82] J.T. Burwell, C.D. Strang, 'On the empirical law of adhesive wear', Journal of Applied Physics 23, 1952, 18-28.

[83] K.M. Lee, C.–D. Yeo, A.A. Polycarpou, 'Nanomechanical property and nanowear measurements for sub-10-nm thick films in magnetic storage', Experimental Mechanics 47, 2007, 107-121.

[84] G. Li, J. Lao, J. Tian, Z. Han, M. Gu, 'Coherent growth and mechanical properties of AlN/VN multilayers', J. Applied Physics 95, 2004, 92-96.

[85] Y. Wang, J. Li, A.V. Hamza, T.W. Barbee, Jr., 'Ductile crystalline–amorphous nanolaminates', Proceedings of the National Academy of Sciences vol. 104, 2007, 11155–11160.

[86] T. Zhu, J. Li, A. Samanta, 'Interfacial plasticity governs strain rate sensitivity and ductility in nanostructured metals', Proceedings of the National Academy of Sciences 104, 2007, 3031-3036.

[87] A.F. Jankowski, 'Vapor deposition and characterization of nanocrystalline nanolaminates', Surface and Coatings Technology 203, 2008, 484-489.

[88] A.F. Jankowski, D.M. Makowiecki, M.A. Wall, M.A. McKernan, 'Subnanometer multilayers for x-ray mirrors: Amorphous crystals', Journal of Applied Physics 65, 1989, 4450-4451.

[89] A.F. Jankowski, R.M. Bionta, P.C. Gabriele, 'Internal stress minimization in the fabrication of transmissive multilayer x-ray optics', Journal of Vacuum Science and Technology A 7, 1989, 210-213.

[90] A.F. Jankowski, 'Deposition optimization of W/C multilayer mirrors', Optical Engineering 29, 1990, 968-972.

[91] A.F. Jankowski, SPIE conf. Proc. 1738, 1992, 10-21.

[92] J.R. Childress, C.L. Chien, A.F. Jankowski, 'Magnetization, Curie temperature, and magnetic anisotropy of strained (111) Ni/Au superlattices', Phys. Rev. B 45, 1992, 2855-2862.

[93] A. Simopoulos, E. Devlin, A. Kostikas, A.F. Jankowski, M. Croft, T. Tsakalakos, 'Structure and enhanced magnetization in Fe/Pt multilayers', Phys Rev B 54, 1996, 9931-9941.

[94] A.F. Jankowski, T. Tsakalakos, 'Phase stability by the artificial concentration wave method', Metallurgical and Materials Transactions A 20, 1989, 357-362.

[95] A. F. Jankowski, C.K. Shaw, 'Diffusion in Ni/CrMo composition-modulated films', Scripta Materialia 51, 2004, 119-124.

[96] A.F. Jankowski, 'Diffusion mechanisms in nanocrystalline and nanolaminated Au-Cu', Defect and Diffusion Forum 266, 2007, 13-28.

[97] D.M. Makowiecki, A.F. Jankowski, M.A. McKernan, R.J. Foreman, 'Magnetron sputtered boron films and Ti/B multilayer structures', Journal of Vacuum Science and Technology A 8, 1990, 3910-3913.

[98] A.F. Jankowski, M.A. Wall, J.P. Hayes, K.B. Alexander, 'Properties of boron/boron-nitride multilayers', NanoStructured Materials 9, 1997, 467-471.

[99] A.F. Jankowski, J.P. Hayes, D.M. Makowiecki, M.A. McKernan, 'Formation of cubic boron nitride by the reactive sputter deposition of boron', Thin Solid Films 308-309, 1997, 94-100.

[100] A.F. Jankowski, J.P. Hayes, C.K. Saw, 'Dimensional attributes in enhanced hardness of nanocrystalline Ta-V nanolaminates', Philosophical Magazine 87, 2007, 2323-2334.

[101] N. Tayebi, T.F. Conry, A.A. Polycarpou, 'Reconciliation of nanoscratch hardness with nanoindentation hardness including the effect of interface shear stress', Journal of Materials Research 19,2004, 3316-3323.

[102] N. Tayebi, A.A. Polycarpou, T.F. Conry, 'Effects of substrate on determination of hardness of thin films by nanoscratch and nanoindentation techniques', Journal of Materials Research 19, 2004, 1791-1802.

[103] N. Tayebi, T.F. Conry, A.A. Polycarpou, 'Determination of hardness from nanoscratch experiments: Corrections for interfacial shear stress and elastic recovery', Journal of Materials Research 18, 2003, 2150-2162.

[104] C. Feldman, F. Ordway, J. Bernstein, 'Distinguishing thin film and substrate contributions in microindentation hardness measurements', Journal of Vacuum Science and Technology A 8, 1990, 117-122.

[105] V. Blank, M. Popov, N. Lvova, K. Gogolinsky, V. Reshetov, 'Nano-sclerometry measurements of superhard materials and diamond hardness using scanning force microscope with the ultrahard fullerite C_{60} tip', Journal of Materials Research 12, 1997, 3109-3114.

[106] N. Gitis, M. Vinogradov, I. Hermann, S. Kuiry, 'Comprehensive Mechanical and Tribological Characterization of Ultra-Thin-Films', Mater. Res. Soc. Symp. Proc. Vol. 1049, 2008

[107] A. Gouldstone, N. Chollacoop, M. Dao, J. Li, A.M. Minor, Y.L. Shen, 'Indentation across size scales and disciplines: Recent developments in experimentation and modeling', Acta Materialia 55, 2007, 4015-4039.

[108] J. Mencik, M.V. Swain, 'Errors associated with depth-sensing microindentation tests', Journal of Materials Research 10, 1995, 1491-1501.

[109] T.G. Nieh, A.F. Jankowski, J. Koike, 'Processing and characterization of hydroxyapatite coatings on titanium produced by magnetron sputtering', Journal of Materials Research 16, 2001, 3238-3245.

[110] H.S.T. Ahmed, A.F. Jankowski, 'Strain rate sensitivity of hydroxyapatite coatings', Poster presented at AVS 56th International Symposium and Exhibition, San Jose, California, November 9-13, 2009.

[111] H.S.T. Ahmed, A.F. Jankowski, 'Strain rate sensitivity of nanocrystalline nanolaminate', Poster presented at the AVS 55th International Symposium and Exhibition, Boston, Massachusetts, October 21-23, 2008.

[112] A.F. Jankowski, H.S.T. Ahmed, 'Plasticity of nanocrystalline nanolaminates: strain-rate sensitivity', 15th International Symposium on Plasticity, ed. Akhtar S. Khan, Proceedings Plasticity 09 (NEAT Press, 2009) 403-405.

[113] A.F. Jankowski, 'Interface Effects on the Mechanical Properties of Nanocrystalline Nanolaminates', Mechanical Behavior at Small Scales – Experiments and Modeling, eds. J. Lou, B. Boyce, E. Lilleodden, L. Lu, Materials Research Society Symposia Proceedings 1224 (2010)

[114] A.F. Jankowski, 'Measurement of lattice strain in Au–Ni multilayers and correlation with biaxial modulus effects', Journal of Applied Physics 71, 1992, 1782-1789.

[115] M.A. Wall, A.F. Jankowski, 'Atomic imaging of Au/Ni multilayers', Thin Solid Films 181, 1989, 313-321.

[116] A.F. Jankowski, 'Modelling the supermodulus effect in metallic multilayers', J. Phys. F: Met. Phys., Vol. 18, 1988, 413-427.

[117] A.F. Jankowski, T. Tsakalakos, 'The effect of strain on the elastic constants of noble metals', J. Phys. F: Met. Phys., Vol. 15, 1985, 1279-1292.

[118] A.F. Jankowski, J. Go, J.P. Hayes, 'Thermal Stability and Mechanical Behavior of Ultra-fine bcc Ta and V Coatings', Surface and Coatings Technology 202, 2007, 957-961.

[119] W. Arnold, S. Hirsekorn, M. Kopycinska-Müller, M. Reinstädtler, and U. Rabe, 'Quantitative measurement of elastic constants of anisotropic materials by atomic force acoustic microscopy', International Committee for Non-Destructive Testing - ICNDT-: 16th World Conference on Nondestructive Testing 2004, pp. TS5.9.3.

[120] M. Reinstädtler, T. Kasai, U Rabe, B Bhushan and W Arnold, 'Imaging and measurement of elasticity and friction using the TRmode', Journal of Physics D: Applied Physics 38, 2005, R269–R282.

[121] D. DeVecchio and B. Bhushan, 'Localized surface elasticity measurements using an atomic force microscope', Rev. Sci. Instrum. 68, 1997, 4498-4505.

[122] S. Etienne, Z. Ayadi, M. Nivoit, J. Montagnon, 'Elastic modulus determination of a thin layer', Materials Science and Engineering A 370, 2004, 181–185.

[123] R Whiting and M A Angadi, 'Young's modulus of thin films using a simplified vibrating reed method', Meas. Sci. Technol. 1, 1990, 662-664.

[124] K-D. Wantke, H. Fruhner, J. Fang, and K. Lunkenheimer, 'Measurements of the surface elasticity in medium frequency range using the oscillating bubble method', Journal of Colloid and Interface Science 208, 1998, 34–48

[125] W.C. Oliver and G.M. Pharr, 'An improved technique for determining hardness and elastic modulus using load and displacement sensing indentation experiments', Journal of Materials Research Vol. 7, 1992, 1564-1583.

[126] A.S. Useinov, 'A nanoindentation method for measuring the young modulus of superhard materials using a NanoScan scanning probe microscope', Instruments and Experimental Techniques, Vol. 47, 2004, 119-123

[127] S.P. Timoshenko, J.N. Goodier, Theory of Elasticity, 3rd edition, McGraw Hill.

[128] K.V. Gogolinski, Z.Ya. Kosakovskaya, A.S. Useinov and I.A. Chaban, 'Measurement of the elastic moduli of dense layers of oriented carbon nanotubes by a scanning force microscope', Acoustical Physics, Vol. 50, 2004, 664-669

[129] A.D. Roberts, PhD Dissertation, 1968, Cambridge University, England.

[130] K.L. Johnson, K. Kendall and A.D. Roberts, 'Surface Energy and the Contact of Elastic Solids', Proc. R. Soc. Lond. A. 324, 1971, 301-313

[131] Ya-Pu Zhao, X. Shi and W.J. Li, 'Effect of work of adhesion on nanoindentation', Rev. Adv. Mater. Sci., Vol. 5, 2003, 348-353.

[132] B.V. Derjaguin, V.M. Muller, YU.P. Toporov, 'Effect of contact deformations on the adhesion of particles', J. of Colloid and Interface Science, Vol. 53, 1975, 314-326.

[133] G.A. Alers, 'Elastic moduli of Vanadium', Physical Review, Vol. 119, 1960, 1532-1535.

[134] F.H. Featherston and J.R. Neighbours, 'Elastic constants of Tantalum, Tungsten, and Molybdenum', Physical Review, Vol. 130, No. 4, 1963, 1324- 1333.

[135] B.T. Bernstain, 'Elastic constants of synthetic sapphire at 27º C', Journal of Applied Physics, Vol. 34, No. 1, 1963, 169-172.

[136] W.A. Brantley, 'Calculated elastic constants for stress problems associated with semiconductor devices', J. Applied Physics, Vol. 44, No. 1, 1973, 534-535.

[137] A.F. Jankowski, 'The strain wave approach to modulus enhancement and stability of metallic multilayers', Journal of Physics and Chemistry of Solids, Vol. 50, 1989, 641-649.

[138] J. Drelich, 'Adhesion forces measured between particles and substrates with nano-roughness', Minerals and Metallurgical Processing, Vol. 23, No. 4, 2006, 226-232

[139] M.M. McCann, 'Nanoindentation of Gold single crystals', PhD. Thesis, Virginia Polytechnic Institute and State University, 2004.

[140] L.E. Goodman, 'Contact stress analysis of normally loaded rough spheres', Journal of Applied Mechanics, 1962, 515-522.

APPENDIX I

(EMAIL WITH DR. ILJA HERMANN: HOW TO SETUP THE NANOANALYZER)

The aim of this section is to target the user of the NanoAnalyzer tool and hence, information that relates to the scratch hardness measurement and tapping mode modulus measurement with the use of the NA head will only be reviewed here. This section will detail instructions beyond the CETR, Inc. manual on how to operate the hardware. Before proceeding with this section, the user should first read the instruction manual, and become familiar with the software interface in the off-line mode. It will better enable the user to follow the controls and instructions of the CETR NanoAnalyzer interface of the Universal Materials Tester (UMT) that is documented in this section.

I.A Starting-up the NanoAnalyzer

I.A.1 Begin with the machine in stop mode, and with no software running. Double click on the UMT icon (shortcut on the desktop) and select Options→Load (from the menu bar). By default, the command opens the C:/NanoAnalyzer/TRIB folder where a folder named 'Option files' is located at. Each option file is written for specific purpose only and will only work with a specific head mounted on the UMT machine. (The reader should consult the manual about how to write an option file: See section 6, Calibration Procedures on page 96 of the UMT user's manual).

I.A.2   From the folder 'Tanvir_Option files', select the option file named

'NanoAnalyzer_Fl-0326.opt'. This option file was written to give output of Fz

and Fx in micro-Newtons from the FL-0326 force sensor.

I.A.3   After selecting the option file, click on the 'automatic panel' button (on

the menu bar) and check that the UMT motors are initialized by pressing

CTRL+ left or right arrow for the slider, i.e. x direction movement; CTRL+ up

or down arrow for carriage, i.e. z direction movement; CTRL+ < or> key for

the spindle, i.e. y-direction movement. The ALT key can also be pressed

instead of the CTRL key, but make sure the head is far from the specimen

stage, because pressing the ALT key will move the stages very fast and can

damage the probe by unintended contact if not done with care.

I.A.4   If the motors are not initialized, the stages will not move. Check if the

emergency button was pressed. Press the reset button and try again. If it does

not work, then load the option file named 'Micro.opt', click on the semi-

automatic panel (on the menu bar), wait for about 10 seconds, close the semi-

automatic panel and click on Tools→Setup motor controllers and check that

the values in the Carriage, Slider, Spindle (fast) and Spindle (Slow) are set at

2000, 20000, 5000 and 100000, respectively. Then click on Set motor

controller defaults and wait until the initialization process is complete.

I.A.5   Once complete, a popup message will be displayed which asks to

restart the UMT software. Click 'Ok' and close the UMT software. Double

click on UMT icon again to start the software. Click Options➔Save as and

save the opt file under the same name to overwrite the existing one.

I.A.6   Verify that the stage motors are initialized by clicking on the

'Automatic Panel' button and check for motions. Load the 'NanoAnalyzer_Fl-

0326.opt' from the 'Tanvir_Option files' folder. Then click the 'Semi-

Automatic Panel' and the 'Plot' icons (on the menu bar). The 'Plot' should

show Fx and Fz in micro-newtons. Click on the 'Data' tab on the 'Semi-

Automatic Panel' and from the menu bar, unbias all the channels (1111) and

then bias them (0000). This will bring the Fx and Fz on the center of the 'Plot'

window.

I.A.7   Now start the NanoAnalyzer (NA) software (NA viewer), go to

'Device' from the menu bar and click on 'Show Device Window'. This will

pop up another window. Every function on this window is designated for

controlling the hardware of the NA head.

I.A.8   From 'Device', click on 'Change Probes' and select the appropriate

probe that is installed on the machine (every probe is recognized with a

number which is written on the base of the probe as well as on the cover of the

probe).

I.A.9   Then, from 'Device', click on 'Run' and it will start up the NA head.

From the move panel, check the responses of the stage motors with the

corresponding arrow buttons (right clicking on any button will show a balloon-

help).

I.A.10   Assuming that the correct probe is loaded, go to the 'Probes' tab and

click on 'Auto set-up'. After this, you are ready to work with the NA.

I.B Hardness Measurement by Nano-Scratch

I.B.1 Producing Nano-Scratch

At this point, you will be running two software programs (NA and UMT)

simultaneously. It is better for the user to keep the UMT software running on one

monitor and NA software running on the other monitor. The standard operating

procedure for producing scratches is as follows:

I.B.1.a   The optical microscope attached with the NA head needs to be

initialized. From the UMT menu bar, click on the 'light' icon, which will turn

on the illuminator. You will have two choices to select the one that best suits

your need. Then click on the 'Run microscope' button (that looks like a green

arrow button on the menu bar) which will initialize the microscope. Note that,

only for the microscope of the NA head, the extra piece of extension cable has

to be plugged in to the microscope.

I.B.1.b   Place a sample on the Y-stage and look it under the optical microscope.

You can focus the microscope from the NA software by moving the carriage (z

height). Then using the x and y movement control from the NA (on the 'Move'

tab), place an area of interest in the middle of the microscope window.

I.B.1.c   From the 'Move' tab on the NA device controller, click on 'Run' (an

icon next to the x and y movement arrows) and click on the 'Indentation' icon.

The 'Run' button will only work if the probe is far from the sample, i.e. not in

contact with the sample. This will move the sample area under the probe.

Correct optical microscope offset (OM offset) needs to be set before this can

work perfectly. This is generally calibrated from the factory, but can be done in

house in case of need, see the Optical microscope manual. Also, please refer to

the section 3.2.24 on page 44 of the NA-2 manual.

I.B.1.d   Once the sample is located under the probe, make sure to turn the

microscope light and the camera off. Keeping them on will use valuable

memory and retard the speed of the data acquisition system.

I.B.1.e   Approach the sample with z-movement with velocities from very fast

to normal (drop down list on the Move tab) with care. Bring the probe to about

half a millimeter above the surface, and then click on 'Find surface'. This will

automatically find the sample without damaging the tip. Once the surface is

found, a new window will pop up with the information ('Surface Found').

Press 'OK' to close that box. Please refer to the image on page 14 of the NA-2

manual.

I.B.1.f   Go the 'Scan' tab. Before producing a scratch (or even an elasticity

curve), it is highly recommended to scan the area. A high resolution scan is not

necessary, as it will unnecessarily wear the tip and can take a lot of time. So,

change the speed and step size of the scan from the 'Scan' tab and then select

the area to scan and click on 'Scan' button. Please refer to the image on page

16 of the NA-2 manual.

I.B.1.g   After the scan is finished, click on the z-image. This will have 'z' at the

end of the name of the image. Other images will have Am or Z(opt) or Fr at the

end of their respective names. Process this image e.g. line tilt, step correction,

filter→ average, etc. from the 'Process' on the menu bar of the NA viewer

according to your need.

I.B.1.h   Move this processed z-image to the measurement panel by clicking on

'M>' icon on the menu bar. Both scratches and elasticity measurement has to

be done from the measurement panel.

I.B.1.i   This version of the NA (i.e. the NA-2) can produce both vertical

scratches and horizontal scratches (as seen on the computer screen). However,

horizontal scratches will move the probe in a lateral direction (perpendicular to

the axis of the probe cantilever) which can put the cantilever under heavy

torsional load. This may reduce the life of the ceramic probe and can break it.

It is NOT recommended to produce horizontal scratches [141]. From the

measurement panel, choose 'Scratch' from the dropdown list. Then, click on

the image that was imported to this panel earlier and draw vertical lines by

dragging the left mouse button. Note that once the line has been drawn, a table

on the bottom of the panel shows the properties of the scratch. Double click on

that cell of the table and input necessary values, for example, the start and end

positions of the scratch and the load value. You may draw as many vertical

lines as necessary (up to certain maximum) and edit them from the table.

Please refer to the image on page 18 of the NA-2 manual.

I.B.1.j   Once the table is finished, the machine is ready to produce scratches at the tabulated locations with the tabulated properties. Now go to the UMT panel and select 'Data' tab from the semi-automatic panel. Click on 'unbias all' (1111) and then 'bias all' (0000). This will bias the force sensor and make the Fx and Fz values zero. Then click on the 'Blackbox' tab and click on 'Browse', give it a filename for the experiment that is going to be conducted and click save. You may choose to record every 10th data point or 20th data point depending on your need, and that can be defined on the field 'record every N^{th} data' or 'average of N data'. Click on 'Run' button from the menu bar of the UMT. This will start recording data points from the force sensor.

I.B.1.k   Now go to the NA software and check that the 'FB' mode is set to 'Close'. This is the force feedback system which needs to be closed for scratches of velocities up to 1000nm/sec. For making higher speed scratches, the feedback mode needs to be open [142].

I.B.1.l   Click on 'Run' button at the bottom of the measurement panel and wait until the scratch experiment is finished. The machine is highly prone to external noise and it is extremely important that the surrounding of the machine is kept to the best possible quietness during the experiments are running.

I.B.1.m   Once the experiment is finished, a window will pop up in the NA software environment to confirm that. Now go to the UMT software and click on the 'Stop' button on the menu bar of the UMT software. This will stop data

collection from the force sensor. Allow it some time for the system to response. Typically it takes about 30 seconds (sometimes less) before the data acquisition system actually stops the data collection. You will see that the number count (the number field next to 'Sample' on the 'Blackbox': Please refer to section 6.7 on page 28 of 'software operating manual' part of UMT user's manual) stops once the data collection is ended. You can later open this file with Fz and Fx information with the 'Viewer' software. The 'Viewer' software can either be opened independently or from the UMT panel's menu bar.

I.B.1.n   After a scratch is produced (vertical scratch), it is recommended to scan the area horizontally (perpendicular to the direction of the scratch to reduce the influence of thermal drift on the calculation of scratch width). The following steps including this step document the procedure of scanning a scratch. The scan is done horizontally by default (if not changed). The direction of scan can be changed from x to y and vice versa from the 'Scan' tab, shown as radio buttons below the imaging area. Please refer to the image on page 16 of the NA-2 manual.

I.B.1.o   To scan the scratch, it is very important to click on the 'Go to Scan' button on the 'Measure' tab (do not click on the 'Scan' tab directly from the top) which would move the probe to the start of the existing scan-area by keeping the co-ordinates same and would show the line trace of the scratch on the to-be-scanned area. It is recommended to produce a low resolution scan of the scratched area and perform a high resolution scan thereafter. During nano-

indentation/ scratch tests, the surface roughness plays a major role in the uncertainty of the scratch width calculations. Thus, a step size of about 5% of the width of the scratch is fully sufficient in resolving the width [143], i.e., there should be twenty or more data points to define the scratch geometry in cross-section. Higher resolution scans can be done on the area, but the amount of time and associated tip wear would not add up to the resolution of the width by much. The accuracy of the test can instead be improved by doing more than one scratch at same condition at more locations. It is very well possible that the probe increased in temperature during scratch test and hence thermal drift will occur. The phenomenon of thermal drift is observable during scanning an area. If the probe is drifting, a vertical scratch will appear inclined. Thus, it is recommended to use 'Probe Correction' from the 'Probe' tab before scanning, which would take care of the thermal drift automatically (Please refer to the image on page 20 of the NA-2 manual). Once the image is imported from the 'Measure' tab to 'Scan' tab using 'Go to Scan' button, moving to the 'Probe' tab will not erase the to-be-scanned area from the 'Scan' tab. The difference between 'Auto Setup' and 'Probe Correction' is that 'Auto Setup' is mainly intended to find the resonance of the probe. It can take care of the thermal drift too, but will retract the tip from the sample surface if used while in contact with the surface. The 'Probe Correction' on the other hand only takes care of the thermal drift issue and does not retract the probe from the sample. During high resolution scanning (after the low resolution quick scan), the noise of scanning may go up which would be evident on the Frequency feedback plot.

Ideally, the Frequency (the error signal) should be close to zero during scanning, but may go up to several hundred Hz in practice during the high resolution scan. This noise can be taken care of by reducing the Gain control. A high gain image will look sharper and crisper whereas a low gain image will look dull. However, a high gain image means more noise. So, the gain control is a compromise between noise and resolution that has to be optimized during the actual scanning. Tip contamination can also lead to poor images. So, it is necessary to clean the tip using an alcohol rinse from time to time (only when the probe is far from the sample surface and the machine is not being in use) [144].

I.B.1.p   During scanning of the scratched area, it is possible that the probe may loose contact with the sample surface which will become evident as the 'Z(nm)' indicator will go up without staying at the middle operating zone of the entire range. Or, at this point, the so-far-scanned image will become dark without showing the topography any more. The former case may happen mainly due to thermal drift, high surface inclination, as well as due to contact with some surface features caused by pile-ups of sample material/debris along the path of long scratches. That is, artifacts can arise if the probe has to scan an area with a significant difference in 'Z', i.e. the height levels. This problem can be taken care of by waiting for few minutes or by putting more force on the cantilever of the probe (accomplished with decreasing the set point on the feedback panel). However, care must be taken not to decrease the set point too much. This can break the ceramic cantilever. A general rule to follow is not to

decrease the set point by more than 2% as based on current setting. For highly

inclined surfaces, the z limit of initial surface approach may need to be

decreased from the default value of 50% [145] since decreasing the value

determines the z level at which the surface is found, but not less than 30%

(from Device → Settings → Find Surface → Critical Z level). In the event of

imaging distortion due to some surface artifacts, a built-in snipping tool (or

scissor tool) is available to cut the black image from the rest of the shiny

yellow image and then processing the black image with auto-pallet [146].

Also, **it is recommended** to scan at the very beginning of the scratches and to

scan only a small area associated with the scratch. A high resolution large area

scan will take hours as well as introduce thermal drift. However, it is advisable

to choose an area that will cover about 5 to 10 times the width of the scratch on

both sides.

I.B.1.q   Once the scan is complete, process the z-image (line tilt, step

correction, etc.). Then click on the 'Scratch Measurement' tool from the menu

bar of the NA viewer. This will show the scratch lines on the z-image. Left

click on the image and dragging will produce a box around the scratch (Please

refer to the images on page 74 of the NA-2 manual). A new window will also

appear with the scratch-line information. From this new window, position the

left marker at the beginning of the scratch (left click) and position the right

marker at the end of the scratch (right click). The width of the scratch will be

shown as dx value (in nanometers) on the top right corner. The setting is set up

to provide 7 scratch widths on a single window. If necessary, particular scratch

sections can be omitted from measurement. Click on 'Graph Manager' (GM)

from the menu bar and particular scratches can be de-selected from the new

window with left mouse click. This operation is particularly necessary when all

the 7 sections of the same scratch do not provide meaningful data.

I.B.1.r   After the number of sections and their respective widths are defined,

open the 'Hardness Measurement' window from 'Measure' on the menu bar

and create a new sample with a name. Then from the scratch width window,

click 'Apply' from the bottom right corner. This will transfer the width

information from the 'Scratch Measurement' window to the 'Hardness

Measurement' window in a tabulated form (Please refer to section 4.8 on page

70 of the NA-2 manual).

I.B.2 Scratch Hardness Analysis

Hardness as a function of the scratch width can be measured using both the

calibration method, and the direct method:

I.B.2.a   In calibration method, several reference materials with known hardness

values are used as standards for comparison with unknown materials. Most

common reference materials are Polycarbonate (hardness: 0.28±0.02 GPa),

Fused Silica (hardness: 9.5±0.5 GPa) and Sapphire (hardness: 27±1 GPa). At a

particular scratch speed (which can be changed from Device → Settings →

Sclerometry→Scratch Speed), several scratches of nominal loads starting from

200µN to 1500µN need to be done on a reference material. Using 'scratch

width measurement tool' (found on NA software's menu bar), the widths of

the scratches need to be transferred to the hardness calibration window

(Measure → Hardness Calibration) and the calibration file needs to be saved

(*.cbr). The actual load values of scratches will be found from the load versus

time plot which was recorded using UMT software's 'Blackbox' tab of 'Semi

Automatic Panel'. Open that file using the 'Viewer' software and select 'Fz'

from the box on the middle right of the software's start-page. Use the scroll

arrows to find a particular scratch and position the left and right marker on the

start and end of the scratch-load, both by right clicking. This will give an

output of the average and standard deviation of Fz in a lower left field. Record

this data and then position both the left and right markers on a place where

there was no scratch (i.e., the curve looks flat). Take note of this average value

and use this value to adjust the actual Fz force (either by adding them together

or by subtracting the later from the former, depending on the sign in front of

the values). These actual load values need to replace the corresponding

nominal load values on the calibration file that was saved by the NA

software's Measure→ Hardness calibration function. Consult the manual for

details about how to create a calibration file. Calibration files (also sample data

files) can be opened with the built-in software and can be edited for correct

load values. Once this is done, the calibration file is ready to be used as

standard of measuring the hardness of an unknown material. On the sample

surface, similar scratches of nominal loads (200μN to 1500μN) need to be

produced. After the scan is done on the scratches, the width needs to be

calculated using the 'scratch width measurement tool' on the menu bar. The

values need to be transferred to the Measure → Hardness measure window.
The actual values of loads, as recorded by UMT software, need to be put on the
respective field of nominal loads (highlight a cell first and then edit it). For
hardness calculation, an appropriate calibration file (that was saved earlier)
needs to be loaded and a comparing value of hardness, as measured with the
following formula, is automatically calculated by the software:

$$\text{Hardness}_{known}/\text{Force}_{known}=\text{Hardness}_{unknown}/\text{Force}_{unknown} \qquad (I.1)$$

It is noted here that, by connection, only similar width scratches should
be compared to each other. For example, if a scratch on an unknown sample
produces 200 nm width, only a scratch width of 200 nm or similar on
calibration standards should be compared with it [105]. In sclerometry method,
the hardness value is calculated as:

$$H = k_s F_z / w^2 \qquad (I.2)$$

where k_s is the coefficient of the tip shape, F_z is the actual normal load to
produce scratch and w is the width of the scratch. The shape of the indenter is
very important in determining k_s [108] and in reality, is very difficult to
characterize with sufficient accuracy. For similar widths, if the normal load is
F_{zc} on a known material and is F_{zs} on an unknown material, then the hardness
of the unknown sample H_s is computed from equation (I.2) that is a rewrite of
equation (I.1) and is given by:

$$H_s = F_{zs} \frac{H_c}{F_{zc}} \qquad (I.3)$$

Since for the same scratch width, the volume of the tip submerged into the specimens are same, the coefficient of tip shape remains unchanged. Thus comparing similar widths alleviates the necessity of accurately knowing the tip shape coefficient.

I.B.2.b   In the direct method of measuring hardness, only width and actual load values are necessary to be known from the scratch testing. Using the following equations [101, 102, 103] the hardness of the sample H can be determined as:

$$N = \frac{\pi}{2} H r^2 \sin^2 \alpha - s r^2 \{\sin \alpha - \cos^2 \alpha \ln(\sec \alpha + \tan \alpha)\} \quad (I.4)$$

where, N is the normal (actual) load, H is the hardness, r is the radius of the tip (typically about 100 to 500 nm for Berkovich tips), s is the shear stress. The α is the angle related to the tip radius (r) and scratch width (w) such as:

$$\alpha = \sin^{-1}\left(\frac{w}{2r}\right) \quad (I.5)$$

The second term in the equation (I.4) is usually very small. By using the expression for α, the equation for hardness can be simplified to:

$$H = \frac{8N}{\pi w^2} \quad (I.6)$$

Since $8/\pi$ equals the area under the leading half of the surface area for a spherical indenter tip that is on contact with the surface. Note that, equation (I.6) and equation (I.2) are similar. However, the major assumption in this analysis is that the indenter tip does not pass beyond the spherical regime of

the tip. For shallow and narrow scratches, this is true. However, for sharp tips, this assumption becomes questionable, and may not be the case. Moreover, the hemispherical part on the top of the tip is not always perfectly hemispherical. So, it is recommended to keep *w*<2*r* [66].

I.C Elastic Modulus Measurement

I.C.1 Producing approach curves

In approach curve experiments, the UMT software does not need be open. All the necessary operations and data acquisitions can be done from the Nano Analyzer software. For an elastic modulus measurement, the surface of the sample needs to be scanned first, for the presence of any artifacts or prior deformation. Also, for best results, the surface needs to be purely flat, since the underlying assumption of tapping mode elastic measurement is Hertzian contact mechanics, i.e., the probe meets the surface only at a point. However, it may not always be the case and that is why, repeated experiments at same condition will give a better confidence level. Once a defect-free area of the sample is scanned, the standard operating procedure is as follows:

I.C.1.a   The first step is to allocate the amount of frequency shift and the position of the approach curve measurement. For this, the scanned area needs to be sent to the measurement panel, the test mode needs to be changed from scratch to approach curves (from the drop down list in the lower part of the measurement tab), and the amount of frequency shift needs to be put on the dialogue box (Please refer to the image on page 18 of the NA-2 manual). It is recommended to produce at least 3 approach curves for the same frequency

shift. The range of frequency shift is varied, generally, from 200-1200 Hz. For softer materials, lower range is sufficient while for harder (stiffer) materials, a larger range is needed. The aim is to produce approach curves (typically looks like a flattened 'S' curve) which would have a linear elastic regime of loading as well as some plastic loading (see Figure I.1).
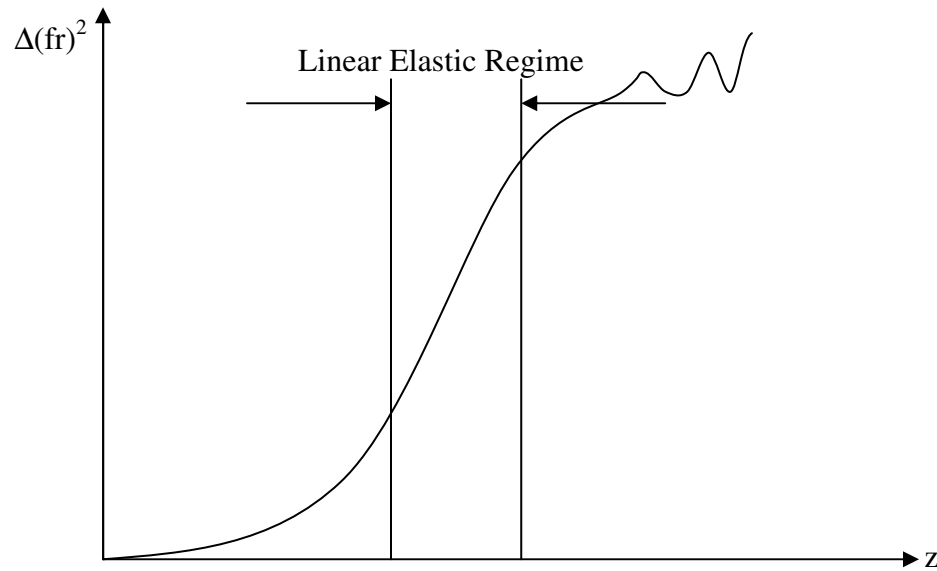
Figure I.1: A typical square of frequency shift versus vertical distance curve

I.C.1.b   Go to Device→Settings→Approach Curves and make sure that the automatic curve processing box is checked. This option will automatically filter the measured curves (user defined, generally the filter coefficient is 3) and square them before plotting.

I.C.1.c   Check that the 'Add' button (on the Menu bar) is pressed. This will plot all the approach curves on a single plot.

I.C.1.d   With a value in the 'Frequency shift' field, click on the scanned image

shown on the measurement panel. A cross-hair would appear on the image,

which denotes the position of the measurement. The table below would also

show this value (position and the amount of frequency shift). You may also

edit those values from the table, in case of need. Once you have positioned all

the points (according to your need) with corresponding frequency shift values,

click on 'Run'. Wait until the experiment is finished.

I.C.1.e   When all the approach curves are measured, all the lines (on the Δf^2

window) need to be aligned with each other, i.e., overlay the individual curves.

For this, there is a function on the graph manager (GM) panel named 'Align'.

However, individual lines can also be aligned by selecting them individually

from the graph manager panel and moving them with the arrow keys on the

keyboard (Please refer to the image on page 28 of the NA-2 manual).

I.C.1.f   Once all the lines are aligned, put the left marker and right marker on

the linear portion of the Δf^2 versus z plot (left and right mouse clicks

respectively). Click on the slope button that will plot the slopes of all the lines

with an average and standard deviation value. This command will not work if

the lines are not squared. If automatic curves processing does not square the

curves, the squaring has to be done manually from the graph manager panel

from 'Process' tool on the menu bar. If the standard deviation is too high

(>10%), deselect some of the lines with high deviating values using the graph

manager panel.

I.C.1.g   Once this task is completed, open the elastic modulus measurement

window from Measure→Elastic Modulus. Create a new material file. If you

are measuring a calibration material, create a new calibration material file; give

it a name and its elastic modulus. Otherwise create a new sample file.

I.C.1.h   On the slope calculation window, click on the 'Add value' button

(Please refer to the images on page 79 of the NA-2 manual). This will add the

average slope (α) of all the curves in the elastic modulus calculation window.

If you are measuring a calibration material, make sure that material is selected

before clicking on 'Add value'. Similarly, for measuring a sample, make sure

that sample is selected beforehand. In the later case, a calibration file needs to

be loaded from the 'Elastic modulus measurement' window. Calibration files

can be made in a similar way for known materials, for example, fused silica,

sapphire, polycarbonate, etc.

I.D Probe Tuning

For probe tuning, it is necessary to copy an existing probe file (with the

extension *.prm) and rename it for the new probe. Probes with ceramic cantilever have

suffixes 'CW' and probes with metallic cantilever have suffixes 'M'. The UNMT

hardware should be turned on only after the physical installation of the new probe. So,

press the red 'Stop' button on the front of the machine before proceeding and press the

green 'Reset' button after the new probe has been installed. Before starting up the NA

hardware from the software environment (i.e., Device→Run), the new renamed probe

should be selected from the 'Change probe' menu (Please refer to the image on page

43 of the NA-2 manual). The standard procedures to follow are:

I.D.1   Run the Auto Setup (from Probe tab) to see if the probe is tunable. The

Auto Setup operation will return a curve which should look like a bell shaped

(see FigureI.2). If the probe does not have any physical or other type of

damages, the maximum point on the bell shaped curve will be close to the set

amplitude value.

Am (nm)

Fr (kHz)
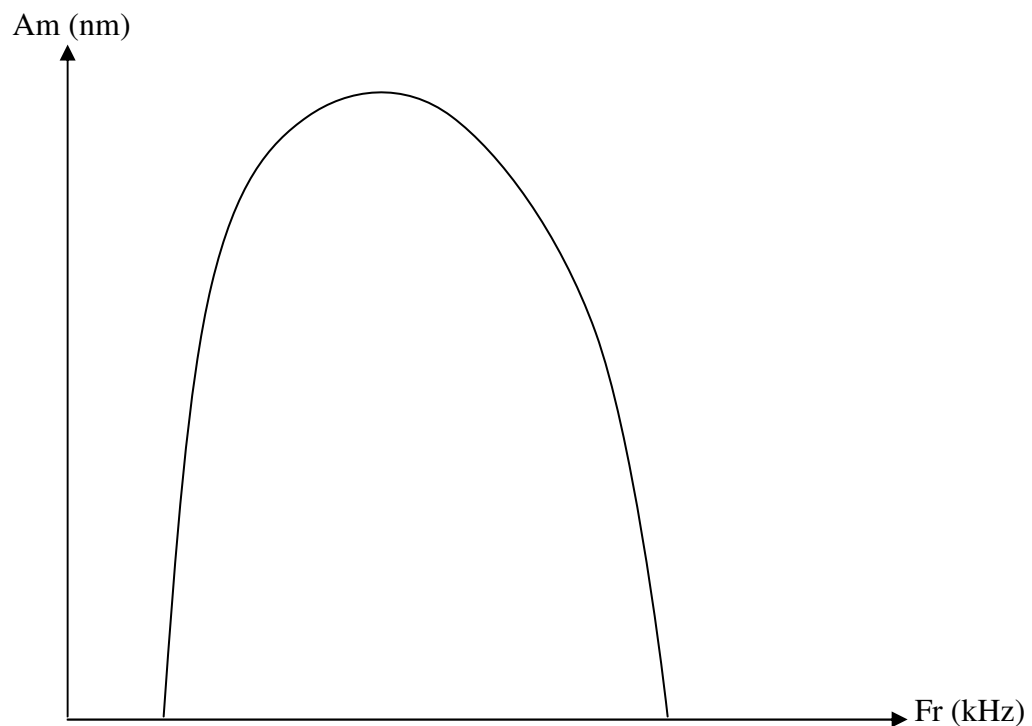
Figure I.2: A typical Auto Setup curve

I.D.2   Next, it is necessary to find a set point at which the Z(nm) indicator

starts to increase. Start from the lower set point and work your way to a higher

set point with an increment of 0.05 by clicking on the arrows below the set

point indicator. Once that unstable set point (z indicator starts to increase

rapidly) is found, decrease the set point by 0.5% and save it. It is necessary to do this only for the first time installation of a new probe.

I.D.3   Next, one of the AFM grids (depending on the tip radius) needs to be mounted on the NA for scanning. The grid needs to be placed in such a way that the grid lines lie perpendicular to the x axis scanning direction (1-2 degrees misalignment is acceptable). About 20 -30 lines (typically in the dimension of 60 μm by 10 μm) need to be scanned along the x axis direction on the grid.

I.D.4   Process the z-image with the line tilt and step correction.

I.D.5   Next, click on Process→Height histogram from the menu. This will reveal the height difference for the whole scanning area. If the probe is not calibrated, the height histogram value returned by the program will be very different compared to the actual height of the grid being used (TGZ1: 20.5±1 nm, TGZ2: 104.5±2 nm, TGZ3: 510±4 nm). These height difference values and the period (3.00±0.01 μm) for the grids are listed on the AFM grid box. Figure I.3 shows the TGZ1 grid scanned using Probe 41m. The height histogram command will return a dx value (at top right corner of the plot that will pop up). A height histogram plot for TGZ1 is shown in Figure I.4. From Device→Calibration→ADC z feedback, this dx value needs to be put into the 'measured z step' field while the actual value (TGZ1: 20.5±1 nm, TGZ2: 104.5±2 nm, TGZ3: 510±4 nm) needs to be put into the 'reference z step' field. For example, if the TGZ2 grid is being used and the height histogram on the

processed z image returns a dx value of 101.2 nm, then on the 'reference z step' field, put 104.5 (the actual height difference for using TGZ2 grid) and on the 'measured z step' field, put 101.2 (the measured value for height difference with the yet-to-be calibrated probe).
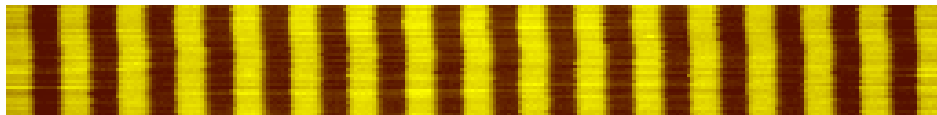
Figure I.3: AFM grid TGZ1 scanned with Probe 41m
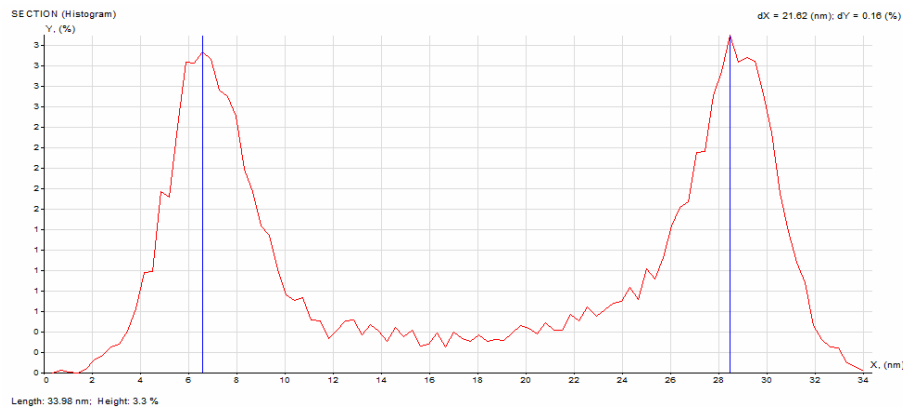
Figure I.4: Height histogram on the z image of TGZ1, after processing

I.D.6   Follow the same procedure stated on I.D.4 and I.D.5 with the ZOpt image. In the Device→Calibration→ADC ZOpt optic sensor, put the measured value of dx from height histogram in the 'measured ZOpt step' and the actual value (which is the same as the z height of the grids as stated above) in the 'reference ZOpt step' field.

I.D.7 Once these steps are complete, it is appropriate to begin the load non-linearity test. First, retract the probe from the sample (i.e., the AFM grid) surface and move it a few millimeters above the surface. Next, run the test from Device→calibration manager→load nonlinearity. Since this load non-linearity test uses ZOpt as input parameter, it is extremely important to finish the ZOpt calibration (I.D.6) first and then to run the test. This test may take 15 to 30 minutes depending on the existence of previous non-linearity tests. Load non-linearity tests are important for the probe to apply a load on a sample close to the nominal input load value. The load non-linearity tests are probe specific and have to be done for every new probe installed for the first time.

I.D.8 After the load non-linearity test is completed, the x and y distance calibration is performed next. Bring back the processed z image file of the AFM grid used in step I.D.3, and using a horizontal marker from the menu, measure a section of the image (with a left and right click). The resulting plot should appear like Figure I.5.
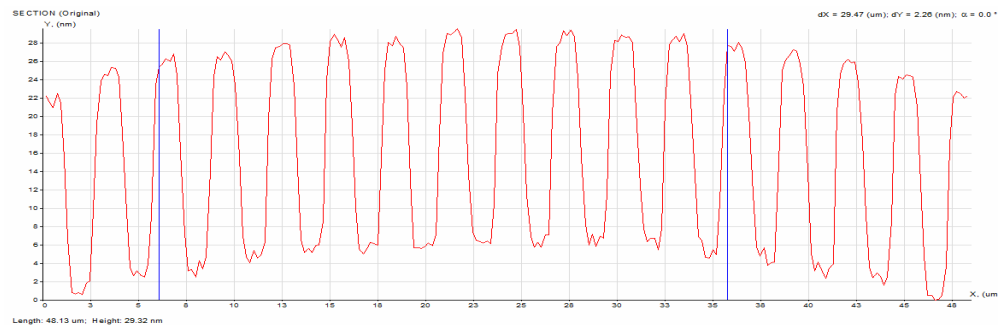
Figure I.5: A horizontal section of the scanned TGZ1, after processing with line tilt and step correction

I.D.9   On the figure from step I.D.8, put the right marker at the beginning of a

cycle and after 10 cycles (or 20 cycles, depending on the size of the area

scanned), place the right marker. Take note of the dx value on the top right

corner of the plot. Now from the Device→Calibration→xy scanner window,

put 3.0 (the width of a cycle in microns, as stated on the AFM grid box) in the

reference x step width field, and the measure dx value (from the mentioned

figure) divided by 10 (or 20, depending on how many cycles you counted) on

the measured x step width field. Press 'OK' to exit the window. You may

check the calibration by scanning an area again on the grid and measuring a

number of cycles.

I.D.10   Rotate the AFM grid by 90 degree and scan in the y-direction (radio

button on the scan panel). After processing the z-image, take a vertical marker,

measure 10 cycles, and note the dx value. This time, put the dx value divided

by 10 on the measured y step width field in the xy scanner window. The

reference value is 3.0, as stated earlier. If you like, you may check the

calibration by scanning the area again. The xy scanner calibration is not probe

specific and hence, needs to be done only once. Even if new probe is installed,

the xy calibration will still hold true, as opposed to z and z-opt calibration and

the load non-linearity.

I.D.11   Once all of these tests and calibrations are done, run the amplitude

correction test from the Device→Calibration→ Amplitude Correction menu.

After the test is complete, a window will appear (see Figure I.6. Also, please

refer to the image on page 58 of the NA-2 manual). Put the left marker on '0'

and the right marker at the beginning of the section where it approaches the set

amplitude value (100). Then click on 'Get from Curve' button.

Am (nm)
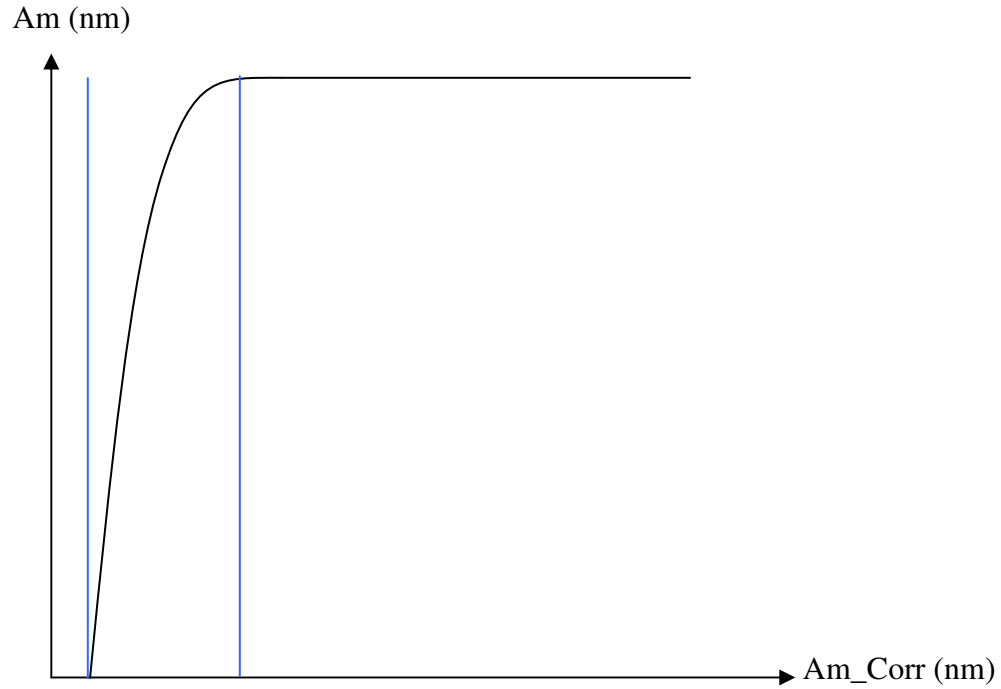
Figure I.6: Amplitude versus Amplitude correction curve

I.D.12   The probe is now ready to be used. Place a soft sample (for example

Polycarbonate) under the probe and do incremental indentations and record the

Fz values with UMT software. If the recorded normal force is considerably less

than the nominal load values at input, the load correction factor (that controls

creep of the probe cantilever) needs to be adjusted (from the Device→Settings

menu; Please refer to section 3.2.16 on page 37 of the NA-2 manual). A higher

load correction factor indicates more creep compensation and therefore applies

smaller biasing load on the cantilever. To bring the actual load closer to the

applied nominal load, the correction factor needs to be increased and

subsequent indentation tests are needed to justify the change.

REFERENCE FOR APPENDIX I

[141] E-mail communication with I. Hermann (CETR), 14-Feb-2008.

[142] E-mail communication with I. Hermann (CETR), 21-Oct-2009.

[143] Training at CETR with I. Hermann, Summer 2008.

[144] Phone conversation with I. Hermann, 13-Mar-2008.

[145] E-mail communication with I. Hermann (CETR), 21-Feb-2008

[146] E-mail communication with I. Hermann (CETR), 28-Feb-2008

APPENDIX II

APPROACH CURVES FOR ELASTIC MODULUS MEASUREMENTS

II.A Frequency shift curves for Calibration samples
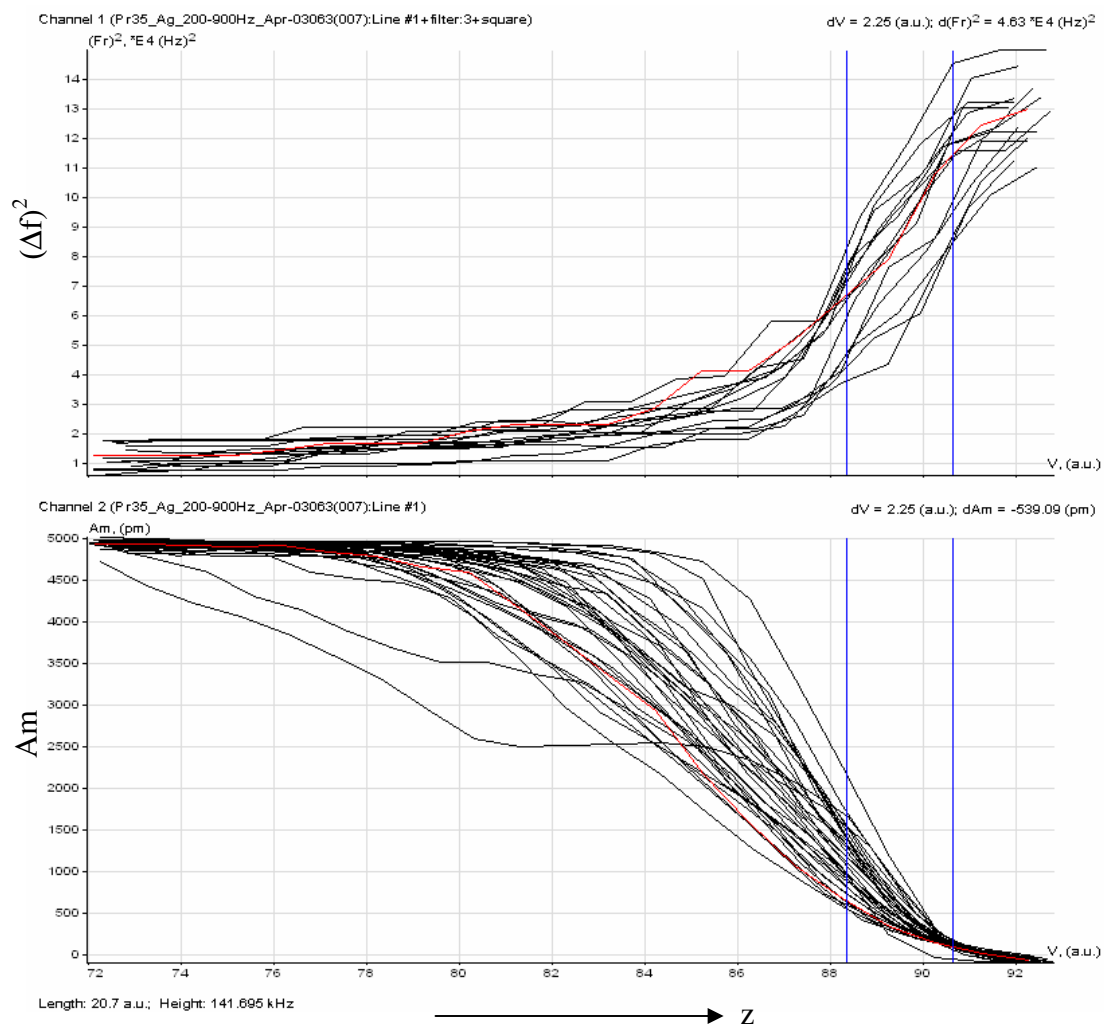
Figure II.1: Frequency shift plot of Ag (111)
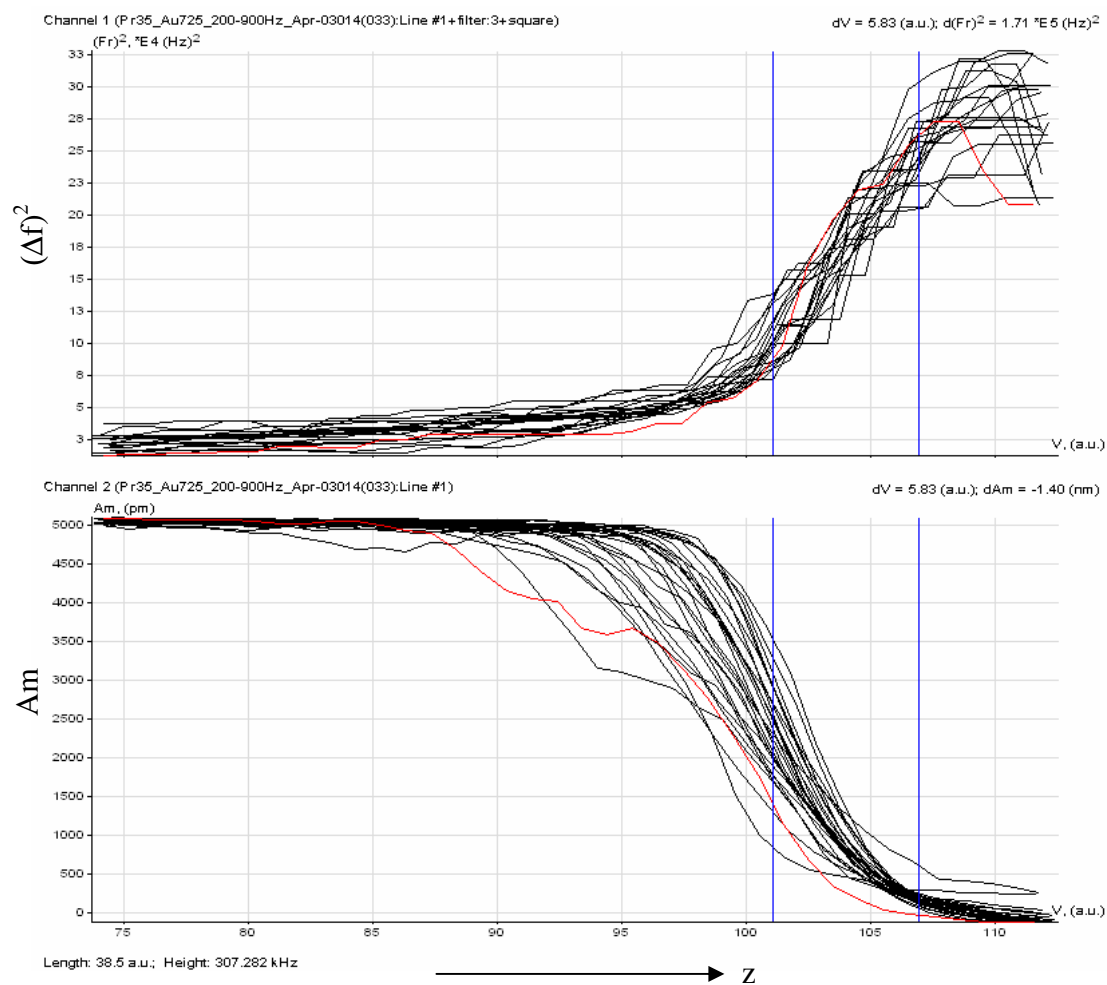
Figure II.2: Frequency shift plot of Au (111)
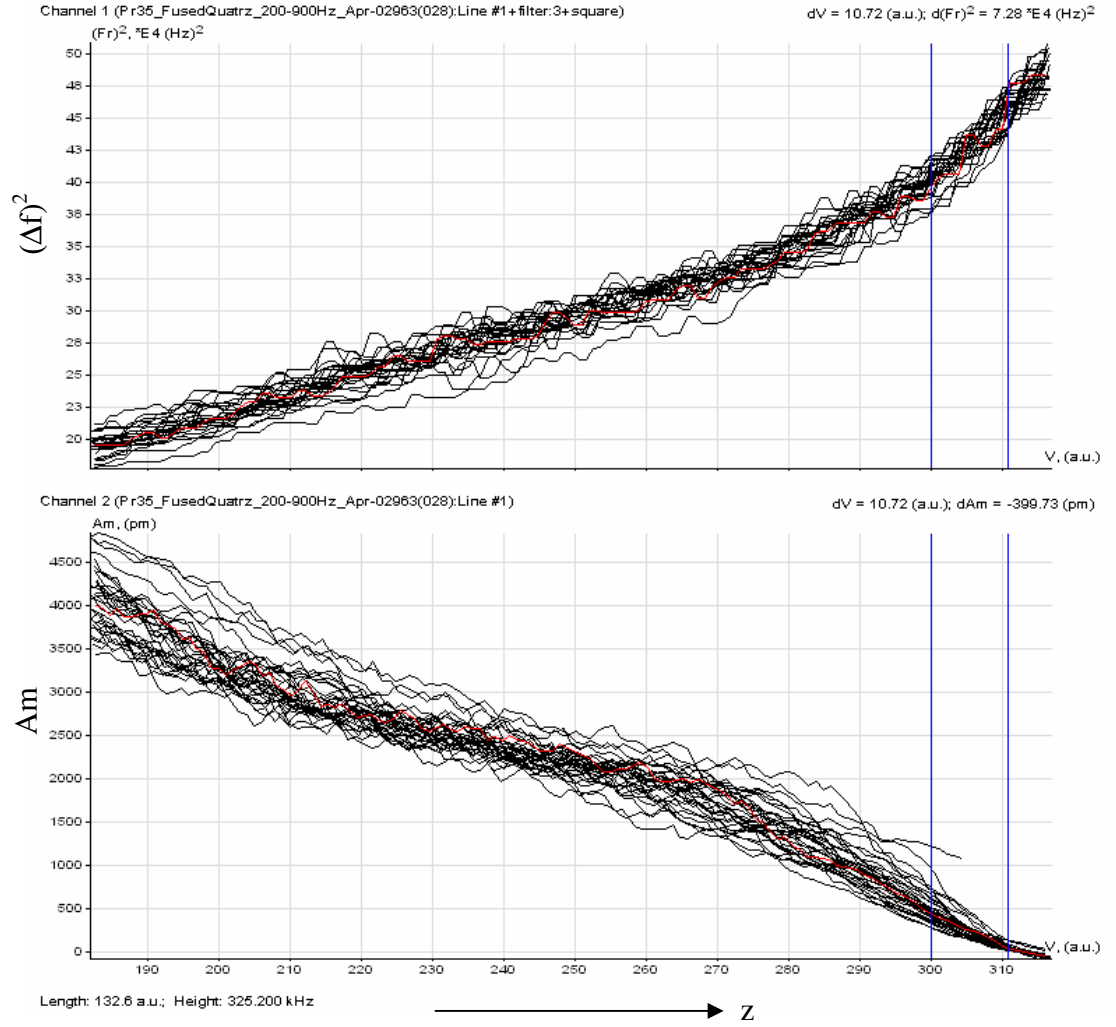
Figure II.3: Frequency shift plot of Fused Quartz
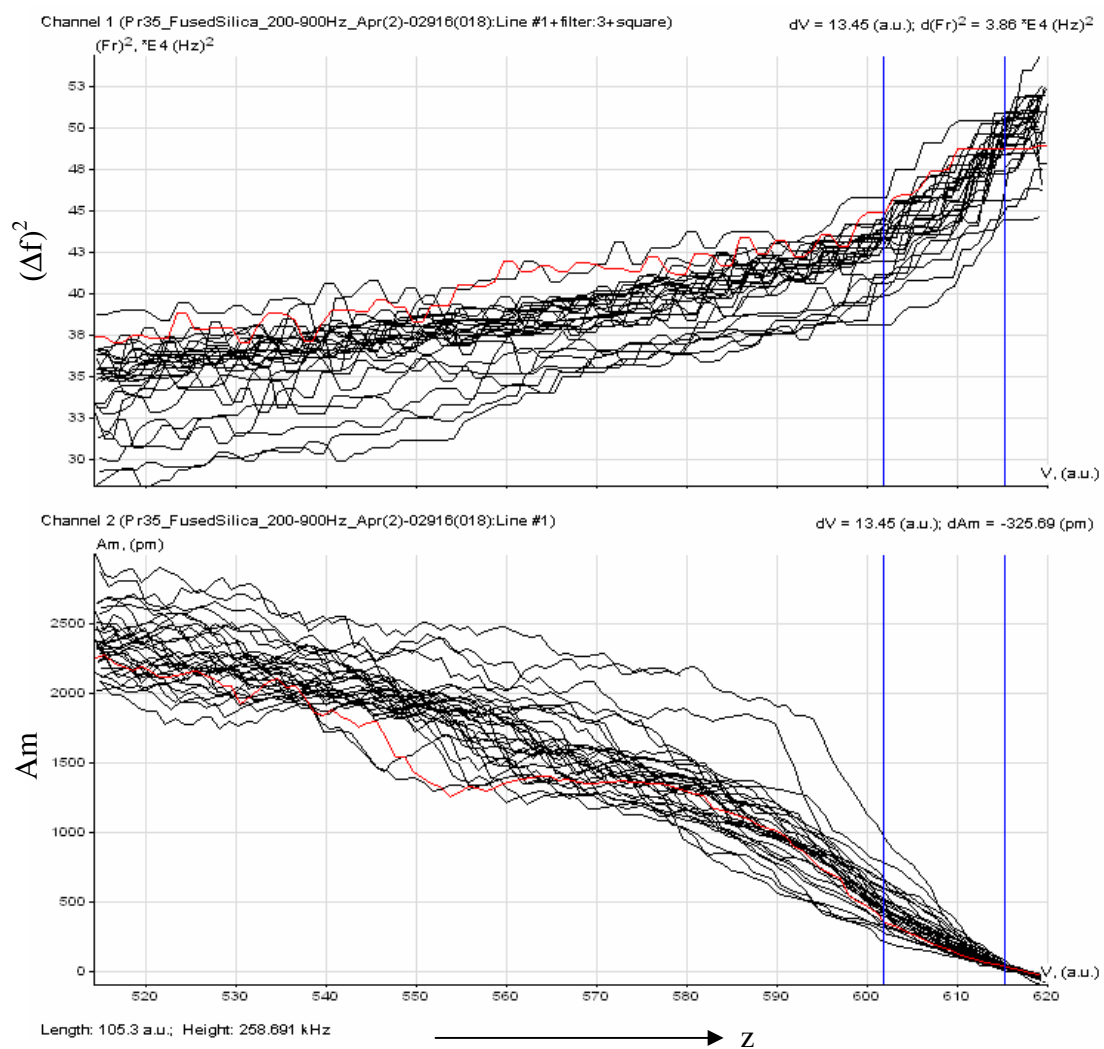
Figure II.4: Frequency shift plot of Fused Silica
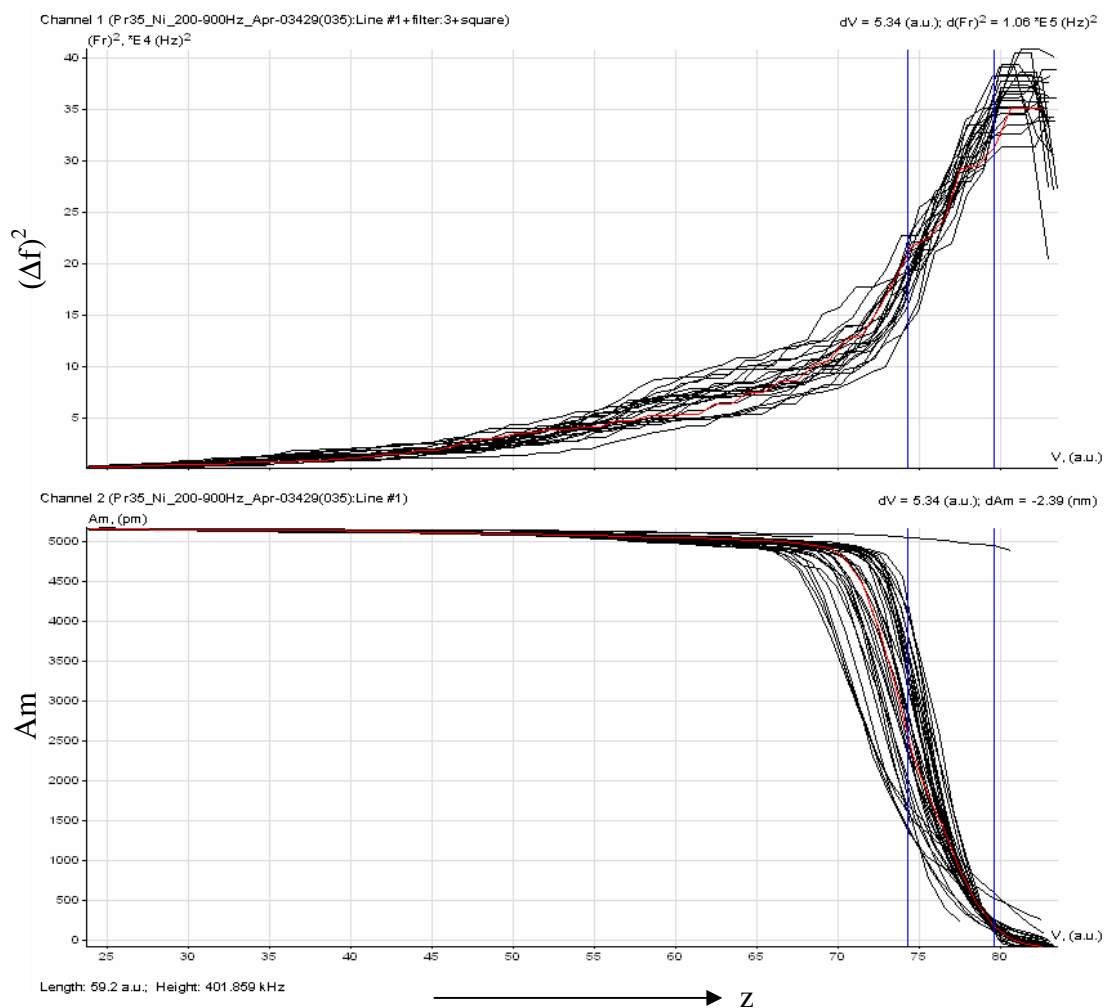
Figure II.5: Frequency shift plot of Nanocrystalline Ni (111)
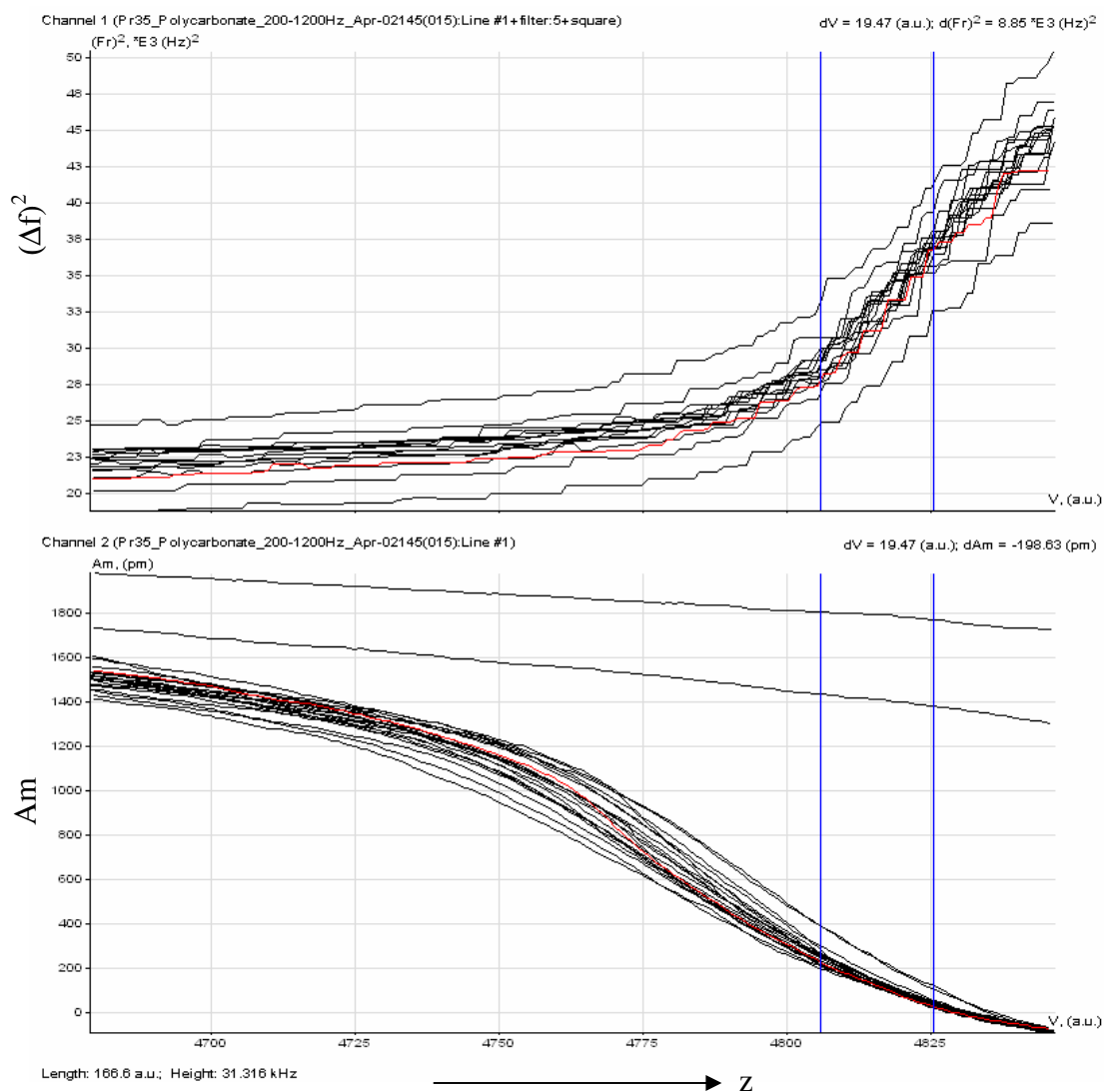
Figure II.6: Frequency shift plot of Polycarbonate
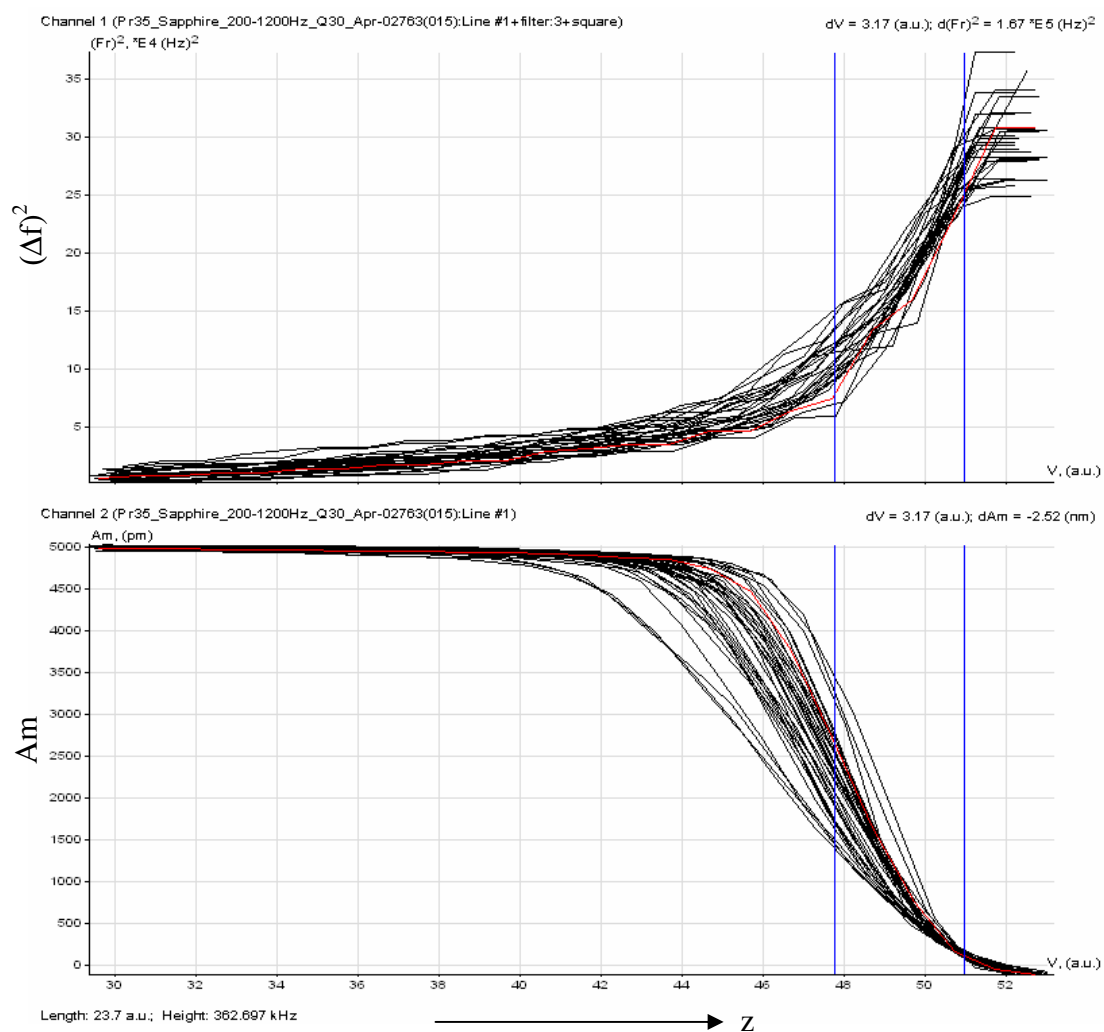
Figure II.7: Frequency shift plot of Sapphire
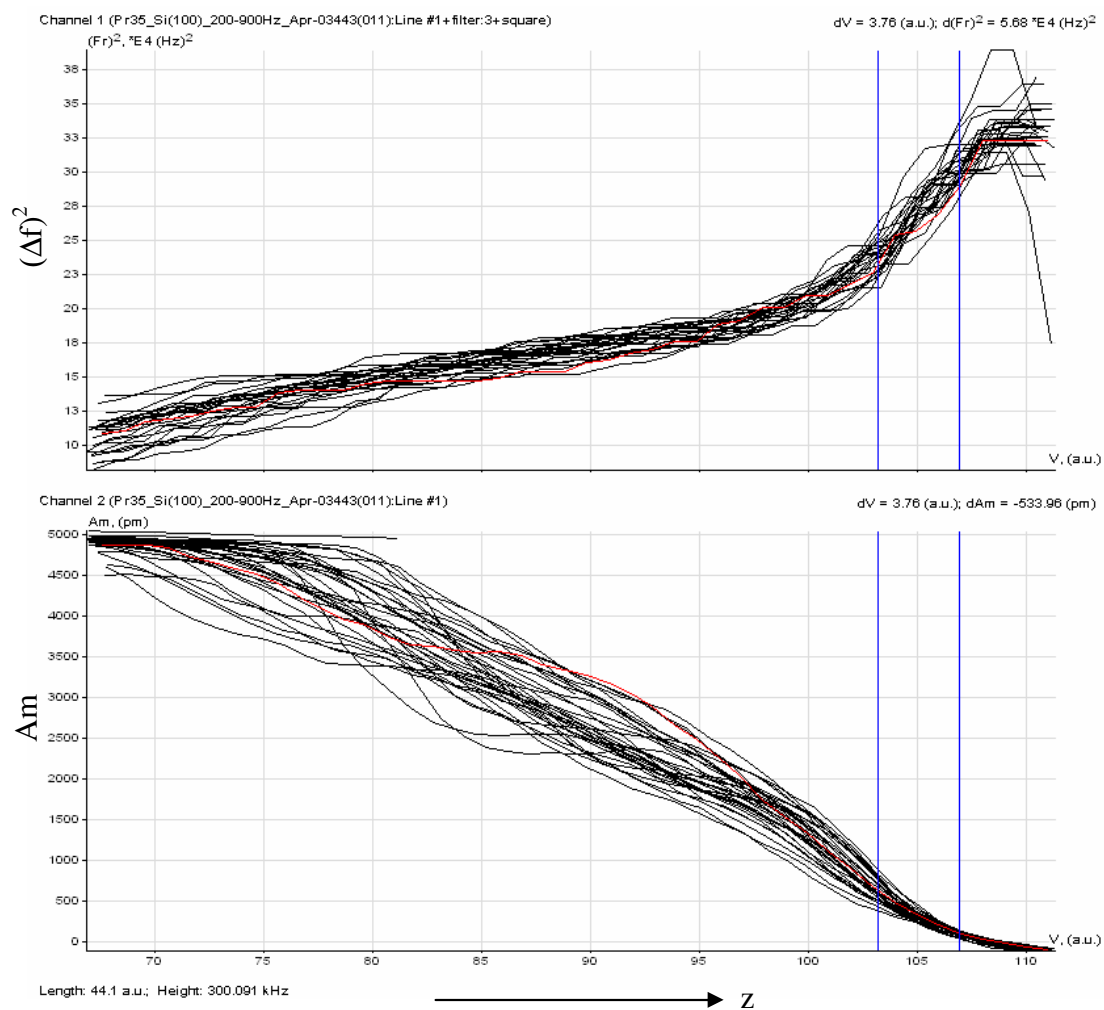
Figure II.8: Frequency shift plot of Silicon 100
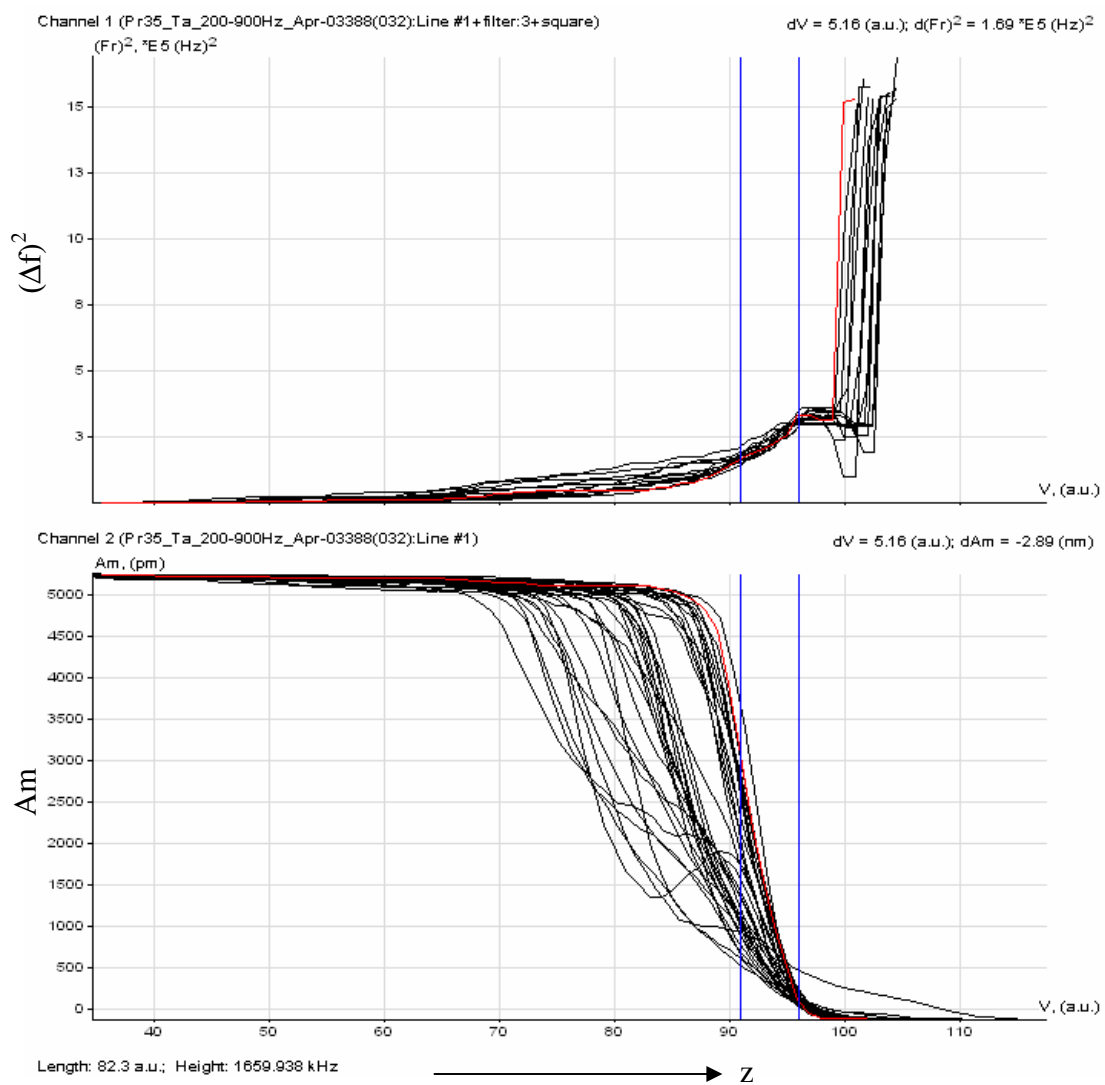
Figure II.9: Frequency shift plot of Ta (110)
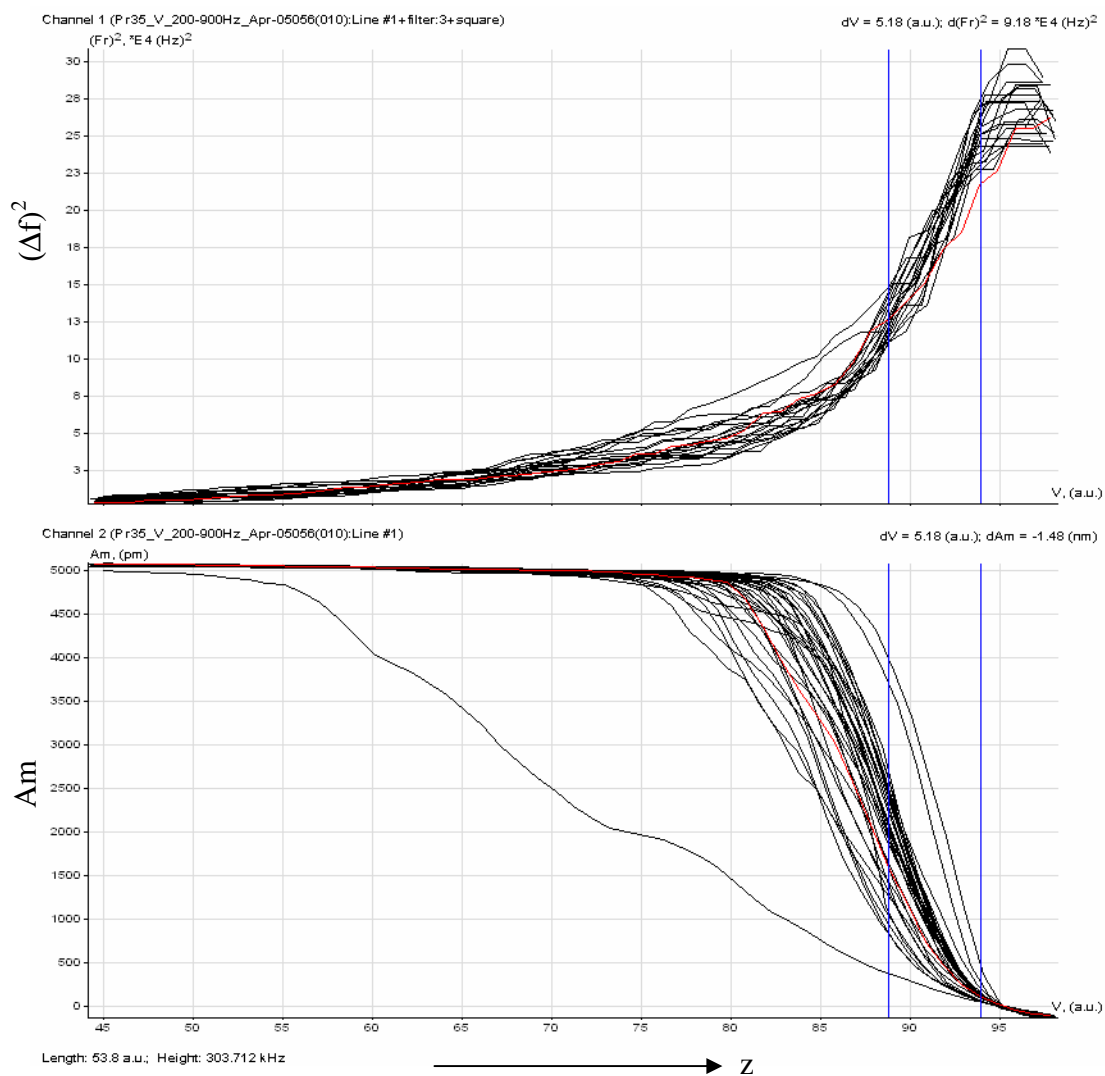
Figure II.10: Frequency shift plot of V (110)

II.B Frequency shift curves of Au-Ni samples
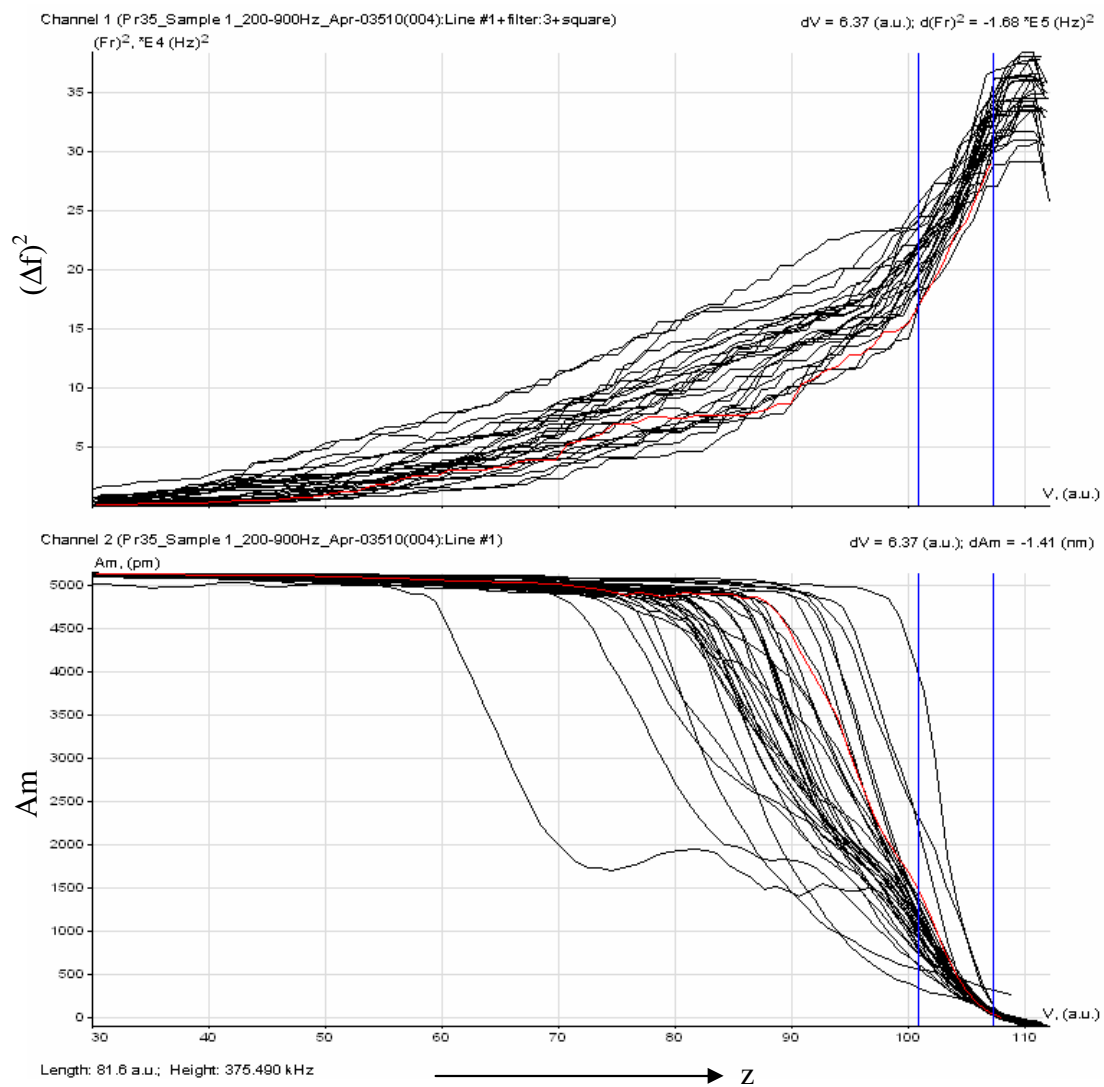
Figure II.11: Frequency shift plot of Au-Ni (λ= 1.7 nm) Sample 1
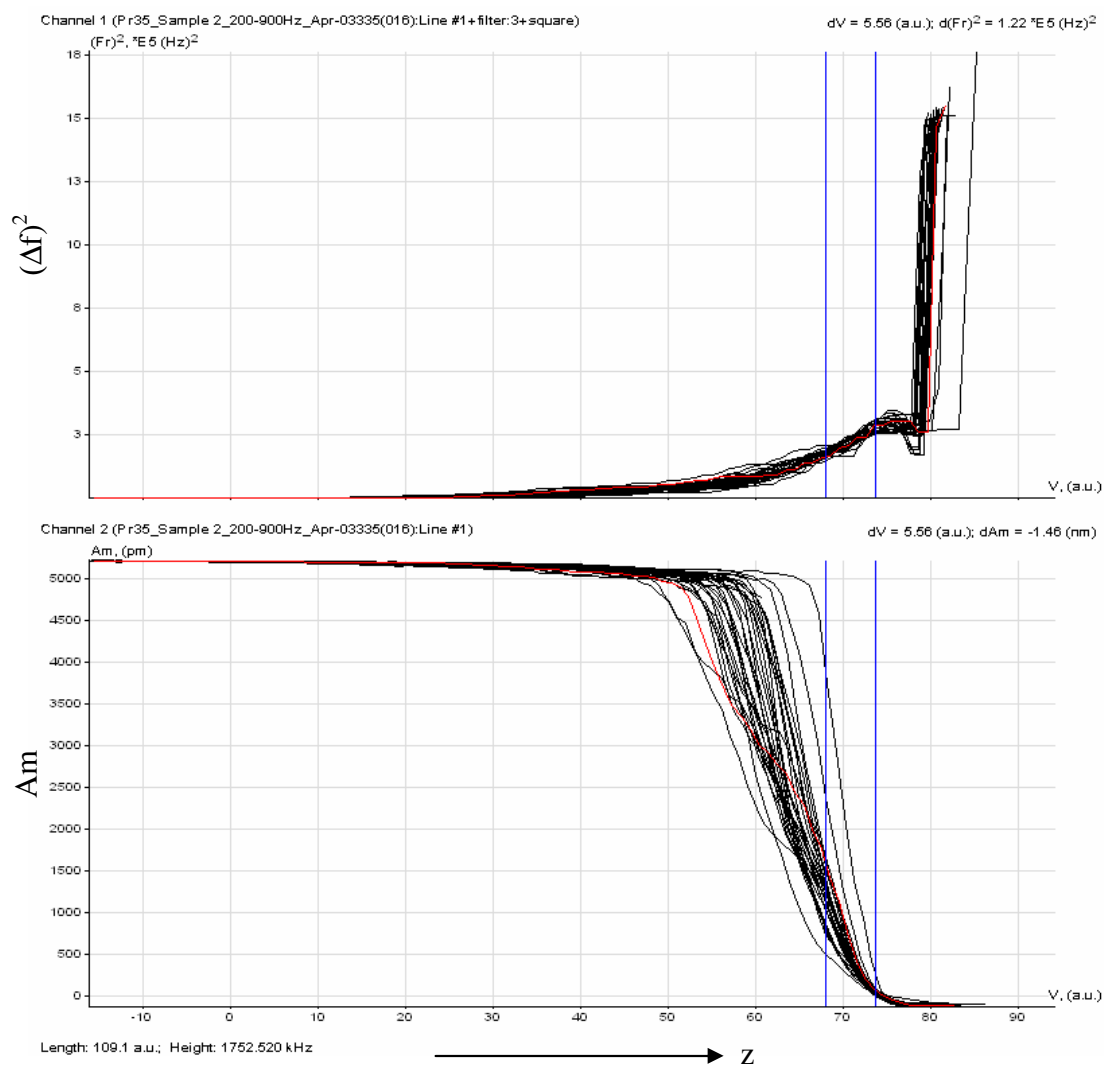
Figure II.12: Frequency shift plot of Au-Ni (d_g=16.0 nm, λ= 0.8 nm) Sample 2
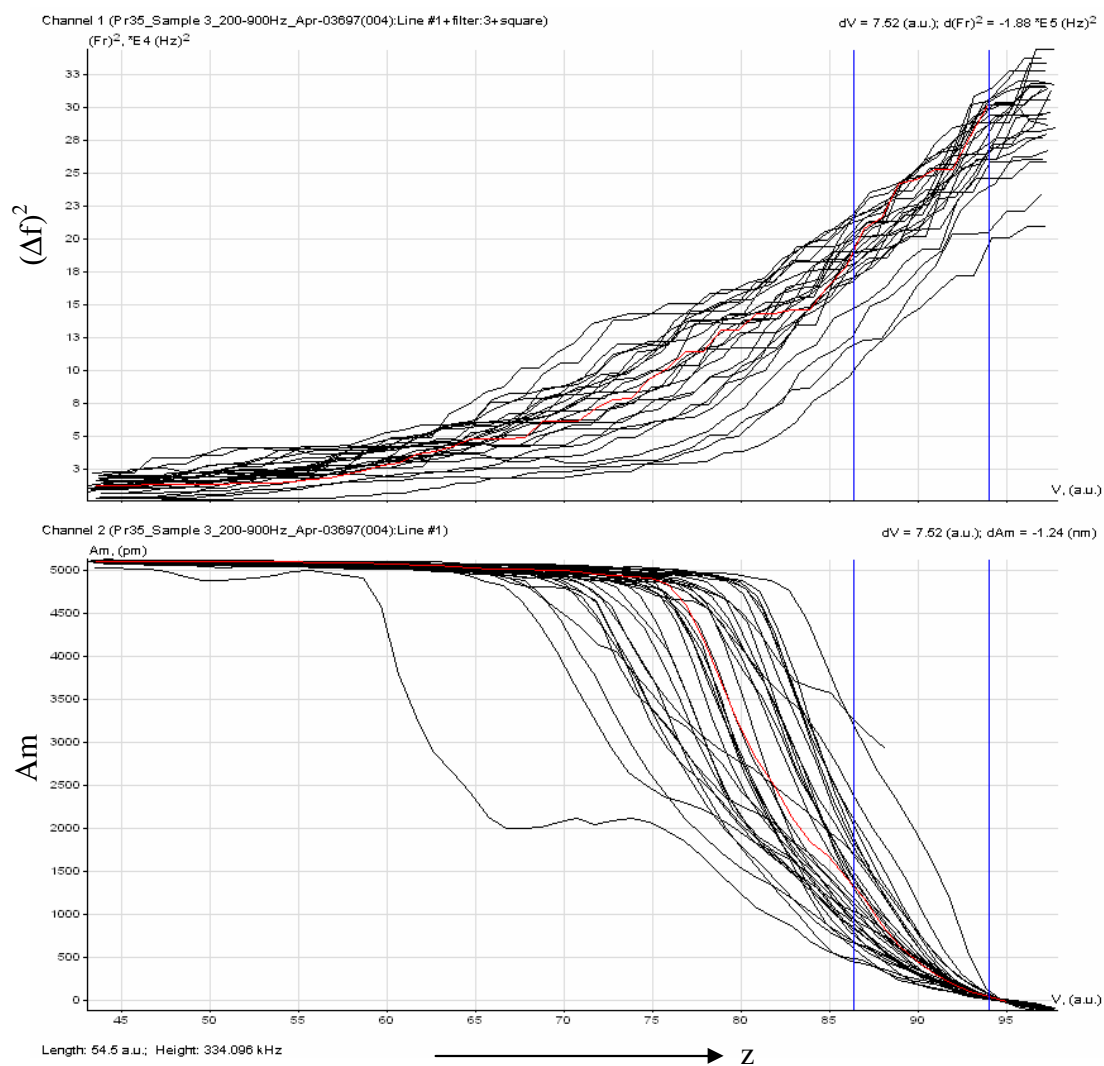
Figure II.13: Frequency shift plot of Au-Ni (λ= 4.0 nm) Sample 3
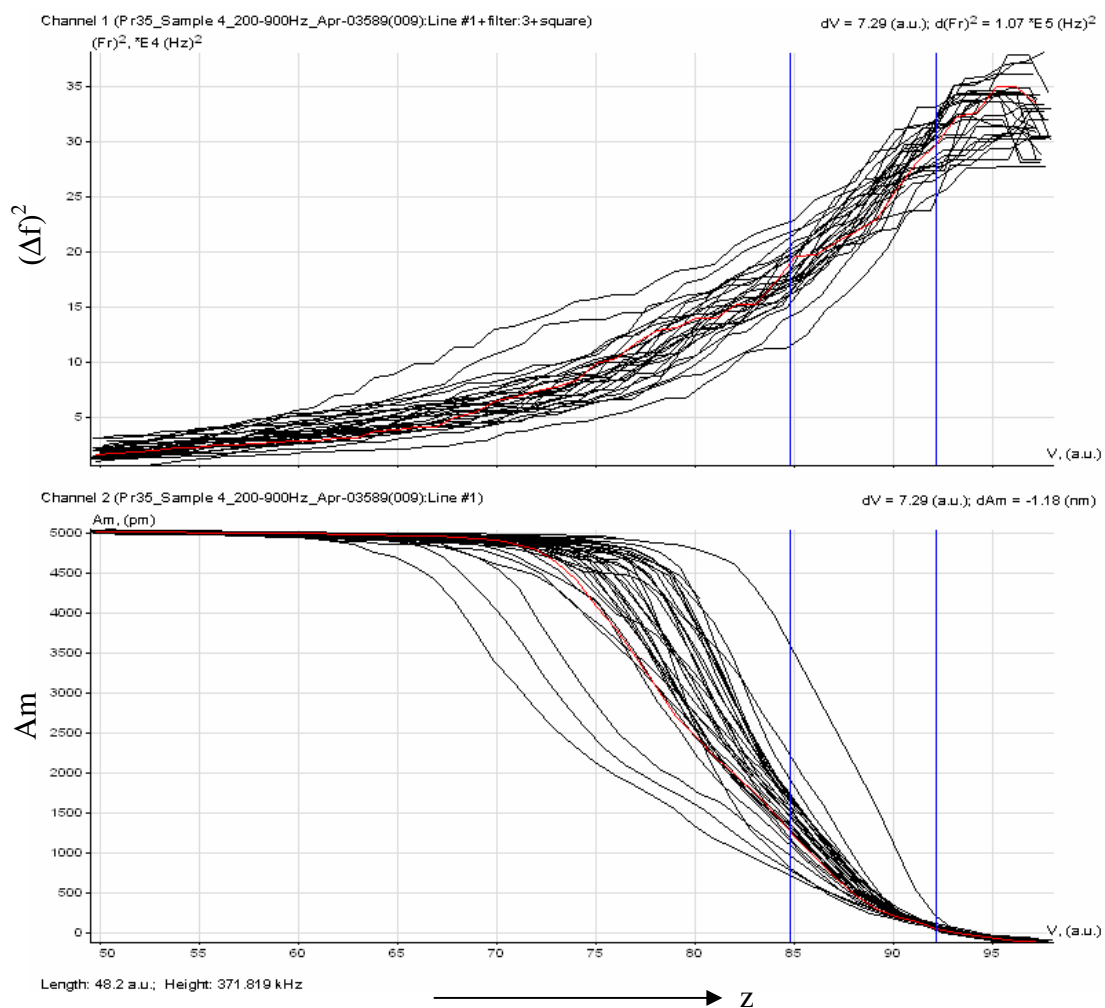
Figure II.14: Frequency shift plot of Au-Ni (λ= 0.9 nm) Sample 4
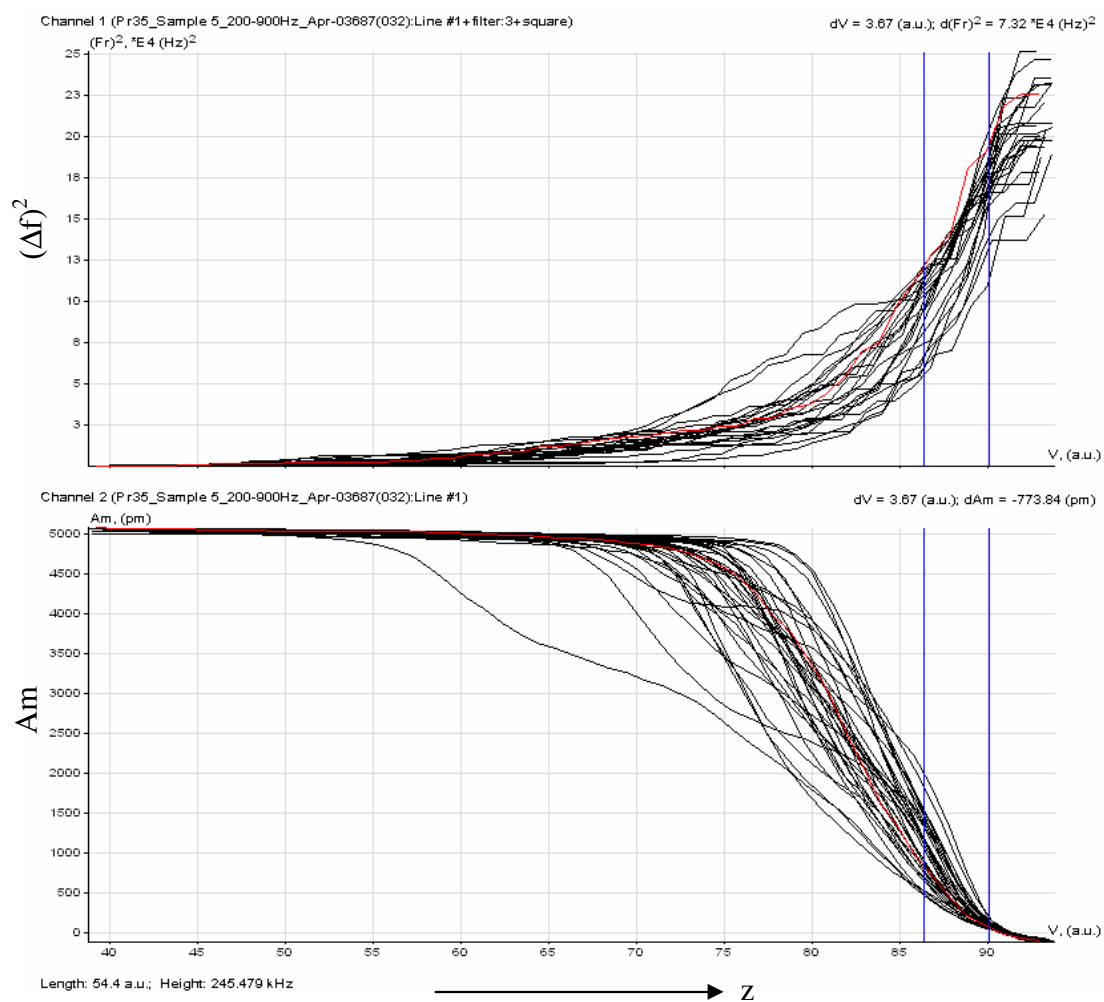
Figure II.15: Frequency shift plot of Au-Ni (λ= 1.2 nm) Sample 5
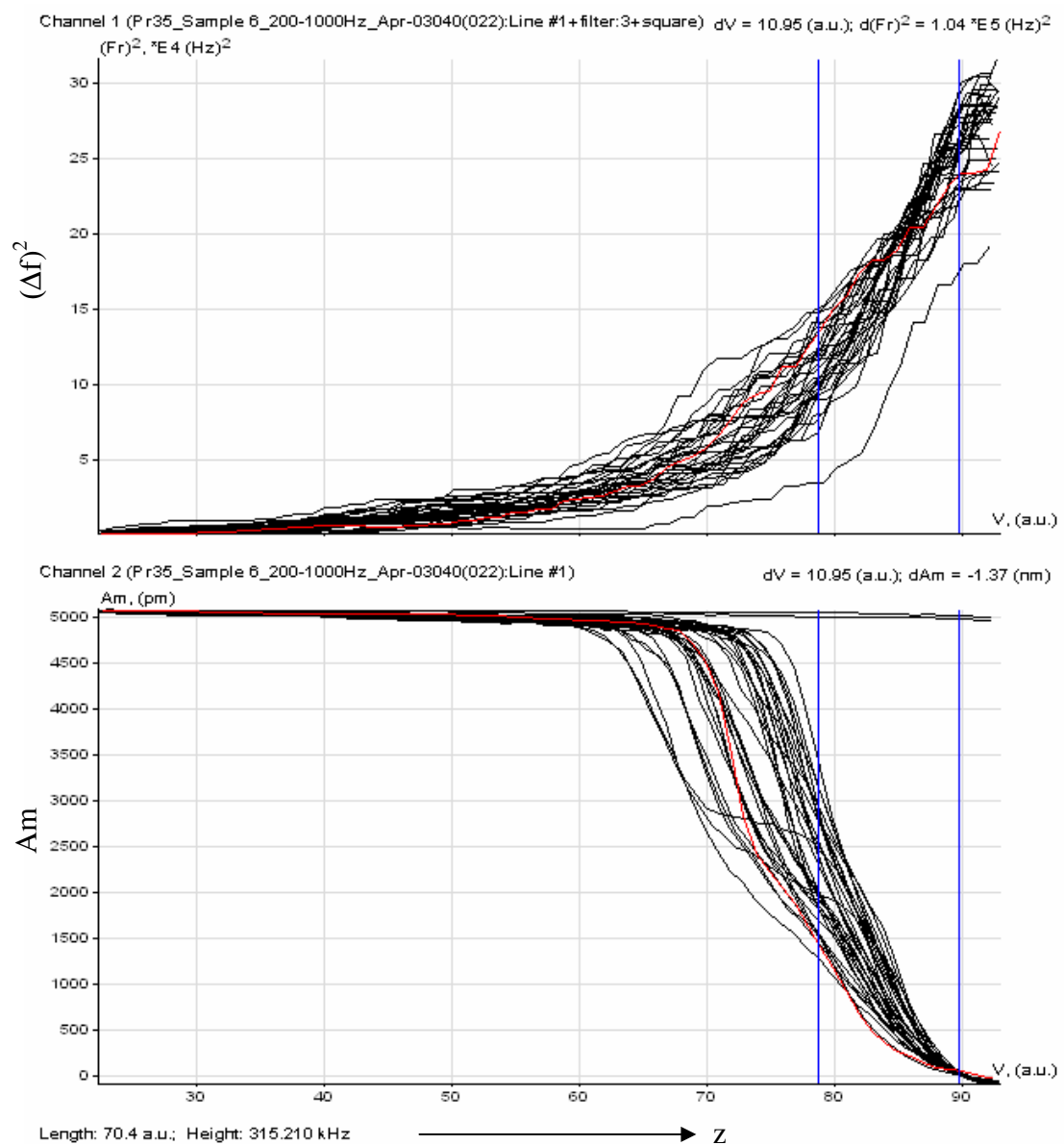
Figure II.16: Frequency shift plot of Au-Ni (d_g=15.2 nm, λ= 4.5 nm) Sample 6
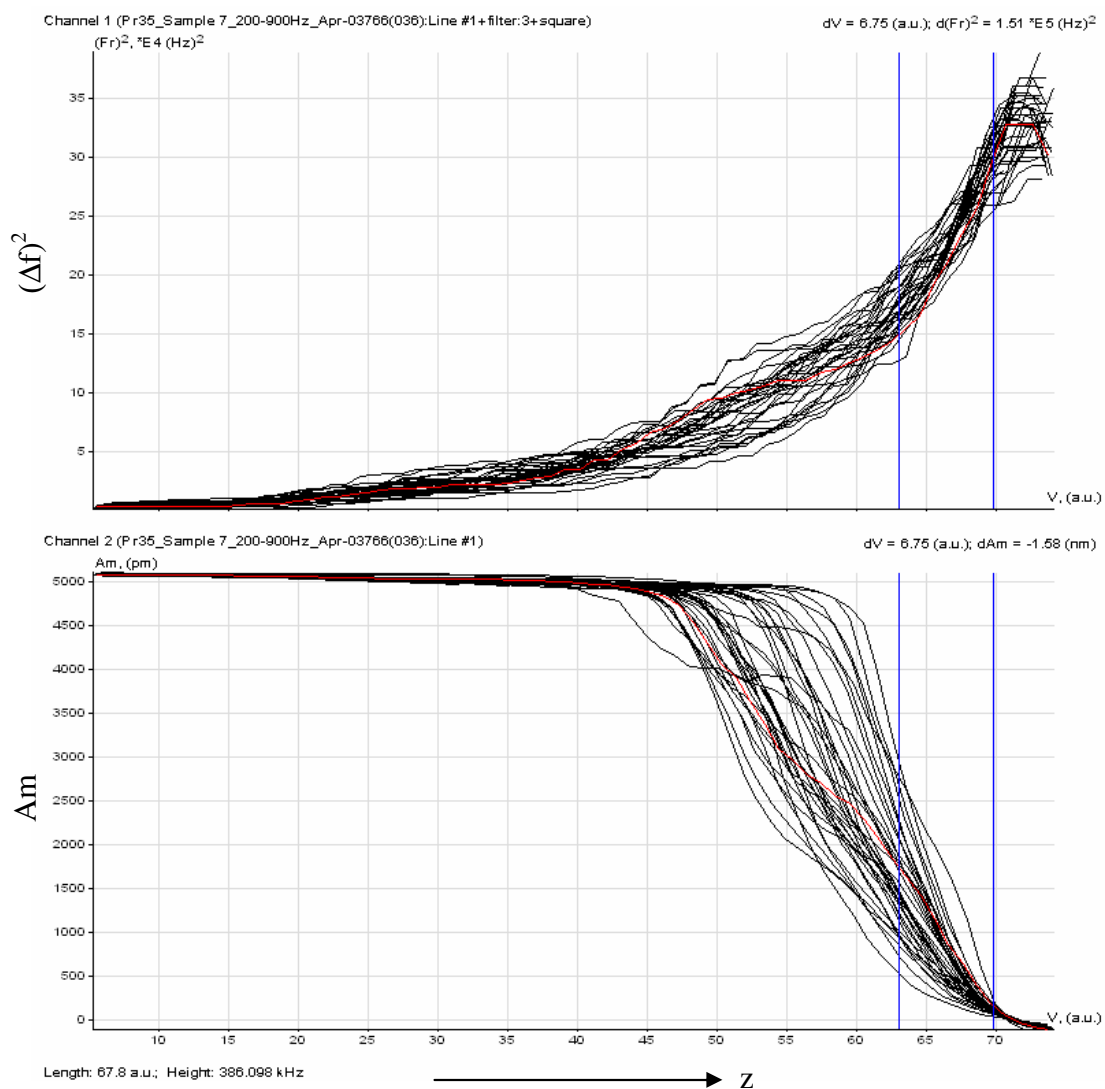
Figure II.17: Frequency shift plot of Au-Ni (λ= 1.9nm) Sample 7
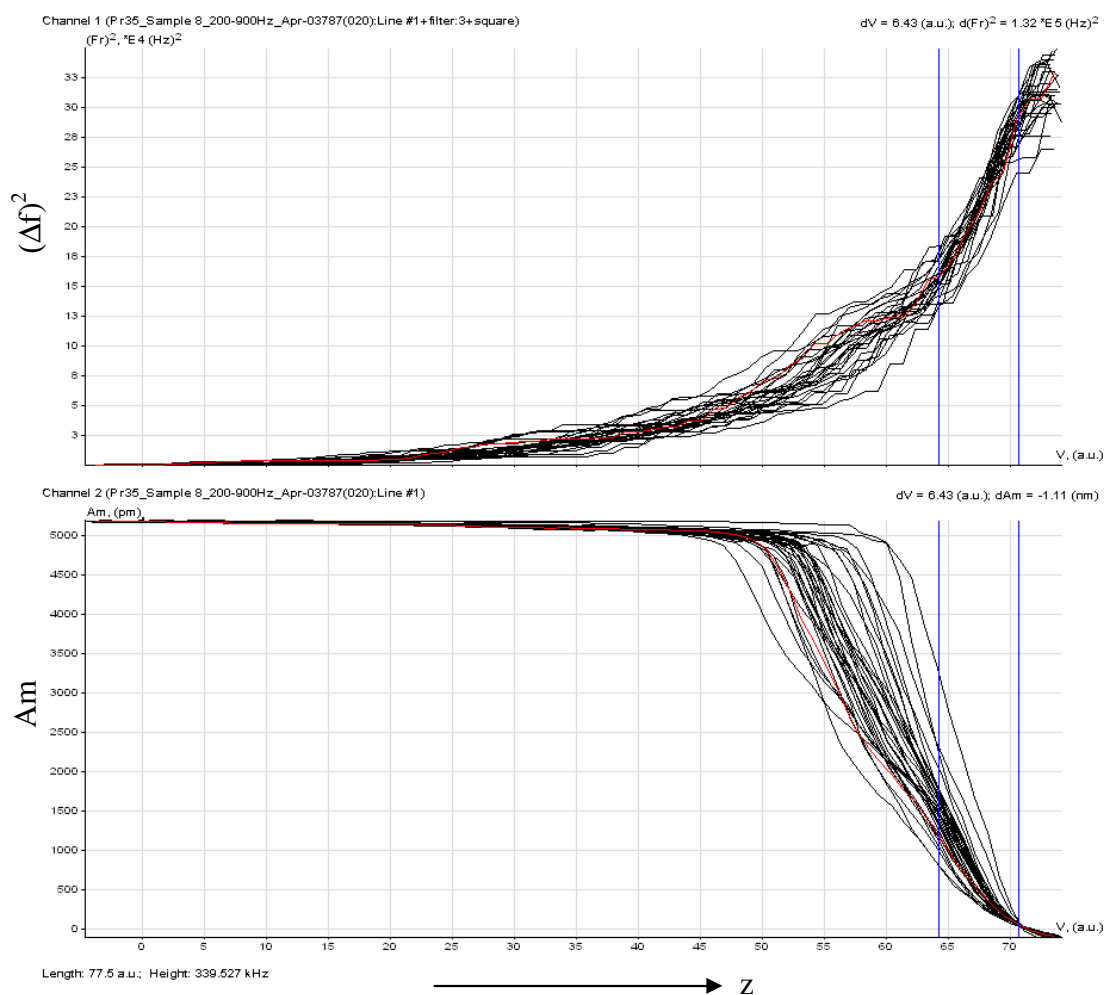
Figure II.18: Frequency shift plot of Au-Ni (λ= 1.6nm) Sample 8
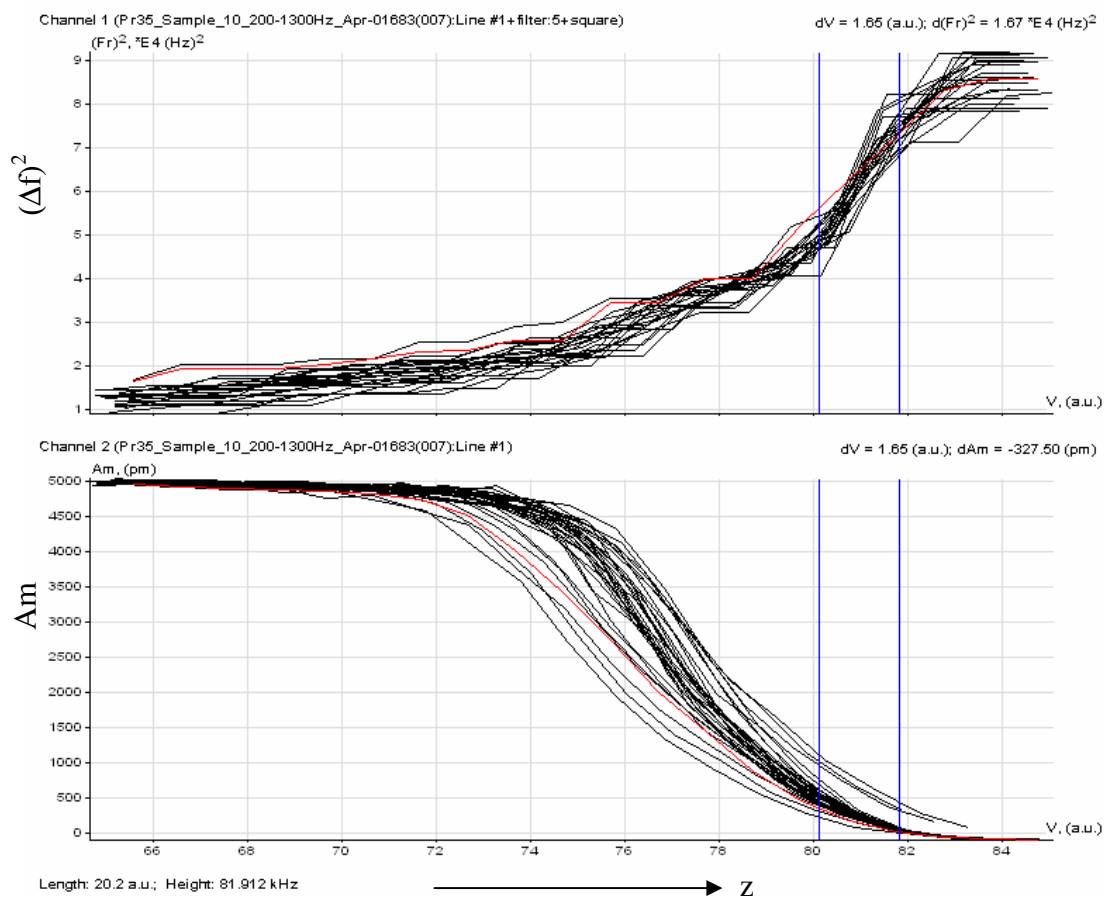
Figure II.19: Frequency shift plot of Au-Ni (d_g=6.9 nm, λ= 1.8 nm) Sample 10
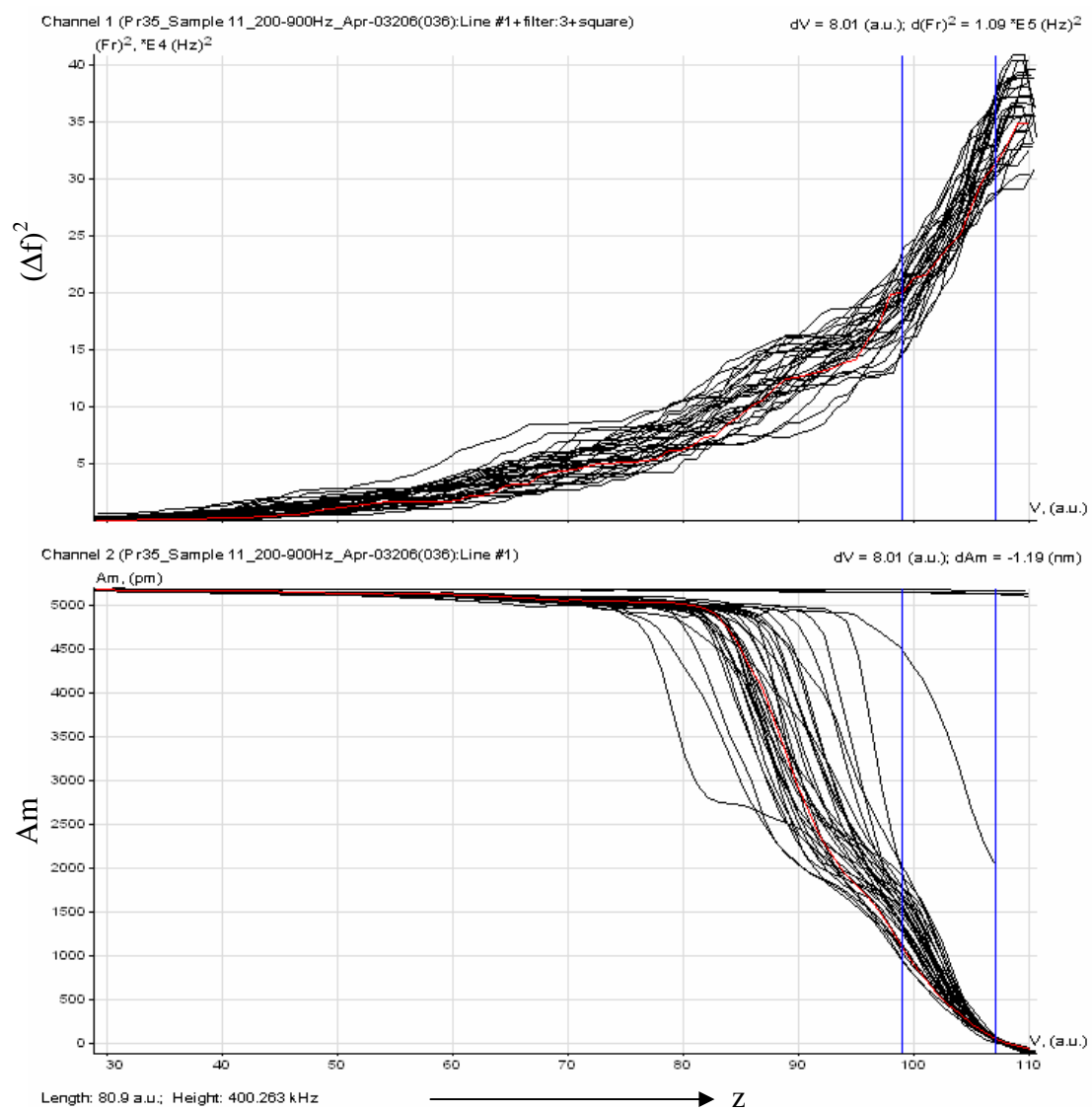
Figure II.20: Frequency shift plot of Au-Ni (d_g=13.1 nm, λ= 2.5 nm) Sample 11
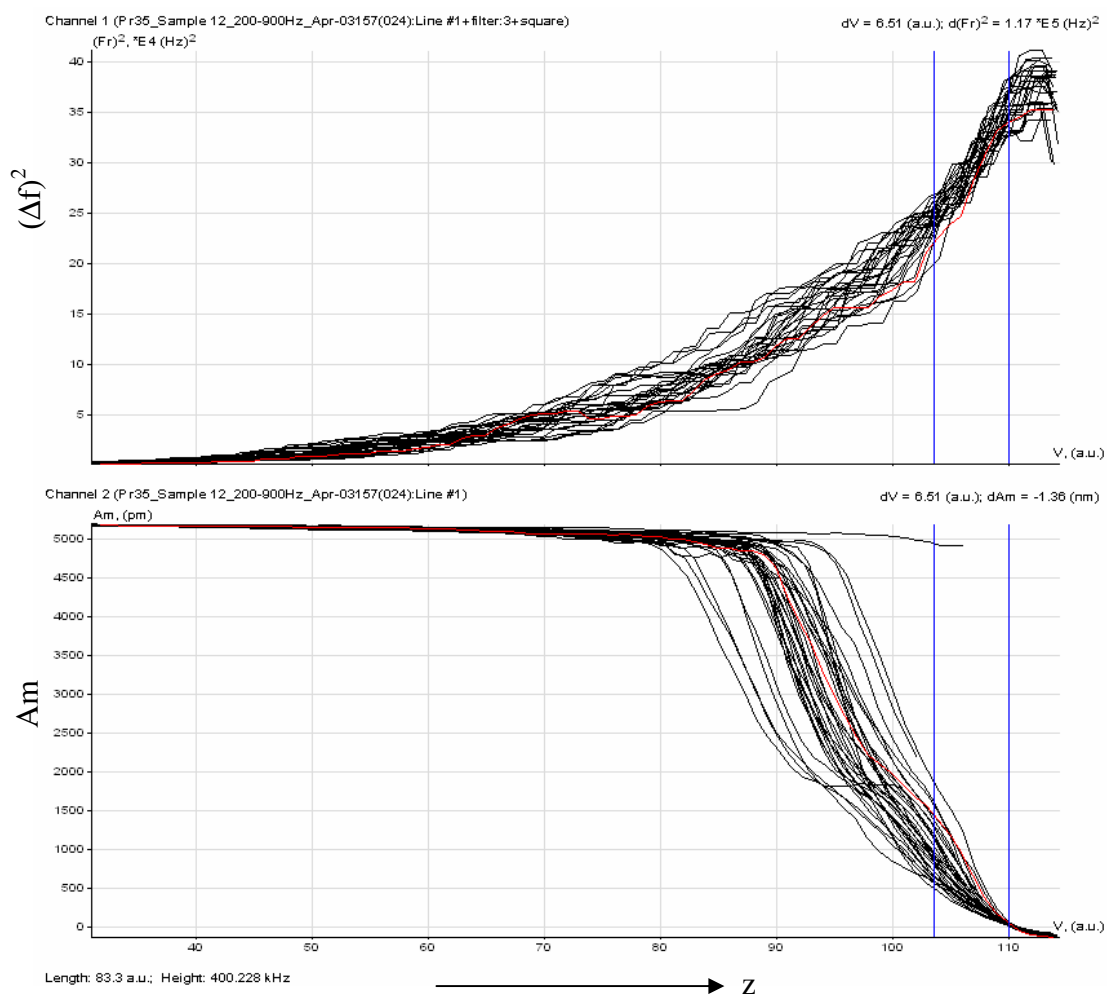
Figure II.21: Frequency shift plot of Au-Ni (d_g=11.4 nm, λ= 1.2 nm) Sample 12
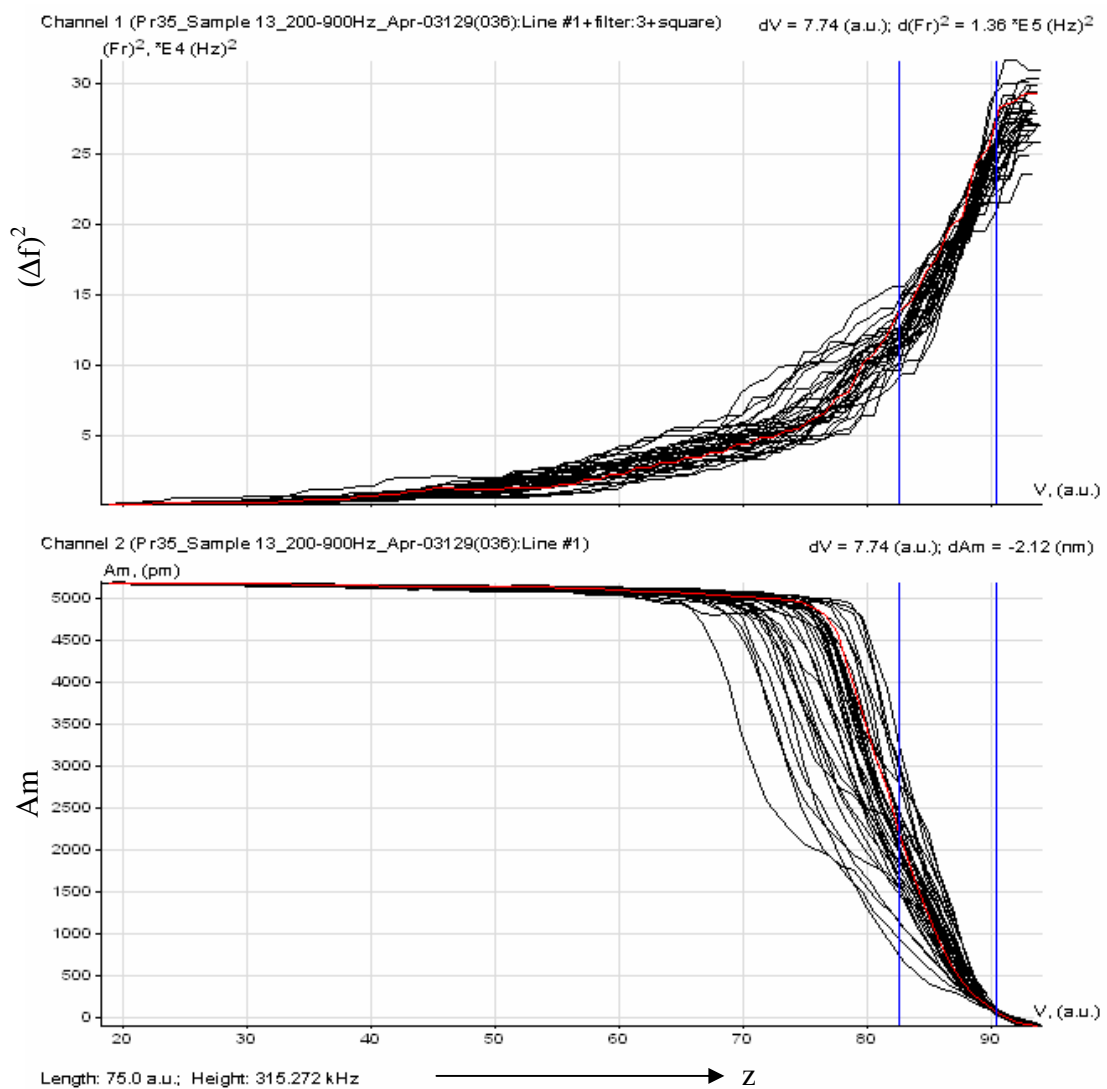
Figure II.22: Frequency shift plot of Au-Ni (d_g=16.7 nm, λ= 2.6 nm) Sample 13
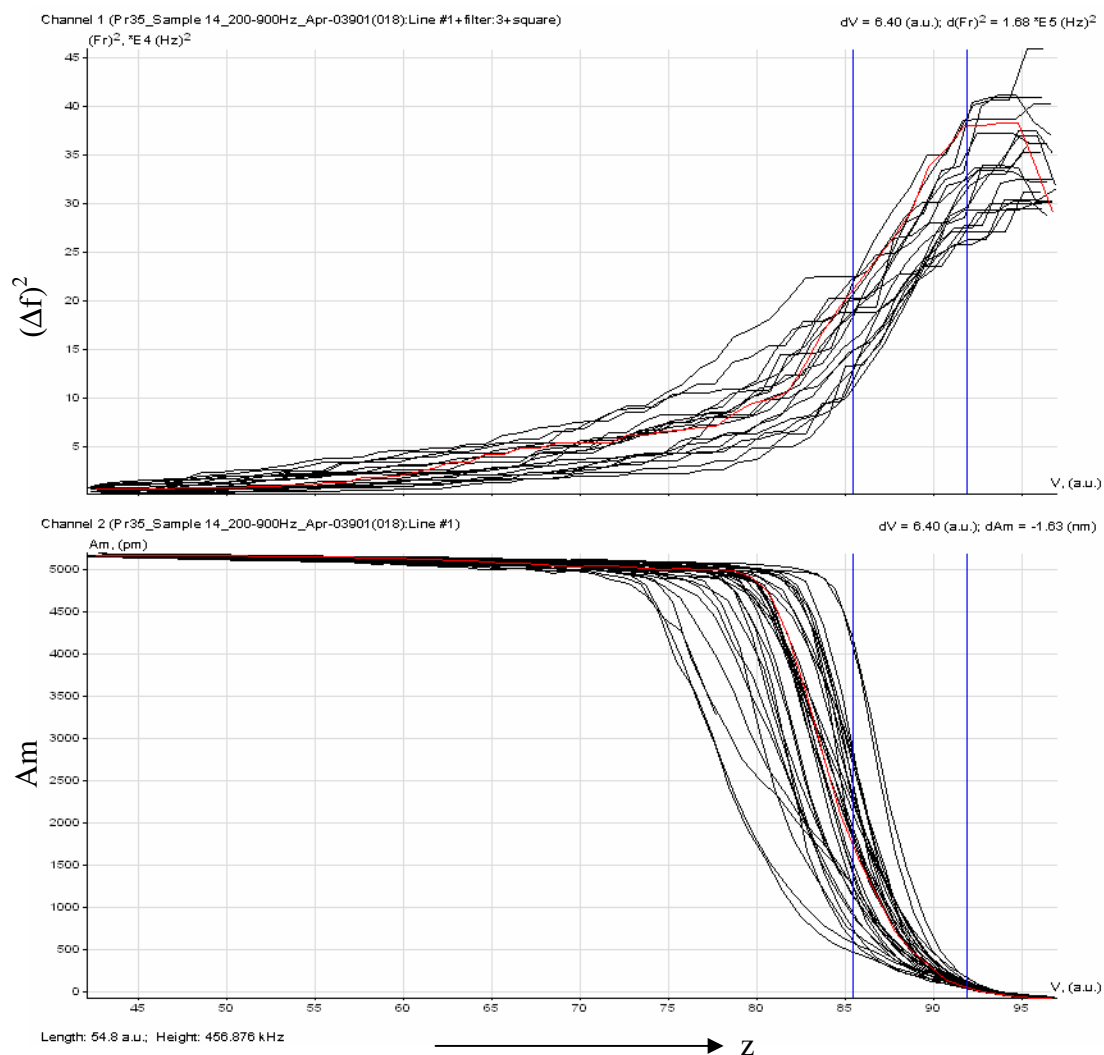
Figure II.23: Frequency shift plot of Au-Ni (λ= 8.9 nm) Sample 14
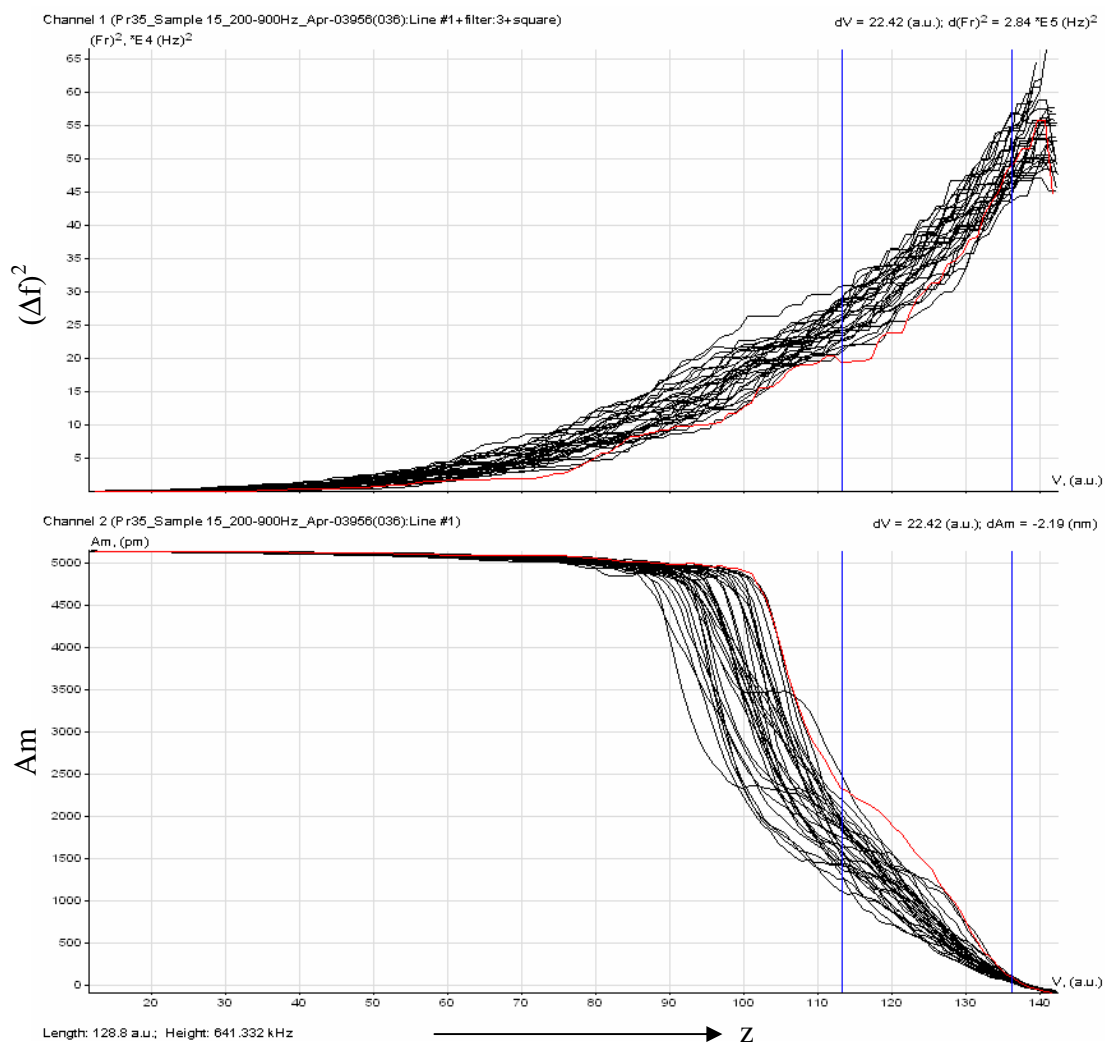
Figure II.24: Frequency shift plot of Au-Ni (λ= 2.1 nm) Sample 15
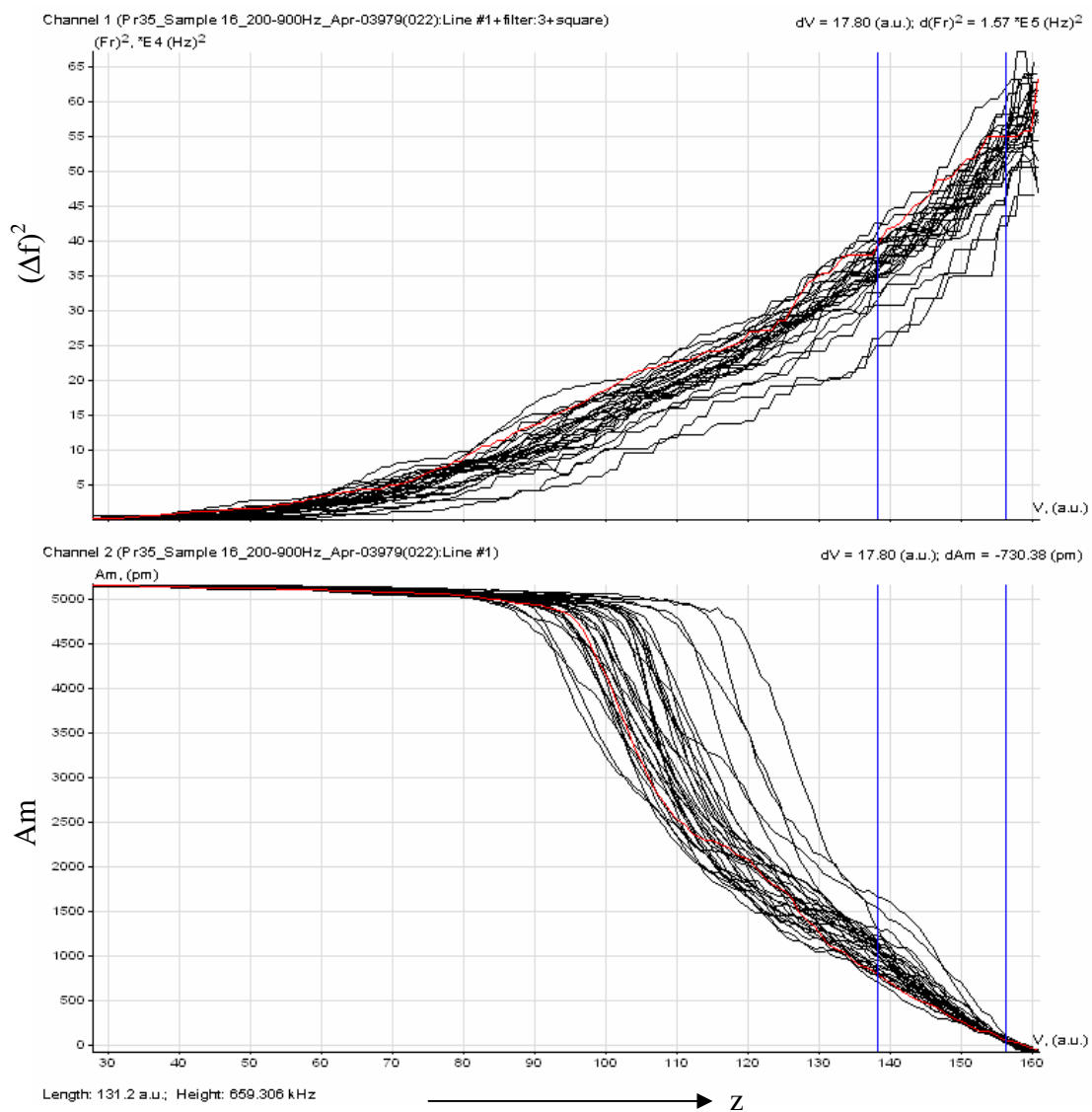
Figure II.25: Frequency shift plot of Au-Ni (λ= 1.3 nm) Sample 16
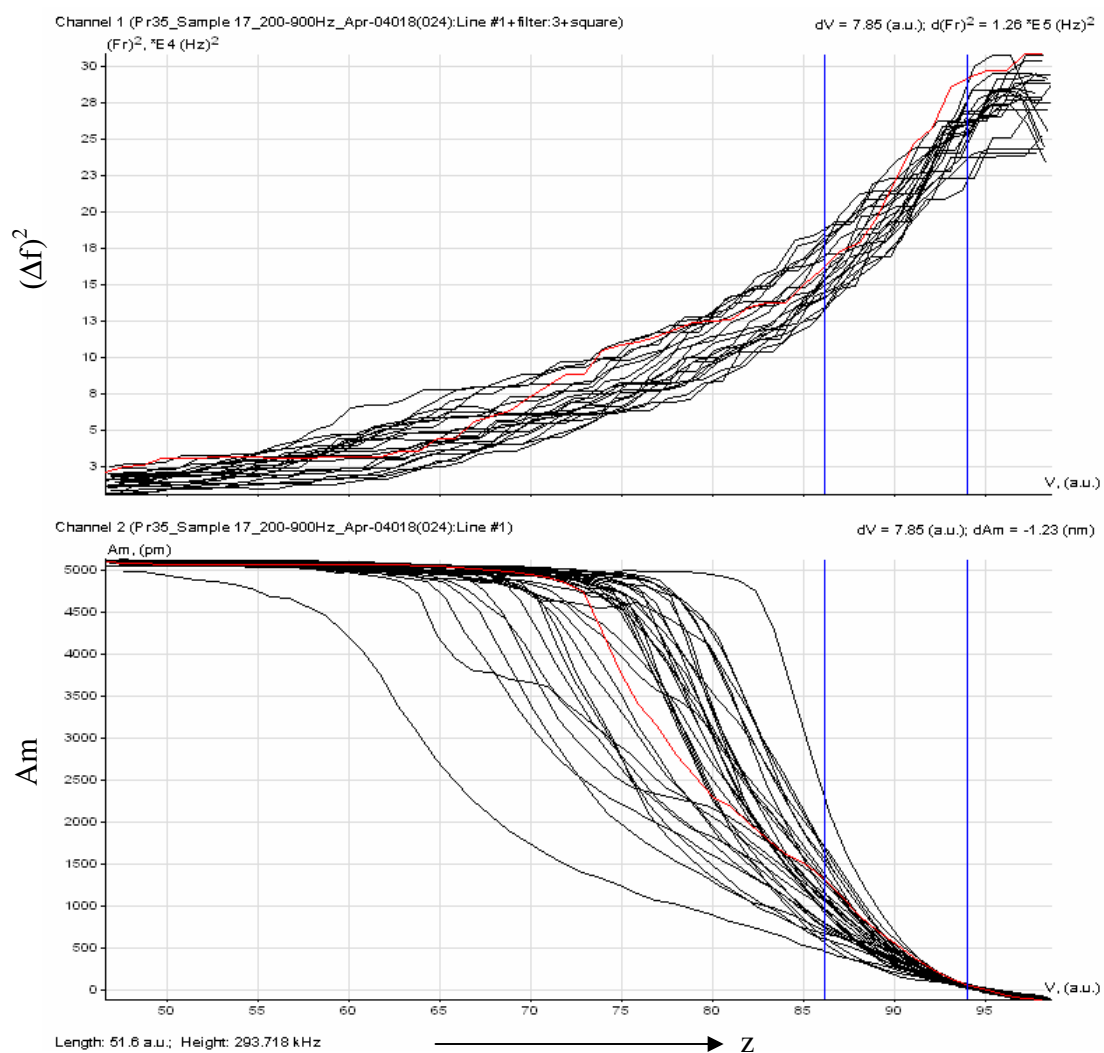
Figure II.26: Frequency shift plot of Au-Ni (λ= 2.9 nm) Sample 17
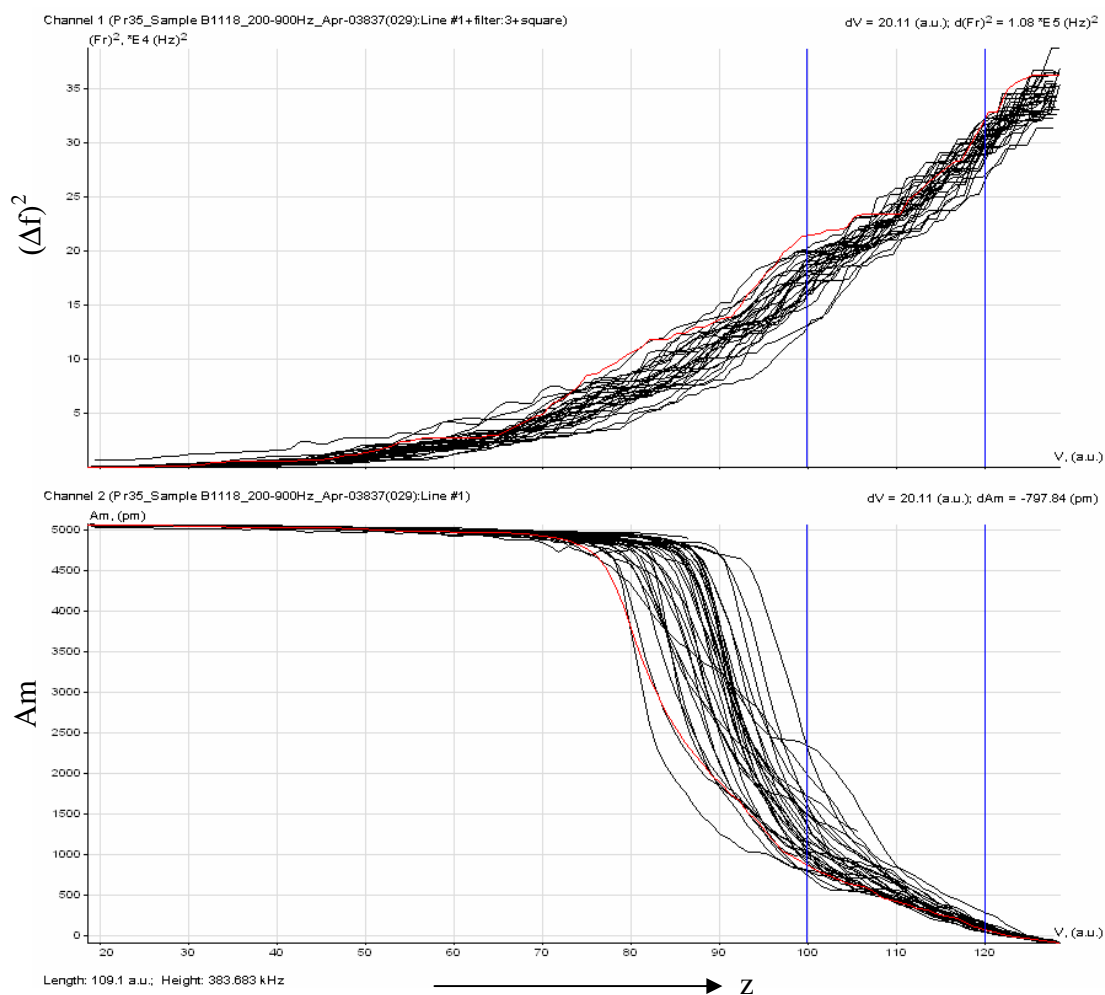
Figure II.27: Frequency shift plot of Sample B1119

II.C Frequency shift curves of Au-Nb samples
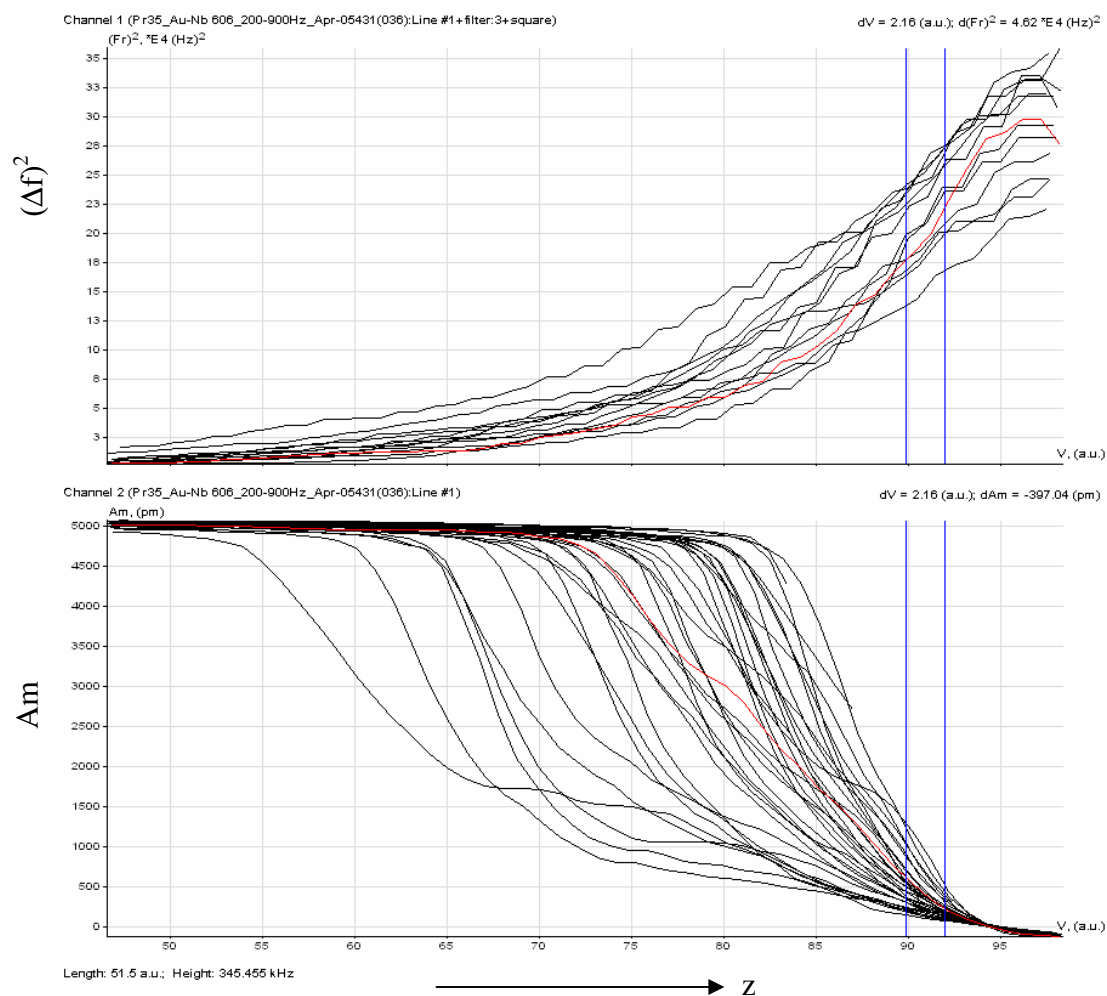
Figure II.28: Frequency shift plot of Sample Au-Nb 606
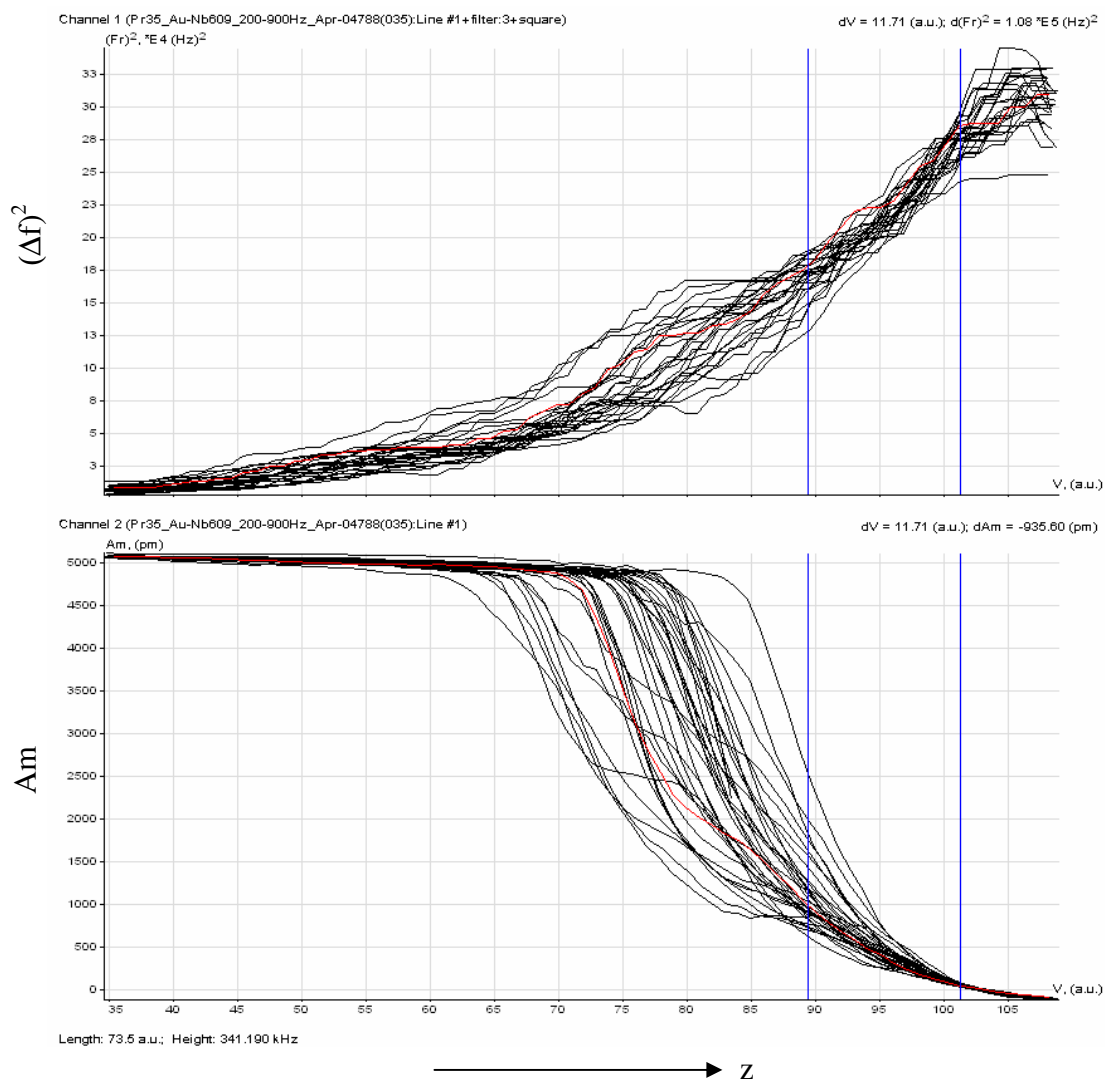
Figure II.29: Frequency shift plot of Sample Au-Nb 609 (λ= 1.6 nm)
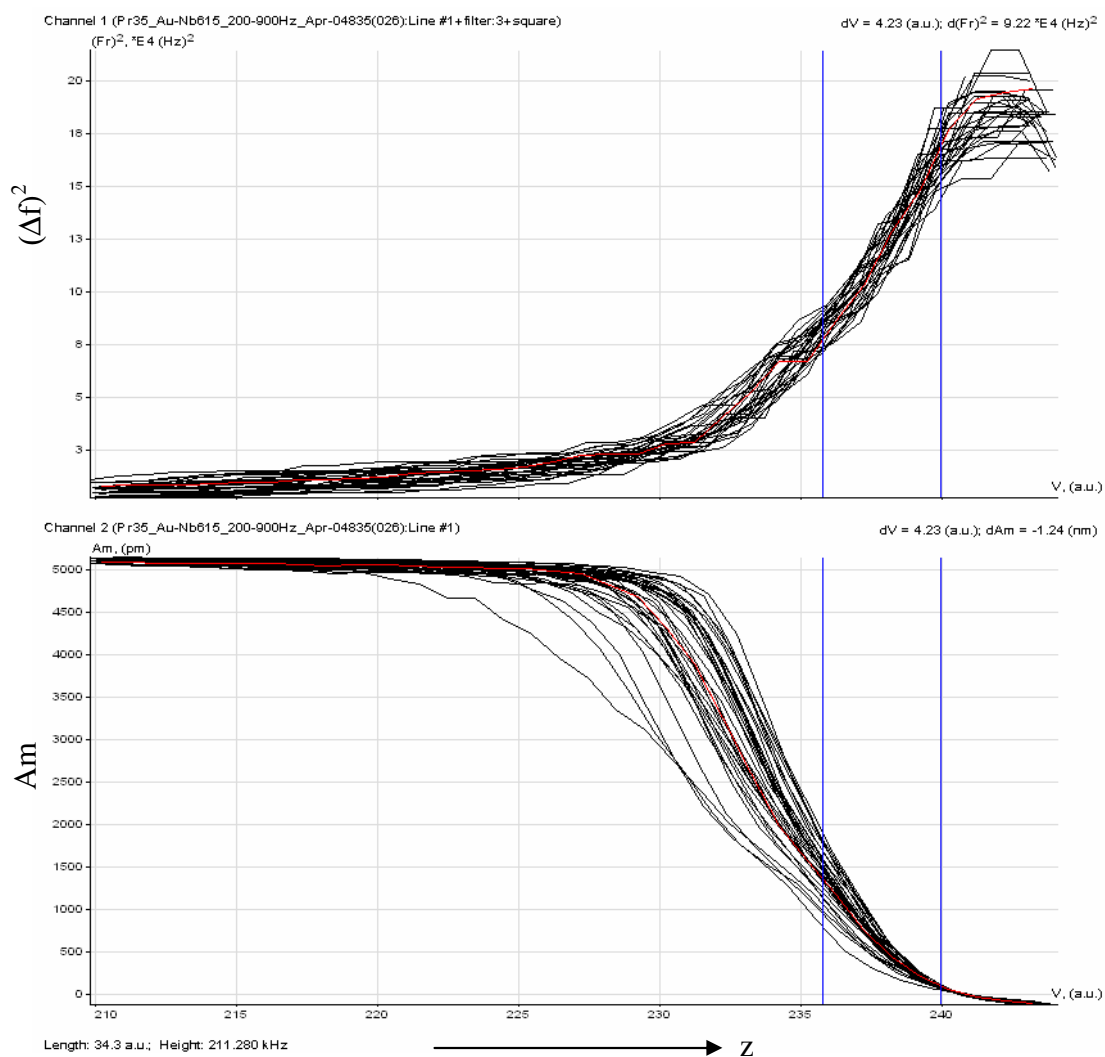
Figure II.30: Frequency shift plot of Sample Au-Nb 615 (λ= 3.2 nm)
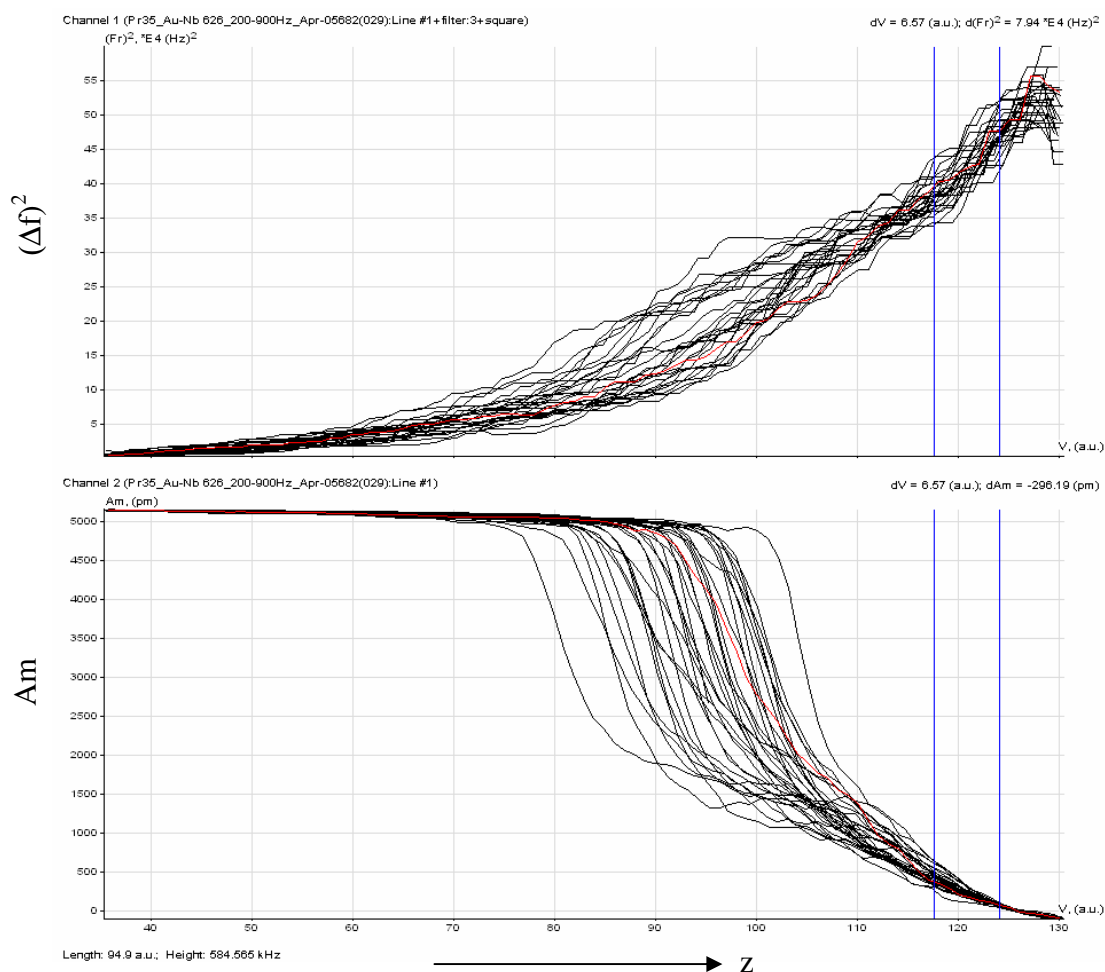
Figure II.31: Frequency shift plot of Sample Au-Nb 626 (λ= 0.46 nm)

II.D Frequency shift curves of Cu-NiFe samples
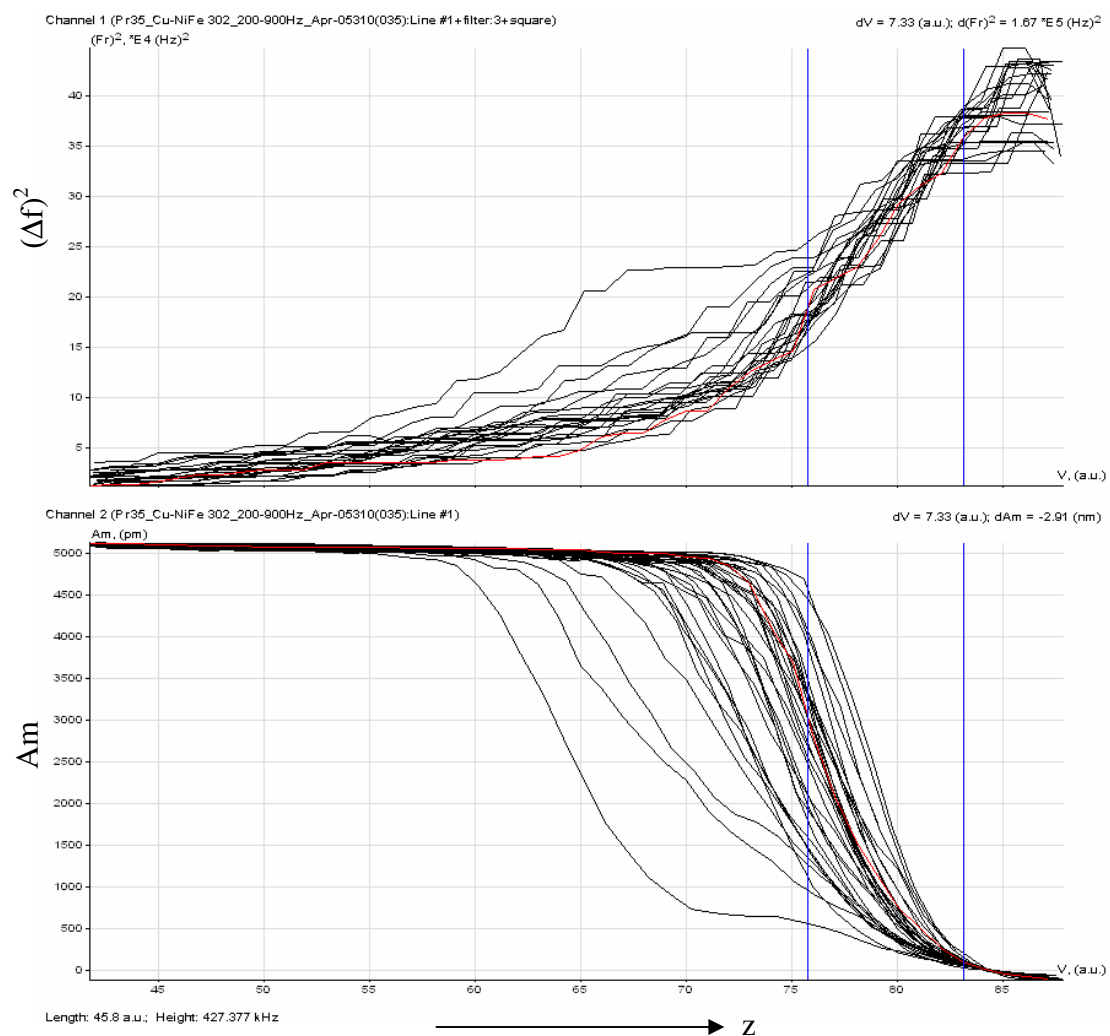
Figure II.32: Frequency shift plot of sample Cu-NiFe 302 (λ= 4.0 nm)
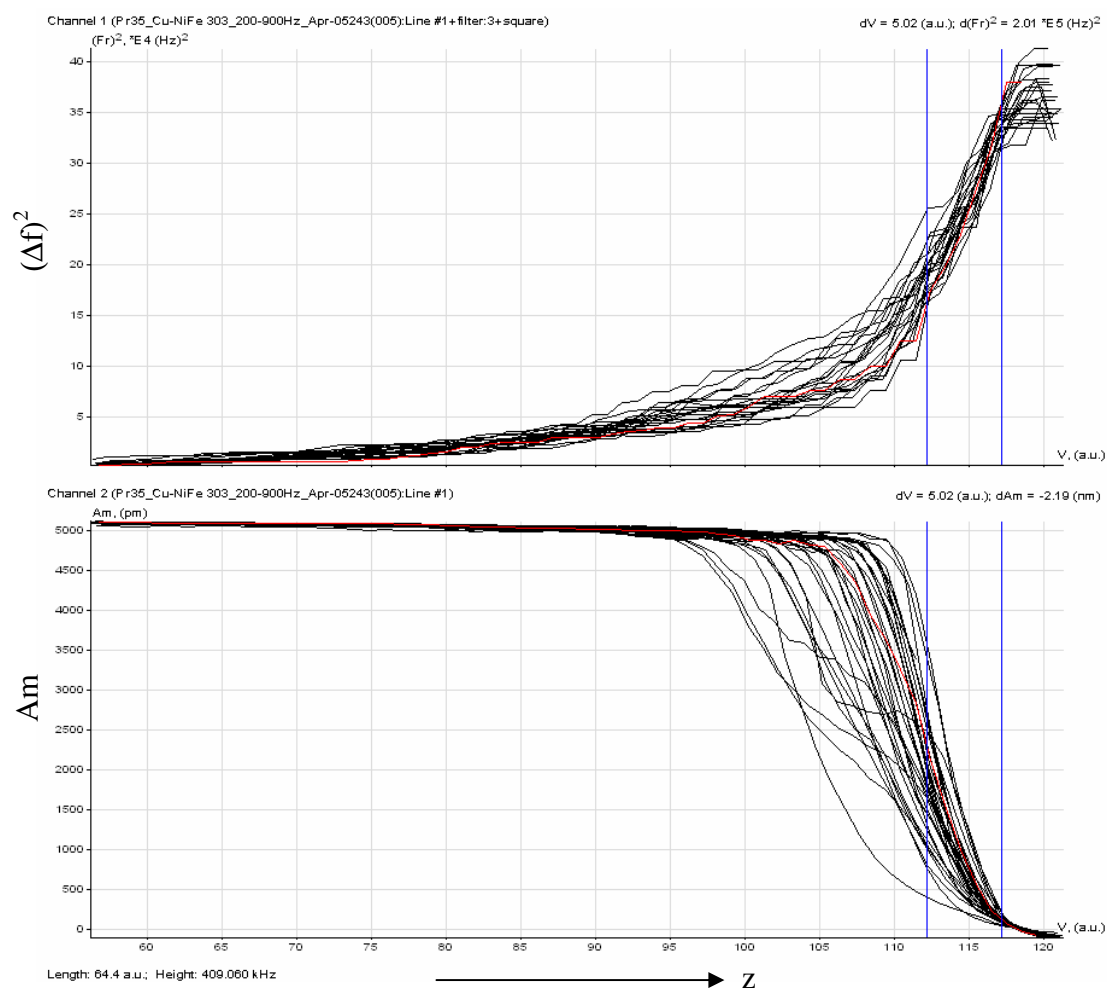
Figure II.33: Frequency shift plot of sample Cu-NiFe 303 (λ= 6.7 nm)

II.E Frequency shift curves of Hydroxyapatite coatings
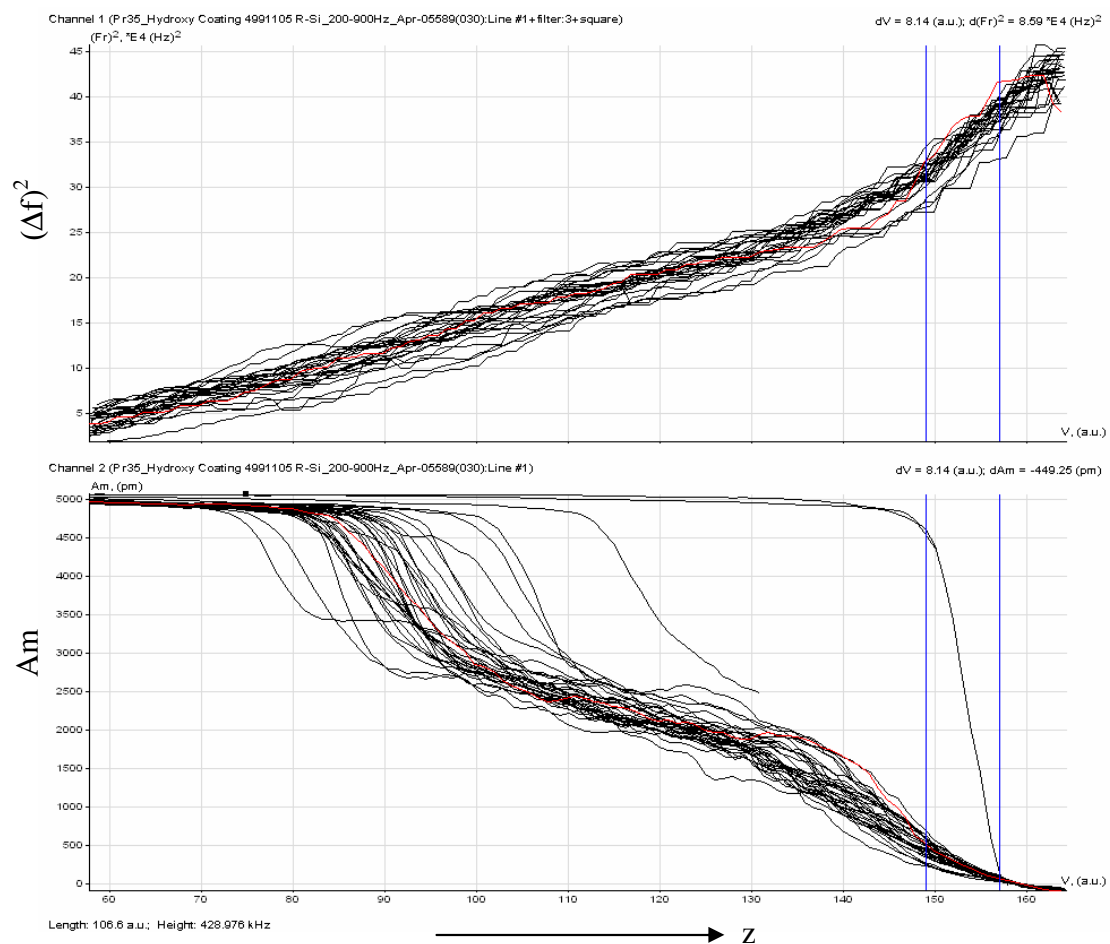
Figure II.34: Frequency shift plot of sample 4991105 R-Si
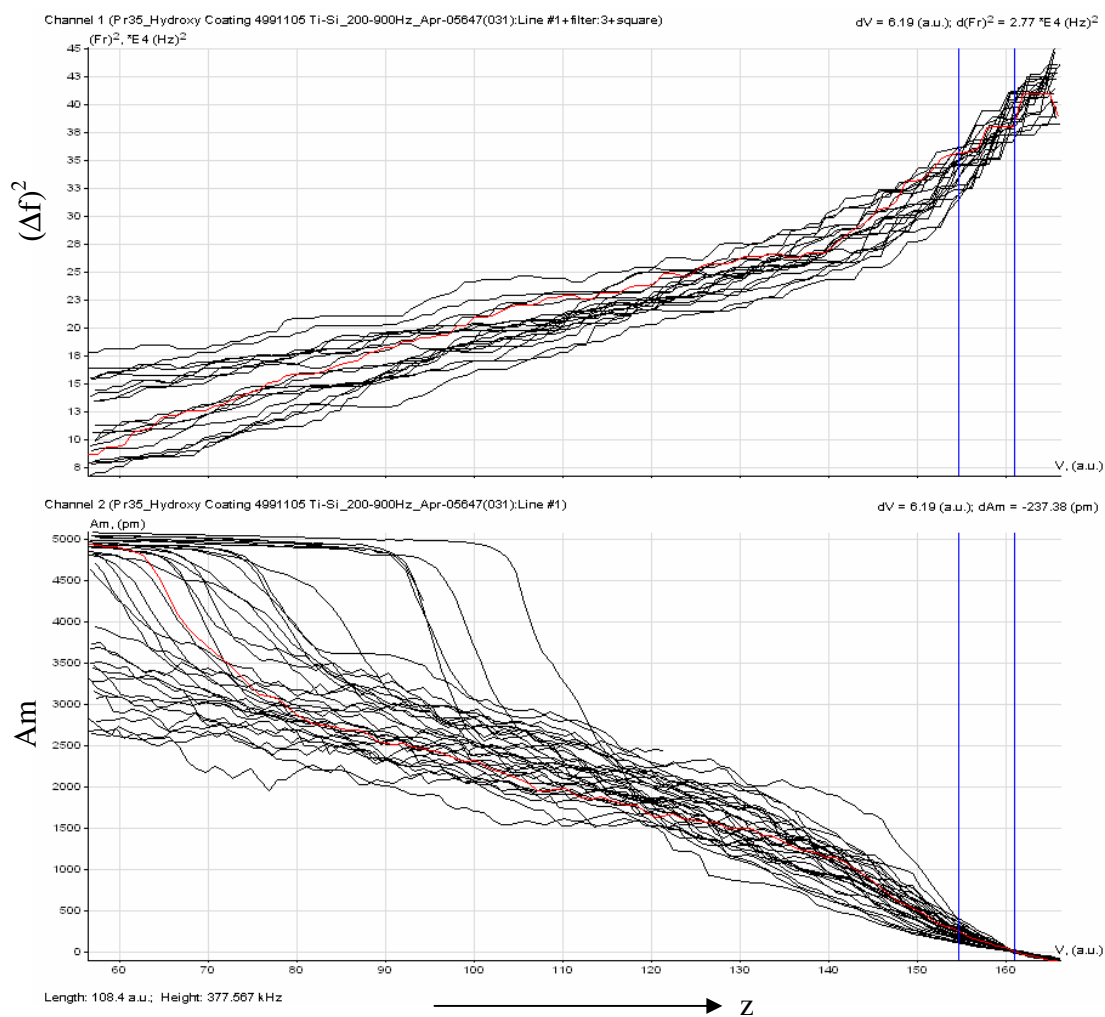
Figure II.35: Frequency shift plot of sample 4991105 Ti-Si
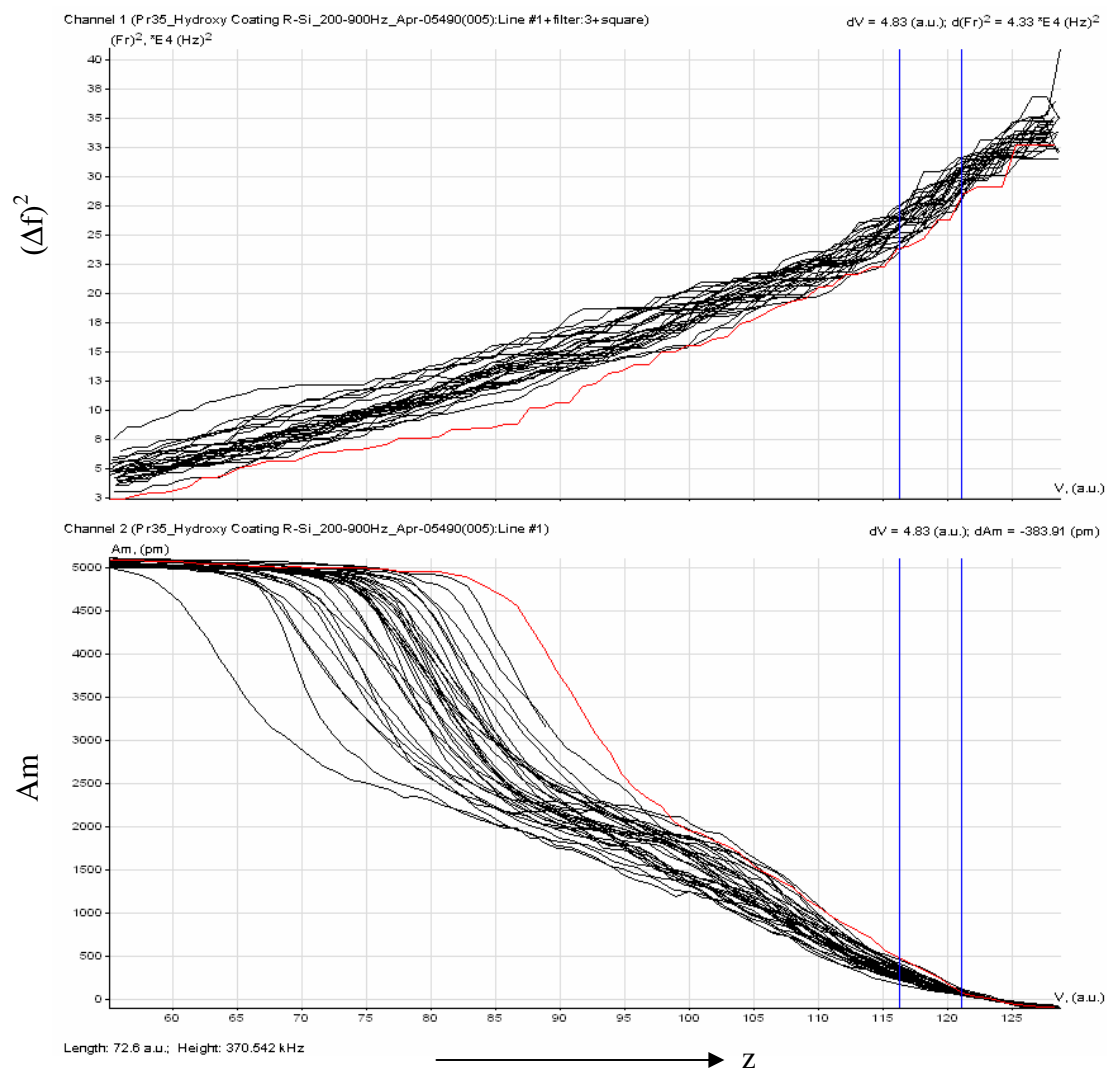
Figure II.36: Frequency shift plot of sample 4991012 R-Si
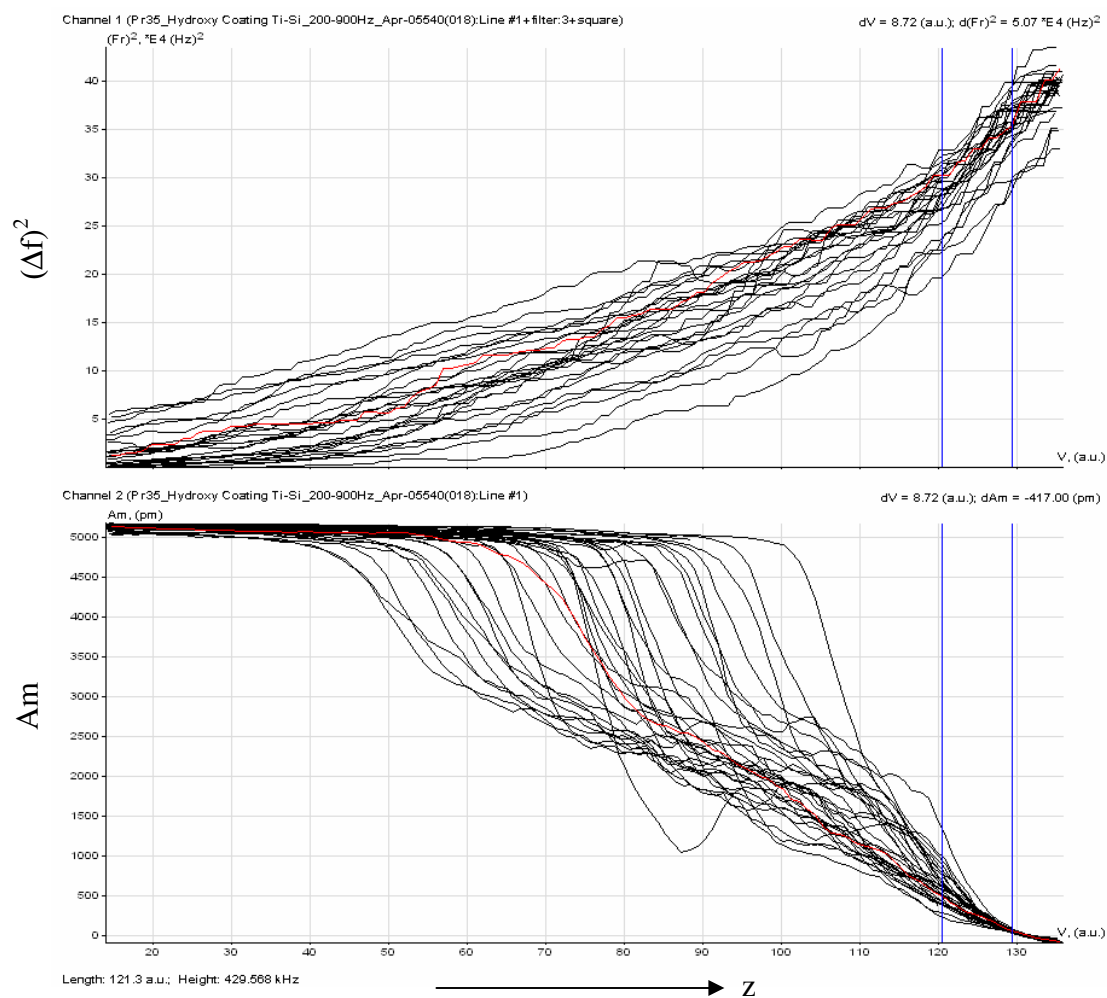
Figure II.37: Frequency shift plot of sample 4991012 Ti-Si

II.F Frequency shift curves of Silicon wafers
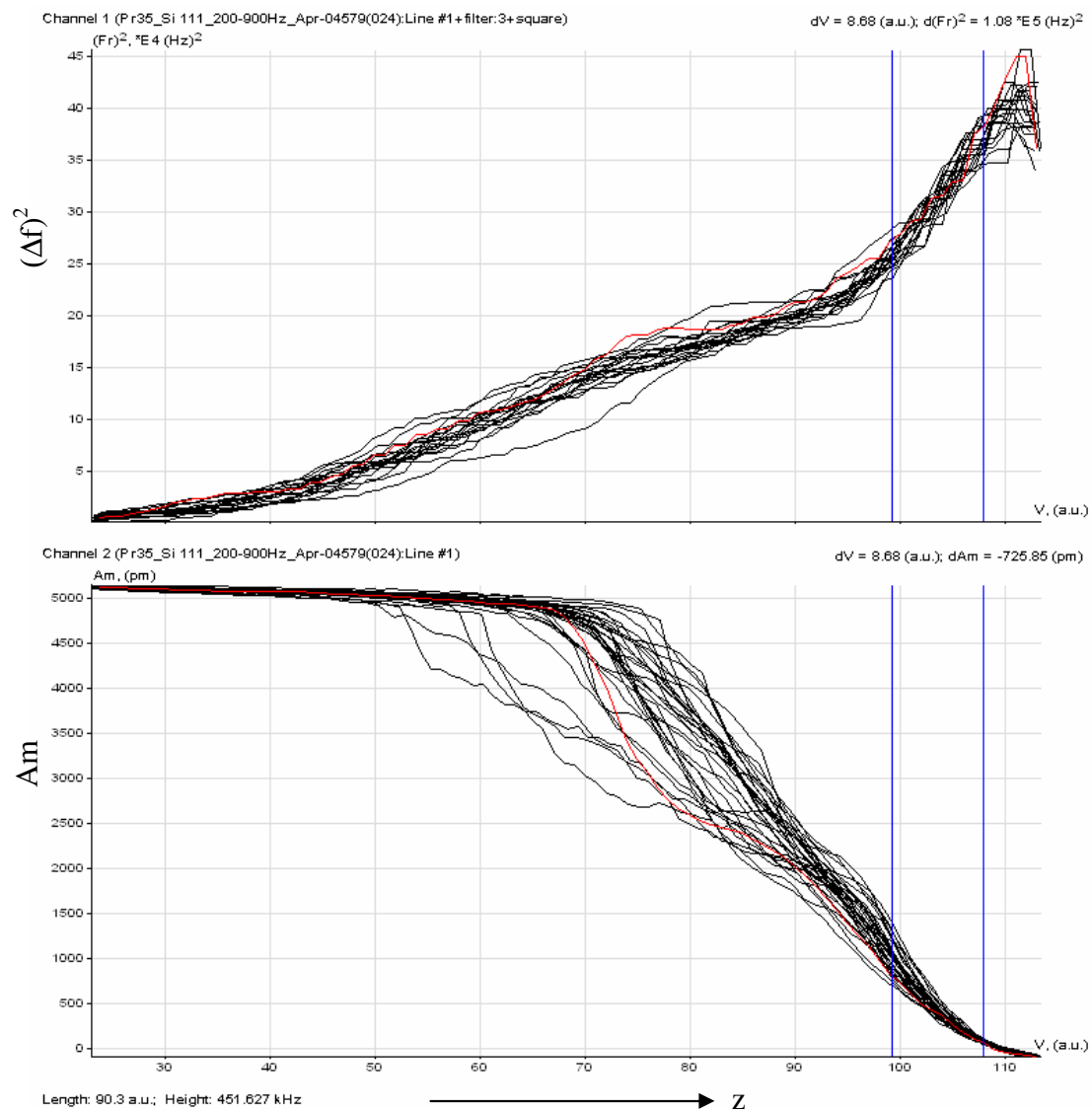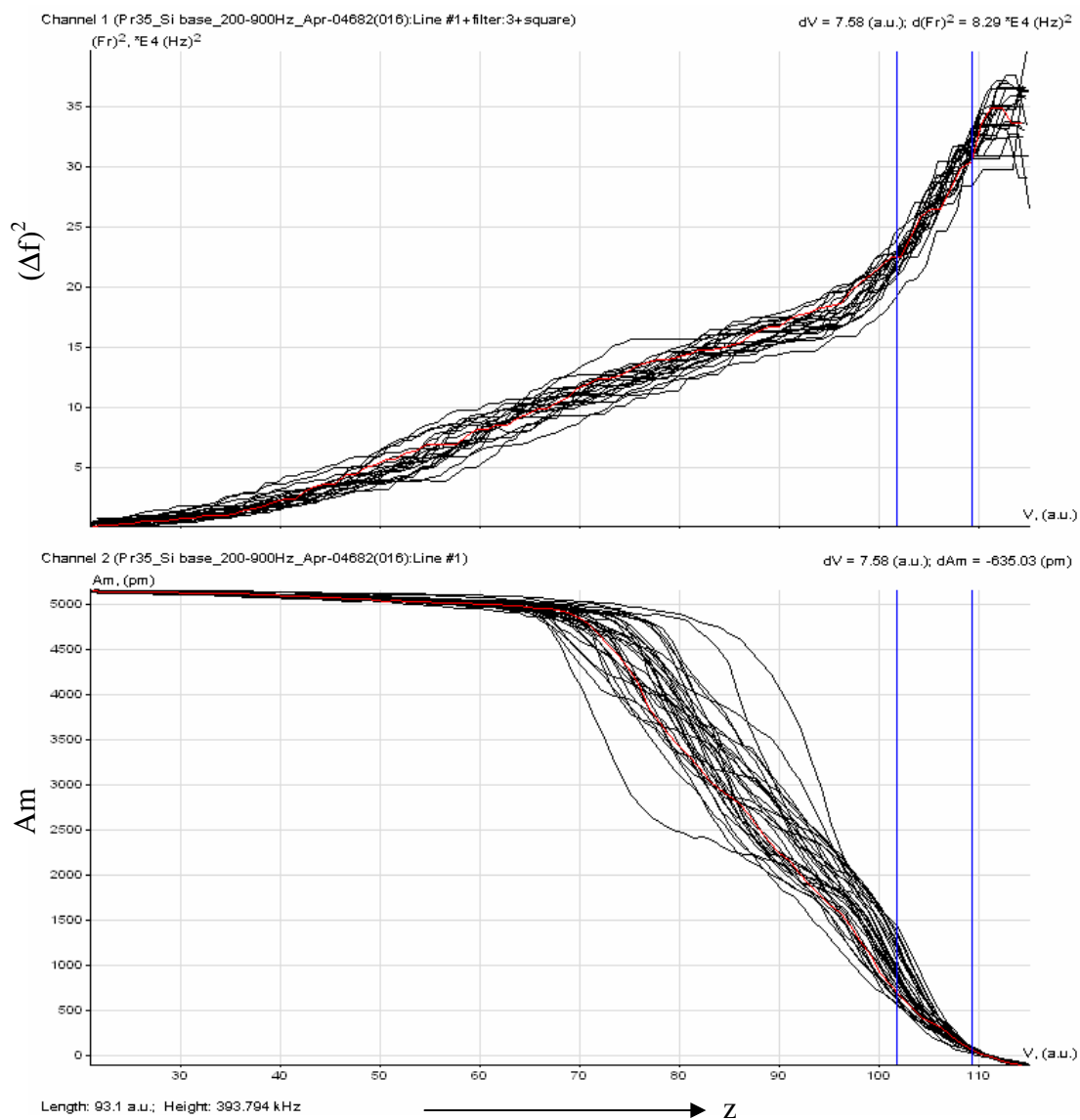

Figure II.38: Frequency shift plot of Silicon (111)

Figure II.39: Frequency shift plot of Silicon (base)

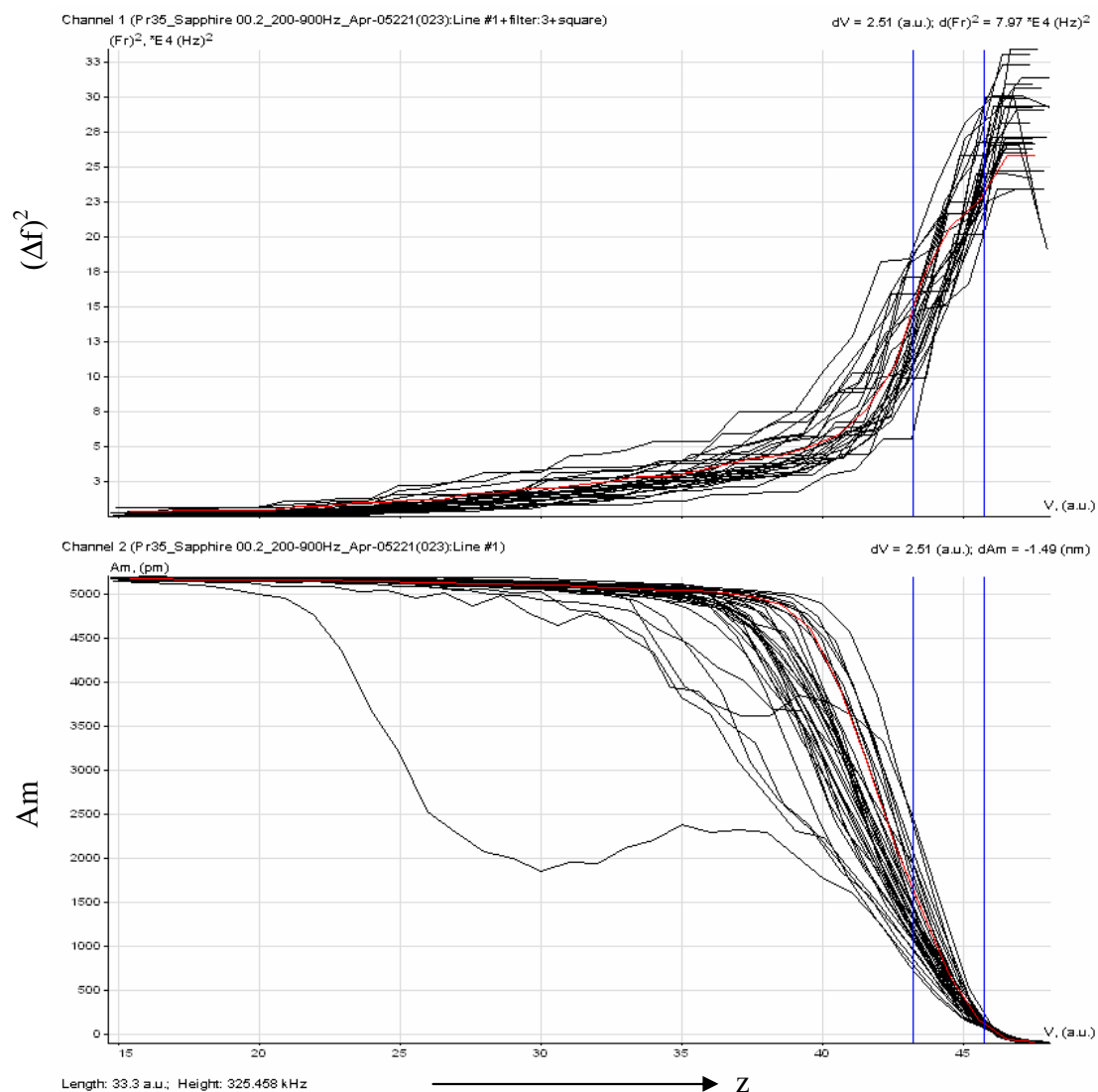## II.G Frequency shift curves of directional sapphire

Figure II.40: Frequency shift plot of Sapphire 00.2

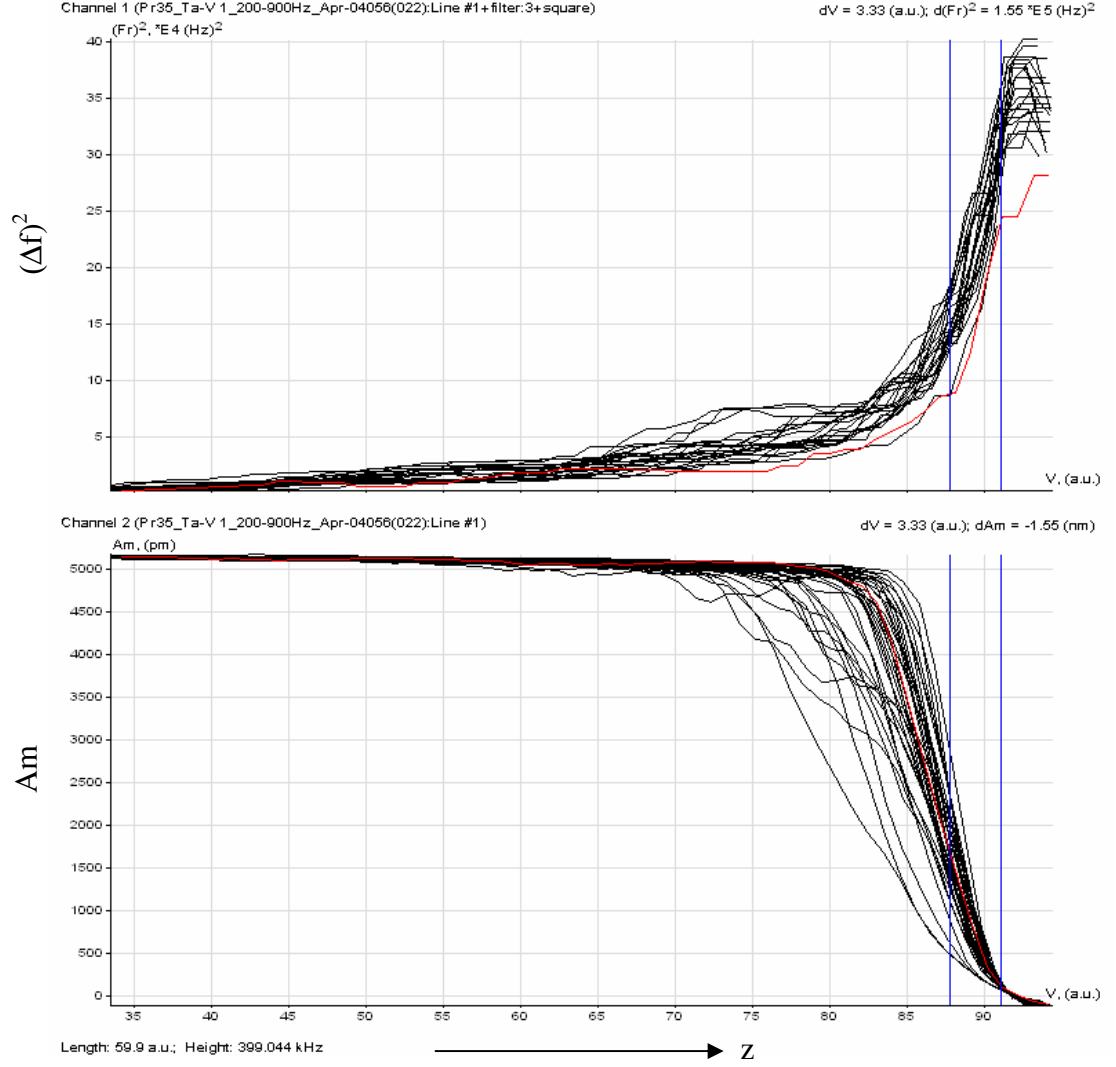## II.H Frequency shift curves of Ta-V samples

Figure II.41: Frequency shift plot of Ta-V (λ=8.07 nm) Sample 1
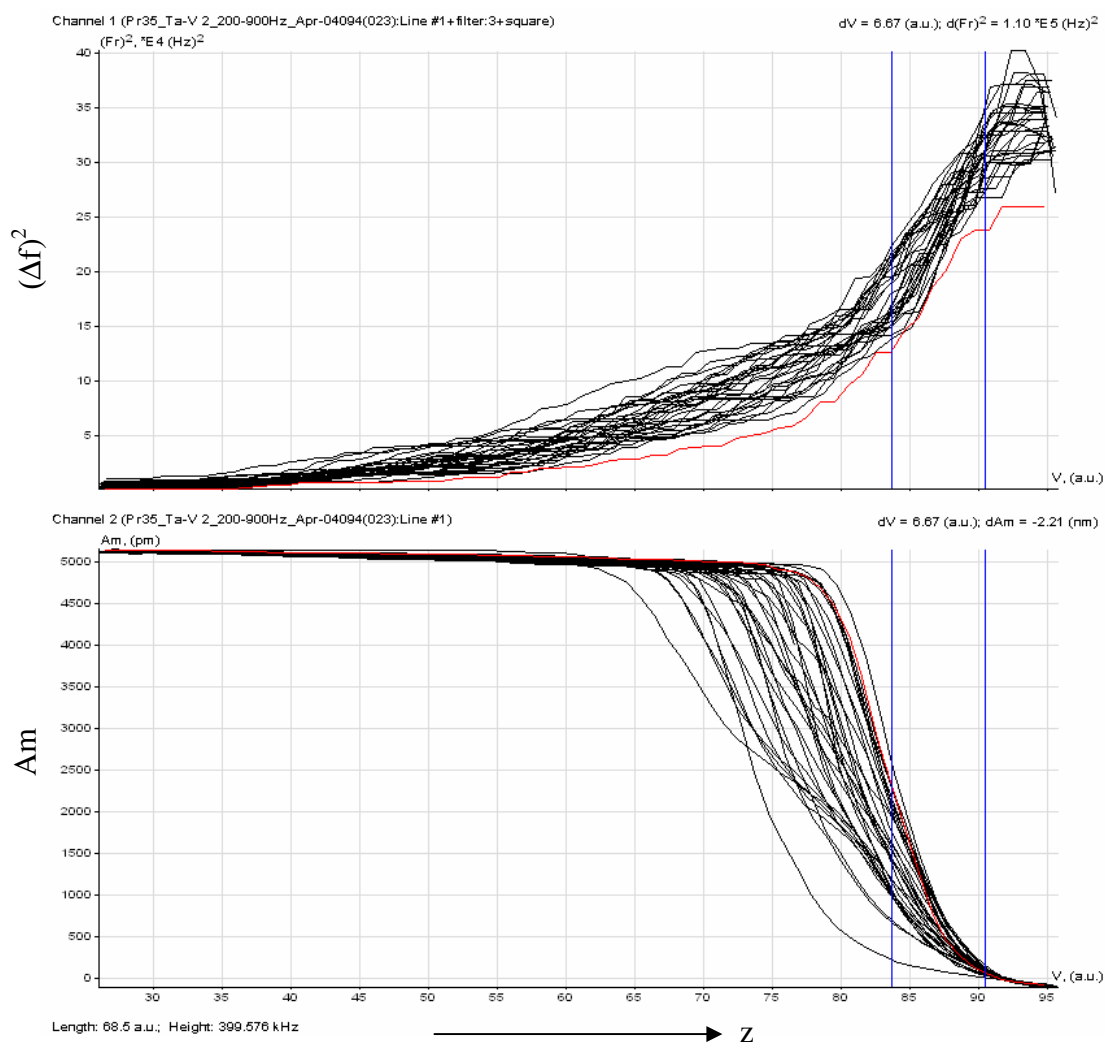
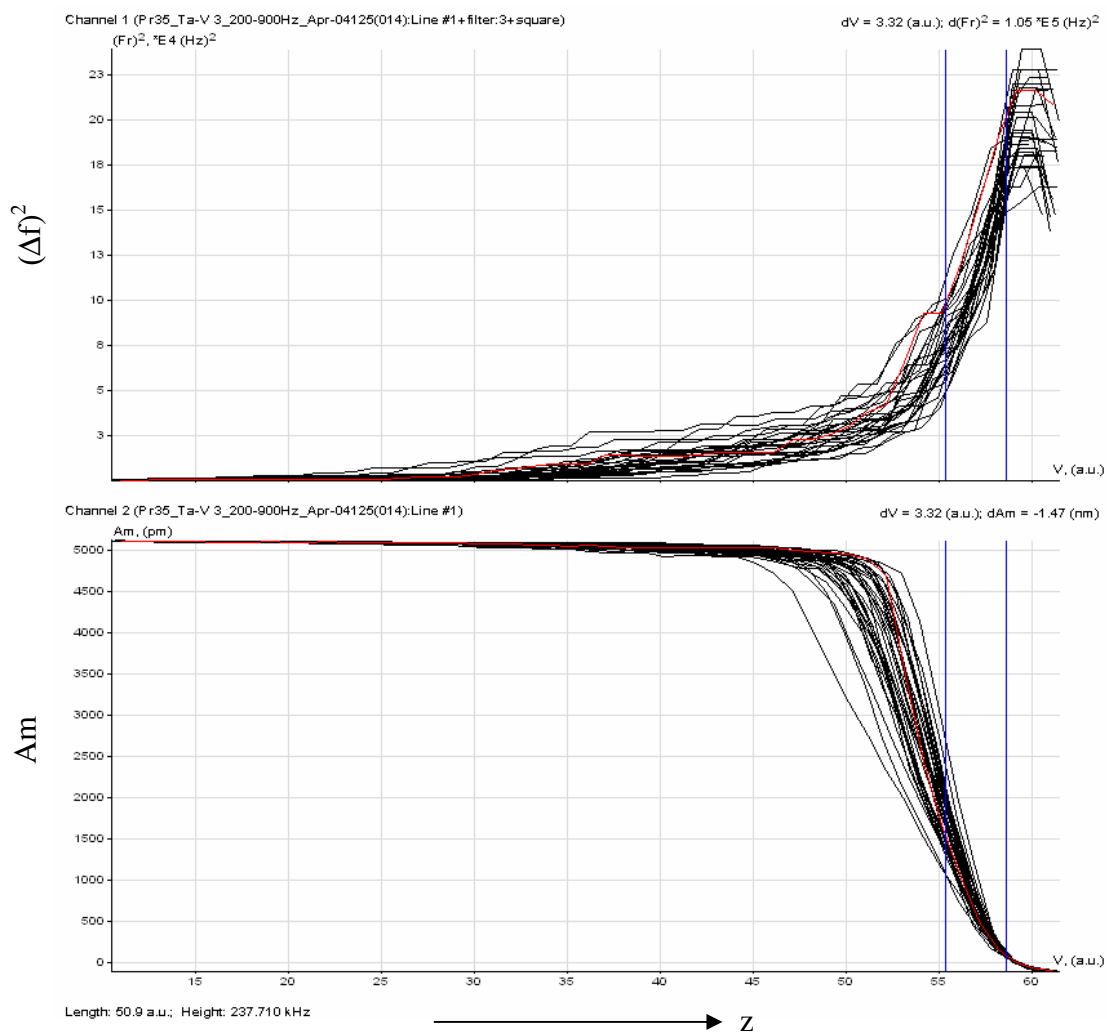**Figure II.42:** Frequency shift plot of Ta-V (λ=3.14 nm) Sample 2

Figure II.43: Frequency shift plot of Ta-V (λ=8.07 nm) Sample 3
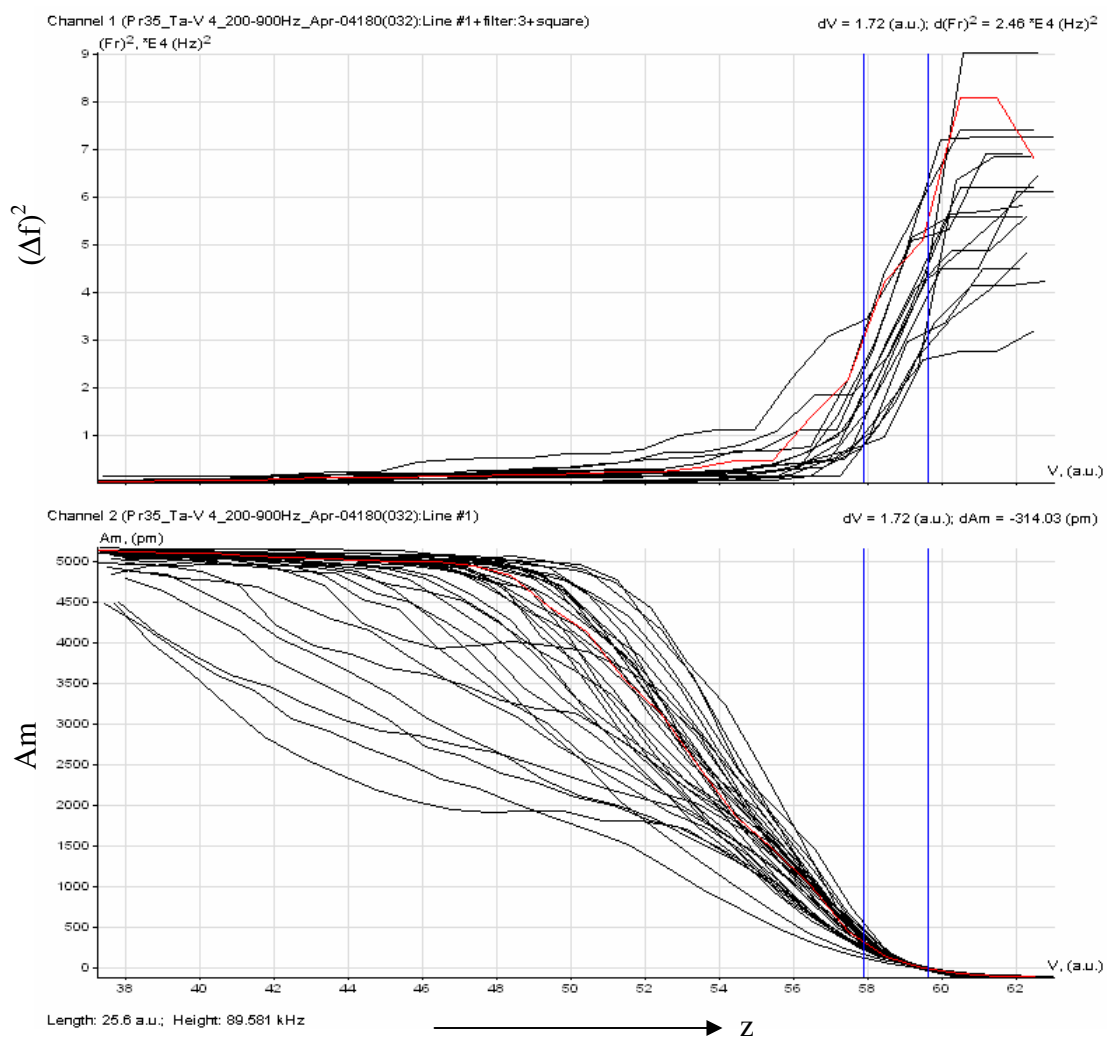
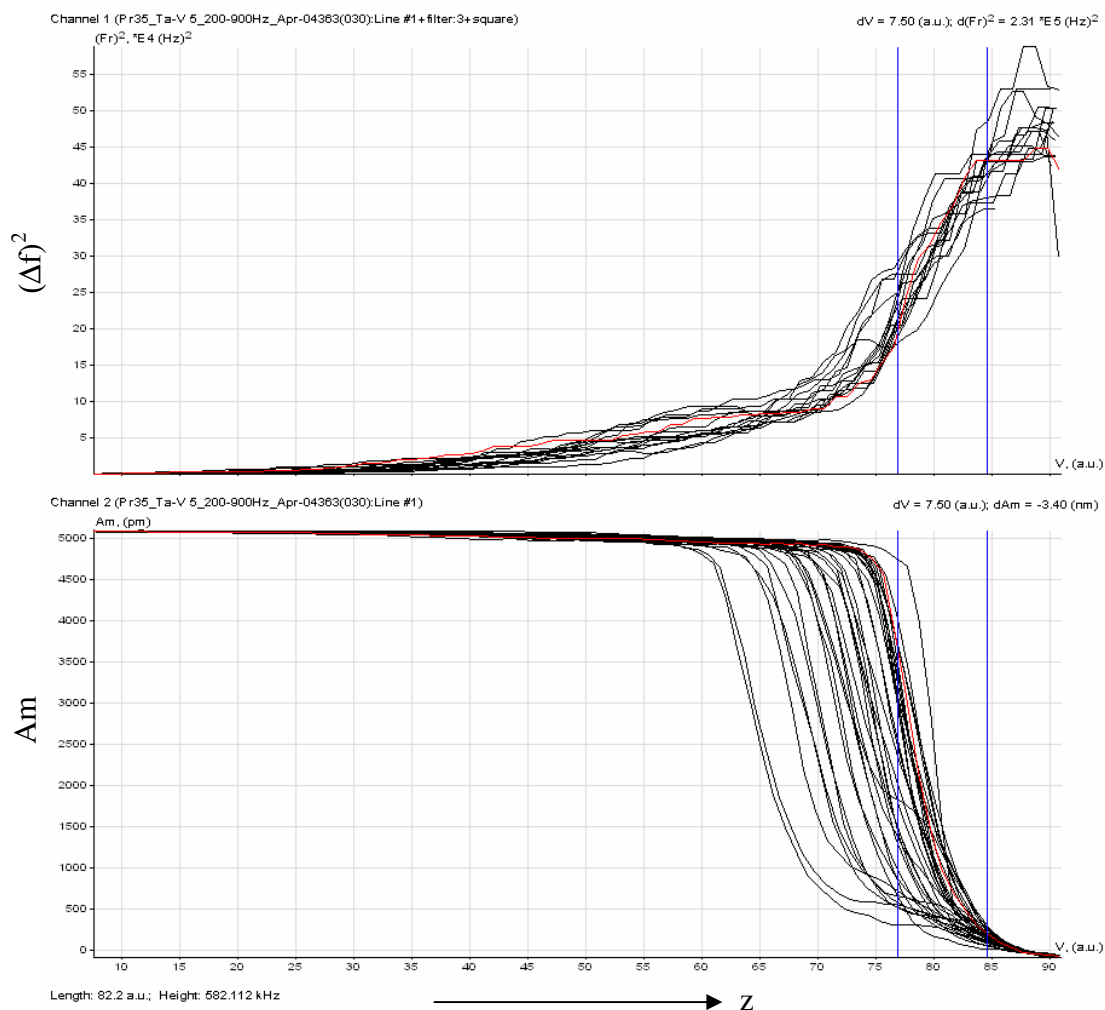**Figure II.44:** Frequency shift plot of Ta-V (λ=3.14 nm) Sample 4

Figure II.45: Frequency shift plot of Ta-V (λ=10.12 nm) Sample 5
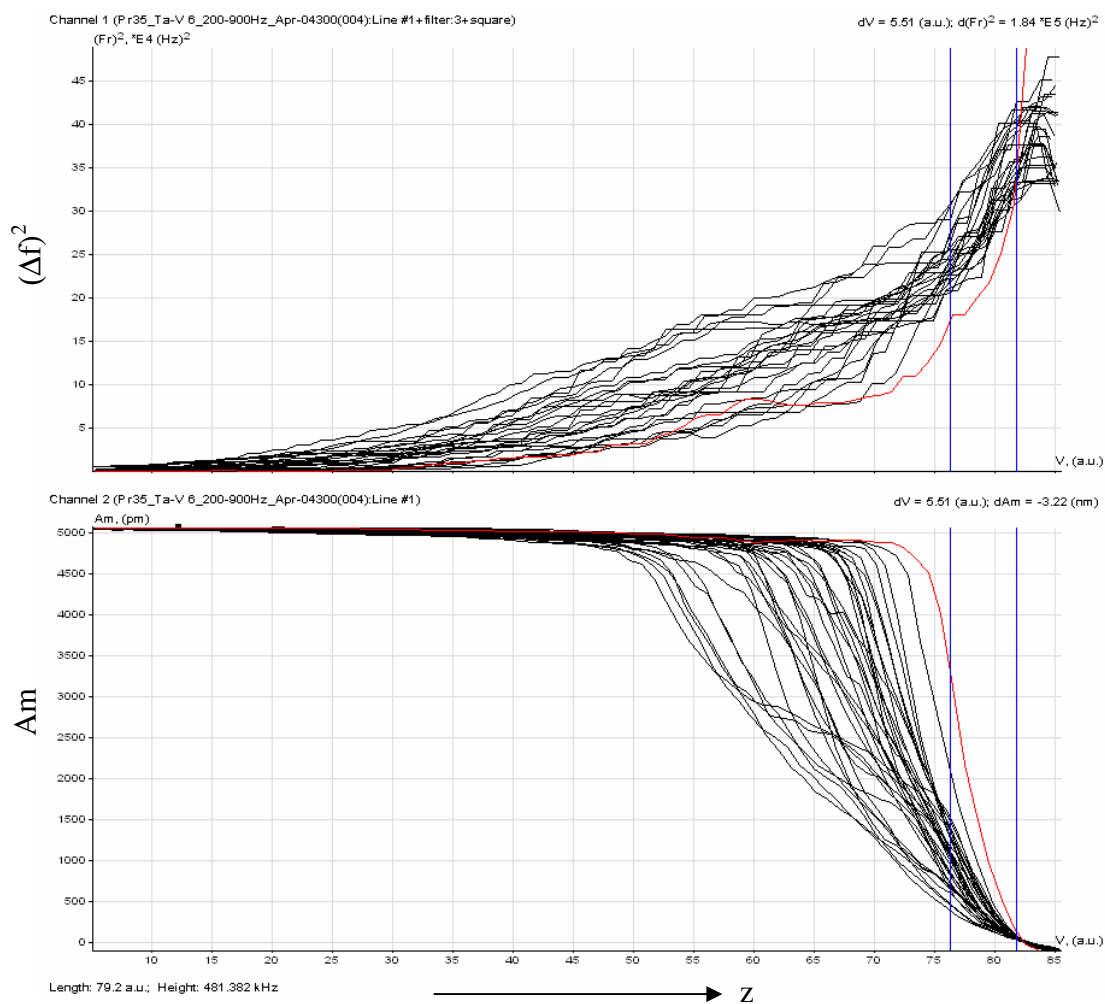
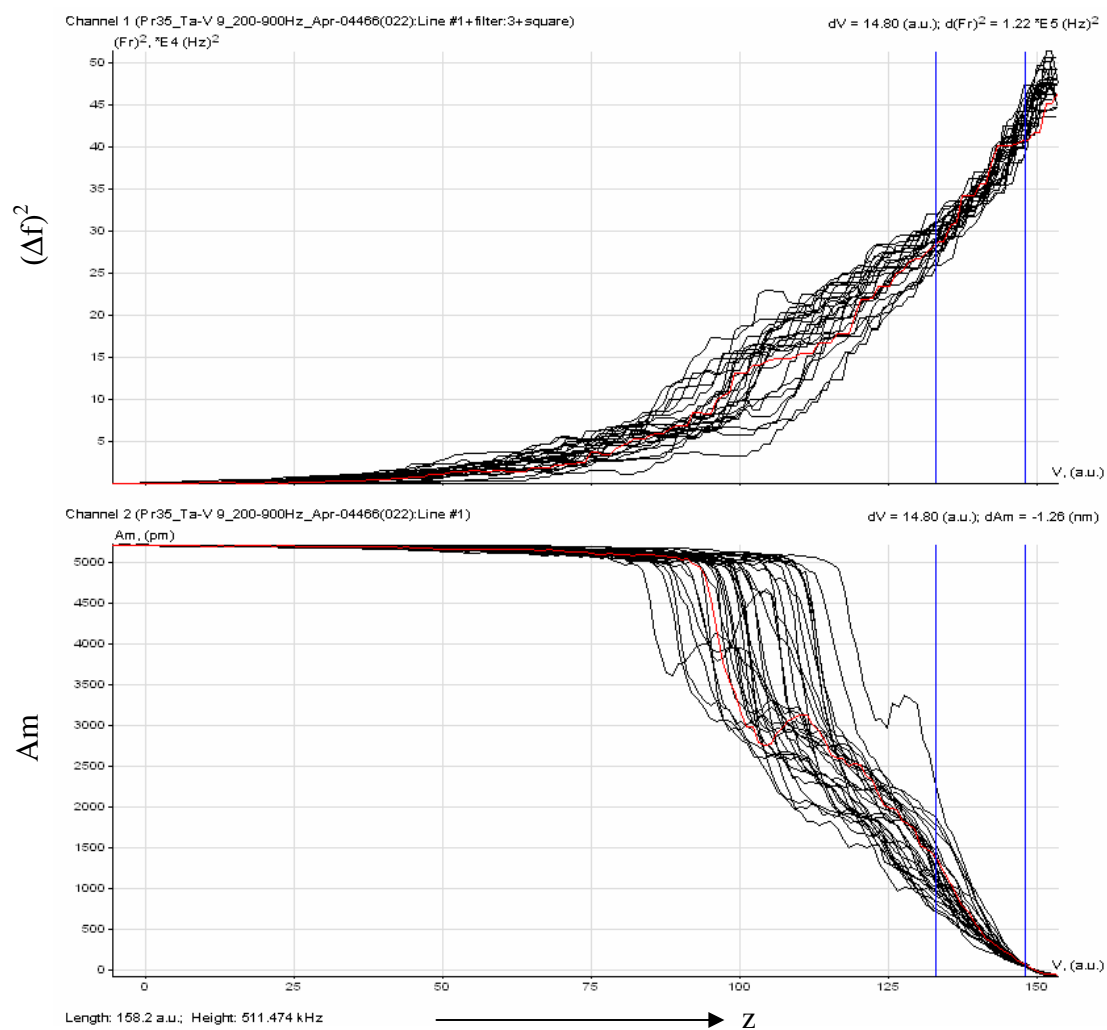**Figure II.46:** Frequency shift plot of Ta-V (λ=3.16 nm) Sample 6

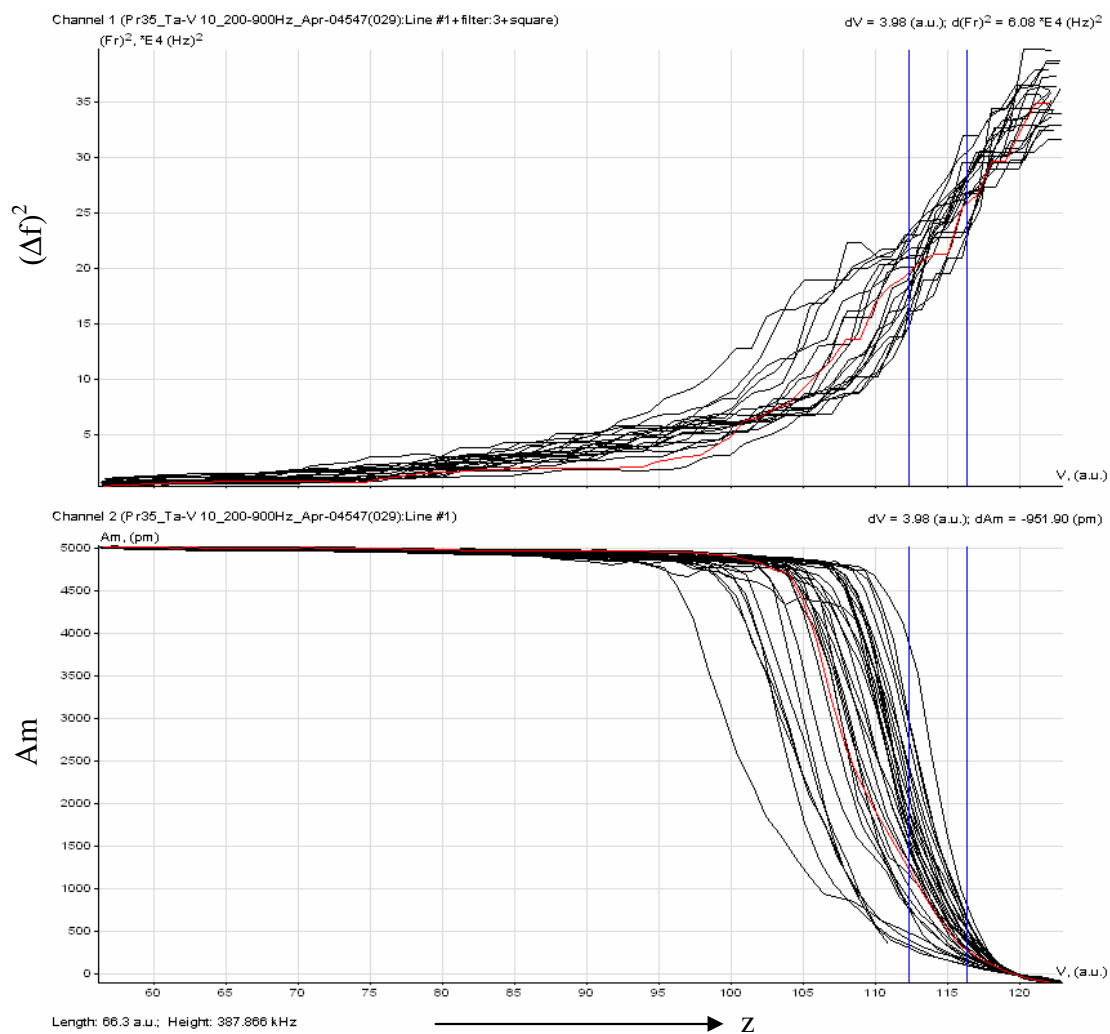**Figure II.47:** Frequency shift plot of Ta-V (λ=2.26 nm) Sample 9

Figure II.48: Frequency shift plot of Ta-V Sample 10

APPENDIX III

PROGRAM AND OUTPUT FOR BOUNDARY INTERFACE AREA CALCULATION OF NANOLAMINATES

III.A MATLAB program

III.A.1 Grain Boundary Intercept Area Calculation

```
close all
clear all

r=50;
w=[1,2,3,4,5,6,7,8,9,10,11,12,13,14,15,16,17,18,19,20,22,24,26,28,30,
...
    40,50,60,70,80,90,100,150,200,250,300,350,400,450,500,550,...
    600,650,700,750,800,850,900,950,1000,1050,1100,1150,1200,1250];

dg=15.2;                        %circular grain size
hg=sqrt(pi()/2/sqrt(3)*dg^2);   %hexagonal grain size
layer_size=4.5;

theta=65.3*pi/180;              %face angle, see geometry
phi=115.13*pi/180;              %angle on the face, see geometry
alpha=77.049*pi/180;            %determined from geometry, very ...
                                %important for measuring height
beta=30*pi/180;                 %half angle of equilateral
triangle,...
                                %60/2=30 deg

w_crit=2*r*cos(alpha)*cos(beta);
vol_sphere=2/3*pi*r^3-pi*r^3*cos(asin(w_crit/2/r))*...
    (sin(asin(w_crit/2/r)))^2-
pi*r^3/2*(cos(3*(asin(w_crit/2/r)))/3+...
    cos(asin(w_crit/2/r)));
vol_grain=sqrt(3)/2*hg^2*(layer_size/100);%(layer_size/100) is the
step size

for i=1:55
    area(i)=0;                      %area initialization
    if w(i)>w_crit
        vol_ind=sqrt(3)/12*w(i)^2*(w(i)/2/tan(phi/2)*cos(theta))-...
sqrt(3)/12*(w_crit)^2*(w_crit/2/tan(phi/2)*cos(theta))+...
            vol_sphere;
        number_of_grain_c=(vol_ind-vol_sphere)/vol_grain;
        %if number_of_grain_c<43.0
        %    area_c_const=(-2e-8*number_of_grain_c^6+...
        %        3e-6*number_of_grain_c^5-
0.0002*number_of_grain_c^4+...
        %        0.0056*number_of_grain_c^3-
0.0861*number_of_grain_c^2+...
        %        0.7155*number_of_grain_c-0.6003)*number_of_grain_c;
```

```
        %else
        %    area_c_const=(0.2056*log(number_of_grain_c)+1.7013)*...
        %            number_of_grain_c;
        %end

        number_of_grain_s=vol_sphere/vol_grain;

        %if number_of_grain_s<43.0
        %      area_s_const=(-2e-8*number_of_grain_s^6+...
        %            3e-6*number_of_grain_s^5-
0.0002*number_of_grain_s^4+...
        %            0.0056*number_of_grain_s^3-
0.0861*number_of_grain_s^2+...
        %            0.7155*number_of_grain_s-0.6003)*number_of_grain_s;
        %else
        %      area_s_const=(0.2056*log(number_of_grain_s)+1.7013)*...
        %            number_of_grain_s;
        %end
        area(i)=(2*sqrt(3)*hg/6)*(layer_size/100)*...
            ((3.0*number_of_grain_c)+(3.0*number_of_grain_s));
            %(area_c_const+area_s_const);
            %((2.0e-12*number_of_grain_c^6-1.0e-
9*number_of_grain_c^5+...
            %5.0e-7*number_of_grain_c^4-1.0e-
4*number_of_grain_c^3+...
            %0.01*number_of_grain_c^2+2.2725*number_of_grain_c-
4.3681)+...
            %(2.0e-12*number_of_grain_s^6-1.0e-
9*number_of_grain_s^5+...
            %5.0e-7*number_of_grain_s^4-1.0e-
4*number_of_grain_s^3+...
            %0.01*number_of_grain_s^2+2.2725*number_of_grain_s-
4.3681));


%((3.2074*number_of_grain_c+1.5873)+(3.0504*number_of_grain_s));
            %use the second comment line instead of the first for my
approximation
    else
        vol_ind=2/3*pi*r^3-pi*r^3*cos(asin(w(i)/2/r))*...
            (sin(asin(w(i)/2/r)))^2-
pi*r^3/2*(cos(3*(asin(w(i)/2/r)))/3+...
            cos(asin(w(i)/2/r)));
        number_of_grain=vol_ind/vol_grain;
        %if number_of_grain<43.0
        %      area_const=(-2e-8*number_of_grain^6+...
        %            3e-6*number_of_grain^5-0.0002*number_of_grain^4+...
        %            0.0056*number_of_grain^3-
0.0861*number_of_grain^2+...
        %            0.7155*number_of_grain-0.6003)*number_of_grain;
        %else
        %      area_const=(0.2056*log(number_of_grain)+1.7013)*...
        %            number_of_grain;
        %end
        area(i)=(2*sqrt(3)*hg/6)*(layer_size/100)*...
```

```
            (3.0*number_of_grain);
            %(area_const);
            %(2.0e-12*number_of_grain^6-1.0e-9*number_of_grain^5+...
            %5.0e-7*number_of_grain^4-1.0e-4*number_of_grain^3+...
            %0.01*number_of_grain^2+2.2725*number_of_grain-4.3681);
    end
end
```

III.A.2 Layer Pair Intercept Area Calculation

```
%To calculate the layer pair intercept area
%all dimesnions are in nm
%width=w, grain size=dg, layer pair= dAB, radius=r,
%face inclination angle=theta(65.3 deg)
%face crest angle=phi(115.13 deg)
%face depth=h_f, scratch depth=h, therefore h=h_f*cos(theta)
%Area of the face=A=0.5*w*h_f
close all
clear all

r=50;
w=[1,2,3,4,5,6,7,8,9,10,11,12,13,14,15,16,17,18,19,20,22,24,26,28,30,
...
    40,50,60,70,80,90,100,150,200,250,300,350,400,450,500,550,...
    600,650,700,750,800,850,900,950,1000,1050,1100,1150,1200,1250];

dg=16.7;
layer_size=2.6;

dAB=layer_size/2;                     %use half the layer pair thickness

theta=65.3*pi/180;                    %face angle, see geometry
phi=115.13*pi/180;                    %angle on the face, see geometry
alpha=77.049*pi/180;                  %determined from geometry,
                                      %very important for measuring
height
beta=30*pi/180;                       %half angle of euilateral triangle,
                                      %60/2=30 deg
w_crit=2*r*cos(alpha)*cos(beta);
for i=1:55
    area_c=0;                         %conical indentation area
initialization
    area_s=0;                         %spherical indentation area
initialization

    if w(i)>w_crit                    % checking if the indent goes to
conical part
        hc_f=1/(2*tan(phi/2))*(w(i)-w_crit);
        hc=hc_f*cos(theta);
        h=r-r*sin(alpha);             %only one height for spherical
indentation
        ht_c_f=w(i)/(2*tan(phi/2));%projected total height along the
face of conical part

        nc_real=hc/dAB;
```

228

```matlab
        nc_int=floor(hc/dAB);
        ht(i)=hc+h;                         %total vertical height

        sum_c=0;
        for j=1:nc_int
            sum_c=sum_c+(sqrt(3)/4)*(2*tan(phi/2)*(ht_c_f-
j*dAB/cos(theta)))^2;
        end

        area_c=1*sum_c;
        %1 is for 1 layer in the interface

        %*********************************
        %spherical indentation starts here
        %*********************************

        if (floor(ht(i)/dAB))>nc_int
            % spherical upper fraction
            h=h-(dAB-dAB*(nc_real-nc_int));
            sum_s=pi*(2*r*h-h^2);
        else
            sum_s=0;
        end
        %sum_s=0;
        n_int= floor(h/dAB);
        for j=1:n_int
            sum_s=sum_s+pi*(2*r*(h-j*dAB)-(h-j*dAB)^2);
        end
        area_s=1*sum_s;

    else

        h=r-sqrt(r^2-(w(i)/2)^2); % for spherical indent, there is
only one height
        ht(i)=h;
        n_int= floor(h/dAB);
        sum=0;
        for j=1:n_int
            sum=sum+pi*(2*r*(h-j*dAB)-(h-j*dAB)^2);
        end
        area_s=1*sum;
    end
    area_layer(i)=area_c+area_s;
end
```
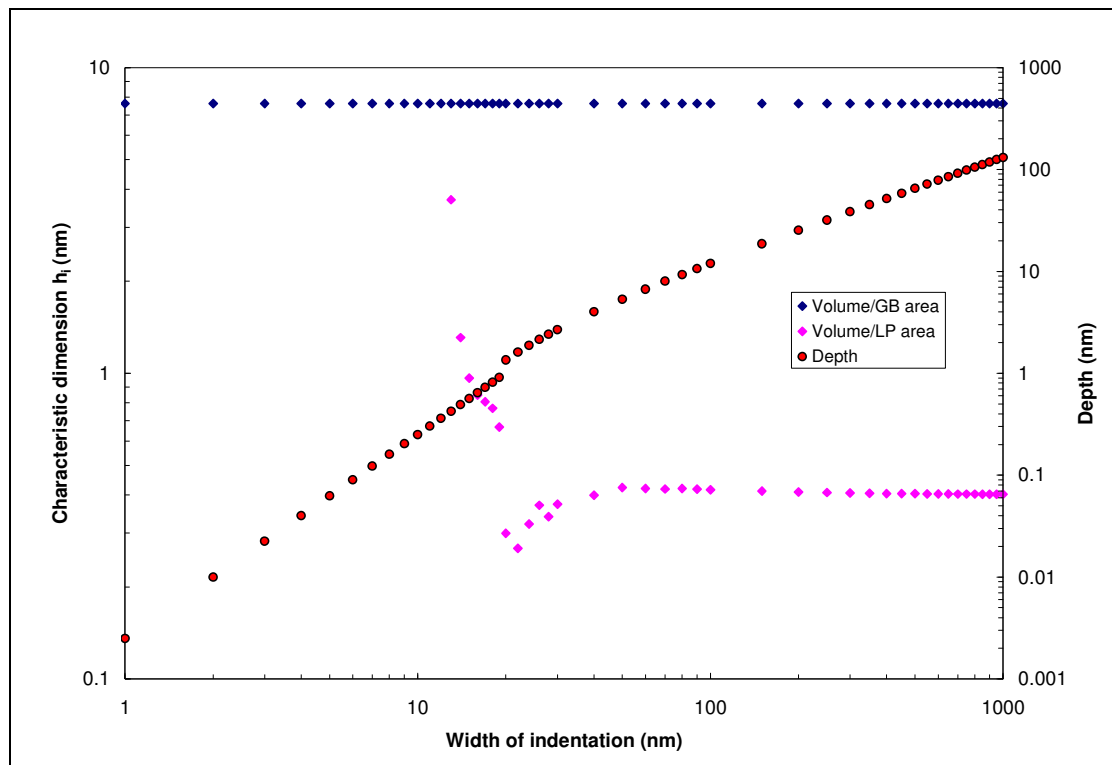
III.B Program Output for Au-Ni Samples

Figure III.1: Program output for Au-Ni (d_g=16.0 nm, λ=0.8 nm)
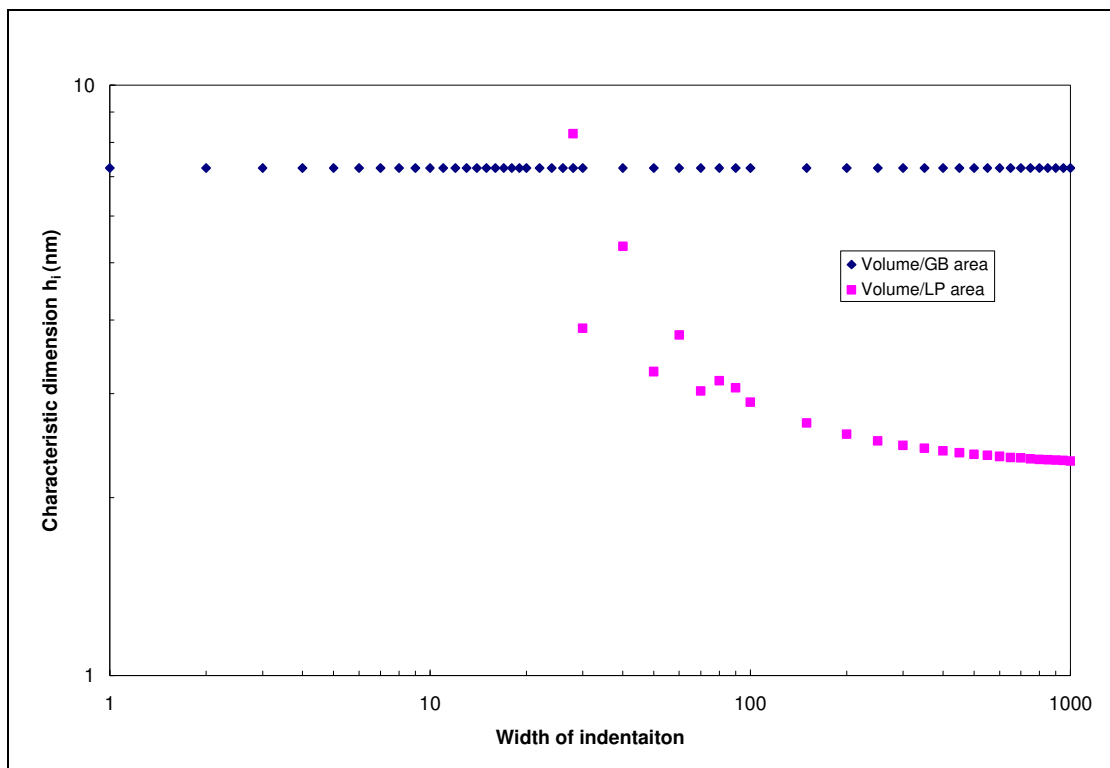
Figure III.2: Program output for Au-Ni (d_g=15.2 nm, λ=4.5 nm)
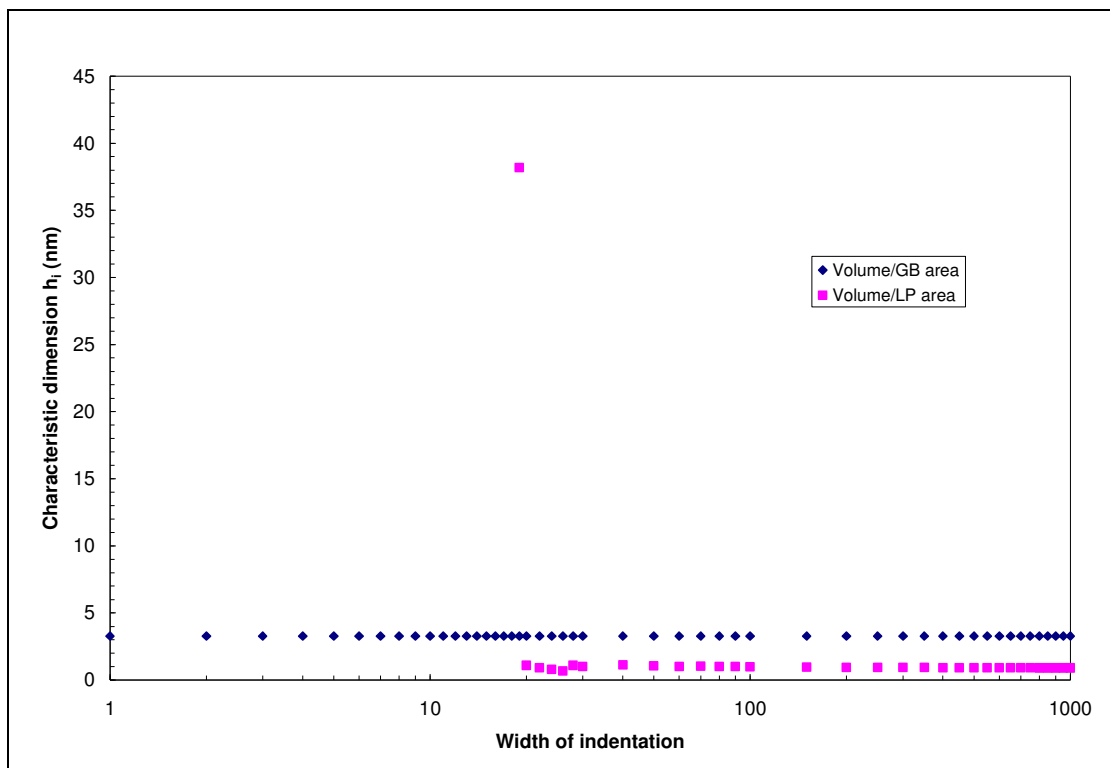
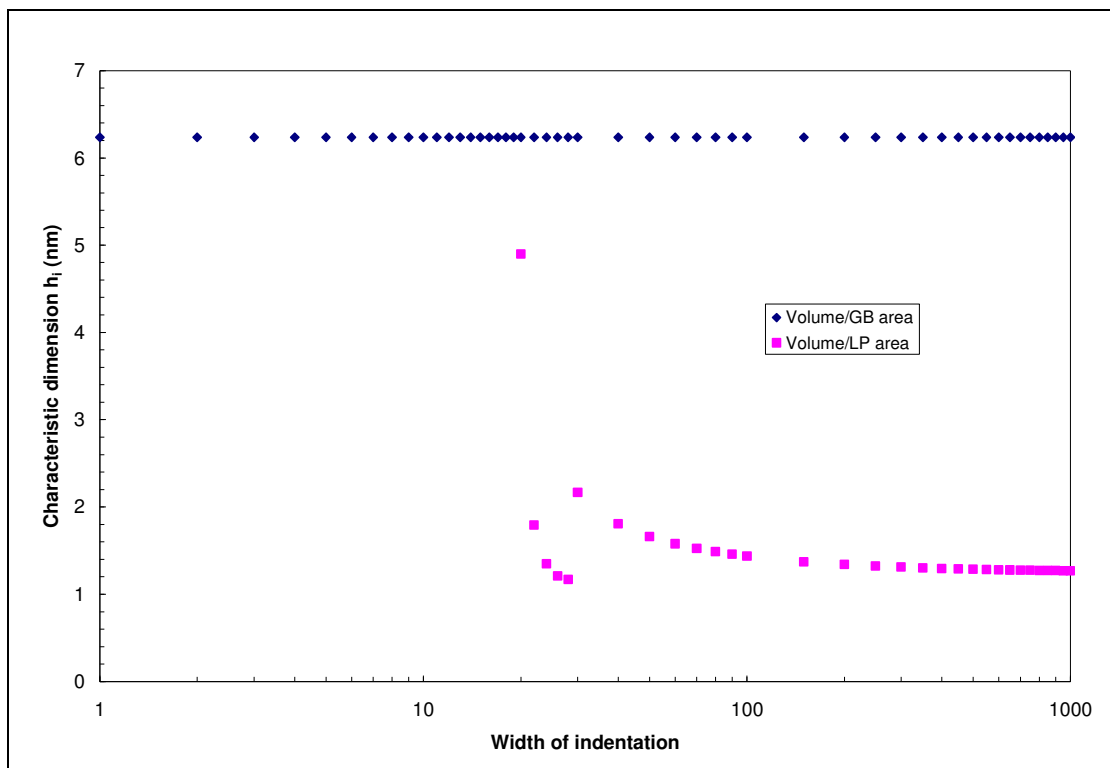**Figure III.3:** Program output for Au-Ni (d_g=6.9 nm, λ=1.8 nm)

Figure III.4: Program output for Au-Ni (d_g=13.1 nm, λ=2.5 nm)
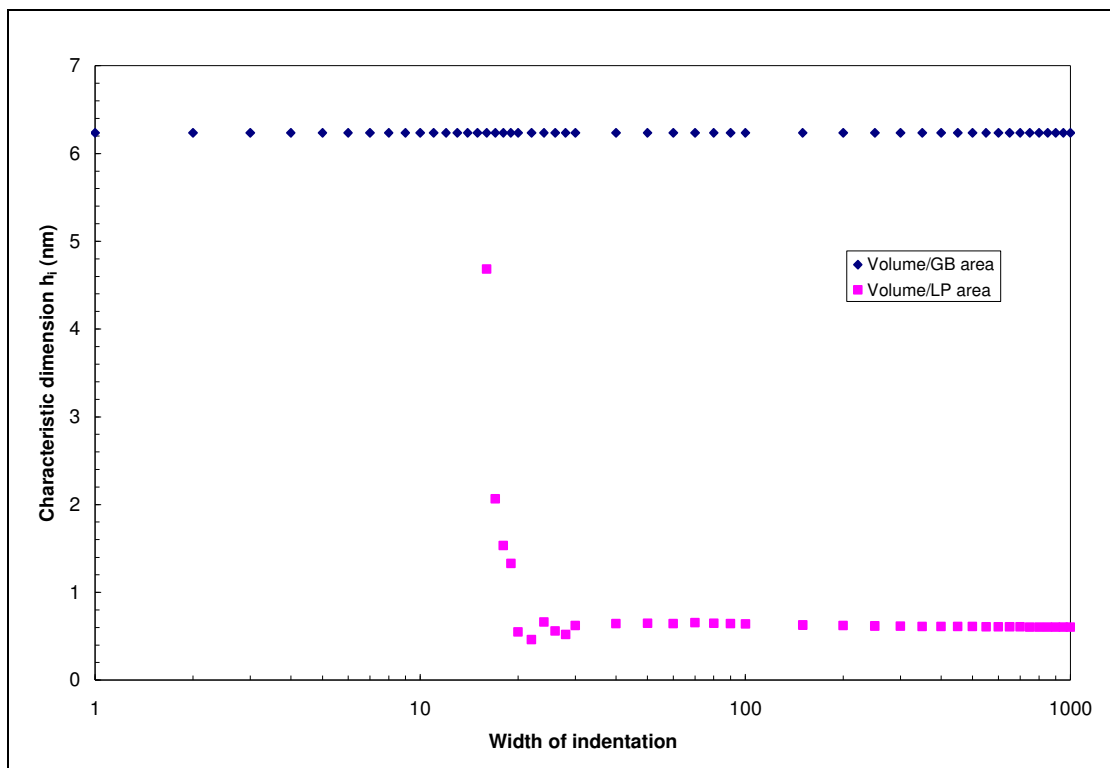
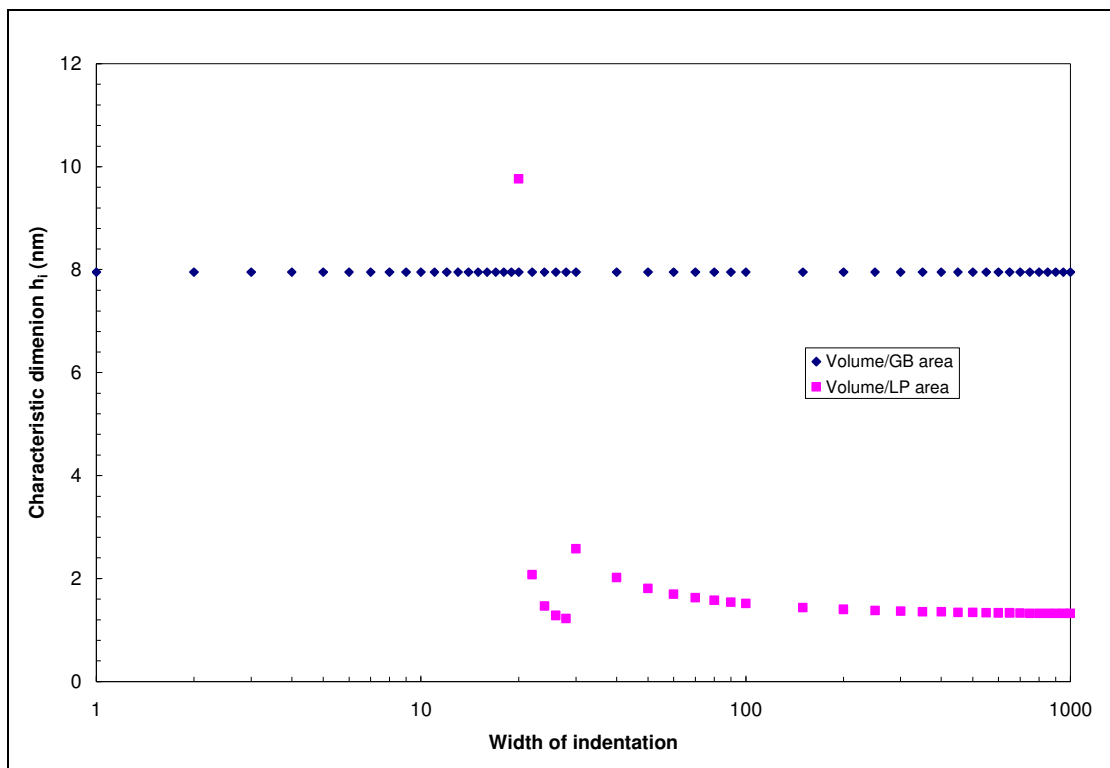**Figure III.5:** Program output for Au-Ni (d_g=11.4 nm, λ=1.2 nm)

Figure III.6: Program output for Au-Ni (d_g=16.7 nm, λ=2.6 nm)

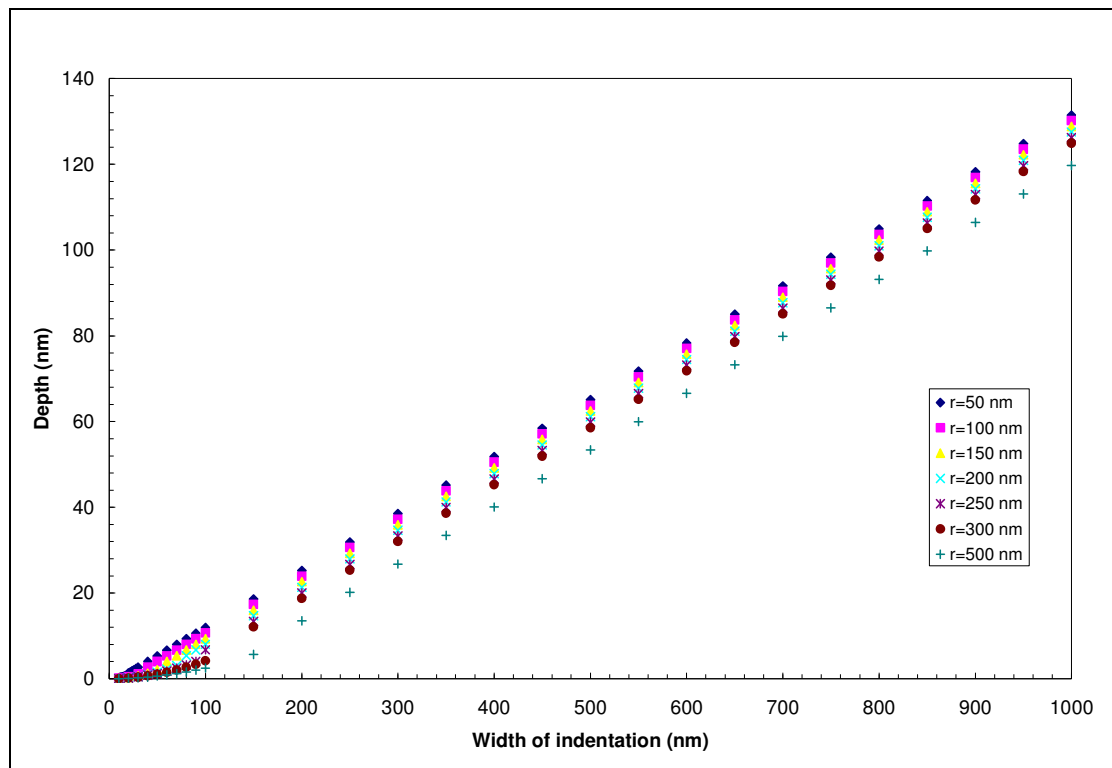## III.C Depth of Indentation as a Function of Tip Radius (nm)

III.C.1 Berkovich tip

Figure III.7: Change in depth of indentation as a function of the tip radius of a
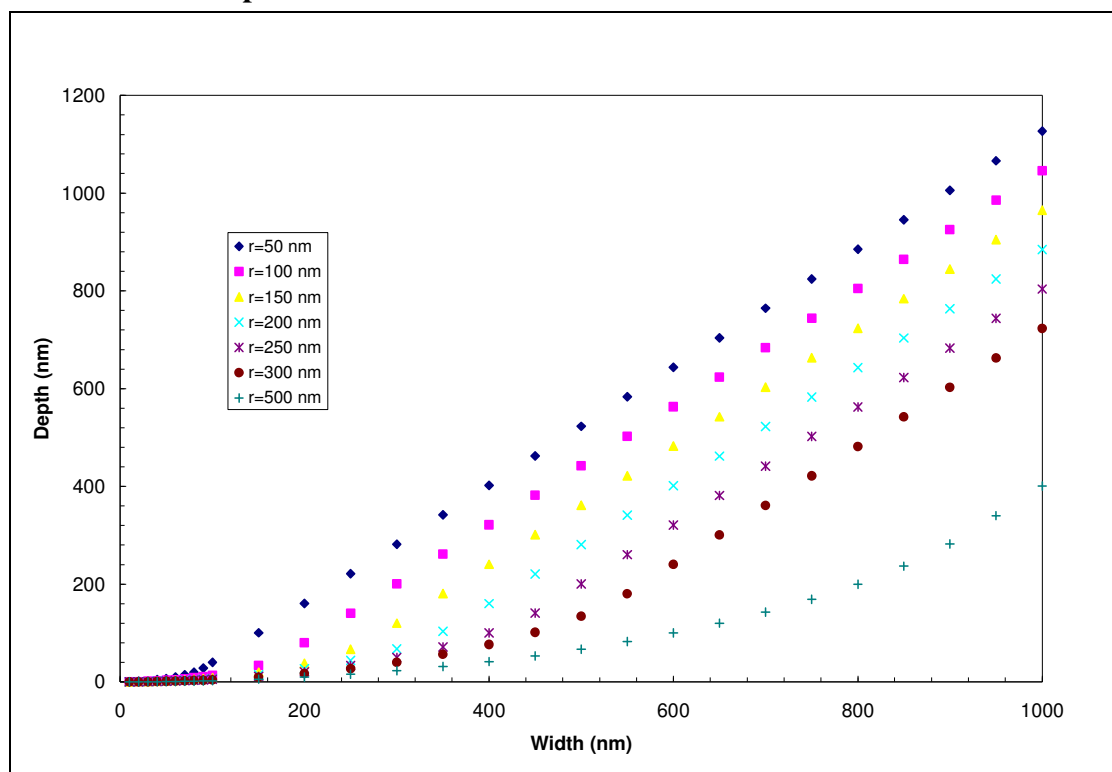
Berkovich tip

III.C.2 Conical tip

Figure III.8: Change in depth of indentation as a function of the tip radius of a

Conical tip with 90º angle
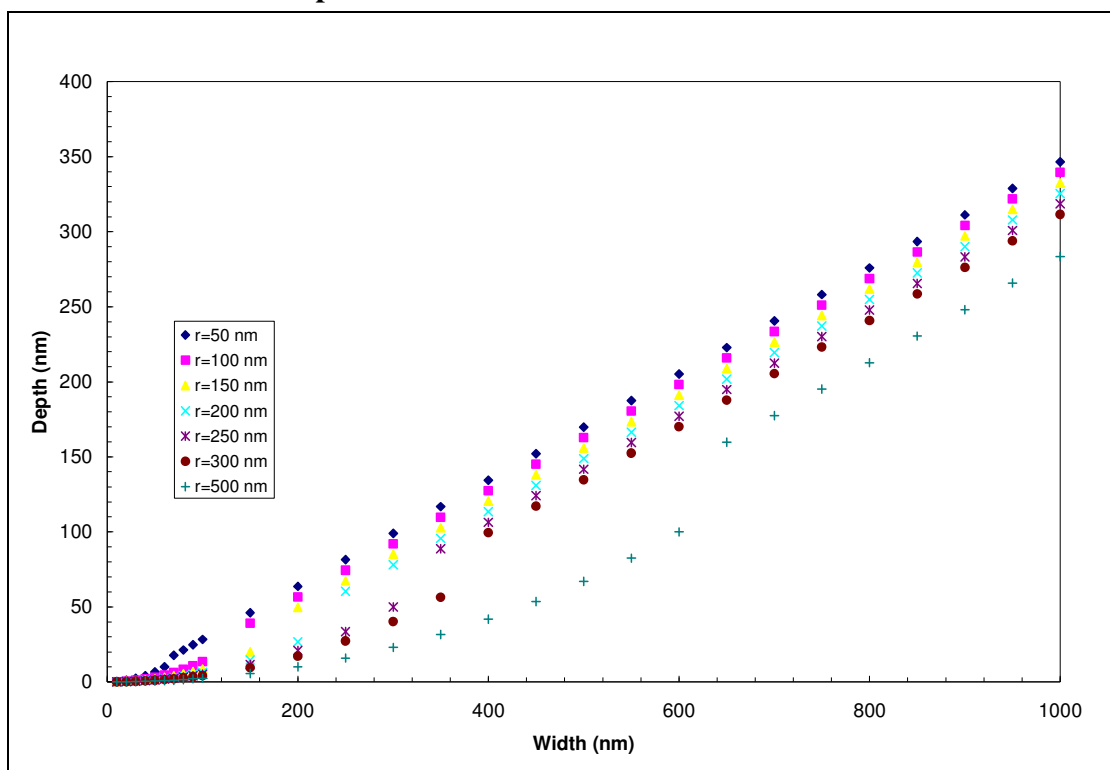
III.C.3 Cube Corner tip

Figure III.9: Change in depth of indentation as a function of the tip radius of a Cube

Corner tip with 90º angle